Recherche de technihadrons dans le spectre di-électrons et alignement temporel du calorimètre Argon liquide de l'expérience ATLAS

Ludovica Aperio Bella

UNIVERSITÉ DE GRENOBLE

THÈSE

Pour obtenir le grade de

DOCTEUR DE L'UNIVERSITÉ DE GRENOBLE

Spécialité: **Physique des Particules**

Arrêté ministériel: 7 août 2006

Présentée par

Ludovica Aperio Bella

Thèse dirigée par **Lucia Di Ciaccio**
codirigée par **Tetiana Berger-Hryn'ova**

préparée au sein du **Laboratoire d'Annecy-le-Vieux de Physique des Particules**
dans l'**École Doctorale de Physique de Grenoble**

Recherche de thechnihadrons dans le spectre di-électrons et alignement temporel du Calorimètre Argon Liquide de l'expérience ATLAS

Thèse soutenue publiquement le **14 Septembre 2012**,
devant le jury composé de :

Mme. Tetiana BERGER-HRYN'OVA
LAPP - Annecy-le-Vieux, Directrice de thèse
M. Marc BESANCON
CEA - Saclay, Rapporteur
Mme. Lucia DI-CIACCIO
LAPP - Annecy-le-Vieux, Directrice de thèse
M. Jean-Pierre LEES
LAPP - Annecy-le-Vieux, Président
M. Aleandro NISATI
Roma La Sapienza, Examinateur
M. Guillaume UNAL
CERN, Rapporteur

Université Joseph Fourier / Université Pierre Mendès France / Université Stendhal / Université de Savoie / Grenoble INP

Université de Grenoble

—

Laboratoire d'Annecy-le-Vieux de Physique des Particules

THESE

présentée pour obtenir le grade de

Docteur de l'Université de Grenoble

Spécialité : Physique des Particules

par

Ludovica Aperio Bella

Search for Technihadrons in Dielectron channel and Alignments of the ATLAS Liquid Argon Electromagnetic calorimeters.

Soutenue publiquement le 14 Septembre 2012 devant le jury composé de

Tetiana	BERGER-HRYN'OVA	Annecy-le-Vieux	*Directrice de thèse*
Marc	BESANCON	CEA Saclay	*Rapporteur*
Lucia	DI-CIACCIO	Annecy-le-Vieux	*Directrice de thèse*
Jean-Pierre	LEES	Annecy-le-Vieux	*Président du jury*
Aleandro	NISATI	Roma La Sapienza	*Examinateur*
Guillaume	UNAL	CERN	*Rapporteur*

ii

A mio Nonno

Contents

Introduction

One of the most challenging scientific endeavors is the discovery and investigation of the building blocks of nature. The Standard Model (SM) of particle physics summarizes today's grasp for the elementary particles and the interactions between them. However, the mechanism that breaks electroweak symmetry in the SM has not been verified experimentally. This mechanism, which gives mass to massive elementary particles, implies the existence of a scalar particle, the SM Higgs boson. The search for the Higgs boson, the only elementary particle in the SM that has not yet been observed, is one of the highlights of the Large Hadron Collider (LHC) physics program.

This summer both the ATLAS and CMS Collaborations reported a 5σ excesses of events in their 2011 and 2012 datasets of proton-proton collisions at centre-of-mass energy $\sqrt{s} = 7$ TeV and $\sqrt{s} = 8$ TeV at the LHC. The decays to pairs of vector bosons whose net electric charge is zero identify the new particle as a neutral boson. The observation in the diphoton channel disfavors the spin-1 hypothesis. Although these results are compatible with the hypothesis that the new particle is the Standard Model Higgs boson, more data are needed to assess its nature in detail.

This thesis describes the work that I have done during the three years of my PhD on the ATLAS experiment. In each chapter are reported the different activities performed. Starting with the commissioning of the detector performances, the performance studies of the physics object reconstruction and finally conducting a search for new physics phenomena.

In the first chapter of this thesis, an introduction to the SM is given. This introduction summarizes the success of the SM and explain the generation of the masses *via* the Higgs mechanism. The shortcomings of the SM are also presented. In particular alternative models, called TechniColor (TC), to the SM Higgs mechanism are presented. In TC theories, the scalars fields which provide the electroweak symmetry breaking are composites and produced by new strong dynamics at a new strong scale. And therefore the Higgs sector of the SM becomes an effective description of a more fundamental theory.

The ATLAS experiment is one of the two general purpose experiments located around the LHC ring. It has been designed for the search of the Higgs boson and new physics phenomena. In the first part of the second chapter of this thesis, the LHC accelerator complex and the operational parameter for the 2010/2011 data taking are presented. In the second part the ATLAS experiment is presented, concentrating in more detail on the performances of the subsystems which are used in this thesis.

Most of the detector related effort was applied on the ATLAS Liquid Argon Calorimeter (LAr). The LAr calorimeters are introduced in details, in the third chapter of this thesis. The main goal of this calorimetry system is to measure the energy of electrons and photons over a broad energy range up to a few TeV. To insure the optimal energy reconstruction and also to synchronize the detector readout system with the LHC bunch crossing the time over

all the calorimeter channels has to be aligned. Moreover an accurate timing alignment of the ATLAS LAr Calorimeter is important to achieve a good time resolution in the calorimeter and has several physics application in the ATLAS environment. The third chapter of this thesis describes the timing analysis performed with the LHC proton-proton collision data collected in the 2011.

The fourth Chapter of this thesis describes the measurements of the trigger, the reconstruction and the identification electron efficiency using $Z \to ee$ events observed in 5 fb^{-1} of data collected in 2011 at a center-of-mass energy of $\sqrt{s} = 7$ TeV. The precise determination of the electron performance of the ATLAS detector is indeed essential for any search for new phenomena with electrons in the final state.

Finally the last chapter of this thesis presents a search for new physics in the dielectron finale state. The dilepton spectrum is a model-independent probe of new physics. Any observed excess above the SM expectation can be interpreted as evidence of new physics. Many models predict resonances at high dilepton masses such as the TC models where a composite signal is revealed by an excess of events at large lepton pair invariant mass. The presence of a TC particle would be detected in ATLAS by the observation of resonance peaks in the dilepton mass spectrum over the Drell-Yan process which constitutes the main SM background. This background falls sharply with increasing dilepton mass and we expect it to be well modeled using the extrapolation from the low mass part of the spectra.

Chapter 1

Standard Model of Particle Physics and beyond

The energy at which the Large Hadron Collider (LHC) operates is determined by the need to answer to the questions that the Standard Model (SM) [1,2] of the particle interactions has left open and, in particular, to understand the origin of mass of the elementary particles. The SM constitutes one of the most successful models of nature. However several considerations of different kind call for a more fundamental description of nature.

1.1 The Standard Model Theory

At microscopic level all the observed phenomenology in molecular, atomic, nuclear and subnuclear physics, can be understood in terms of three fundamental interactions: strong, electromagnetic and weak interactions.

In the SM the fundamental constituent of the matter and the particle responsible of their interaction are represented by fields. The SM is a quantum field theory, which is invariant under the local gauge transformations of these fields, based on the symmetry group $SU(3)_C \otimes SU(2)_L \otimes U(1)_Y$. The $SU(3)_C$ is the "color" group of the theory of strong interactions (QCD: Quantum Chromo-Dynamics [3,4]) and the $SU(2)_L \otimes U(1)_Y$ is the symmetry group which describes the electroweak (EW) interactions [1,5].

The SM gauge symmetry group has $8 + 3 + 1 = 12$ generators. To each generator a vector boson (also said gauge boson) is associated with the same quantum numbers. If the gauge symmetry is unbroken, this boson is of vanishing mass. These vector (i.e. of spin 1) bosons act as mediators of the corresponding interactions.

In the SM there are 8 massless gluons associated to the $SU(3)_C$ color generators, while for $SU(2)_L \otimes U(1)_Y$ there are 4 gauge bosons W^+, W^-, Z^0 and γ. Of these, only the photon is massless. The masses of W^+, W^-, Z^0 ($m(W) \sim 80.4\,\text{GeV}$, $m(Z) \sim 91.2\,\text{GeV}$) are quite large compared to the masses of the elementary particles (except to the top quark). In fact in the electroweak sector the group symmetry is broken "spontaneously".

In the SM the EW spontaneous symmetry breaking is realized by the Higgs mechanism (describe in more details in section 1.1.4). Four scalar fields are introduced with a potential that produces an infinite number of degenerate vacuum states. The choice of one of these vacuum states breaks spontaneously the symmetry. As result one scalar neutral particle (the Higgs) must necessarily be present in the spectrum of the physical states with masses very close to the range so far explored.

3

It is expected that the mechanism which leads to the EW symmetry breaking will be explain at the LHC thus completing the experimental verification of the SM.

The SM is a renormalizable field theory which means that the ultra-violet divergences that appear in loop diagrams can be eliminated by a suitable redefinition of the parameters already appearing in the bare Lagrangian: masses, couplings and field normalizations.

1.1.1   The Particle in the SM

The fermionic (spin 1/2) matter fields of the SM are quarks and leptons. Quarks and leptons are grouped in 3 "families" or "generations" with equal quantum numbers but different masses (Table 1.1).

Table 1.1: Fermions of the Standard Model with their charge and mass. [6]

Generation	First		Second		Third	
Leptons	$\boldsymbol{\nu_e}$ $\quad Q=0$		$\boldsymbol{\nu_\mu}$ $\quad Q=0$		$\boldsymbol{\nu_\tau}$ $\quad Q=0$	
	mass$< 2 \times 10^{-6}$ MeV		mass< 0.19 MeV		mass< 18.2 MeV	
	$\boldsymbol{e}$ $\quad Q=-1$		$\boldsymbol{\mu}$ $\quad Q=-1$		$\boldsymbol{\tau}$ $\quad Q=-1$	
	mass$= 0.511$ MeV		mass$= 105.7$ MeV		mass$= 1.777$ GeV	
Quarks	$\boldsymbol{u}$ $\quad Q=\frac{2}{3}$		$\boldsymbol{c}$ $\quad Q=\frac{2}{3}$		$\boldsymbol{t}$ $\quad Q=\frac{2}{3}$	
	mass$= 1.7 - 3.3$ MeV		mass$= 1.27$ GeV		mass$= 171.2$ GeV	
	$\boldsymbol{d}$ $\quad Q=-\frac{2}{3}$		$\boldsymbol{s}$ $\quad Q=-\frac{2}{3}$		$\boldsymbol{b}$ $\quad Q=-\frac{2}{3}$	
	mass$= 4.1 - 5.8$ MeV		mass$= 101$ MeV		mass$= 4.2$ GeV	

Leptons

Leptons couple only via the electroweak interactions. They are classified into left-handed doublets and right-handed singlets of isospin. As neutrinos couple only via the weak interaction in the SM, right-handed neutrinos are usually not considered. Lepton representations under $SU(2)_L$ are:

$$\left(\begin{array}{c} \nu_e \\ e^- \end{array} \right)_L, \left(\begin{array}{c} \nu_\mu \\ \mu^- \end{array} \right)_L, \left(\begin{array}{c} \nu_\tau \\ \tau^- \end{array} \right)_L, e^-_R, \mu^-_R, \tau^-_R.$$

This means that under $SU(2)_L$, a left-handed electron and an electronic neutrino are "the same particle".

The neutrinos are massless in the SM. However the detection of neutrino oscillations [6] have shown that they should have a mass of the order of the eV. It is however unknown whether neutrinos are Majorana particles, with identical left-handed and right-handed states, or Dirac particles with separate right handed degrees of freedom.

Quarks

Quarks couple through the electroweak and strong interactions. Their representation under $SU(2)_L$ is:

$$\left(\begin{array}{c} u \\ d \end{array} \right)_L, \left(\begin{array}{c} c \\ s \end{array} \right)_L, \left(\begin{array}{c} t \\ b \end{array} \right)_L, u_R, d_R, c_R, s_R, t_R, b_R.$$

Results [6], have shown that weak interactions in the quark sector do not conserve flavor. For example a u quark can transform to an s quark by the exchange of a W. This means that the quarks mass states are not eigenstates of flavor, but are a linear combination of the mass states. This formalism has been introduced by Cabibbo, Kobayashi and Maskawa [7,8]:

$$\begin{pmatrix} d' \\ s' \\ b' \end{pmatrix} = V_{CKM} \begin{pmatrix} d \\ s \\ b \end{pmatrix} \quad ,$$

Where the V_{CKM} matrix gives the mixing between the quark generations.

$$V_{CKM} = \begin{pmatrix} V_{ud} & V_{us} & V_{ub} \\ V_{cd} & V_{cs} & V_{cb} \\ V_{td} & V_{ts} & V_{tb} \end{pmatrix} \quad .$$

It can be described by four real parameters: three angles α, β, γ, and a complex phase. The latter gives the source of CP violation in the SM.

The quark color charge can take three values and three anti values written: $r, \bar{r}, g, \bar{g}, b, \bar{b}$. For example the representation of the quark u under $SU(3)_C$ will be:

$$\begin{pmatrix} u_r \\ u_g \\ u_b \end{pmatrix}_C$$

Due to the confinement properties of QCD, the quarks cannot exist as free particles. They exist as bound states, either of a quark-antiquark pair forming a mesons or a three-quark system forming a baryon.

Bosons

In quantum field theory forces are described as an exchange of particles between the particles of matter. This is a major difference compared to classical physics where forces were assumed to act instantaneously. The exchanged particles are integer spin particles (spin 1) called gauge bosons. The forces are described via gauge symmetry groups [9]. Of the four forces known in nature: gravitational, electromagnetic, weak and strong, only the last three are included in the SM. Table 1.2 gives a summary of the properties of SM bosons, and which force they mediate.

EW			QCD
γ $\quad Q = 0$	Z^0 $\quad Q = 0$	$W^\pm$ $\quad Q = \pm 1$	$n = 8$ g $\quad Q = 0$
m= 0 GeV	m= 91.1876 GeV	m= 80.399 GeV	m= 0 GeV

Table 1.2: Bosons of the Standard Model with their charge and mass. [6]

1.1.2 The Quantum Chromodynamics

The QCD sector of the SM has a simple structure but a very rich dynamical content, including the observed complex spectroscopy with a large number of hadrons. The most prominent

properties of QCD are *asymptotic freedom* and *confinement*. In QCD the relevant coupling parameter that appears in physical processes is:

$$\alpha_s = \frac{e_s{}^2}{4\pi}$$

where e_s is the coupling constant of the basic interaction vertices of quark and gluons: *qqg* or *ggg*.

In field theory the effective coupling of a given interaction vertex is modified by the interaction. As a result, the measured intensity of the force depends on the transferred (four)momentum squared, Q^2, among the participants. This means that the coupling constants are dependent on the chosen scale, and is said to be *running*.

Asymptotic freedom means that the effective coupling becomes a function of Q^2 and $\alpha_s(Q^2)$ decreases for increasing Q^2 and vanishes asymptotically. Thus, the QCD interaction becomes very weak in processes with large Q^2 , called hard processes or deep inelastic processes (i.e. with a final state distribution of momenta and a particle content very different than those in the initial state). This is an important properties since it allows at high Q^2 to treat the QCD using a perturbation theory. The effective coupling decreases very slowly at large momenta with the inverse logarithm of Q^2 :

$$\alpha_s(Q^2) = \frac{1}{b \log\left(\frac{Q^2}{\Lambda_{QCD}{}^2}\right)} \qquad (1.1)$$

where b is a known constant and Λ_{QCD} is an energy of order a few hundred MeV.

At high transferred momenta the potential between two color charges is similar to the Coulomb potential, i.e. proportional to $\alpha_s(r)/r$, with a small effective coupling constant. On the contrary the interaction strength becomes large at small transferred momenta, of order $Q \lesssim \Lambda_{QCD}$.

The property of *confinement* is the impossibility of separating color charges, like individual quarks and gluons or any other colored state. This is because in QCD the interaction potential between color charges increases at long distances linearly in r. In fact all observed hadrons are tightly bound composite states of quarks (baryons are made of *qqq* and mesons of $q\bar{q}$), with compensating color charges so that they are overall neutral in color.

When it try to separate the quark and the antiquark that form a color neutral meson the interaction energy grows until pairs of quarks and antiquarks are created from the vacuum and new neutral mesons are coalesced and observed in the final state instead of free quarks. For example, consider the process $e^+e^- \to q\bar{q}$ at large center of mass energies. The final state quark and antiquark have large energies, so they separate in opposite directions very fast. But the color confinement forces create new pairs in between them. What is observed is two back-to-back jets of color-less hadrons with a number of slow pions that make the exact separation of the two jets impossible. In some cases a third well separated jet of hadrons is also observed: these events correspond to the radiation of an energetic gluon from the parent quark-antiquark pair.

At high energy Parton Distribution Functions (PDFs) are used to parameterize the quark content of hadrons. PDFs parameterize the fraction of momentum carried by each constituent of a particle. These PDFs are necessary to making predictions of cross sections and kinematic distributions at hadron colliders.

Due to the non-perturbative nature of QCD at low energy different techniques have been developed to allow better comprehension of the dynamics at low scale.

1.1.3 The Electroweek Theory

In the EW sector the SM provides a well-defined and consistent theoretical framework including weak interactions and quantum electrodynamics in a unified picture. The weak interactions derive their name from their intensity. At low energy the strength of the effective four-fermion interaction of charged currents is determined by the Fermi coupling constant G_F. For example, the effective interaction for muon decay is given by:

$$\mathcal{L}_{eff} = \left(G_F/\sqrt{2}\right)\left[\bar{\nu}_\mu\gamma_\alpha\left(1-\gamma_5\right)\mu\right]\left[\bar{e}\gamma^\alpha\left(1-\gamma_5\right)\nu_e\right] \tag{1.2}$$

with $G_F = 1.16639(1)\times10^{-5}\text{GeV}^{-2}$ [6], γ_5 and γ_α are the Dirac matrices and μ, e and ν_e and ν_e are the lepton fields. In natural units G_F has dimensions of $(\text{mass})^{-2}$. As a result, at low energy the weak interactions are characterized by an effective four fermion couplings Lagrangian with the intensity proportional to $\propto G_F E^2$ where E is the energy scale for a given process. The quadratic increase with energy cannot continue for ever, because it would lead to a violation of unitarity. In fact, at large energies the propagator effects can no longer be neglected, and the "current–current" interaction is resolved into "current–W" gauge boson vertices connected by a W propagator. The strength of the weak interactions in the standard weak theory is:

$$\alpha_W = \sqrt{2}\ G_F\ \frac{m_W^2}{\pi} \cong \frac{1}{30},$$

with a range r_W very short:

$$r_W = \frac{\hbar}{m_W\ c} \simeq 2.5\times10^{-16}\text{cm},$$

corresponding to $m_W = 80.4\,\text{GeV}$. This very large value for the W (or the Z) mass makes a drastic difference, compared with the massless photon and the infinite range of the QED force. The unification [9] of the weak and electromagnetic interactions in a single electroweak interaction is introduced through the invariance of the Lagrangian under the gauge group $SU(2)_L \otimes U(1)_Y$. The triplet of gauge fields $W^\mu(x) = (W_1^\mu, W_2^\mu, W_3^\mu)$ assure the invariance of the Lagrangian under a local transformation of $SU(2)_L$, and a new gauge boson B_μ associated with the $U(1)_Y$ group is introduced. The neutral sector of the interaction is, therefore, composed of two states which can mix. As will be detailed below, one can consider in particular the basis obtained by a rotation of θ_W, called the weak mixing angle [9] or Weinberg angle, defined by

$$\begin{cases} \cos\theta_W &= \frac{g}{\sqrt{g^2+g'^2}} \\ \sin\theta_W &= \frac{g'}{\sqrt{g^2+g'^2}} \end{cases} \tag{1.3}$$

Where g and g' are respectively the weak and electromagnetic coupling constant. The corresponding gauge boson component are then:

$$\begin{cases} W^+ &= \frac{1}{\sqrt{2}}(W_1 - iW_2) \\ W^- &= \frac{1}{\sqrt{2}}(W_1 + iW_2) \\ Z^\mu &= \cos\theta_W W_3^\mu - \sin\theta_W B_\mu \\ A^\mu &= \sin\theta_W W_3^\mu + \cos\theta_W B_\mu \end{cases} \tag{1.4}$$

The field A^μ is associated to the photon and mediates the electromagnetic interaction. The field (Z^μ) is associated to the Z boson and mediates the neutral current of the weak interactions. The fields $(W^\pm)$ are associated to the W bosons and mediate the charged currents.

1.1.4   The EW symmetry breaking

A major difficulty in unifying the weak and electromagnetic interactions was the fact that e.m. interactions have infinite range ($m_\gamma = 0$), whilst the weak forces have a very short range, owing to $m_{W,Z} \neq 0$. The observed W and Z with longitudinal polarization, are not present in an unbroken gauge theory (massless spin-1 particles, like the photon, are transversely polarized). The longitudinal degree of freedom for the W or the Z have to be explained in a different way. The solution of this problem is in the concept of spontaneous symmetry breaking realized by the Higgs mechanism [10–12].
In this picture the EW symmetry is spontaneously broken with the introduction of a complex scalar field ϕ that transforms as weak-isospin doublet, and acquires a nonzero vacuum expectation value, by virtue of its self-interaction. The complex doublet ϕ corresponds to four real
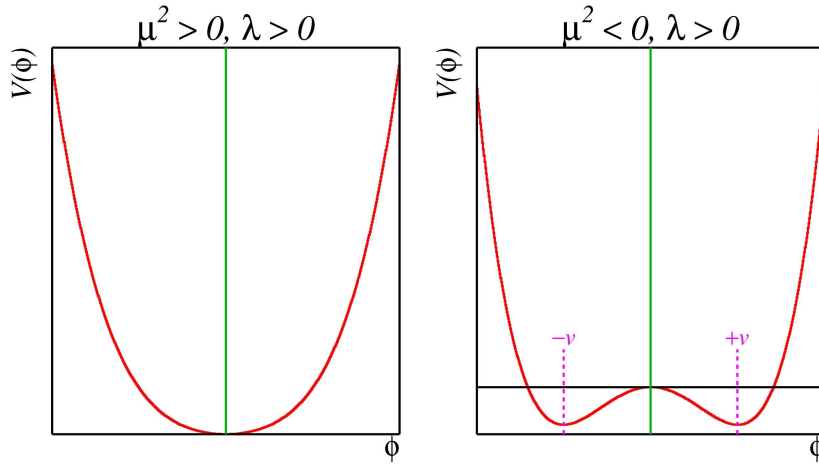
Figure 1.1: Protection on a plain of the potential $V(\phi^\dagger \phi) = \mu^2(\phi^\dagger \phi) + |\lambda|(\phi^\dagger \phi)^2$ for positive (left) or negative μ^2 (right).

scalar fields. The complex doublet is introduced as the agent of electroweak symmetry breaking and its self-interactions ($O(\lambda)$), given by the potential in Equation 1.5, are arranged so that the vacuum state corresponds to an internally broken-symmetry solution.

$$V(\phi^\dagger \phi) = \mu^2(\phi^\dagger \phi) + |\lambda|(\phi^\dagger \phi)^2 \tag{1.5}$$

The electroweak symmetry is spontaneously broken if the mass term in the potential has $\mu^2 < 0$: this is the condition for the existence of a non unique lowest energy state (see Figure 1.1). In this case gauge invariance leads to the freedom to choose the state of minimum energy (the vacuum state) to:

$$\langle \phi \rangle_0 = \left\langle \begin{pmatrix} \phi^+ \\ \phi^0 \end{pmatrix} \right\rangle_0 = \begin{pmatrix} 0 \\ v/\sqrt{2} \end{pmatrix} \tag{1.6}$$

where $v/\sqrt{2} = \sqrt{-\mu^2/|\lambda|}$ is the vacuum expectation value (VEV) of $\langle \phi \rangle_0$. Three of the 4 degrees of freedom of ϕ become the longitudinal components of the gauge bosons W^+, W^-, Z^0. The fourth emerges as a massive scalar particle H, called the Higgs boson, with its mass given by : $M_H^2 = -2\mu^2 = 2|\lambda|v^2$.

For $\lambda \sim O(1)$ the Higgs mass should be of the order of the weak scale v_{weak}:

$$v_{weak} = v/\sqrt{2} = \sqrt{-\mu^2/|\lambda|} = 2^{-2/3} G_F^{-1/2} \approx 175 \, \text{GeV}.$$

The Higgs mechanism allow to give mass also to the fermions with a Yukawa coupling terms as: $M_f = \lambda_f \frac{v}{\sqrt{2}}$, where the λ_f values are free parameters of the theory.

1.1.5 The Problems of the SM

The SM is a quite powerful theory which has predicted many particles before their discovery such as the top quark or the W and Z bosons. However there is also a number of problems that have no solution.

The SM can be viewed as a low-energy effective theory valid up to an energy scale Λ. Above this scale any new phenomena could emerge. At low energies with respect to this scale the existence of new physics is expressed via effective operators. The success of the SM is due to the fact that most of the corrections to its physical observables depend only logarithmically on the scale Λ. In fact, in the SM exists only one operator which acquires corrections quadratic in Λ. This is the squared mass operator of the Higgs boson. If the SM is valid up-to the Planck scale the correction to the Higgs mass are very big and it is hard to explain naturally why at the end the mass of the Higgs is of the order of the EW scale $\simeq O(100 \, GeV)$. This is the hierarchy problem, which suggests that the SM may be a low-energy effective theory of a new fundamental theory, whose validity may not reach much beyond the TeV scale.

Even if the SM Higgs would be discovered the SM has conceptual problems:

- The Higgs mechanism is introduced in an *ad hoc* way in the SM. It explains how vector bosons and fermions acquire masses but not why.
  - The Standard Model contains free parameters, which have no theoretical underpinning. They have been introduced by hand in the theory to fit observations.
  - There is no explanation to the hierarchy of the fermions masses within the SM. For example the up and down quarks masses are separated by almost six order of magnitude from the mass of the top quark.
  - The Hierarchy problem: the quadratic corrections to the Higgs mass leads to an unnaturally high mass of the Higgs boson as the cutoff scale of the SM is raised. It is possible to restore the proper Higgs mass, but this requires fine tuning of the SM parameters, which is not intellectually satisfactory.

- It is known [13] that neutrinos have mass, but the exact nature of the mass terms remains unknown.

- Indirect proof of Dark Matter have been detected through the astrophysical observation [14, 15] but there is no suitable particle content in the SM to account for this observation.

- Gravitation is not included in the SM.

These arguments do not imply that the SM is necessarily incorrect, but it must be extended to answer any of the questions raised above.

1.2 Technicolor Theories

In the models consider in this thesis the EW symmetry breaking (EWSB) and the mechanism which allows to give masses to particles are explained in terms of strong dynamics. One

possibility is to introduce a completely new strong sector, in terms of a model called Techni-Color (TC). In TC theories, the scalars fields which provide the EWSB are composites [16] and produced by new strong dynamics at a new strong scale. The Higgs sector of the SM becomes an effective description of a more fundamental theory. This idea comes from the possibility to break the EW symmetry with the standard QCD dynamics.

The scheme is motivated by the observation of an interesting analogy between the properties of Dirac particles and the quasi-particle excitations that appear in the theory of superconductivity [17, 18]. In a superconductive system Bardeen, Cooper, and Schrieffer [19] observed that a pair of superconductive electrons (called Cooper pair) leads at the spontaneous breaking of the $U(1)_Q$ electric symmetry.

1.2.1   The Quantum Chromodynamics at high mass scale

The QCD Lagrangian is invariant under a *chiral* gauge symmetry $SU(2)_L \otimes SU(2)_R$ in which independent gauge transformations ($SU(2)_L$ and $SU(2)_R$ respectively) are applied to the left- and right-handed fermions. When the running QCD coupling constant becomes large at the QCD scale, the strong interactions bind quark anti-quark pairs into a composite neutral scalar field $Q\bar{Q}$. This develops a non-zero vacuum expectation value:

$$\langle Q\bar{Q}\rangle_0 = \langle 0|\bar{q}_L q_R + \bar{q}_R q_L|0\rangle \simeq \Lambda_{QCD}^3 \qquad (1.7)$$

This, in turn, spontaneously breaks the chiral symmetry $SU(2)_L \otimes SU(2)_R$ down to $SU(2)$ of isospin. The pions, the lightest pseudoscalar mesons, are the Nambu-Goldstone [20] bosons associated with the spontaneous symmetry breaking and are massless.

The QCD-driven condensate of Equation 1.7, in analogy with the scalar H field, has $\langle Q\bar{Q}\rangle_0 \neq 0$ and since is a doublet of $SU(2)$ when the EW interactions are switched on the electroweak gauge bosons couple with the Goldstone bosons (the pions) acquire mass of orderer $\sim g f_\pi$. Where $f_\pi \approx 92$ MeV is the decay constant of the pion. Because $f_\pi \simeq 93$ MeV is so small compared to $v_{weak} \approx 175$ GeV, the familiar hadronic strong interactions cannot be the source of EWSB in nature.

However, it is clear that EWSB could well involve a new strong dynamics similar to QCD, with a higher-energy-scale, $\Lambda \sim v_{weak}$, with chiral symmetry breaking, and "pions" that become the longitudinal $W^\pm$ and Z^0 modes.

1.2.2   Minimal Technicolor models

Minimal models of Technicolor (TC) were first introduced in the mid-1970's by S. Weinberg and L. Susskind [21, 22]. Those models postulate the existence of a new strong gauge interaction to generate the EWSB, and therefore the masses of the Z and W bosons [23]. Leaving aside how to give masses to the quark and the lepton, it is possible to write down a theory in which there are new quarks (techniquarks), coupled to the W and Z bosons, and bound together by new gluons (technigluons) to make technipions. If the chiral symmetries of the techniquarks are exact, some of the technipions become exactly massless, and if they have decay constants, $F_{\pi_T} \sim v_{weak}$ the proper mass of the W and Z bosons are provided. This new strong interaction is assumed to be invariant under a $SU(N_{TC})_{TC}$ gauge group [1].

New massless fermions sensitive to this interaction are introduced, the technifermions. The number of such new fermions is denoted by N_{Tf}. Technifermions are assumed to be only

---

1. For $N_{TC} = 3$ the TC model is equivalent to QCD with a higher mass scale.

sensitive to the new TC interactions and to the EW interactions. Therefore they are classified in N_D doublet of weak isospin:

$$\left(\begin{array}{c} Q_U \\ Q_D \end{array} \right)_L, Q_{U_R}, Q_{D_R}$$

There are as usual $N = N_{TC}^2 - 1$ gauge bosons associated with the TC gauge group, called technigluons.

As for QCD, the theory is invariant under a chiral version of the TC symmetry:

$$SU(N_{TC})_L \otimes SU(N_{TC})_R$$

which is dynamically broken at a scale Λ_{TC}, analog to the QCD scale. One can also introduce a technipion decay constant F_{π_T}, related to the f_π of QCD by:

$$F_{\pi_T} = \sqrt{\frac{N_{TC}}{3}} \frac{\Lambda_{TC}}{\Lambda_{QCD}} f_\pi. \tag{1.8}$$

The VEV v occurring in EW symmetry breaking is related to F_{π_T} and to the number of technifermions doublets N_D by

$$v = \sqrt{N_D} F_{\pi_T}. \tag{1.9}$$

Combining these last two equations one gets

$$\Lambda_{TC} = \sqrt{\frac{3}{N_{TC} N_D}} \frac{v}{f_\pi} \Lambda_{QCD}. \tag{1.10}$$

TC, like QCD, is assumed to be a confining theory and has an intrinsic (confinement) mass scale Λ_{TC}.

In a simple TC model where $N_{TC} = 4$ and $N_D = 1$, the physical spectrum will consist of two type of techniquark bound states: $Q\bar{Q}$ states called technimesons, and $QQQQ$ states called technibaryons. The Goldstone bosons originating from the symmetry breaking are technipions, and it is interesting to note that in particular the EW gauge bosons have a technimeson component through their longitudinal mode.

The relevant corrections due to the presence of new physics trying to modify the electroweak breaking sector of the SM would appear in the vacuum polarization of the electroweak gauge bosons. These can be parameterized in terms of the Peskin-Takeuchi parameters S, T, and U(the oblique parameters) [24, 25], and confronted with the electroweak precision data. The minimal TC models usually fail the constraints from precision EW measurements. Figure 1.2 gives the results of the SM parameters fit in the plane of the S and T parameters. In the SM, one has $S = 0.01 \pm 0.10(-0.08)$ and $T = 0.03 \pm 0.11(+0.09)$ [24, 25]. This is in good agreement with the experimental values, but disagrees with the prediction $S >> 0$ and $T \approx 0$ coming from simple TC models.

Also, in the minimal TC models no mechanism can account for technibaryon decays to lighter states, so the lightest one should be stable. Moreover if there exist more than three technimesons, they should give some new massive particles which will have a mass on the order of the SM EW gauge bosons [26]. None of these particles has ever been observed.

Finally the minimal TC models gives only mass to the SM gauge bosons and not to the SM fermions.
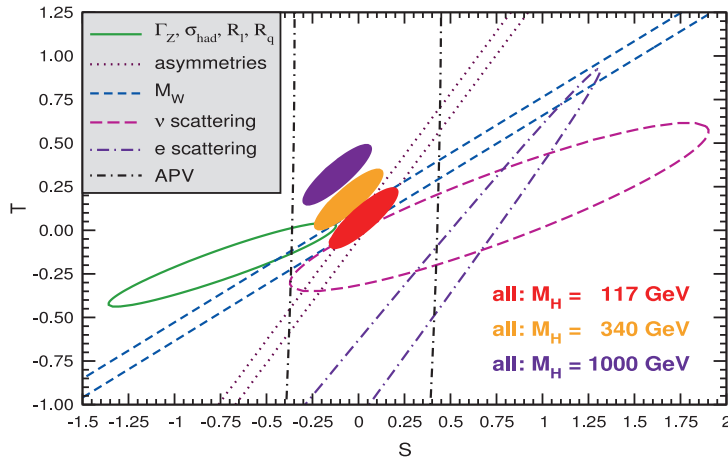
Figure 1.2: Values of the S and T parameters in the SM. The ellipses in the plot show the constraints coming from various sets of observables. The M_H ellipses are given for different Higgs Mass scenario [6].

1.2.3   Extended TC

In order to address how the SM fermions acquire a mass, Extended TC (ETC) [26, 27] was introduced. It introduces a new gauge group, usually assumed to be of the form $SU(N_{ETC})$, which contains the SM group $SU(3) \otimes SU(2) \otimes U(1)$ and the TC group $SU(N_{TC})$. This new group contains the SM, so the interaction of the ETC gauge bosons with the SM fermions will allow them to acquire their mass, after the ETC symmetry is dynamically broken.
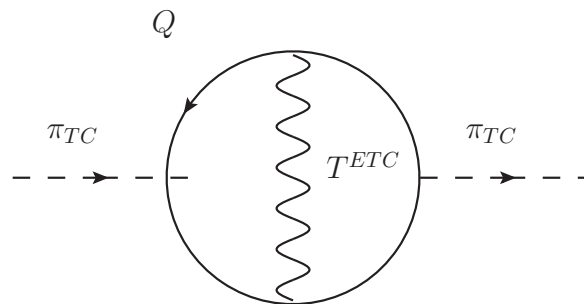
Figure 1.3: Feynman Diagram of the correction to the propagator of a technimeson *via* the exchange of an ETC gauge boson. This diagram leads to scale up the mass of the technimeson.

An effective ETC Lagrangian can be written as the sum of three different four-fermion opera-

tors:

$$\mathcal{L}_{ETC} = \alpha_{ab} \frac{\bar{Q}\gamma^{\mu}T^{a}Q\bar{Q}\gamma_{\mu}T_{b}Q}{\Lambda_{ETC}^{2}} + \beta_{ab} \frac{\bar{Q}\gamma^{\mu}T^{a}\psi\bar{\psi}\gamma_{\mu}T_{b}Q}{\Lambda_{ETC}^{2}} + \gamma_{ab} \frac{\bar{\psi}\gamma^{\mu}T^{a}\psi\bar{\psi}\gamma_{\mu}T_{b}\psi}{\Lambda_{ETC}^{2}}, \qquad (1.11)$$

where ψ represents the fields of SM fermions and Q the fields of techniquarks. The α_{ab}, β_{ab} and γ_{ab} terms represents the different coupling of ETC to the SM and TC fermions.

The α_{ab} term represents the interaction between a techniquark and an ETC gauge boson. The corrections added by this term will raise the masses of the technimesons and solve the problem of the lightest technimeson not being detected. Figure 1.3 gives an example of a Feynman diagram of the interaction of a technipion and an ETC gauge boson.

The β_{ab} term allows the mixing of SM fermions to technifermions and gives the strength of the coupling to the ETC gauge bosons. This term explains the decay of the technibaryons and also the masses of the fermions. Figure 1.4 (left) gives an example Feynman diagram of such interactions. The mass term is proportional to

$$m_{f} \approx \frac{g_{ETC}^{2}}{\Lambda_{ETC}^{2}} < \bar{Q}Q >_{ETC} \qquad (1.12)$$

where m_{f} is the mass of a SM fermion, g_{ETC} is the ETC gauge coupling constant evaluated at the ETC scale, Λ_{ETC} is the mass-scale of an ETC gauge boson and $< \bar{Q}Q >_{ETC}$ is the TC condensate where the operator is evaluated at the ETC scale.

Note that to account for the observed mass hierarchy of the SM families the ETC gauge group is assumed to spontaneously break 3−times down to $SU(N_{TC})$ (where 3 corresponds to the SM generation). In this model the heavy masses are provided by the breaking at low energy and the light masses are provided by breaking at higher energy scales:

$$\Lambda_{ETC}^{(1)} \to \Lambda_{ETC}^{(2)} \to \Lambda_{ETC}^{(3)} \to \Lambda_{TC} \qquad (1.13)$$

Schematically the $SU(N_{TC} + 3)$ which breaks to $SU(N_{TC} + 2)$ at the scale $\Lambda_{ETC}^{(1)}$ providing the first generation of fermions with a typical mass $m_{1} \sim 4\pi(F_{\pi_{T}})^{3}/\Lambda_{ETC}^{(1)2}$. At this point the gauge group breaks to $SU(N_{TC}+1)$ with dynamical scale $\Lambda_{ETC}^{(2)}$ leading to a second generation mass of the order of $m_{2} \sim 4\pi(F_{\pi_{T}})^{3}/\Lambda_{ETC}^{(2)2}$. Finally the last breaking $SU(N_{TC})$ at scale $\Lambda_{ETC}^{(3)}$ leading to the last generation mass $m_{3} \sim 4\pi(F_{\pi_{T}})^{3}/\Lambda_{ETC}^{(3)2}$.

The last term γ_{ab} leads to Flavor Changing Neutral Current (FCNC) interactions through the coupling of different flavors of SM fermions Figure 1.4 (right). The FCNC are strongly constrained within the SM. There is therefore a tension between the need to enhance the mass of the fermions to their proper value and the need to simultaneously suppress the FCNC interactions.

The value of the TC condensate used when giving mass to the ordinary fermions should be evaluated not at the TC scale but at the ETC one. Via the renormalization group one can relate the condensate at the two scales:

$$< \bar{Q}Q >_{ETC} = < \bar{Q}Q >_{TC} e^{\int_{\Lambda_{TC}}^{\Lambda_{ETC}} \frac{d\mu}{\mu} \gamma_{m}(\alpha(\mu))} \qquad (1.14)$$

where μ is the energy scale moving from Λ_{TC} to Λ_{ETC} and $\gamma_{m}(\alpha(\mu))$ is the anomalous dimension of the techniquark mass-operator. The boundaries of the integral are at the ETC scale and the TC one.

(a)   (b)

Figure 1.4: Left: Feynman Diagram of the correction to the propagator of a SM fermion *via* the exchange of an ETC gauge boson, allowing the mass of the fermion. Right: Feynman Diagram of the exchange of a quark pair into a lepton pair *via* an ETC gauge boson leading to a FCNC interaction.

For TC theories with a running of the coupling constant similar to the one in QCD (see Eq. 1.1), $\alpha(\mu) \propto \frac{1}{\ln \mu}$ for $\mu > \Lambda_{TC}$, then the anomalous dimension of the techniquark masses $\gamma_m \propto (\alpha(\mu))$. Thus when computing the integral in Equation 1.14 one gets:

$$< \bar{Q}Q >_{ETC} \approx \ln(\frac{\Lambda_{ETC}}{\Lambda_{TC}})^{\gamma_m} < \bar{Q}Q >_{TC} \tag{1.15}$$

which is a logarithmic enhancement of the operator $< \bar{Q}Q >_{TC}$. Is then possible to neglect this correction and use directly the value of the condensate at the TC scale when estimating the generated fermionic mass from Equation 1.12:

$$m_f \approx \frac{g_{ETC}^2}{\Lambda_{ETC}^2} \Lambda_{TC}^3 \;, \quad < \bar{Q}Q >_{TC} \sim \Lambda_{TC}^3 \tag{1.16}$$

Therefore, although ETC is a nice enhancement of minimal TC models, allowing in particular to explain naturally the mass of the fermions and address the problem of the TC bound states not seen, it brings FCNC interactions and also does not address the discrepancy between TC and the precision EW measurements.

Walking TC

The tension between having to reduce the FCNCs and at the same time provide a sufficiently large mass for the heavy fermions in the SM can be reduced if the dynamics of the underlying TC theory is different from the one of QCD.
The computation of the TC condensate at different scales shows that if the dynamics is such that the TC coupling does not run to the ultraviolet fixed point but rather slowly (walking) evolves over range $\Lambda_{TC} \lesssim \mu \lesssim \Lambda_{ETC}$ ones achieves a net enhancement of the condensate itself. This allows to release the pressure on the FCNC interactions while moving up the mass of the SM fermions. This kind of dynamics has been denoted as of *walking* type in which a fixed point is introduced where the coupling constant stays constant for a wide energy range.
In Figure 1.5 the comparison between a running and walking behavior of the coupling is qualitatively represented. Therefore in the walking regime from Equation 1.14:

$$< \bar{Q}Q >_{ETC} \approx (\frac{\Lambda_{ETC}}{\Lambda_{TC}})^{\gamma_m(\alpha^C)} < \bar{Q}Q >_{TC} \tag{1.17}$$

where α^C is the value of the coupling at this fixed point. Here γ_m is evaluated at the would be fixed point value α^C. Walking can help resolving the problem of FCNCs in TC models since with a large enhancement of the $< \bar{Q}Q >_{ETC}$ the α_{ab} and the β_{ab} terms are enhanced by a factor of $(\Lambda_{ETC}/\Lambda_{TC})^{\gamma_m}$ while the γ_{ab} term involving only SM fermions is not enhanced.
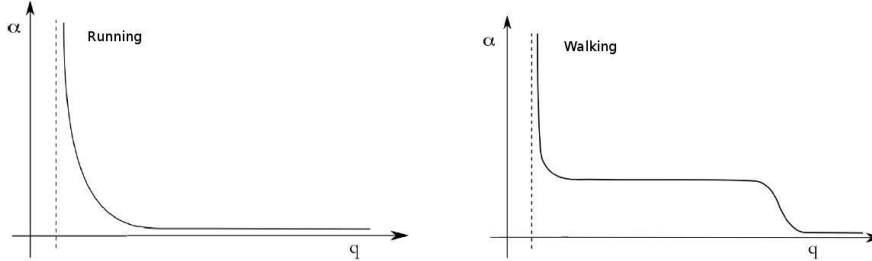

Figure 1.5: (left) QCD-like behavior of the coupling constant as function of the momentum (Running). (right) Walking-like behavior of the coupling constant as function of the momentum (Walking)

Two approaches can be used to create a fixed point for the coupling. One can introduce a large number of technifermions N_D, using Equation 1.10; this leads to $\Lambda_{TC} \approx 100$ GeV. Alternatively, one introduces two scales of TC, with one being much lower than 250 GeV.
The *walking* feature also makes the S and T parameters of TC not directly calculable from the analogy with QCD, relaxing the constraints from precision EW measurements. Some studies [28] have also shown that walking TC could lead to precision EW predictions values compatible with the SM.

1.2.4 Low-Scale Technicolor Model

A specific subclass of walking TC models called Low-Scale TechniColor (LSTC) is of particular interest at LHC, since new vector technimeson resonances could give a striking signal. A simple version of an LSTC model [26, 27, 29–31] is implemented in PYTHIA [32]. This simplified model was used for most of the LEP and Tevatron TC studies. It is also the model used as a benchmark to study TechniColor in ATLAS [33, 34].
This model follows the basic principles outlined in the previous sections. The TC group used is $SU(N_{TC})$ and there are N_f technifermions classified in N_D doublets of weak-isospin carrying an electrical charge.
The lightest isospin doublet of technifermions is a singlet of $SU(3)_C$ and is independent of the other doublets. It gives the dominant effect at low energy. The other doublets might interact under $SU(3)_C$. All the fermions acquire mass via ETC. The masses of the ETC gauge bosons are set around 10^{3-4} TeV to give the correct masses to the fermions and suppress FCNC interactions. The walking TC gauge coupling requires a large number N_D of technifermion doublets so that $\Lambda_{TC} \simeq 250\,\text{GeV}/\sqrt{N_D} \lesssim 100\,\text{GeV}$.
By analogy with QCD bound states of the lightest technifermion color-singlet EW doublet, (T_U, T_D) are labeled the pseudoscalar π_T, the axial a_T and the vector singlet ω_T and triplet ρ_T technimesons.
These technihadrons may be treated in isolation, without significant mixing or other interference from higher-mass technihadrons. The $\bar{T}T$ technipions Π_T are not mass eigenstates, but they may be treated as simple two-state mixtures of the longitudinally-polarized SM gauge

bosons, $W_L^{\pm,0}$, and mass-eigenstate $\pi_T^{\pm,0}$:

$$|\Pi_T\rangle = \sin\chi|W_L^{\pm,0}\rangle + cos\chi|\pi_T^{\pm,0}\rangle, \tag{1.18}$$

where χ is a mixing angle defined by

$$\sin\chi = \frac{F_{\pi_T}}{VEV} \simeq \frac{1}{\sqrt{N_D}}. \tag{1.19}$$

If techni-isospin is a good symmetry the ρ_T and the ω_T are nearly degenerate in mass. Walking enhances the masses of pseudo-Goldstone technipions, π_T , more than those of their vector partners, ρ_T and ω_T. Thus the mass spectrum is generally such that, $m_{\rho_T}, m_{\omega_T}, m_{a_T} < 2m_{\pi_T}$, since the technimesons decays in technipions are kinematically forbidden, and therefore the technimeson resonances are expected to be narrow with $\Gamma(\rho_T, \omega_T, a_T) \approx 1$ GeV.
The main decay channels of the ρ_T, ω_T and a_T at the LHC are: $\omega_T \to Z\gamma$, $a_T \to W\gamma$ and $\rho_T \to WZ, W\gamma$. However, the decay of ρ_T/ω_T and a_T to SM lepton pairs $l\bar{l}$, and particularly to either e^+e^- or $\mu^+\mu^-$, offers a very clean search channel at a hadron collider. Figure 1.6 shows
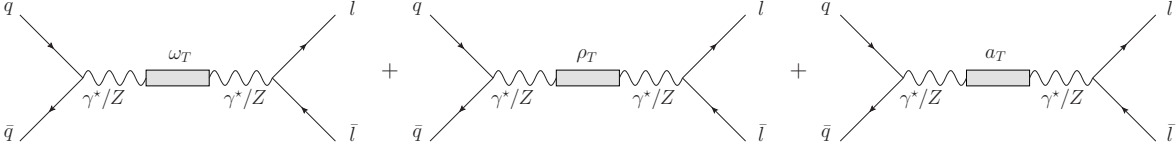
Figure 1.6: Feynman Diagram of the LSTC process giving fermion pairs $l\bar{l}$ as a final state.

the Feynman diagram for such a process to fermion pairs. The production mechanism is $q\bar{q}$ annihilation which produces a Z/γ^* which "resonates" through a ρ_T, ω_T or a_T and then back through Z/γ^* which decays to the lepton pairs that are observed. This makes the continuum Drell-Yan process the dominant and irreducible background. The collider signature for such a new particles search would be one or more narrow resonances in the dilepton invariant mass spectrum.
The coupling strength of the technimesons with the Z/γ^* comes from suitably modified Z/γ^* propagator matrix to add the TC resonances and including the effects of kinetic mixing [32]. The not zero off-diagonal entries of the matrix determine the strength of the kinetic mixing and are fixed by the quantum numbers of the technifermions in the theory. Therefore the strength of the kinetic mixing of the neutral technimesons and the SM Z/γ^* bosons is define by the parameters: $f_{\gamma\rho_T,a_T} = \xi$, $f_{\gamma\omega_T} = \xi(Q_U+Q_D)$, $f_{Z\rho_T} = \xi\cot 2\theta_W$ and $f_{Z\omega_T} = -\xi(Q_U+Q_D)\tan\theta_W$ where $\xi = \sqrt{\frac{\alpha}{\alpha_{TC}}}$.

The following default values of the LSTC parameters were used for the current study:
- The number of techniquark doublets is set to $N_D = 9$. This leads to $F_{\pi_T} \approx 82$ GeV.
- The difference between the techniquark charges is taken to be $Q_U - Q_D = 1$.
- The mixing angle between the techniquarks is taken to be $\sin\chi = 0.333$.
- The ratio of technipion couplings is taken to be $\frac{g_{a_T\pi_T\pi_T}}{g_{\omega_T\pi_T\pi_T}} = 1$.
- The gauge group used is $SU(4)$.

The values of the masses of the resonances are not predicted by the model and are therefore free parameters. By analogy with QCD it is expected that the ρ_T and ω_T are almost degenerate,

with a somewhat higher value for the mass of the a_T. In this study we take the ρ_T and ω_T masses to be exactly equal, and assign a 10% higher value to the mass of the a_T.
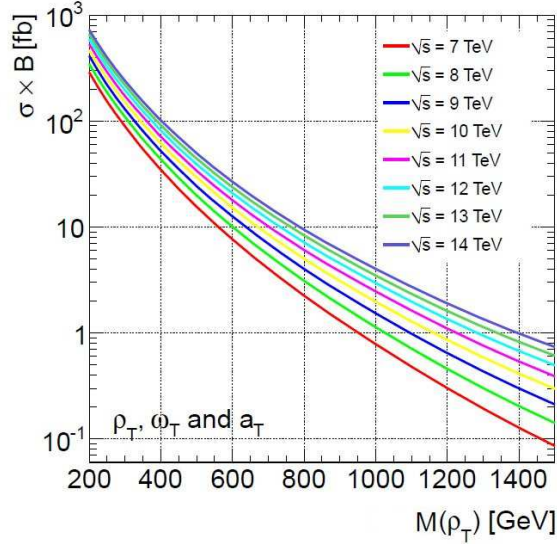
Figure 1.7: Technicolor cross section time branching ratio in the dilepton channel as a function of the ρ_T mass for multiple center of mass energies, from Ref [35].

The cross section times branching ratio in the dilepton channel as a function of mass of the ρ_T resonance for eight different values of LHC center of mass energy is shown in Figure 1.7. The branching fraction to fermion pairs is dependent on what other decay channels are available.

The upper bound for the LSTC mass scale should be in the order of a few hundred GeV, in order for the theory to naturally describe electroweak symmetry breaking. The range of interest for the LSTC parameters is bounded by current experimental constraints shown in Figure 1.8. The latest limits on LSTC models have been set at the LHC.
The ATLAS collaboration studied the production of technimesons (where the a_T contribution is neglected) decaying into a lepton pairs [36] with the first fb^{-1} of 2011 data, and excluded ρ_T and ω_T masses in the range 130-480 GeV and π_T in the range 50-480 GeV. The ATLAS collaboration has also recently published [37] a search for resonant WZ production in the first fb^{-1} of 2011 data, and LSTC ρ_T technimesons with masses from 200 GeV up to 483 GeV are excluded at 95% CL. Also the CMS experiment performed a search in the diboson final state and has excluded the technicolor ρ_T with masses between 167 and 687 GeV at 95% CL [38]. Previous searches at Tevatron were performed for ρ_T and ω_T in the dilepton final state by CDF collaboration and lead to a lower bound at 95% CL on the ρ_T and ω_T masses of 280 GeV [39]. A recent work from the CDF collaboration [40, 41] leads to an unexplained $\approx 3\sigma$ excess of the di-jet mass spectra in the $W + jj$ final state. Some studies [42] interpret it as the result of the decay of a ρ_T of mass $M_{\rho_T} \approx 290$ GeV decaying into a W and a π_T of mass $M_{\pi_T} \approx 160$ GeV. But for now this results have not been confirmed by the D∅ collaboration [43], and not by the ATLAS experiment [44].
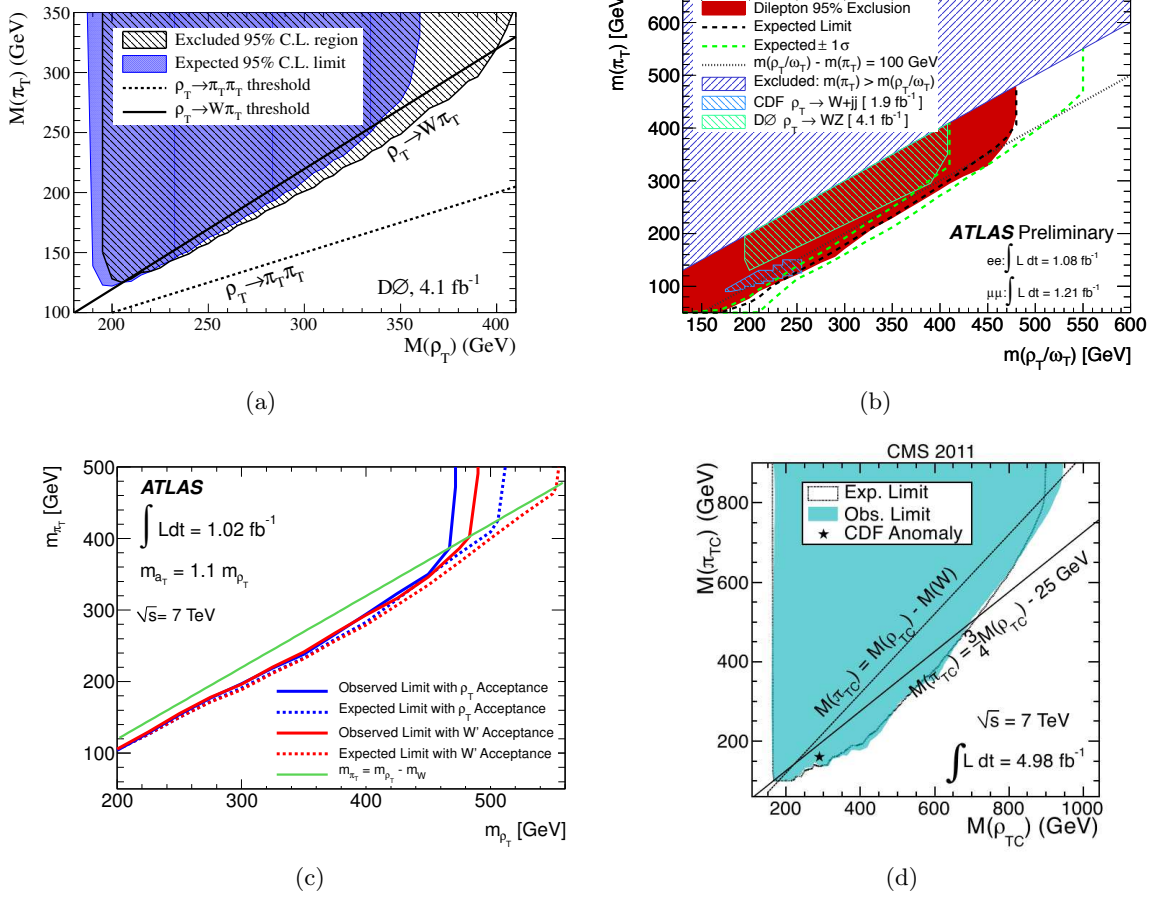
Figure 1.8: Current limits on LSTC. (a) 95% exclusion region in the plane of ρ_T vs. π_T masses in $WZ \rightarrow lll\nu$ channel from the DØ collaboration, using 4.1 fb^{-1} of data [45]. (b) 95% exclusion region in the plane of ρ_T vs. π_T masses from the ATLAS collaboration, in $\rho_T/\omega_T \rightarrow ll$ decay channel where the a_T contribution is not taken into account. Are also quoted the previous exclusion limits from CDF and DØ collaborations [36]. (c) The 95% CL expected and observed excluded mass regions in the plane of ρ_T vs. π_T masses in $WZ \rightarrow lll\nu$ channel from the ATLAS collaboration using ~ 1 fb^{-1} of data [37]. (d) The 95% exclusion region in the plane of ρ_T vs. π_T masses in $WZ \rightarrow lll\nu$ channel from the CMS collaboration, using 5 fb^{-1} of data [38].

1.2.5 Minimal Walking Technicolor

In this section the SU(2) theory with two techniflavors in the adjoint representation which is called Minimal Walking Technicolor (MWT) is presented.

In MWT the extended SM gauge group is $SU(2)_{TC} \otimes SU(3)_C \otimes SU(2)_L \otimes U(1)_Y$ and the field content of the TC sector is constituted by four techni-fermions and one techni-gluon all in the adjoint representation of $SU(2)_{TC}$. There is also a pair of Dirac leptons, whose left-handed components are assembled in a weak $(SU(2)_L)$ doublet.

The condensate is $\langle \bar{U}U + \bar{D}D \rangle$ which correctly breaks the electroweak symmetry as already argued for ordinary QCD in Eq. 1.7.

The MWT has the simplest chiral symmetry, $SU(2)_L \otimes SU(2)_R$ since it is expected to be near walking with just two Dirac flavors. In this model the Goldstone bosons produced in the chiral symmetry breaking become the longitudinal components of the SM W and Z bosons, as well as a composite Higgs which is coupled at Λ_{ETC} with the fermions.

The MWT model can be characterized by the following parameters:

- bare axial and technivector masses: M_A and M_V;

- $\tilde{g}$, the strength of the spin one resonance interaction;

- S, the S-parameter obtained using the zeroth Weinberg Sum Rule;

- m_H, Higgs boson mass;

- s, coupling of Higgs boson to composite spin-1 states.

The $\tilde{g}$ parameter represents the coupling among the technivectors and the ratio: $g/\tilde{g}$ (where g is the standard EW coupling strength) is phenomenologically very important because it sets the mixing among the SM eigenstates and composite technivectors eigenstates.

In order to constraint the M_A and M_V parameters of the MWT model the Weinberg Sum Rules (WSRs) are used [46]: The zeroth WSR defines the S parameter:

$$S = 4\pi \left[\frac{F_V^2}{M_V^2} - \frac{F_A^2}{M_A^2} \right]. \tag{1.20}$$

The first WSR is:

$$F_V^2 - F_A^2 = F_{\pi_T}^2 \tag{1.21}$$

In these equations M_V (M_A) and F_V (F_A) are mass and decay constant of the vector-vector (axial-vector) technimeson, respectively, in the limit of zero electroweak gauge couplings. Since this is a model of dynamical electroweak symmetry breaking, $F_{\pi_T} = 246 \,\text{GeV}$.

The second WSR [2] receives an important contributions from the MWT dynamics, and is modified to:

$$F_V{}^2 M_V{}^2 - F_A{}^2 M_A{}^2 = a \frac{8\pi^2}{d(R)} F_\pi{}^4 \tag{1.22}$$

where a is expected to be positive and $O(1)$, and $d(R)$ is the dimension of the representation of the underlying fermions [46]. For each of these sum rules a more general spectrum would involve a sum over all the vector and axial states.

The effective Lagrangian of the MWT model is implemented in event generators such as Mad-Graph [47] or CalcHEP [48] in order to compare the predictions of the model for different choices of its parameters with the experimental data. For this study some model parameters are fixed as recommended in Ref. [49], namely $m_H = 200$ GeV, $s = 0$ and $S = 0.3$. The remaining parameters: M_A and $\tilde{g}$, are leave free and are limited with theoretical and experimental

---

2. Corresponding to a zero on the right hand side of the following equation.

bounds.

When the effective MWT Lagrangian is introduced, the only new particles produced are two triplets of heavy technimesons, of which the lighter (heavier) ones are denoted by $R_1^\pm$ ($R_2^\pm$) and R_1^0 (R_2^0)[3]. Figure 1.9 shows the spectrum for the technivector boson masses versus different
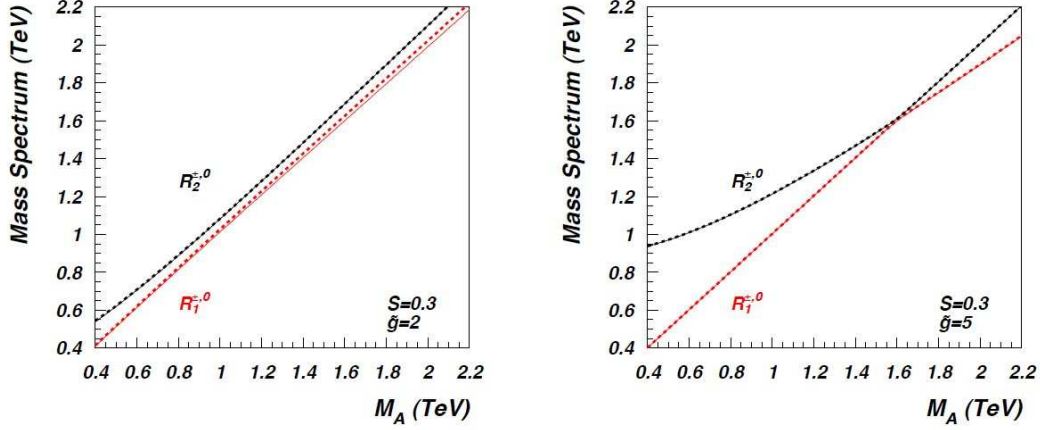
Figure 1.9: From Reference [50]: The mass spectrum of the $M_{R_{1,2}^{\pm,0}}$ vector technimesons versus M_A for $\tilde{g} = 2$ (left) and $\tilde{g} = 5$ (right). The masses of the charged vector technimesons are denoted by solid lines, while the masses of the neutral technimesons are denoted by dashed lines.
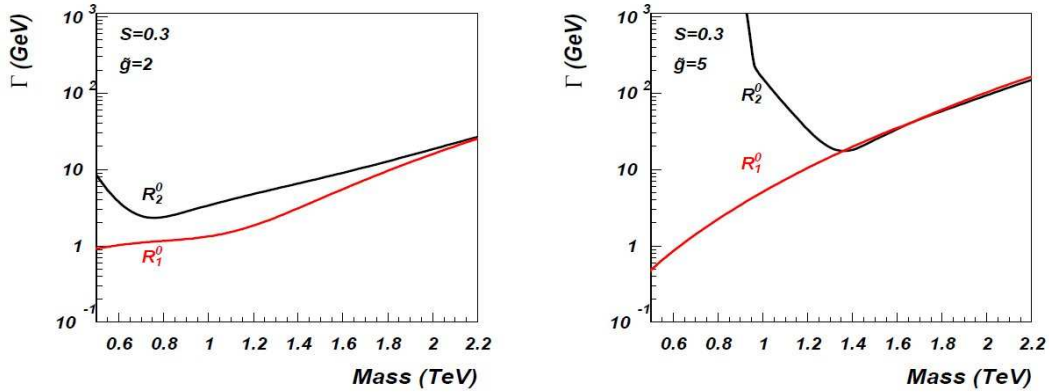
Figure 1.10: Decay width of the neutral vector technimesons for $S = 0.3$ and $\tilde{g} = 2$ (left) and $\tilde{g} = 5$ (right). Those values are obtained with the $m_H = 0.2\,\text{TeV}$ and $s = 0$ from Reference [50].

M_A. The widths of the heavy technivectors are displayed in Figure 1.10. The lighter technimeson, R_1, is very narrow. The heavier technimeson, R_2, is very narrow for small values of $\tilde{g}$. In fact in this case $M_{R_2} \simeq M_{R_1}$, forbidding decays of R_2 to R_1 (+anything). For larger $\tilde{g}$, R_2 is very narrow at large masses, but then becomes broader when the $R_2 \to R_1, X$ channel opens, where X is a SM gauge boson. This is only important below the inversion point, where R_1 is not too heavy, it becomes very broad when the $R_2 \to 2R_1$ decay channel opens, when R_2

---

3. Note that R_1 and R_2 behave like ρ_T and a_T interchangeable depending on M_A.

is essentially a spin one vector and $M_{R_2} > 2M_{R_1}$.

The R_1 branching ratios are shown in Figure 1.11 for two different value of $\tilde{g}$. The wild variations observed around 1.6 TeV reflect the mass inversion of the vector and axial component $M_V - M_A < 0$; in fact for $S = 0.3$ the $M_{inv} \simeq 1.6\,\text{TeV}$. Here the mixing between R_1 and the SM bosons vanishes, suppressing the decay to SM fermions. The other observed structure for the decays in ZH and WH channels at low masses is due to the opposite and competing contribution coming from the technicolor and electroweak sectors. This is technically possible since the coupling of the massive technivectors to the longitudinal component of the gauge bosons and the composite Higgs is suppressed by the small value of S.
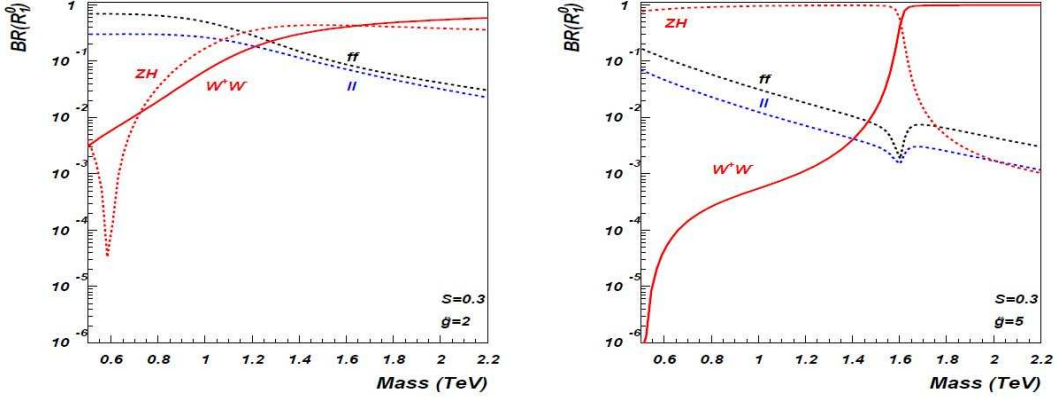
Figure 1.11: The branching ratios of the neutral R_1 resonance for $S = 0.3$ and $\tilde{g} = 2$ (left) and $\tilde{g} = 5$ (right). Those values are obtained with the $m_H = 0.2\,\text{TeV}$ and $s = 0$ from Reference [50].
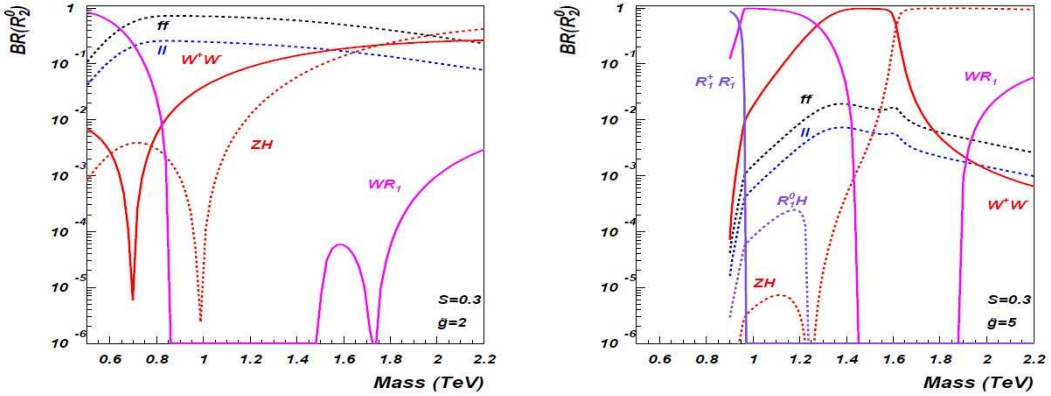
Figure 1.12: The branching ratios of the neutral R_2 resonance for $S = 0.3$ and $\tilde{g} = 2$ (left) and $\tilde{g} = 5$ (right). Those values are obtained with the $m_H = 0.2\,\text{TeV}$ and $s = 0$ from Reference [50].

The R_2 branching ratios are displayed in Figure 1.12. R_2 is heavier than R_1 by definition, thus new channels like $R_2 \to 2R_1$ and $R_2 \to R_1 X$ are possible, where X denotes a SM boson. Notice, that there is a qualitative difference in the R_2 decay modes for small and large values of $\tilde{g}$. First, for small $\tilde{g}$ the $R_2 - R_1$ mass splitting is not large enough to allow the decays $R_2 \to 2R_1$ and $R_2 \to R_1 H$, which are present for large $\tilde{g}$. Second, for small $\tilde{g}$ there is a wide

range of masses for which the decays to R_1 and a SM vector boson are not possible, because of the small mass splitting. Note, that the R_2 branching ratio to fermions does not drop at the inversion point, because the R_2 and the SM bosons mixing does not vanish.
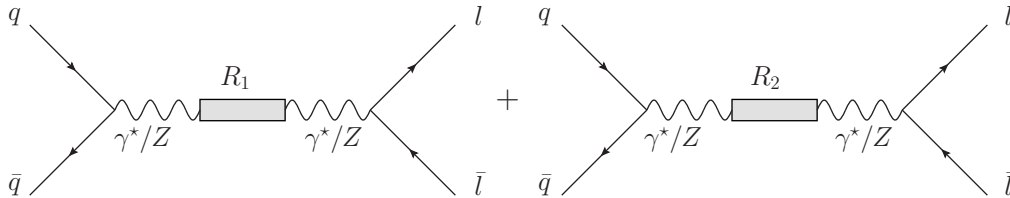
Figure 1.13: Feynman Diagram of the MWT process giving fermion pairs $l\bar{l}$ as a final state.

Figure 1.13 shows the Feynman diagram for such a process to fermion pairs. The production mechanism is $q\bar{q}$ annihilation which produces a Z/γ^* which "resonates" through a R_1^0 or R_2^0 and then back through Z/γ^* which decay to the lepton pairs that are observed. This makes the smoothly falling Drell-Yan spectrum the dominant and irreducible background.

The current limit on the MWT model come from an interpretation [49] of the limit results on the masses of possible new spin one resonances, performed using $36 - 40 \text{ pb}^{-1}$ of data collected during the 2010 by the CMS experiment. Exploring the signal from the process $pp \rightarrow R_{1,2} \rightarrow l\nu$ was possible to limit the values for the parameters M_A and $\tilde{g}$ [49]. The resulting $(M_A : \tilde{g})$ plane is presented in Figure 1.14 for $m_H = 200$ GeV and $s = 0$. The upper bound for $\tilde{g}$ is dictated by the internal consistency of the model:

$$\tilde{g} < \sqrt{\frac{8\pi}{S}} \tag{1.23}$$

and for $S = 0.3$ this gives $\tilde{g} = 9.15$.
In the right side of the plot the upper bound for M_A corresponds to the value for which both WSR's are satisfied in a running regime:

$$M_A{}^2 < \frac{4\pi F_\pi{}^2}{S} \left(1 + \frac{1}{\sqrt{1 - \frac{\tilde{g}^2 S}{8\pi}}} \right) \tag{1.24}$$

The uniformly shaded region on the left is excluded by the CDF searches of the resonance in the the $p\bar{p} \rightarrow e^+ e^-$ process. The striped region in the lower left corner is excluded by the measurements of the electroweak precision parameters adapted for models of MWT in Reference [50]. The CDF exclusion limit is sensitive, indirectly, to the mass of the composite Higgs and the coupling s via properties of the new heavy spin one states. However, the edge of the excluded area varies only very weakly as a function of s and m_H. The CMS search imposes a 95% CL exclusion bound described with the thick solid (red) line. The thick dashed and dotted lines (blue) are three and five sigma exclusion limits for 7 TeV and 5 fb^{-1}. The thin dotted and dashed lines describe the reach of the LHC with 100 fb^{-1} at 13 TeV. The three and five sigma exclusion limits are calculated using Poisson distribution. Due to the effective description, the K-factors corrections were not employed calculating the exclusion limits.
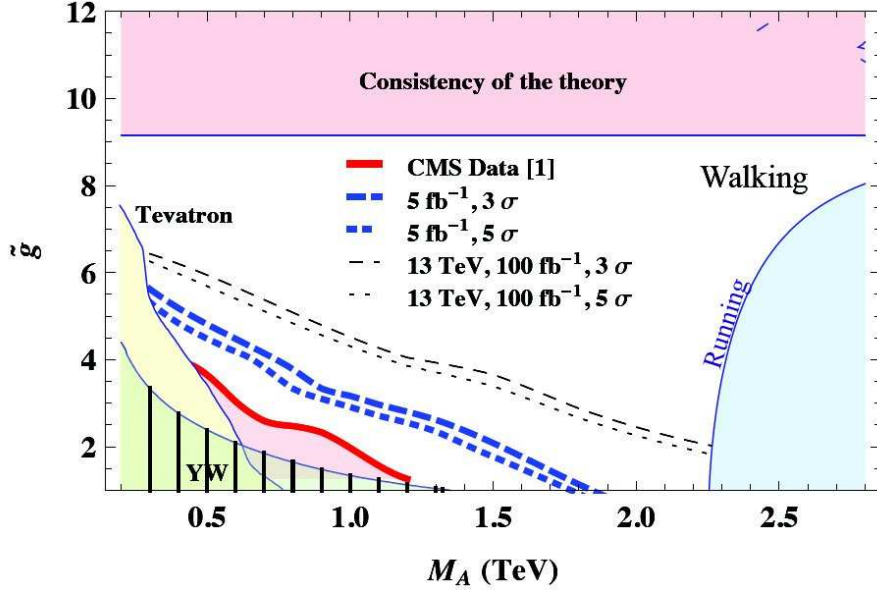
Figure 1.14: Bounds in the $(M_A, \tilde{g})$ plane of the MWT parameter space: (i) CDF direct searches of the neutral spin one resonance excludes the uniformly shaded area in the left, with $m_H = 200\,\text{GeV}$ and $s = 0$. (ii) The 95% confidence level measurement of the electroweak precision parameters excludes the striped area in the left corner. (iii) Imposing the modified WRSs excludes the uniformly shaded area in the right corner. (iv) The horizontal stripe is excluded imposing reality of the axial and axial-vector decay constants. (v) The area below the thick uniform line is excluded by an interpretation of the CMS data. (vi) Dashed and dotted lines are expected exclusions using different values of the integrated luminosity and center of mass energy.

To note that the m_H can have some impact on the couplings of the mostly axial of the R_1 and R_2 resonances (for M_A values before the inversion point the mostly axial resonance is R_1). This means that if the H is very heavy then the BR of the $R_1 R_2 \to f\bar{f}$ is larger and vice-versa. Difference between 200 GeV and 125 GeV should be very small since the masses scanned of the R_1 and R_2 are significantly larger then both cases of the m_H.

Chapter 2

The Large Hadron Collider and The ATLAS detector

In this chapter the Large Hadron Collider (LHC) accelerator complex and the ATLAS detector will be presented. In Section 2.1 after the introduction on the LHC accelerator a summary of the operational parameters for the 2010/2011 proton-proton (pp) data taking is given. The ATLAS detector is presented in Section 2.2.

2.1 The Large Hadron Collider - LHC

2.1.1 CERN accelerator complex

The Large Hadron Collider (LHC) is a two-ring-superconducting hadron accelerator and collider, installed in a 26.7 km tunnel [51]. One of the main missions of this machine is to produce the highest energy pp collisions ever performed, in order to have an energy reach, up to few TeV to search for new particles or physics processes beyond the Standard Model predictions. As those are expected to be rare phenomena with a production cross sections of the order of hundred pb or lower one of the main requirement on the machine is to deliver a large number of collisions.

The LHC is designed to produce pp collisions at a center of mass (CM) energy of $\sqrt{s} = 14$ TeV. It is the last stage of a complex system of accelerators that exploits different machines built at CERN over the past 40 years (Fig. 2.1). Protons are extracted from a hydrogen tank and they are injected in the Linear Accelerator 2 (Linac2), where they are accelerated up to 50 MeV, then they pass to the Proton Synchrotron Booster (PSB), where they reach the momentum of 1.4 GeV. From the PSB, protons are injected in the Proton Synchrotron (PS) accelerator and then in the Super Proton Synchrotron accelerator (SPS), where they finally reach 450 GeV. Once the bunches are accumulated in the SPS they are injected into the LHC. When the injection is completed, the procedure of ramping starts and each beam can be accelerated up to 7 TeV.

Following the accident occurred in September 2008 [52], for safety reasons, the first three years of operation the LHC was run at half of the design energy, i.e. $\sqrt{s} = 7$ TeV in 2010 and 2011, $\sqrt{s} = 8$ TeV in 2012.

On the LHC accelerator ring, four experiments are installed. ATLAS and CMS are general purpose experiments, built mainly to search for the Higgs bosons and new Physic and to study Standard Model phenomena. LHCb is an experiment for the physics of the beauty quark,
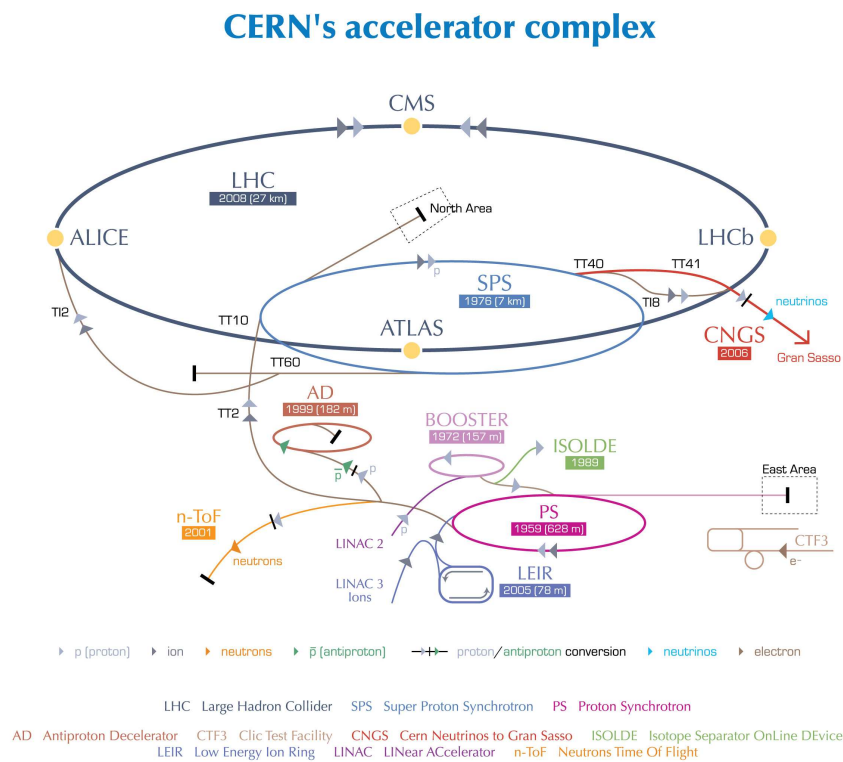
Figure 2.1: The CERN accelerator complex, CERN$^{©}$.

built to study, in particular CP-violation effects in the B-hadron sector. ALICE is a dedicated heavy-ion experiment, built to study the quark gluon plasma properties.

2.1.2 Luminosity

The luminosity (L) is an important parameter of the accelerator since it is the proportionality factor between the rate of a given process (R) and its production cross section (σ): $R = L\sigma$. It is operationally defined by colliding beams parameters at the interaction points. The SI unit dimension of luminosity is $[L] = [cm]^{-2}[s]^{-1}$. The cross section express the probability for a given collision process to occur and its dimension in SI unit is $[\sigma] = [cm]^2$. If a phenomena has a low cross section then the luminosity required to get a few events of this kind needs to be high.

The luminosity of the LHC accelerator is given by:

$$L = f\frac{n_1 n_2}{4\pi\sigma_x\sigma_y} \tag{2.1}$$

Where:
- f is the colliding frequency.
- n_i the number of colliding particles in beam i.
- σ_i characterize the Gaussian transverse beam profiles in the horizontal and vertical directions.

Another parameter is introduced, the integrated luminosity over time:

$$L_{\text{int}} = \int L dt \quad \text{and therefore:} \quad N_{Events} = L_{\text{int}}\sigma \tag{2.2}$$

were N_{Events} is the number of events produced for a defined process. The instantaneous design luminosity of the LHC is $L = 10^{34}\,cm^2 s^{-1}$ for the ATLAS and CMS experiments[1], leading to an integrated luminosity ≈ 100 fb^{-1} per year [53].

2.1.3 LHC operations

The LHC campaign in the first years of data taking was successful. The first collision at an energy higher than the injection regime at 2.26 TeV took place in November 2009. At the beginning of 2010 the LHC started with two *pp* colliding bunches in the full accelerator and by the end of that year reached 368 bunches spaced by 150 ns. By the end of the 2010 [55], 50 pb^{-1} of data at 7 TeV, were delivered by the LHC.

The 2011 run has allowed to record more than 5 fb^{-1} of data at $\sqrt{s} = 7$ TeV in ATLAS. The LHC has been operated almost during the full year with 1380 bunches, spaced by 50 ns. In the 2011 data taking the LHC increased the luminosity in *pp* runs with respect to 2010, reaching a peak luminosity of $3.65 \times 10^{33} cm^{-2} s^{-1}$ which is only a factor of three below the design value. In 2012 the collision CM energy was increased to $\sqrt{s} = 8$ TeV and the plan is to collect up to 15 fb^{-1} of data in ATLAS.

In 2013-2014, a 15 months shutdown is foreseen in order to improve the protection system of the machine against magnetic quenches, so that the LHC would be able to run safely at the nominal energy.

An important parameter to increase the luminosity is the intensity of the bunches (i.e. the

---

1. For comparison the nominal instantaneous luminosity expected in the LHCb and the ALICE experiments are respectively $L = 10^{32} cm^{-2} s^{-1}$ and $L = 10^{27} cm^{-2} s^{-1}$.
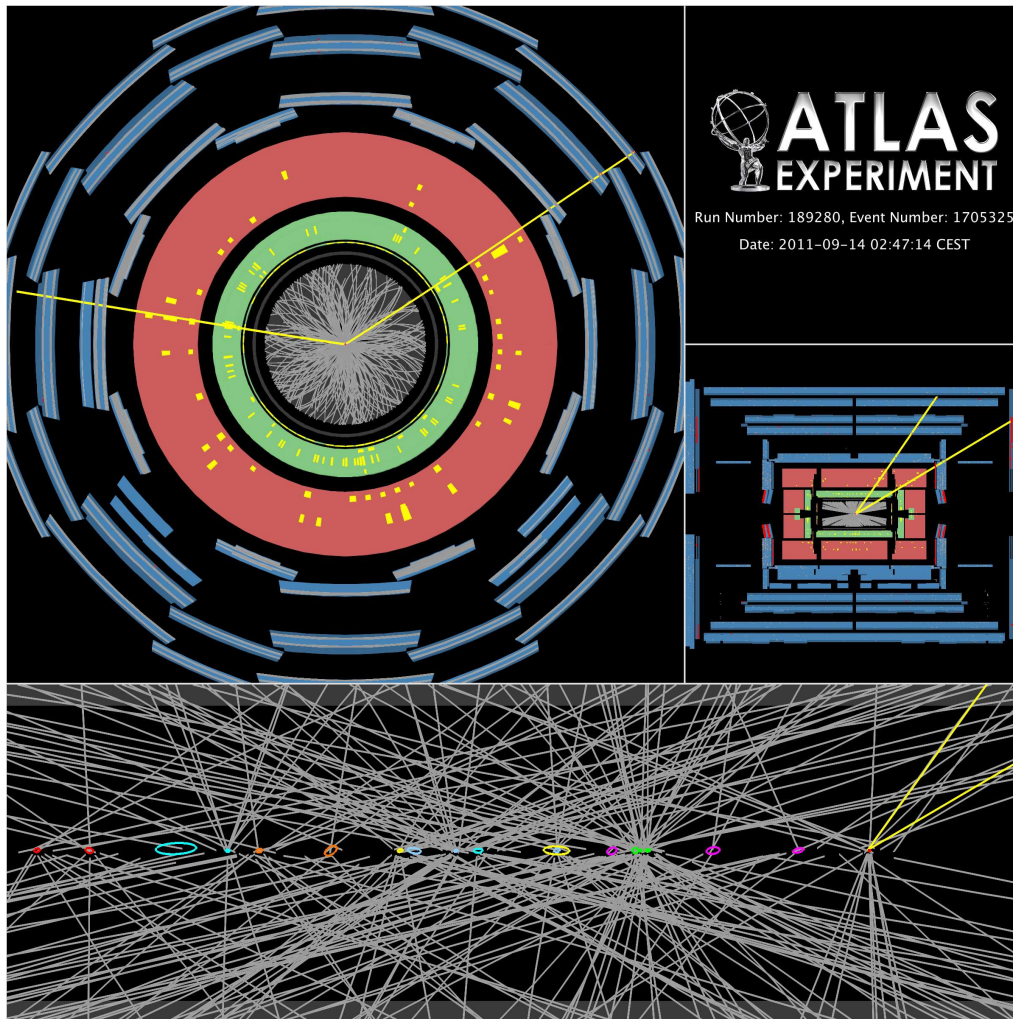
Figure 2.2: Event display of $Z \to ee$ event recorded in 2011 by the ATLAS detector. Twenty interaction vertices were reconstructed [54].

number of protons within a bunch). The LHC design luminosity of $L = 10^{34} cm^{-2} s^{-1}$ foresees 2808 bunches per beam in the ring with 25 ns spacing between bunches, with an estimate of the average number of interactions per crossing of the order of 20. The superposition of these interactions to the triggered one is called pile-up.

(a) 2010 run.

(b) 2011 run.
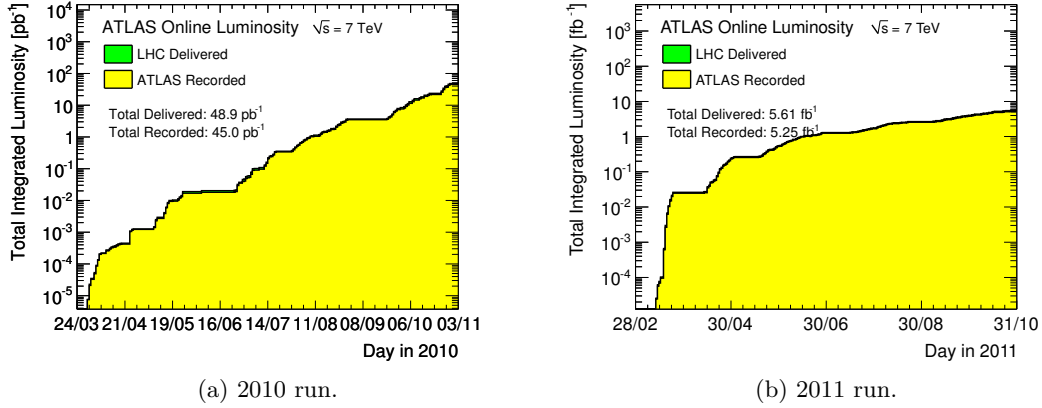
Figure 2.3: Total integrated luminosity recorded by the ATLAS experiment in 2010, and up to October 2011 [56].

At the end of the 2011 data taking with about 1400 bunches LHC has reached a peak luminosity of $L = 3.65 \times 10^{33} cm^{-2} s^{-1}$ where the average number of pile-up events is typically about 11[*]. To get an idea of the pile-up impact, Figure 2.2 shows an ATLAS event display of a $Z \to ee$ event recorded in 2011, where twenty interactions vertices were reconstructed.

Table 2.1 summarizes the LHC run parameters for the nominal running conditions [55, 57] for 2010 and 2011 runs and Figure 2.3 shows the total integrated luminosity recorded by the ATLAS experiment in 2010 and 2011.

Table 2.1: LHC running conditions for design, 2010 and 2011 pp runs.

Parameter	2010 run	2011 run	Nominal run
CM Energy	7 TeV	7 TeV	14 TeV
Number of bunches	368	1400	2808
colliding bunches in ATLAS	233	1331	2808
Number of p per bunch	1.1×10^{11}	1.3×10^{11}	1.1×10^{11}
Bunch spacing	150 ns	50 ns	25 ns
Peak Luminosity	$2.07 \times 10^{32} cm^{-2} s^{-1}$	$3.65 \times 10^{33} cm^{-2} s^{-1}$	$10^{34} cm^{-2} s^{-1}$
Integrated lumi per year	50 pb^{-1}	5.6 fb^{-1}	100 fb^{-1}
Average Number of pileup events	3	11*	20

The results presented in this thesis have been obtained with 2011 pp collision data collected by the ATLAS detector.

---

[*]. Reached at the end of the data-taking period.

2.2   The ATLAS detector

The ATLAS experiment [58] is one of the two general purpose experiments located around the LHC ring. A cut-away view of the detector is presented in Figure 2.4. The detector is installed 95 m underground. It is 44 m long, 22 m high and weight about 7000 tons. It has
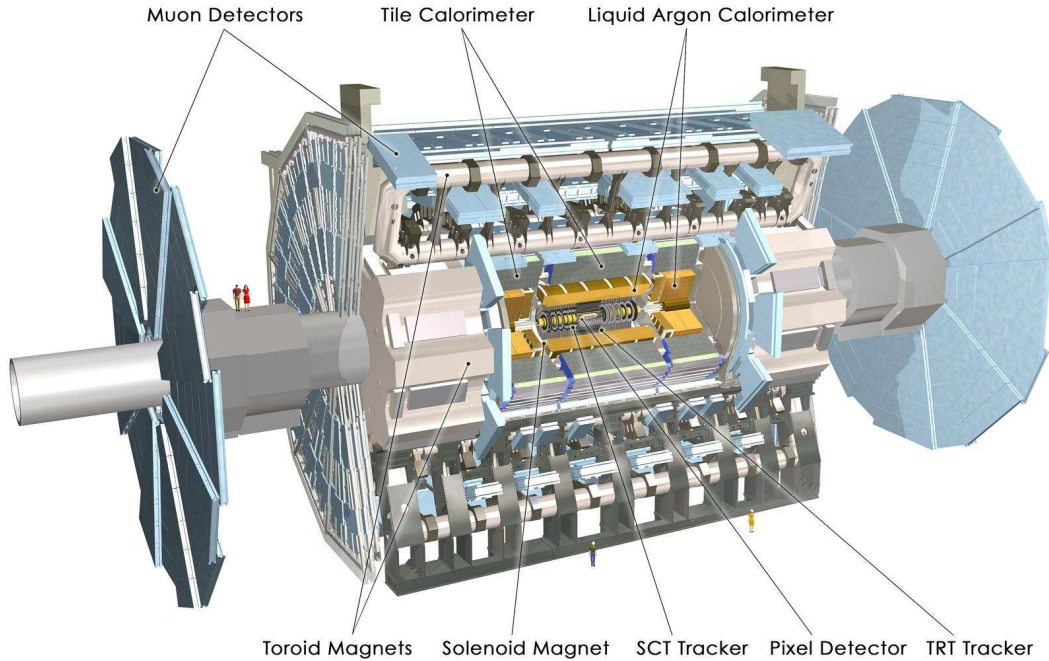
Figure 2.4: The ATLAS Experiment [58].

a cylindrical multi-layer shape around the beam pipe and it is forward-backward symmetric with respect to the interaction point. The nominal interaction point is defined as the origin of the coordinate system. The beam direction defines the z-axis and the x-y plane is transverse to the beam direction. The positive x-axis is defined as pointing from the interaction point to the center of the LHC ring and the positive y-axis is defined as pointing upwards. The side-A of the detector is defined as the one with positive z and the side-C is the one with negative z. The azimuthal angle ϕ is measured around the beam axis while the polar angle θ is the colatitude with respect to the beam axis. As the angle θ is not invariant under the Lorentz transformations, the rapidity y is introduced as

$$y = \frac{1}{2} \ln \left(\frac{E + p_z}{E - p_z} \right) \tag{2.3}$$

where E is the energy of the particle and p_z is the momentum of the particle in z-direction. The particles produced in the majority of the pp collisions have an approximately uniform distribution (dN/dy) in this variable. In the limit of vanishing masses, the rapidity simplifies to the so-called pseudo-rapidity η, which is defined as:

$$\eta = -\ln \tan \left(\frac{\theta}{2} \right). \tag{2.4}$$

The distance ΔR between two reconstructed particles in the pseudorapidity-azimuthal angle space is defined as:

$$\Delta R = \sqrt{\Delta\eta^2 + \Delta\phi^2}. \tag{2.5}$$

Were $\Delta\eta = \eta_1 - \eta_2$ and $\Delta\phi = \phi_1 - \phi_2$ are the difference of the η and ϕ position of the two particles respectively.

It is important to note that the hadronic nature of the interactions makes the effective center of mass energy of the colliding partons unknown at each bunch crossing. Nevertheless the transverse momentum component (p_T) of each parton in the proton is generally negligible with respect to the longitudinal one. This means that the total transverse momentum, i.e. that one defined in the x−y plane, is zero in the initial state and since the p_T is conserved each event can be fully reconstructed in this plane. This is the reason why transverse quantities such as the transverse momentum, the transverse energy (E_T) , and the missing transverse energy (E_T^{miss}) are used in the hadron collider physics rather than the total ones.

The ATLAS subsystems

In order to achieve a good spatial coverage the ATLAS detector was build in three parts. A barrel region and two end cap regions that are made with wheels disposed on each side of the barrel closing hermetically the detector.

To achieve a powerful particle identification and to fulfill its physics requirements [59] the ATLAS detector has two magnetic fields (a central solenoidal one and a toroidal external one) and is composed of three main systems.

- *The Inner Detector* is close to the beam pipe and provides charged particle tracking. In association with the solenoidal magnetic field, it can be used for charged-particle momenta reconstruction, particle identification, reconstruction of the interaction vertex, *etc.*
- *The calorimetry system* measure the energy of the electromagnetic particles and jets and provides also a measurement of the missing transverse energy.
- *The Muon Spectrometer* combined with the toroidal magnetic field allows a precise measurement of the muon momentum.

In the following a brief description of the various systems is given, concentrating in more detail on the subsystems as the Inner Detector, electromagnetic calorimeter and the trigger which are used later in this thesis.

2.2.1   Magnet system

The Inner Detector is immersed in a constant solenoidal magnetic field provided by superconducting magnets cooled down to 4.5 K in a cryostat, which is shared with the calorimeter to minimize the usage of material. This central magnetic field of 2 T deflects the charged particles in the transverse plane. The toroidal field is a unique ATLAS feature, unusual for this kind of experiments. In the barrel, eight coils surround the calorimeters, providing a variable magnetic field from 0.15 to 2.5 T. In the endcaps two smaller toroidal magnets are installed. They provide a variable magnetic field from 0.2 to 3.5 T.

2.2.2   The Inner detector

The ATLAS Inner Detector [58] provides precise track reconstruction over $|\eta| < 2.5$. It consists of three layers of pixel detectors close to the beam-pipe, four layers of silicon microstrip
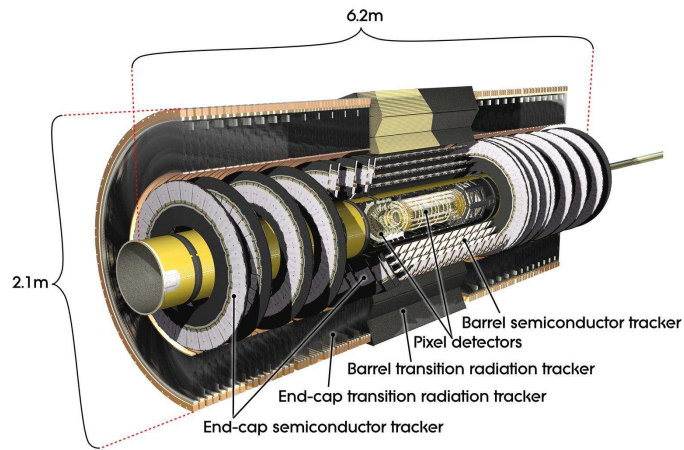
(a) The Atlas Inner Detector. The central and end caps region are visible.
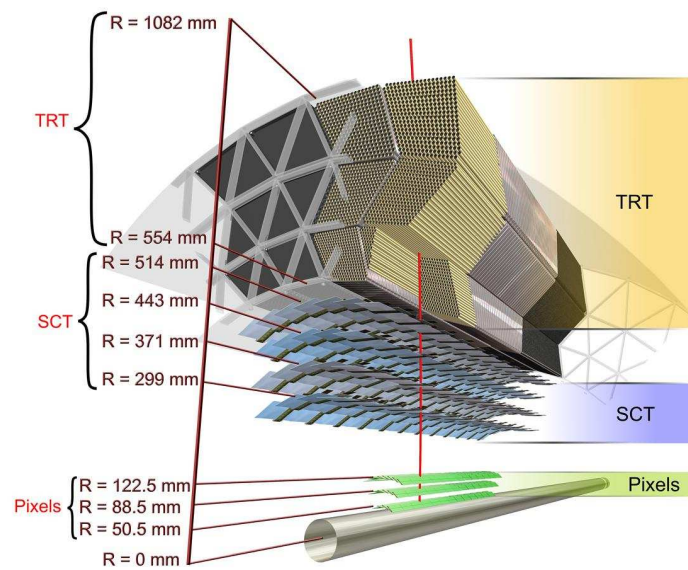
(b) Sectional view of the barrel Inner Detector. The straight line in the middle of the figure represent a 10 GeV track with $\eta = 0.3$.

Figure 2.5: The ATLAS Inner Detector [58].

detectors (SCT) providing eight hits per track at intermediate radii, and a transition radiation tracker (TRT) at the outer radii, providing about 35 hits per track (in the range $|\eta| < 2.0$). Figure 2.5 shows two sectional views of the Inner Detector, where is possible to distinguish the three sub-detectors.

The first pixel layer (also called the B-layer [2]) is located just outside the beam-pipe at a radius of 50 mm, and provides precision vertexing and significant rejection of photon conversions (through a requirement of a track with a hit in this layer). A fine granularity of this detector allows a very precise measurement of the position of each hit. The nominal space resolutions [60] for the barrel pixels are $\sigma_{R-\phi} = 10$ μm, $\sigma_z = 115$ μm, and for the endcap pixels are $\sigma_{R-\phi} = 10$ μm, $\sigma_R = 115$ μm.

With the SCT detector potentially eight measurement points in the central region and eighteen points in the endcaps are expected for a high momentum charged particle. The nominal SCT module spatial resolutions [60] are: $\sigma_{R-\phi} = 17$ μm, $\sigma_z = 580$ μm for the barrel, and $\sigma_{R-\phi} = 17$ μm, $\sigma_R = 580$ μm for the endcaps.

The TRT also provides discriminating power between electrons and pions over a wide energy range (between 0.5 and 100 GeV). The nominal single hit resolution [60] of the TRT is $\sigma_{R-\phi} = 130$ μm thanks to the drift time measurement, but no measurement along the proportional drift tubes direction is given. In addition to tracking capabilities, the TRT provides electron identification by detection of transition radiation photons emitted in the polypropylene fibres (barrel) or foils (end-caps) interleaved between the proportional drift tubes.

2.2.3 The Calorimetry system
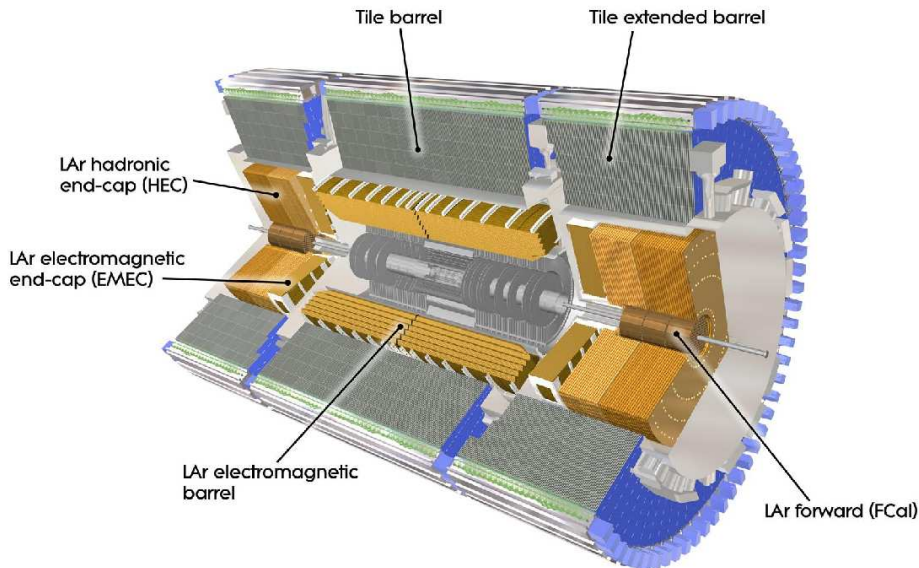
Figure 2.6: Atlas Calorimeter systems [58].

The ATLAS calorimetry system [61] is shown in Figure 2.6. It consists of various sampling

---

2. Due to its position, the B-layer, allow a measurement of displaced secondary vertex coming from the b-quark decays.

calorimeters to satisfy physics requirements and to cope with the radiation environment. It covers a rapidity range up to $|\eta| < 4.9$.

The main goal of the calorimetry system is to measure the energy of electrons, photons and jets over a broad energy range up to a few TeV. The system has also the task to provide a powerful electron and photon identification and also to ensure a good missing transverse energy measurement, crucial for new phenomena searches.

For the above mentioned reasons a good containment of the electromagnetic (EM) and hadronic showers is important and thus a sufficient calorimeter depth is crucial. The total thickness of the EM calorimeter is well above 20 radiation length up to $|\eta| \simeq 1.4$ as shown in Figure 2.7. The hadronic calorimeter has approximately 10 interaction lengths of material (roughly $5 - 10$ times more than in EM part) to ensure good jet energy resolution.

Two types of technology are used in the ATLAS calorimeters. A sampling Liquid Argon technology ensures EM measurements over the full $|\eta| < 4.9$ range as well as providing hadronic measurements in the $1.5 < |\eta| < 4.9$ region. For hadronic measurements in the central region scintillator plastic tiles with iron are used (Tile calorimeter).

The Liquid Argon Calorimeter

The Liquid Argon Calorimeter (LAr) as shown in Figure 2.6 consists of four subdetectors: the electromagnetic Barrel (EMB), the electromagnetic Endcap (EMEC), the hadronic Endcap (HEC) and the forward calorimeter (FCal). The EMB covers the pseudorapidity range of $|\eta| < 1.475$. The EMEC is built of two wheels: the part closest to the beam pipe is called EMEC Inner Wheel ($2.5 < |\eta| < 3.2$) and the part further from the beam pipe called EMEC Outer Wheel ($1.375 < |\eta| < 2.5$). They are located on each side of the EM Barrel, at $|z| \approx 4.3\,m$ in two independent cryostats.

The detailed layout and readout of the LAr system is given in Chapter 3. The EMB and the EMEC are lead/liquid argon sampling calorimeters with absorbers and electrodes with accordion shape. The accordion geometry was chosen to prevent cracks in azimuthal angle
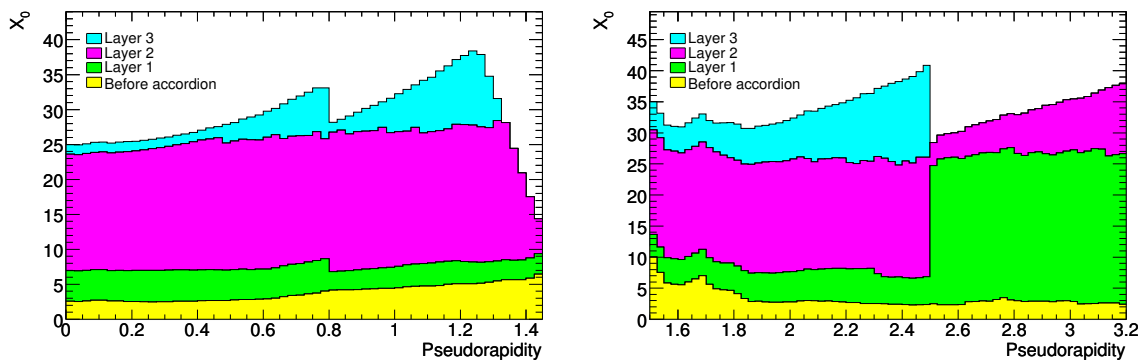
Figure 2.7: Cumulative amounts of material, in units of radiation length (X_0) and as a function of $|\eta|$, in front of and in the electromagnetic calorimeters [58]. For the barrel (left) and end-cap (right) is shown the thicknesses of each accordion layer as well as the amount of material in front of the accordion.

ϕ and hence to allow a full ϕ-coverage. Moreover, this design ensures that approximately all tracks transverse the same amount of material.

The main idea of sampling calorimetry is to develop an electromagnetic or hadronic shower in a dense material, and to sample the energy lost by the particles in a sensitive medium.

An important aspect for optimal performance is the material budget in front of the calorimeter because a significant fraction of the particle energy is lost in the inactive material in front of the calorimeter thus causing a fluctuation in the energy measurement which reflects in a worst energy resolution. Figure 2.7 shows the number of electromagnetic radiation lengths (X_0) of materials in front of and in the electromagnetic calorimeters in the ATLAS detector. In order to correct for the energy lost in the Inner Detector, services and cryostat, the EM Calorimeter is preceded by a pre-sampling detector [62]. In the transition region between barrel EMB and EMEC the material length is on the order of 7 X_0, which makes the insertion of scintillators between barrel and endcap cryostat necessary.

The energy resolution in a calorimeter is parametrized by the following formula:

$$\frac{\sigma(E)}{E} = \frac{a}{\sqrt{E[GeV]}} \oplus \frac{b}{E[GeV]} \oplus c \tag{2.6}$$

where a is the sampling term which describes the statistical fluctuations of the electromagnetic shower, b is the noise term due to the electronic noise and finally c is the constant term which takes into account the non uniformity of the calorimeter and of its response.

The construction tolerances and the calibration system ensure that the LAr calorimeter response is locally uniform within 0.5% [63]. This uniformity is expected to be inter-calibrated in situ to 0.5%, achieving a global constant term [3] of about 0.7% [61].

At low energy, the energy resolution is expected to be dominated by the contribution from the sampling term $a \simeq 0.1$. It is assumed that the term a is well described as a function of η by the MC simulation.

The noise term also contributes only at low energy. The noise description is derived from calibration data runs.
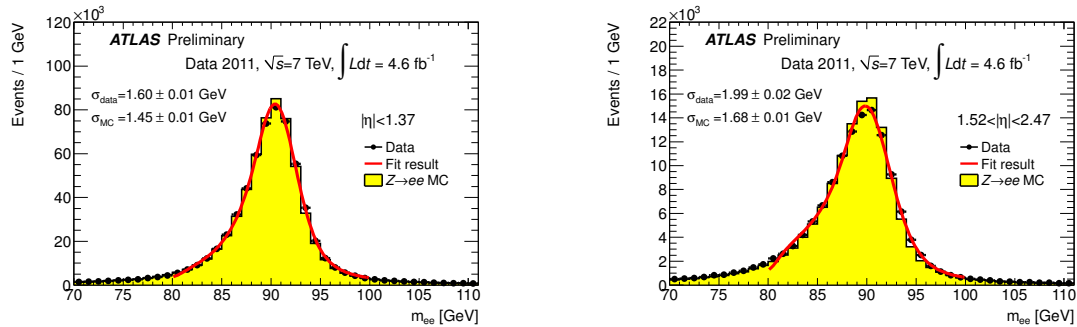
Figure 2.8: The observed di-electron invariant mass distribution in Z candidates events is well described by the MC simulation. The energy corrections applied to the electrons are within 0.5% in the barrel region (right), and within 1% in the endcaps (left). The mass peak resolution has been determined by fitting the distributions with a Breit-Wigner distribution convoluted with a Crystal Ball function.

At high energies, which are important for this thesis, the resolution is dominated by the constant term. The effective constant term, which includes both the calorimeter constant term

---

3. The long-range constant term is the residual miscalibration between the different calorimeter regions, and the global constant term is the quadratic sum of the local and long-range constant terms.

and the effect of inhomogeneities due to possible additional material, has been measured from data using the dielectron mass of $Z \to ee$ decays. An example of the dielectron mass distribution is shown in Figure 2.8 where both electrons are reconstructed within $|\eta| < 1.37$ (left) and $1.52 < |\eta| < 2.47$ (right). The effective constant term, measured by fitting the $Z \to ee$ line shape with the 2011 data was founded compatible within the systematic uncertainty with the 2010 data measurement and is displayed in Table 2.2 for the different calorimeter regions.

Table 2.2: Measured effective constant term c (see Eq. 2.6) from the observed width of the $Z \to ee$ peak for different calorimeter regions.

Sub-system	η-range	Effective constant term, c_{data}
EMB	$|\eta| < 1.37$	$1.2\%^{+0.5\%}_{-0.6\%}$
EMEC-OW	$1.52 < |\eta| < 2.47$	$1.8\% \pm 0.4\%$
EMEC-IW	$2.5 < |\eta| < 3.2$	$3.3\% \pm 1.1\%$
FCal	$3.2 < |\eta| < 4.9$	$2.5\%^{+1.0\%}_{-1.5\%}$

The Tile Calorimeter

The ATLAS Hadronic Tile Calorimeter covers an η-region up to $|\eta| < 1.0$, and is positioned around the EM Calorimeter from the radius 2.28 m to 4.23 m. An extended barrel region covers the η-region of $0.8 < |\eta| < 1.7$. Iron plates are used as absorber material and are also used as return yoke for solenoidal magnet field. Scintillator plastic tiles are used as active medium. The readout of the tiles is achieved with optical fibers. Readout cells are formed by a cluster of tiles and are projective to the interaction point.
The barrel is segmented into three independent layers. The readout cells provide a three dimensional measurement of the deposited energy, which is needed for the reconstruction and the triggering of jets. They provide a granularity of $\Delta\phi \times \Delta\eta = 0.1 \times 0.1$, in the first two layers, and $\Delta\phi \times \Delta\eta = 0.2 \times 0.2$ in the last layer. With this segmentation the whole Tile Calorimeter corresponds to roughly 10,000 individual channels.

2.2.4 The Muon Spectrometer

One of the particles not absorbed by the calorimeters and reaching the most external sub-detector are the muons.
The layout of the ATLAS Muon Spectrometer (MS) is shown in Figure 2.9.
The MS is a tracking detectors which measures the magnetic deflection of muon tracks in a large superconducting air-core toroidal magnetic field. Instrumented with separate fast response trigger and high-precision tracking chambers, a combination of four complementary technologies are used to achieve its physics performance goals.
Over most of the angular coverage, precision measurement of the track momentum is provided by the Monitored Drift Tubes (a proportional wire drift chamber). For $2.0 < |\eta| < 2.7$, Cathode Strip Chambers (CSCs), multi-wire proportional chambers with segmented cathode strips and higher granularity, are used. The CSCs are designed to withstand the demanding rate and background conditions of this high particle flux and radiation region. The fast response trigger chambers cover the range $|\eta| < 2.4$. In the barrel ($|\eta| < 1.05$) Resistive Plate Chambers are used and in the region $1.05 < |\eta| < 2.4$ Thin Gap Chambers are used. The trigger chambers for the
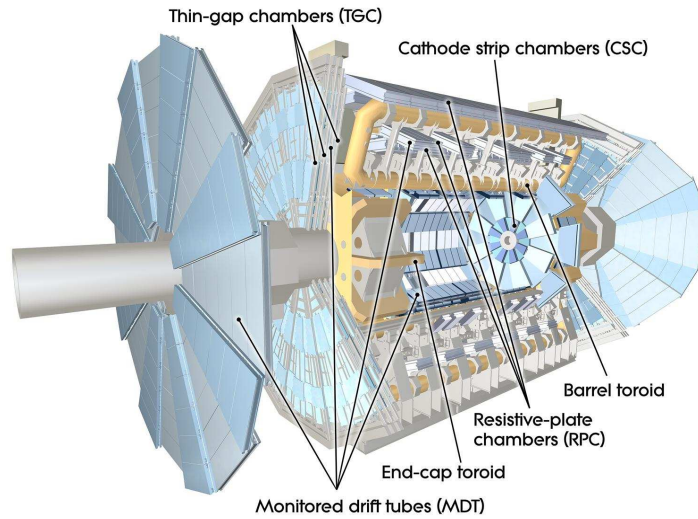
Figure 2.9: Atlas muon spectrometer system [54].

Muon Spectrometer serve a threefold purpose: provide bunch-crossing identification (BCID), provide a trigger with well-defined momentum thresholds, and measure the ϕ coordinate of the muons for track reconstruction.

In the barrel and end-cap regions, tracks are measured in chambers arranged in three cylindrical layers in the central region and three disks in the endcap region. These three layers are called stations and are symmetric around the beam axis. In the transition region between the barrel and endcap toroids, where the magnetic field has large variations, additional chambers are installed to add measurement points and improve the muon momentum resolution.

2.2.5   The Trigger system

In hadron colliders, selecting events is crucial due to a high collision rate. High-performance trigger system has been designed to reduce the rate of events from 40 MHz to a few hundred Hz in three stages [59]. Figure 2.10 shows a schematic view of the ATLAS trigger system.

The hardware-based first level trigger (L1) performs a fast event selection by searching for high-E_T objects and large missing or total energy using reduced granularity data from the calorimeters and the muon system. This trigger level reduces the event rate to a maximum of 75 kHz. It is followed by a software-based second-level trigger (L2) and an event filter (EF), collectively referred to as the high-level trigger (HLT). The reconstruction at L2 is seeded by the L1 result. It uses, with full granularity and precision, all the available detector data (including the information from the inner detector) but only in the regions identified by the L1 as Regions of Interest (RoI). The L2 selection is based on fast custom algorithms processing partial event data within the RoIs identified by L1. After L2 selection, the event rate is few thousand Hz. The EF is selected by the L2 results and has full event information and is using the offline algorithms, calibration and alignment. It reduces the event rate to a few hundred Hz.

The trigger system is configured via a trigger *menu* which defines trigger *chains* that start from a L1 trigger and specify a sequence of reconstruction and selection steps for the specific trigger signatures required in the trigger chain. When referring to a particular level of a trigger, the level (L1, L2 or EF) appears as a prefix, so for example, L1_EM10 refers to the L1 trigger
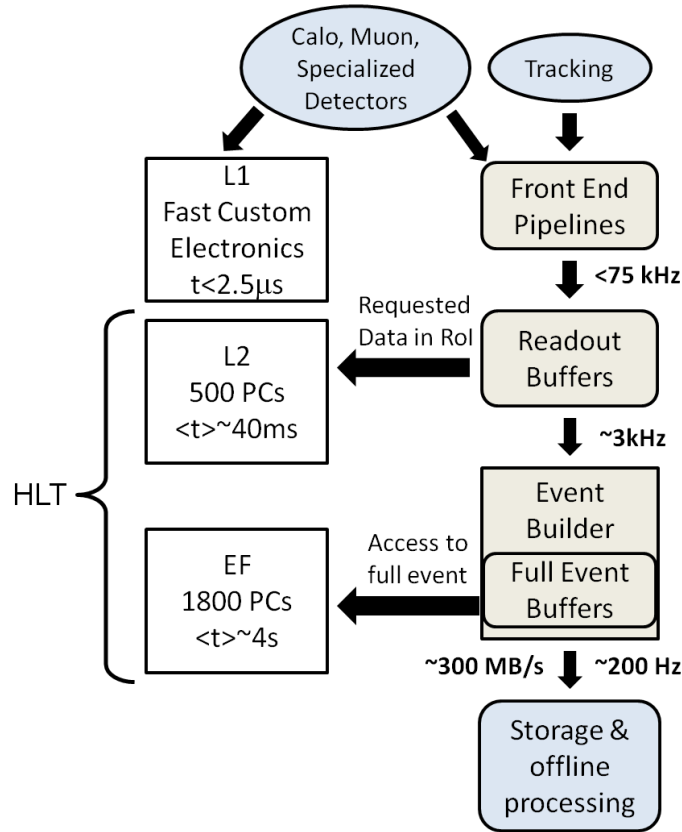
Figure 2.10: The ATLAS trigger system [58] schema.

item with a 10 GeV electromagnetic threshold. A name without a level prefix refers to the whole trigger chain. A trigger chain is often referred to simply as a trigger.

Approximately 500 triggers are defined in the current trigger menu. Those triggers correspond to selected physics objects, defined using a specific notation where a letter representing a particle type [4] is preceded by a multiplicity value and followed by an E_T-threshold value, e.g *2g20_loose* corresponds to a requirement of two or more photon objects, each with E_T above 20 GeV and satisfying *loose* photon identification criteria.

The trigger menu was adjusted during the year to keep the rates within limits at all trigger levels. The L1 output rate was kept below 60 kHz, L2 output rate below 5 kHz and EF output rate at about 400 Hz averaged over the LHC fills. The bandwidth allocated to the electron and photon triggers was about 30% of the total EF bandwidth. More details about them are given in Appendix A.

The events selected by the trigger system are written to inclusive data *streams* based on the trigger type. There are four primary physics streams (*Egamma*, *Muons*, *JetTauEtmiss*, *MinBias*) plus several additional calibration streams. In addition to writing complete events to a stream, it is also possible to record partial information from one or more sub-detectors. Such events, used for detector calibration, are written to the calibration streams.

---

4. e stands for electron, g for photon, j for central jet, fj for forward jet.

Chapter 3

The LAr Timing Alignment

The LAr calorimeter is a sampling calorimeter made of liquid argon as the active material and lead, copper or tungsten as the passive absorber, depending on the position. When charged particles cross the liquid argon gap between electrodes and absorbers, they ionize it. Under the influence of the electric field, the ionization electrons drift towards the electrode inducing a current which is translated in a digital signal.

The time over all the calorimeter channels has to be aligned not only to synchronize the detector readout system with the LHC bunch crossing but also to insure the optimal energy reconstruction. An accurate timing alignment of the ATLAS Liquid Argon Calorimeter is important to achieve a good time resolution in the calorimeter and has several physics application in the ATLAS environment. It can help in the identification of long lived particles and in the measurement of their decay time. One typical example occurs in the Gauge Mediated Supersymmetric Models in which the neutralino travels a significant distance before decaying into an invisible gravitino and a non-pointing and out-of-time photon [64]. This feature can be used to measure the neutralino lifetime using timing information from the electromagnetic calorimeter and the reconstructed photon direction. A delayed cluster time with respect to the trigger time is expected from the photon, because of the value of $\beta = \frac{v}{c} < 1$ of the massive neutralinos and the longer trajectory through the detector. Timing information could also be used in searches for massive instable exotic particles with anomalously high ionization energy losses, which are therefore delayed, to distinguish them from SM backgrounds [65].

Since the beginning of the ATLAS data taking several studies were performed and a few nanoseconds time alignment was reached [66, 67].

This chapter describes the Liquid Argon Calorimeter timing alignment achieved with the LHC proton proton collision data collected in 2011 [68]. The structure of this chapter is the following: in Section 3.1 the LAr geometry and the readout system are described, the previous timing results are presented in Section 3.2, Section 3.3 presents the timing analysis method and finally in Section 3.4 the results are reported.

3.1 The ATLAS Liquid Argon calorimeter

As shown in Figure 3.1 the ATLAS LAr calorimeter consists of four subdetectors: the electromagnetic Barrel (EMB), the electromagnetic Endcap (EMEC), the hadronic Endcap (HEC) and the forward calorimeter (FCal). As for ATLAS, the side-A of the LAr detectors is defined as that one with positive z (the beam direction axis) and the side-C is that one with negative z.
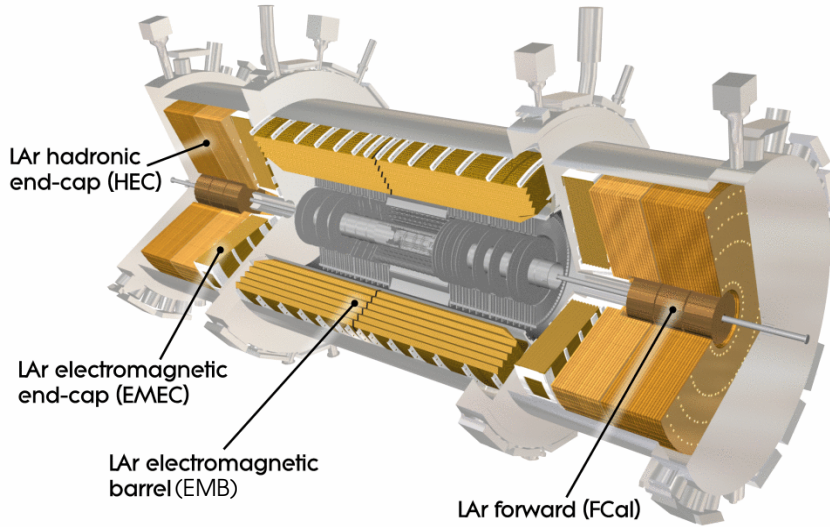
Figure 3.1: Cut-away view of the LAr Calorimeters.

The EMB and the EMEC are lead/liquid argon sampling calorimeters with accordion shape absorbers and electrodes covering respectively an η-range of $|\eta| < 1.475$ and $1.375 < |\eta| < 3.2$. In addition to a transverse segmentation along η and ϕ, the EMB and EMEC are separated into three different longitudinal compartments or layers (Figure 3.2).

At high energy, most of the EM shower energy is collected in the second layer (Layer 2) which has a lateral granularity of 0.025×0.025 in $\eta \times \phi$ space. The first layer (Layer 1) consists of finer-grained strips in the η-direction (with a coarser granularity in ϕ), their size is $\Delta\eta \times \Delta\phi = 0.0031 \times 0.1$ (for $|\eta| < 1.40$) which offer excellent $\gamma - \pi^0$ discrimination.

In the range $|\eta| < 1.8$, these two layers are complemented by a coarse granularity ($\Delta\eta \times \Delta\phi = 0.025 \times 0.1$) presampler (PS) consisting of a thin active LAr layer (Layer 0) placed in front to correct for energy loss in the material before the calorimeter. Finally a back layer (also referred to as Layer 3), which enables a correction to be made for the tail of very energetic EM showers, is behind Layer 2 in the range $|\eta| < 2.5$. It is coarser in η but finer in ϕ for the EMB and for the EMEC.

The transition region between the Barrel and Endcap EM calorimeters, $1.37 < |\eta| < 1.52$, is expected to have poorer performance because of the large amount of material in front of the first active calorimeter layers.

EMEC is built of two wheels: the part closest to the beam pipe is called EMEC Inner Wheel ($2.5 < |\eta| < 3.2$) which has only Layer 1 and Layer 2, and the part further from the beam pipe called EMEC Outer Wheel ($1.375 < |\eta| < 2.5$) which has the standard longitudinal segmentation of four layers (PS and the three EM layers).

The HEC is a copper/liquid argon sampling calorimeter covering the $1.5 < |\eta| < 3.2$ region. It consists of two independent wheels located behind the end-cap electromagnetic calorimeter, each wheel is divided into two longitudinal segments and their granularity in $\eta \times \phi$ is 0.1×0.1

Figure 3.2: Sketch of a barrel module where the different layers are clearly visible with the accordion structure in ϕ. The granularity in η and ϕ of the cells of each layers and of the trigger towers is also shown.

Table 3.1: Cell sizes of the different LAr Calorimeter sub-detectors. The sizes are given in terms of $\Delta\eta \times \Delta\phi$ for all sub-detectors, except for the FCal, where the sizes are in mm^2. [58]

	$|\eta|$ range	Layer 0	Layer 1	Layer 2	Layer 3	# channels
EMB	$[0 - 1.52]$	0.025×0.1	—	—	—	109568
	$[0 - 1.35]$	—	0.0031×0.1	0.025×0.025	0.05×0.025	
	$[1.35 - 1.40]$	—	0.0031×0.1	0.025×0.025	—	
	$[1.40 - 1.475]$	—	0.025×0.025	0.075×0.025	—	
EMEC	$[1.375 - 1.425]$	—	0.05×0.1	0.05×0.025	—	640
	$[1.425 - 1.5]$	—	0.025×0.1	0.025×0.025	—	1837
	$[1.5 - 1.8]$	0.025×0.1	$0.025/8 \times 0.1$	0.025×0.025	0.05×0.025	22300
	$[1.8 - 2.0]$	—	$0.025/6 \times 0.1$	0.025×0.025	0.05×0.025	12411
	$[2.0 - 2.4]$	—	$0.025/4 \times 0.1$	0.025×0.025	0.05×0.025	20569
	$[2.4 - 2.5]$	—	0.025×0.1	0.025×0.025	0.05×0.025	3737
	$[2.5 - 3.2]$	—	0.1×0.1	0.1×0.1	—	2250
HEC	$[1.5 - 2.5]$	0.1×0.1	0.1×0.1	0.1×0.1	0.1×0.1	5632
	$[2.5 - 3.2]$	0.2×0.2	0.2×0.2	0.2×0.2	0.2×0.2	
FCal	$[3.1 - 4.9]$	—	$2\ mm^2$	$3.5\ mm^2$	$5.6\ mm^2$	3524

for $1.5 < |\eta| < 2.5$ and 0.2×0.2 for $2.5 < |\eta| < 3.2$.

Finally the LAr forward region $3.1 < |\eta| < 4.9$ is covered by the FCal which is segmented into three modules in longitudinal direction in each end-cap. The material of the passive absorbers, copper or tungsten, depends on the position of the modules: the first is made of copper and optimized for electromagnetic measurements, the others are made of tungsten and optimized for hadronic measurements.

Due to this segmentation the whole LAr detector has a total of 182468 readout channels. Table 3.1 summarizes for each sub-system the number of readout channels and their granularity for each layer.

3.1.1   The electronic chain
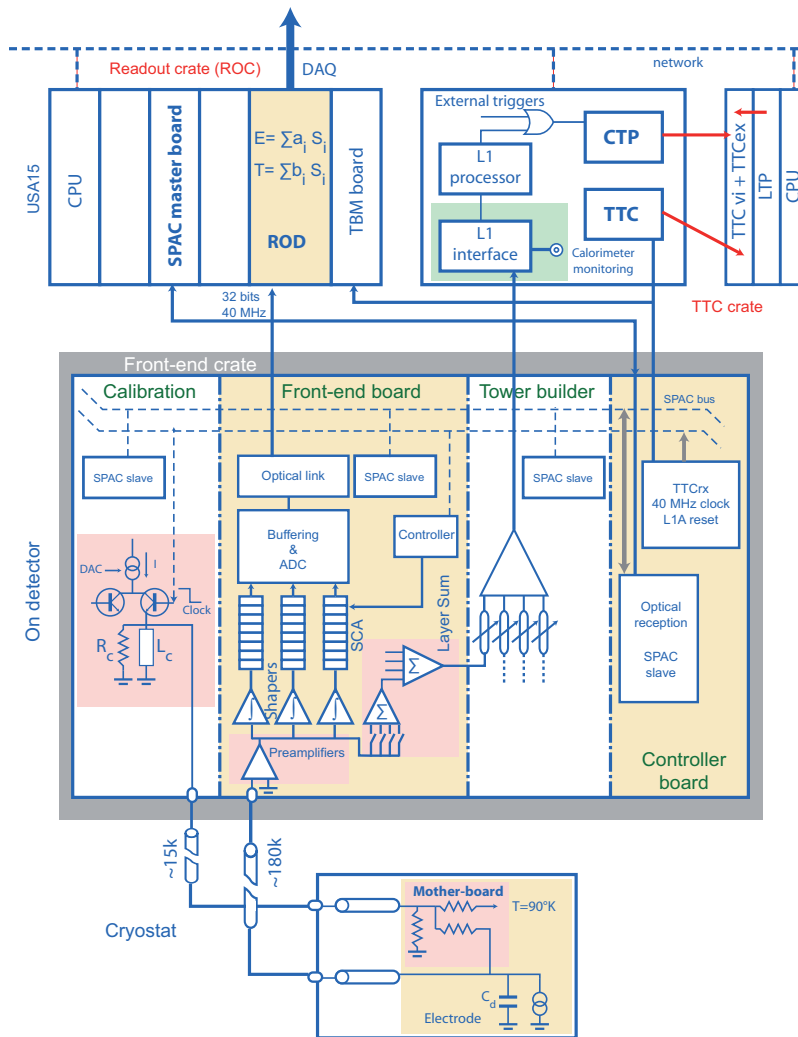

Figure 3.3: Block diagrams showing the architecture of the overall LAr Calorimeter readout electronic.

The overall architecture of the LAr readout electronics is shown in Figure 3.3. The ionization signal for each readout channel is driven through feed-throughs (FTs) into Front-End crates (FEC) located on the edge of the cryostat. The front-end boards (FEBs) and the calibration

boards are housed in the FEC. The LAr geometry is that each FT covers different ϕ-region, thus the readout channels in all the FTs have a defined ϕ symmetry.

The Calibration boards [69] generate and distribute adjustable currents to all the readout channels through the FT. A calibration board has 128 channels referred to as "calibration lines". Each calibration line injects charge simultaneously onto a fixed number of channels, this number varying from 1 to 32 depending on layer and detector, according to specific injection patterns optimized for each readout layer [70].

A FT bring the signals to 14 (barrel) or 15 (end-cap special crates) FEBs, each FEB is identified by its η-position (called slot) in the FT. With each FEB handling up to 128 channels, a total of 1524 FEBs are required. In the FEBs the signal is amplified, shaped and digitized. The triangular input current pulse from the detector and the shaped output pulse from the FEB are depicted for the case of a barrel electromagnetic channel in Figure 3.4.
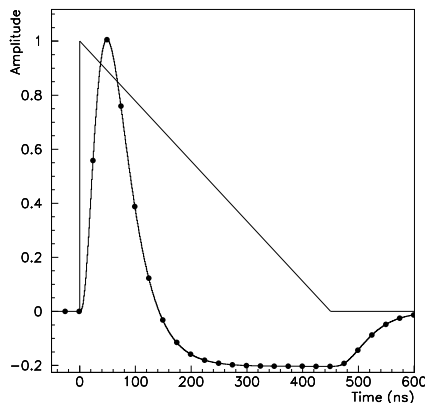
Figure 3.4: Amplitude versus time for triangular pulse of the current in a LAr barrel electromagnetic cell and of the FEB output signal after bi-polar shaping. Also indicated are the sampling points every 25 ns.

In order to accommodate the large dynamic range of pulses (from tenths of MeV to a few TeV) and minimize the total noise from the electronics, each channel is piped through 3 different readout gains. The ratios between the gains are $\sim$ 10 with gain values of 0.8 for low gain (LG), 8.4 for medium gain (MG), and 82 for high gain (HG).

For a given channel three signals, each corresponding to each gain, are stored in an analog pipeline (Switch Capacitor Array) [71] that operates at the 40 MHz frequency allowing to wait the L1 decision. When the trigger decision is made the ionization signal from the most suited gain [1] is digitized by a 12 bit Analog-to-Digital Converter (ADC) in five [2] samples spaced by 25 ns and sent to the read-out driver (ROD).

For each FEB a Timing Trigger and Control receiver chip (TTCRx) [72] has the role to adjust the phase of the sampling command (for the 128 channels of the given FEB) with respect to the LHC clock signal. The TTCRx can delay the LHC clock by steps of 25 ns (coarse delay) and 0.104 ns (fine delay).

---

1. The gain selection is done according to the amplitude of the signal in the medium gain.

2. The number of the reconstructed signal samples have changed during the different ATLAS data taking periods. Has been frozen to five from the 2011 start-up. To note also that in the calibration runs the number of sampling can vary.

The reconstruction of the time and raw energy deposited in a given readout cell is performed in the ROD by the Online Digital Signal Processor (DSP) and it is based on an Optimal Filtering algorithm [73].

3.1.2   The Optimal Filtering Method

The Optimal Filtering (OF) technique allows to reconstruct the time and the energy of the signal from the ionization pulse in each channel. The OF method requires that the exact shape of the expected ionization signal after the electronic readout chain is known. The expected pulse shape for each channel is obtained from dedicated calibration runs, called Delay runs, which measure the shape of the pulse as a function of time for each readout channel using a known injecting current [69]. To obtain the expected ionization shape from the calibration pulse a transfer function is needed for every channel. This procedure allows to built for each readout channel a predicted ionization pulse shape (also called reference ionization pulse shape).

The Optimal Filtering Coefficients (OFCs) a_i and b_i are computed per channel from the predicted ionization pulse-shape [73] and they are used to reconstruct both the energy and the time of each pulse using the following formulas:

$$A = \sum_{i=1}^{5} a_i s_i \tag{3.1}$$

$$A\tau = \sum_{i=1}^{5} b_i s_i \tag{3.2}$$

where A is the ionization pulse amplitude in ADC counts, τ measure the relative time between the predicted pulse and the ionization pulse and s_i are the signal digitized (ADC) samples and where five is the number of reconstructed signal samples.

In order to provide unbiased results, Equation 3.1 requires that the ionization signal and the reference signal shape used to calculate the OF Coefficients are in phase up to a small deviation τ, which is estimated by Equation 3.2. The requirement for unbiased reconstructed energy is that τ is no larger than $2 - 3$ ns [3] [74].

In physics run there are eight sets of OFCs with 3 ns phase-shift between each other, while 24 sets with 1 ns phase-shift are used in the calibration runs to construct the reference ionization pulse shape [4]. With eight phases with 3 ns shift the different OFC sets are chosen in a way that the fourth set of OFCs corresponds on average to a pulse shape with the signal peak on the third sample.

At the beginning of the LHC data taking, the OFC sets loaded in the LAr DSP were chosen according to the timing information extracted from calibration data and the knowledge of the readout path [66]. Since the τ value obtained was large, the first 2010 collision data were reconstructed offline using an OF iterative procedure, using different sets of the OFCs with appropriate phases until the values of τ obtained are less than ~ 3 ns.

From the beginning of 2011 data taking the OFC iteration are no more computed during the offline reconstruction and for each signal the energy and the time are computed with the same OFCs set as the one loaded in the DSP level.

---

3. A time misalignment of ~ 5 ns between the phase of the signal samples and the OFC used to reconstruct the signal amplitude induces a bias on the reconstructed energy of $\sim 0.5\%$

4. The predicted pulse is defined with a time difference of $\frac{25ns}{24}$ ns between two consecutive samples and is binned in 24 delay steps spaced by ~ 1.04 ns

3.2 Previous timing studies

The time of the maximum amplitude of a ionization pulse depends on two parts: the cable delay (called T_0) and the rising time of the pulse. The rising time of the pulse is a function of the cell capacitance and the characteristic time of the shaper. T_0 is related to all the cable lengths the signal goes through.

Since the beginning of the ATLAS data taking several studies were performed to achieve the best time alignment between the signal from the $\sim 2 \times 10^5$ LAr channels. There are two main sources of the LAr time misalignment: the relative FEB to FEB timing variations and the single channel time misalignment.

The relative FEB timing offset can vary by up to ± 10 ns due to the T_0 difference because of the cable lengths to reach a given FEB, and can be corrected by setting suitable delay on each FEB.

The second contribution comes from the single channel timing variation of ± 3 ns within each FEB, and is accounted when the OFC are computed.

The FEB timing offsets for the entire LAr calorimeter were estimated from a calculation of the time delay introduced by the cables [66], and checked using cosmic ray and *beam splash* data (proton bunch hitting a upstream collimator and producing a large spray of particles) [5] in 2009 [67]. With these studies a timing accuracy of a few ns was reached. The LAr timing alignment was re-tuned in 2010 using collision data [68].

3.3 Analysis Method

This analysis is done with the collisions data at the center of mass energy of $\sqrt{s} = 7$ TeV collected in the 2011 by the ATLAS detector.

3.3.1 Calibration_LArCells stream

The data used for this analysis comes from *Calibration_LArCells* stream. This stream is reconstructed offline in parallel to the physics streams (for more details see Section 2.2.5), using HLT selection and a partial event building technique describe below.

Calibration_LArCells stream uses standard photon, jet and forward jet trigger reconstruction algorithms. To increase the rate of the recorded events while keeping the total stream size small, the high level trigger reconstruction is performed only in the $\Delta\eta \times \Delta\phi \sim 0.2 \times 0.2$ (0.4×0.4 for the jets trigger items) LAr sector, around the RoI. Thereafter only the calorimeter information inside the selected RoI is recorded.

Typical list of the trigger items which go into the *Calibration_LArCells* stream, with the relative pre-scales, is shown in Figure 3.5. They are all single object items for photons, jets and forward jets of certain transverse energy thresholds. The exact values of pre-scales vary as a function of luminosity.

---

5. A beam splash event is equivalent to a flux of particles traveling at the speed of light (parallel to the z axis) which illuminate most of the calorimeter channel with an high energy deposit which offer a good tool to check the relative timing between calorimeter cells.

	EF Chain	PS	PT	STP	L2 Chain	PS	PT	L1 item	L1 prescale
LArCells									
⊕	EF_g15_loose_larcalib	1.0	0.0	1	L2_g15_loose	879.0	0.0	L1_EM10	1
⊕	EF_g20_loose_larcalib	1.0	0.0	1	L2_g20_loose	93.6	0.0	L1_EM14	1
⊕	EF_g40_loose_larcalib	1.0	0.0	1	L2_g40_loose	6.5	0.0	L1_EM30	1
⊕	EF_g60_loose_larcalib	1.0	0.0	1	L2_g60_loose	1.0	0.0	L1_EM30	1
⊕	EF_g80_loose_larcalib	1.0	0.0	1	L2_g80_loose	1.0	0.0	L1_EM30	1
⊕	EF_g11_etcut_larcalib	1.0	0.0	1	L2_g11_etcut	30.6	0.0	L1_EM5	350
⊕					L2_j95_larcalib	19.2	0.0	L1_J75	1
⊕					L2_j50_larcalib	1.0	0.0	L1_J30	330
⊕					L2_fj25_larcalib	2.7	0.0	L1_FJ10	68
⊕					L2_fj50_larcalib	2.4	0.0	L1_FJ30	20
⊕					L2_j25_larcalib	1.1	0.0	L1_J10	899

Figure 3.5: The composition of the trigger menu for the *Calibration_LArCells* stream for a run in 2011. In the table the pre-scale (PS) values of the trigger items are specify. A PS value of 1.0 means that the items is unprescaled. When the pass-through option (PT) is different from zero, a fraction of data is selected without any HLT selection. Finally in the Table are also displayed the stream pre-scales (STS) which are only applied for the express stream (for all other streams they are 1).

3.3.2 Electronic Noise suppression

To measure the baseline level of a channel readout electronics and its noise properties, during the LAr calibration campaigns, special Pedestal runs [74] are taken. In those runs the response of the readout electronics is recorded without any signal injected. Therefore in randomly triggered events the samples that come from each channel are distributed around a central pedestal value. When the signal reconstruction algorithm is applied to these samples it results in a Gaussian distribution of energies centered around zero. The standard deviation, σ_{noise}, of this distribution will be referred to as the noise level.

Above a certain threshold it is extremely unlikely that a signal is due to the electronic noise, therefore in the timing studies a selection of signals above $3\sigma_{noise}$ is applied to remove the events in which the ionization signal comes most probably from noise.

3.3.3 Timing Analysis

To reach the best timing alignment over the whole LAr calorimeter the analysis is performed in two steps. First of all in order to correct for the relative FEB timing delays, timing offsets for each FEB are derived; then the single channel misalignment is corrected by adjusting the phase of the OFCs.

Depending on the spatial position of the LAr channels a different number of signals per channel (events) is collected. Lower event statistic leads to a less precise timing measurement. The following strategy is devised to take into account the different statistics.

The individual channel time, $< time >_{ch}$, is calculated as described below. For each LAr channel with more than five events, the time distribution is fit with a single Gaussian, and the $< time >_{ch}$ is the mean value of the fit if:

- the fit converged [6],

- the values of the mean are not at the border of the fit range constraint $[-10 : 10]$ ns.

- and if the sigma of the fit is not four times bigger than the RMS of the channel time distribution.

If less then five events are collected, the $< time >_{ch}$ is the median [7] of the channel time distribution.

The FEB time offset ($< time >_{FEB}$) is defined for each FEB as the median of the $< time >_{ch}$ distribution for the channels with at least two events, and $< time >_{FEB}$ is computed only for the FEBs which have more than ten channels with two entries recorded.

For a given channel in a collision event, a number of effects are expected to contribute to the measurement of the channel time distribution which could degrade its accuracy and precision. For this reason in this analysis the selection outlined below is performed to select only good ionization pulses.

To decrease the effect of the electronic noise, only the events in the stable beam lumi-block region are considered and the lumi-blocks in which high noise activity is detected are removed [8]. Furthermore to be insensitive to misbehaving channels, all the channels which appears on the

---

6. The status of the fit is successful

7. The median is the numeric value separating the higher half of a population from the lower half.

8. Note that no other particular selection is applied to insure that only collision events are selected. Small contamination from non-collision events is possible ($< 10\%$).

bad channel list [9] are removed. Since the readout electronics is different for each gain, the
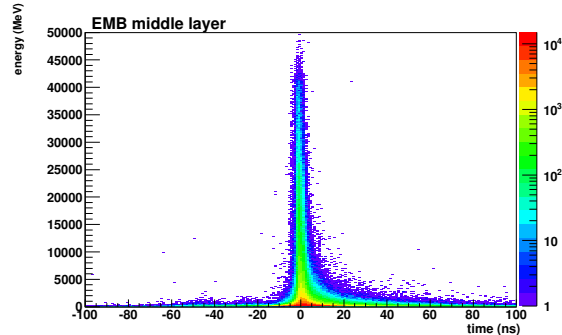analysis is performed separately for HG, MG and LG.

Figure 3.6: The energy versus time distribution for all channels in the middle layer of the EM Barrel.

As is shown in Figure 3.6 for the channels in a single LAr layer the energy versus time
distribution is not symmetric. To reduce the bias on the $< time >_{ch}$ and $< time >_{FEB}$
measurement, coming from the energy versus time tail, only the time computed for channels
with an energy above a certain threshold is used.

Table 3.2: Optimized energy cut for each layer of each LAr sub-detectors

LAr Partition	Layer 0 Energy cut [GeV]	Layer 1 Energy cut [GeV]	Layer 2 Energy cut [GeV]	Layer 3 Energy cut [GeV]
EMB	1	1	3	1.5
EMEC$_{Outer}$	1.5	1	3	2
EMEC$_{Inner}$	-	2	2	-
FCal	10	10	10	10
HEC	3.5	3.5	3.5	3.5

Two effects should be taken into account to choose the best energy threshold. On one hand
the time resolution, and thus the time measurement, improves with energy; on the other hand
the single channel occupancy decreases with energy and to get a consistent $< time >_{ch}$ a
sufficient event statistics per channel is needed. To find the optimal value for the energy cut,
an energy scan at the level of $< time >_{FEB}$ is performed for each layer of each LAr sub-detector
(more details in Appendix B). The resulting cut values are shown in Table 3.2. The energy
thresholds chosen are the lowest values for which the FEBs time offset remains stable while the
single channel time distribution maintains reasonable statistics. Only the channels in the high
gain which are properly calibrated and for which the OFCs iteration converges are considered
for this scan.

---

9. A list of misbehaving channel is provide for the data quality task to report periodically strange behavior
of the LAr channels.

3.4 Results

(a) EMB

(b) EMEC

(c) FCAL

(d) HEC
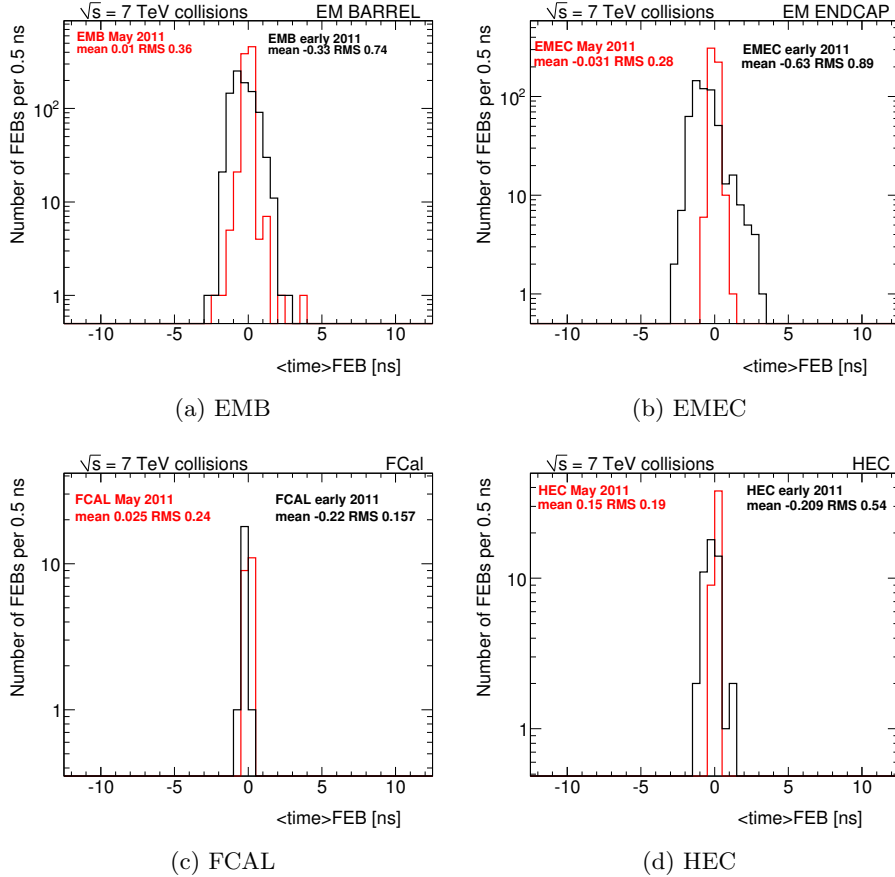
Figure 3.7: LAr FEBs time distribution at the 2011 startup (black histograms) and after (red histograms) the implementation of the FEB corrections on the 13th of April 2011, for all the partitions of the LAr calorimeter.

3.4.1 Time offset per FEB

On the 13th of April 2011 the LAr online database [10] was updated with new delays computed as the FEB time offsets ($< time >_{FEB}$) calculated as described in Section 3.3 using the early data collected in the 2011 which correspond to ~ 9.8 pb^{-1} of collision data (~ 0.96 Mevents). These data have enough statistics to have at least two events in 99.9% of channels.

The FEB corrections, stored in the online database, are read in the TTCRx and applied as a coarse (steps of 25 ns) and a fine (steps of 0.104 ns) delays of the phase of the sampling as described in Section 3.1.1.

The effect of the adjustment of the FEB time is shown in Figure 3.7 for all the LAr sub-detectors. The black histograms show the FEB time offsets in the early 2011 data before the implementation of the timing corrections and the red histograms show the same distributions for collision data collected in May 2011 [11] after the implementation of the timing corrections.

---

10. COOL online system.
11. Corresponding at ~ 40 pb^{-1} of collision data (~ 2.2 Mevents).
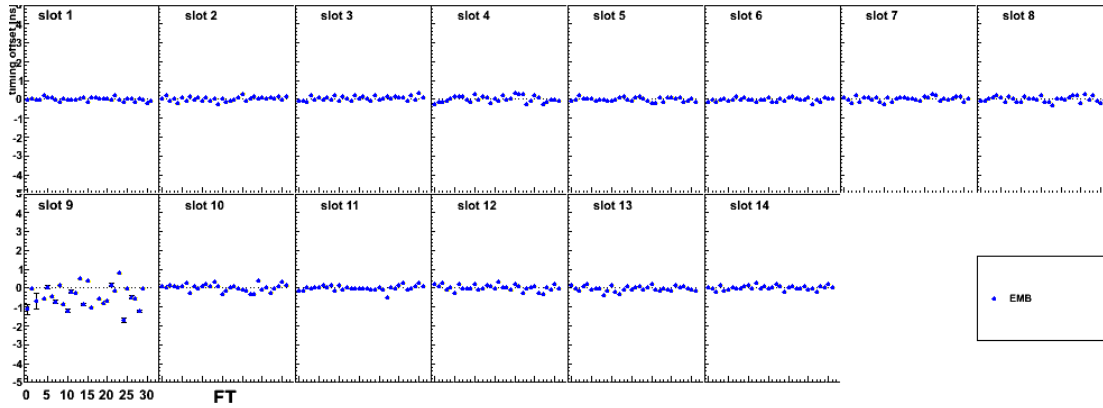
(a) EM Barrel C
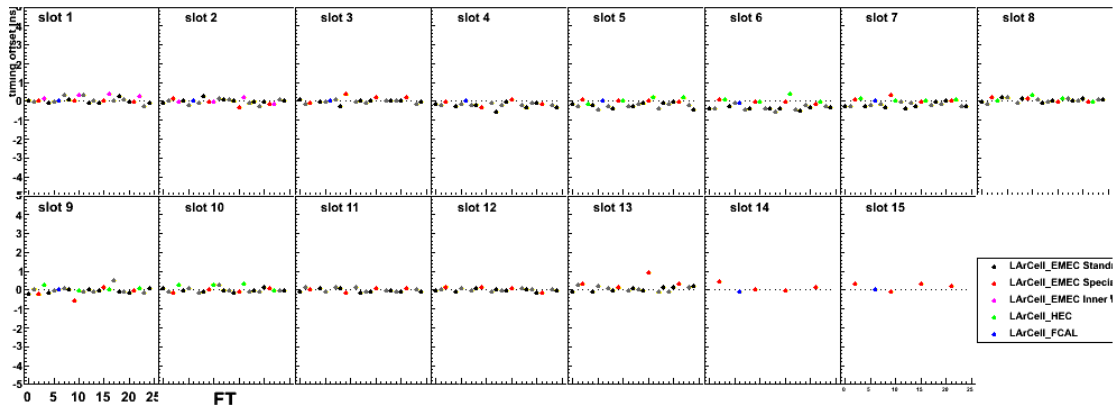
(b) EM Endcap C

Figure 3.8: FEB times for all the LAr subdetectors in side C after the implementation of the correction. Each point represents one FEB in the FT. Each box represents one slot. Each slot covers different η-range and each slot in the different FT has the same ϕ coordinate. The errors evaluated on the plots are statistical only. To note that the remaining small spread in the FEB timing in EMB slot 9 is because the FEB timing corrections for slot 9 were not computed due to the lack of statistics.
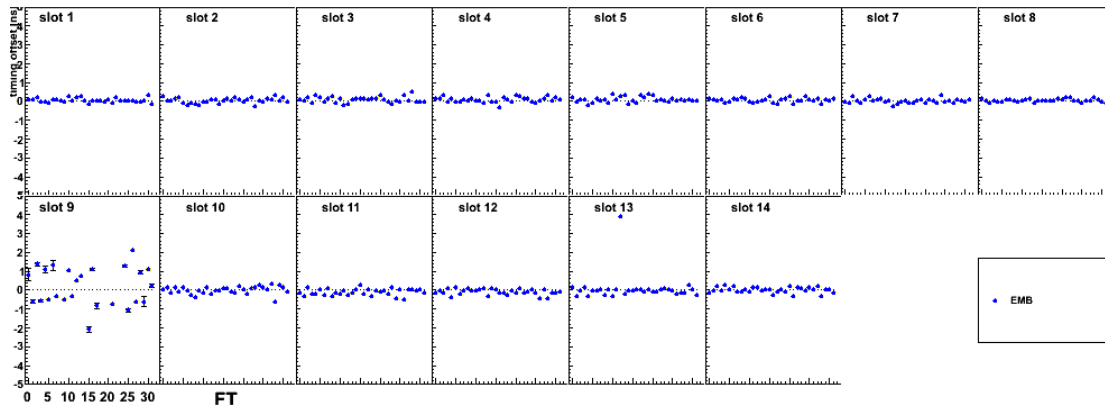
(a) EM Barrel A
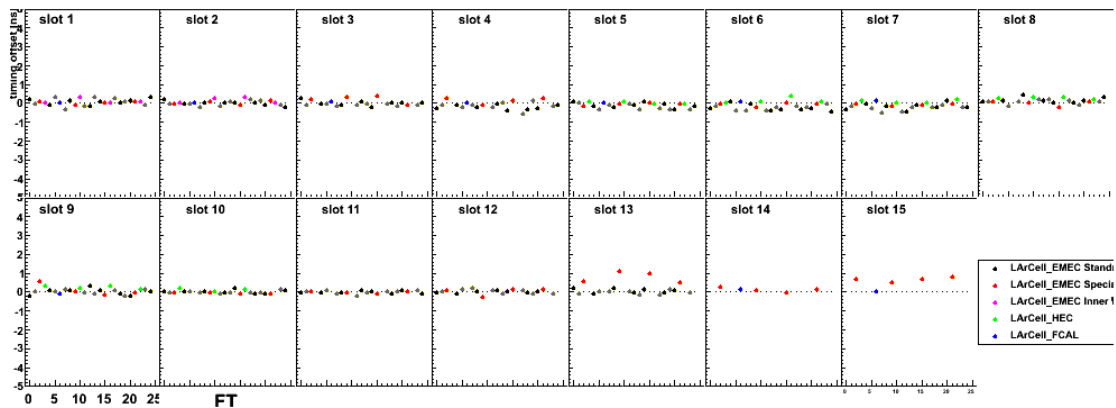
(b) EM Endcap A

Figure 3.9: FEB times for all the LAr subdetectors in side A after the implementation of the correction. Each point represents one FEB in the FT. Each box represents one slot. Each slot covers different η-range and each slot in the different FT has the same ϕ coordinate. The errors evaluated on the plots are statistical only. To note that the remaining small spread in the FEB timing in EMB slot 9 is because the FEB timing corrections for slot 9 were not computed due to the lack of statistics.

From the comparison of the two histograms it is clear that a significant improvement of the timing alignment is obtained. The time of each FEB is centered at zero, with an improvement in all the RMS values which are now decreased to ~ 0.3 ns for all the subdetectors.

After these adjustments the FEB timing alignment is better than ~ 0.5 ns for all LAr partitions. In Figures 3.8 and 3.9 the detailed single FEB times after the corrections are shown for all the LAr subdetectors for side C and side A, respectively.

3.4.2   Channel by Channel adjustment

To perform the channel by channel corrections the difference between the individual channel time and the corresponding FEB offset is considered as

$$< time >_{ch} - < time >_{FEB} \tag{3.3}$$

The difference in Equation 3.3 was used to correct the single channel misalignments to ensure no discrepancy between the $< time >_{FEB}$ result and channel by channel corrections.

The latest channel by channel corrections were introduced before the beginning of the 2011 data taking period, in the COOL[12] offline database, and are applied as a new OFCs phases (see section 3.1.2) for the reconstruction of the energy and the time values of the ionization pulse inside the ATHENA[13] framework. Since the OFCs are computed in integer bin unit and each bin has a width of 1.042 ns, the single channel adjustment has a resolution of about 0.521 ns.

Figure 3.10 shows the residual channel by channel spread within the FEBs for example in slot 2 for the EMB A and in slot 5 for the EMEC A for collision data recorded in April 2011. From Figure 3.10, one can see that the resulting average channels spread is $O(0.5)$ ns for all the LAr partitions, which is compatible with the half size of the OFCs bin.

In September 2011 new channel by channel adjustments are applied only for the channels with a single channel time deviation above 3 ns from the $< time >_{FEB}$ independently for the HG and the MG. Those channels were mostly dead channels during the 2010 data taking and correspond to 0.59% of the total number of the LAr readout channels.

3.4.3   Timing Resolution

The channel time distribution is affected by a bad intrinsic time resolution at the low energy range. The time resolution has a energy dependence described by the empiric formula:

$$\sigma_t = \frac{p_{Res}}{E} \oplus p_{const} \tag{3.4}$$

where the p_{Res} term is correlated with the noise level and therefore has a different value in each layer, and the constant term p_{const} is a combination of all the effects that do not depend on the energy of the LAr channel.

Previous results, using cosmic ray data from October to December 2008 [67], have shown, a p_{const} value of 1.46 ± 0.07 ns for channels in the HG of the EMB middle layer. In that case the p_{const} was equivalent to the RMS of the difference between the measured and predicted times for a single channel.

---

12. The COOL database provides a common software for the storage and management of the conditions data of the ATLAS experiment. The conditions data record the state of the detector at the time when events are collected. Conditions data are extremely important because they are needed for the reconstruction and analysis of the events taken using the detector they describe.

13. The official ATLAS computing framework.
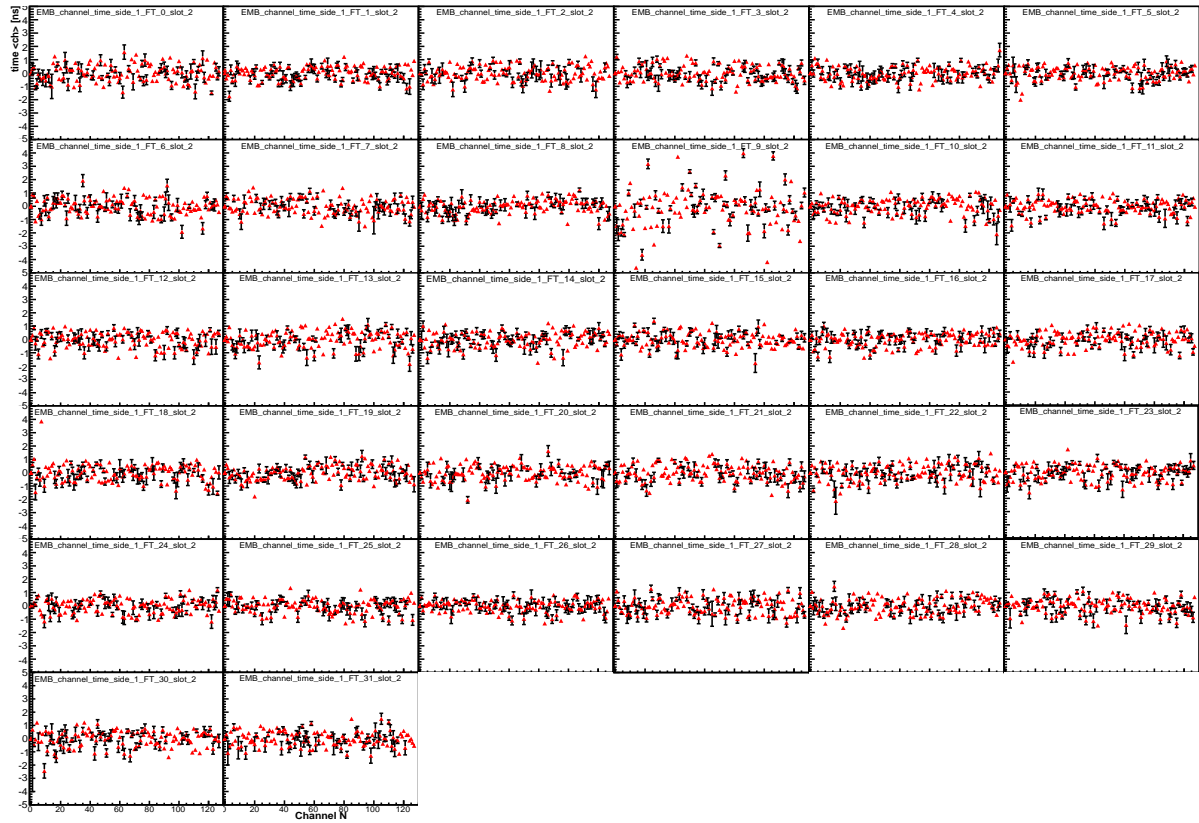
(a) EMB A
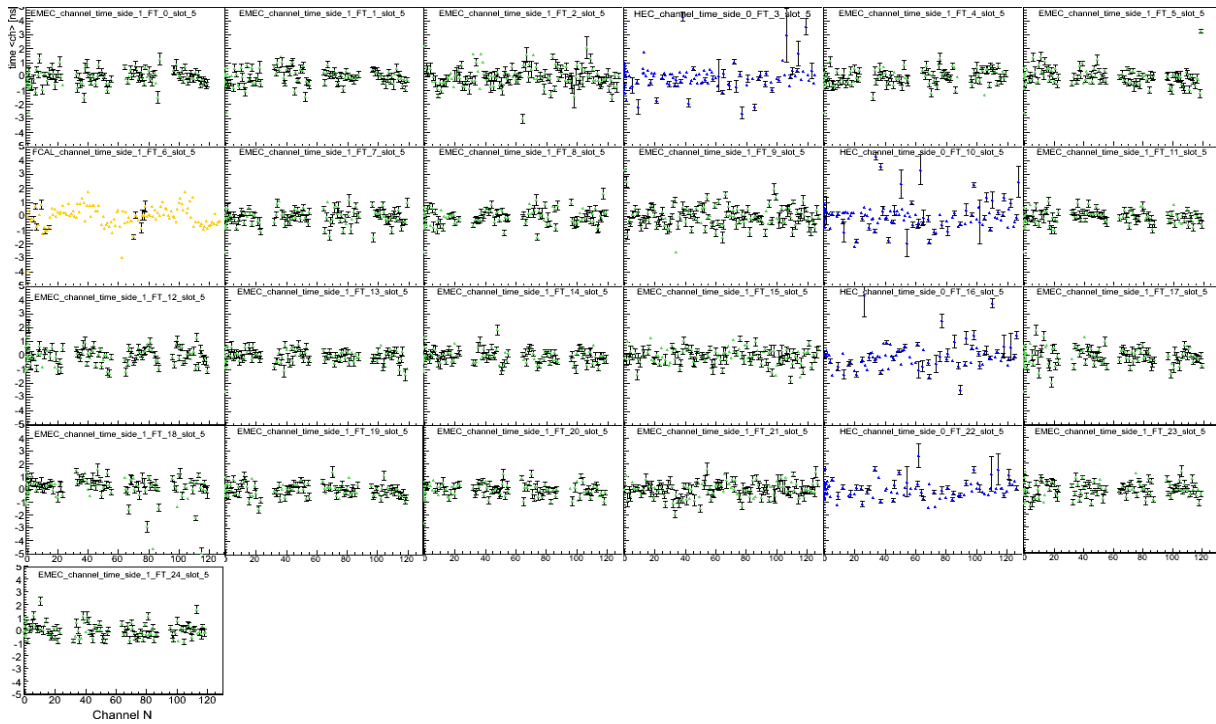
(b) EMEC A

Figure 3.10: For collision data recorded on April 2011. The single channel time spread within a FEB ($< time >_{ch} - < time >_{FEB}$), for all the FEBs in slot 2 for the EMB side A (upper plot) and for all the FEBs in slot 5 for the EMEC side A (bottom plot). Each point represents one channel in the FEB. Each set of axes represents one FT. The errors evaluated on the plots take into account the RMS and the statistic of the $< time >_{ch}$ distribution.
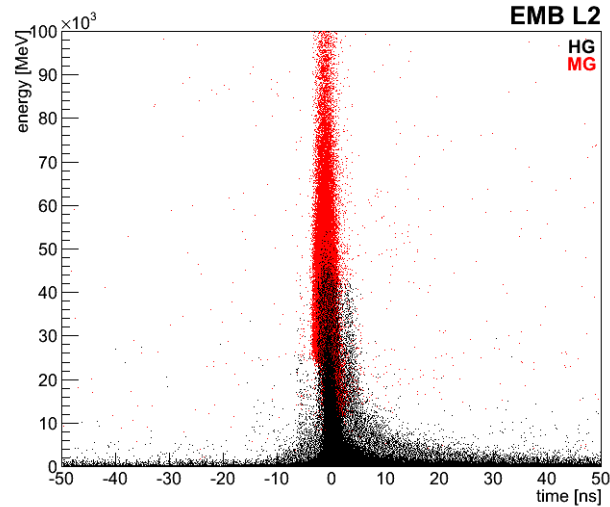
(a) The energy versus the time distribution for all the channels
in the middle layer of the EM Barrel for HG and MG
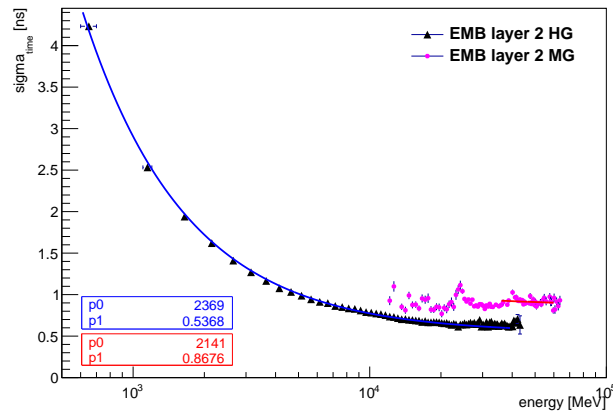
(b) Time resolution as a function of channel energy for the mid-
dle layer of the EM Barrel for HG and MG

Figure 3.11: Upper plot: energy as function of the channel time, in red for HG and in black for the MG
for the barrel middle layer only. Bottom plot: The time resolution as function of the channel energy
fitted with the empiric formula: $\sigma_t = \frac{p_0}{E} \oplus p_1$, where the p_1 parameter corresponds to the resulting value
of p_{const}.

The constant term of the time resolution in collision data, is equivalent to the intrinsic time
spread of the channels with the energy in a certain range.

Figure 3.11 shows for 2011 data the energy versus time distribution for the middle layer of
the EMB for channels in HG and MG (upper plot) and the resulting RMS of the channel time
distribution versus energy slices (bottom plot). To get the corresponding p_{const} value the timing
resolution as function of the channel energy has been fitted with Equation 3.4 for the HG and
the MG components separately, bottom plot of the Figure 3.11. In this studies the constant
term for the middle layer of the EMB LAr calorimeter was measured to be 0.537 ± 0.001 ns

for the HG and 0.868 ± 0.018 ns for MG, where the errors come from the fit only. This values show significant improvement with respect to the previous measurement.

3.5 Conclusions

Table 3.3: Summary of all the timing correction applied on the LAr.

Data used to compute the correction	$< time >_{FEB}$ correction	$< time >_{ch}$ correction
Beam Splash and cosmic ray [66], [67]	2008-2009	-
Collision data 2010 [68]	April 2010	May 2010
Collision data 2010 [68]	February 2011	February 2011
Collision data 2011 [68]	April 2011	September 2011

Table 3.3 shows the dates of all the LAr calorimeter timing corrections applied since 2008. After the latest timing adjustment calculated with the 2011 data the global timing alignment of the whole LAr calorimeter is better than one ns for all the LAr partitions, and the EMB time resolution below a ns level is reached.

More corrections would be needed to achieve the design timing resolution at a level of hundred ps (Ref. [75]).

Chapter 4

Electron Efficiency measurements

The precise determination of the electron performance of the ATLAS detector is essential for any search for new phenomena with electrons in the final state.

Physics processes are expected to produce electrons of a brother energy range up to several TeV. In the searches for new phenomena, an excellent electron identification capability, with high efficiency and high jet rejection rate, is required over a broad energy range to overcome the low signal-to-background ratio.

In the central region, defined as the region with $|\eta| < 2.47$, electron performances are insured by using a powerful combination of different detector technologies: silicon detectors, a transition radiation tracker and a longitudinally layered electromagnetic calorimeter system with fine lateral segmentation. A further strength of the ATLAS detector is its ability to reconstruct and identify energy deposition of EM nature outside the tracking coverage up to $|\eta| < 4.9$. From now on, only the electrons reconstructed in the central region are considered.

This chapter describes the measurements of the trigger, the offline reconstruction and the identification electron efficiency using $Z \to ee$ events observed in 5 fb^{-1} of data collected in 2011 at a centre-of-mass energy of $\sqrt{s} = 7$ TeV.

The structure of this chapter is the following. Section 4.1 describes the electron object reconstruction in ATLAS. Section 4.2 starts with the description of the tag-and-probe method, and then proceeds to present the measurements of the electron trigger efficiency and the electron identification efficiency.

4.1 Electron Objects in ATLAS

The electron reconstruction and identification algorithms used in ATLAS are designed to achieve both a large background rejection and a high and uniform efficiency over the full acceptance of the detector. Isolated electrons need to be separated from hadrons in QCD jets, from background electrons (originating mostly from photon conversions in the tracker material), and from non-isolated electrons from heavy flavor decays. Efficiencies for identification and isolation cuts need to be measured on data [76].

4.1.1 Electron Reconstruction algorithm in ATLAS

The standard electron reconstruction procedure in ATLAS is based on clusters reconstructed in the electromagnetic calorimeter, which then are associated to tracks reconstructed in the Inner Detector. This algorithm has been developed to allow for an optimal reconstruction of the

four-momentum of electrons from a few GeV to a few TeV. Information from both detectors allows electron identification with the lowest possible amount of background contamination, keeping in mind that the optimum between the identification efficiency and background rejection depends on the analysis.

Electron reconstruction begins with the creation of a preliminary set of seed clusters with transverse energy (E_T) above 2.5 GeV. They are formed by a *sliding window* algorithm, where the seed clusters are 3×5 in $\eta \times \phi$ middle layer cell units (eg. 0.075×0.25).
An electron is defined by the existence of one or more reconstructed tracks matched to a seed cluster. The track-to-cluster matching thus forms the central part of the electron reconstruction. Reconstructed tracks are matched to seed clusters by extrapolating them from their last measurement point to the second layer of the calorimeter. The impact point η and ϕ coordinates are then compared to the corresponding seed cluster η and ϕ in that layer. If the difference $\Delta\phi = \phi_{clu} - \phi_{trk}$ and $\Delta\eta = \eta_{clu} - \eta_{trk}$ is below a certain threshold then the track is considered matched to the cluster.
The track matching is affected by Bremsstrahlung losses which result in an asymmetric sign-dependent $\Delta\phi$ distribution. Therefore to account for these losses, the size of the sign corrected $\Delta\phi$ window is larger on the side where the extrapolated track bends as it traverses the solenoidal magnetic field.
An electron is reconstructed if at least one track is matched to the seed cluster. In the case where several tracks are matched to the same cluster, tracks with silicon hits are preferred, and the one with the smallest $\Delta R = \sqrt{\Delta\eta^2 + \Delta\phi^2}$ distance to the seed cluster is chosen.
The information related to the track-to-cluster matching is retained for all the tracks assigned to the reconstructed electron object and is used during the particle identification based on *medium* and *tight* sets of cuts[1], as is shown in Table 4.1.
The electron cluster is then rebuilt using 3×7 (5×5) longitudinal towers of calorimeter cells in the barrel (endcaps) which correspond to 0.075×0.175 (0.125×0.125) in $\eta \times \phi$. These lateral cluster sizes are optimized to take into account the different overall energy distributions in the barrel and endcap calorimeters. The cluster energy is then determined [59] by summing four different contributions:

1. the estimated energy deposit in the material in front of the EM calorimeter,

2. the measured energy deposit in the cluster,

3. the estimated external energy deposit outside the cluster (lateral leakage),

4. the estimated energy deposit beyond the EM calorimeter (longitudinal leakage).

The four terms are parametrized as a function of the measured cluster energies in the presampler detector (if it is present) and in the three EM calorimeter longitudinal layers based on detailed simulation of energy deposition in both active and inactive material in the relevant detector systems. A good description of the detector in the Monte Carlo (MC) simulation is therefore essential in order to correctly reconstruct the electron energy.
Finally the electron four-momentum is computed using information from both the final cluster and the best track matched to the original seed cluster. The energy of the reconstructed electron is given by the cluster energy, and the ϕ and η directions are taken from the corresponding track parameters unless the track contains no silicon hits, in which case η is provided by the η-pointing matched cluster.

Table 4.1: Definition of variables used for *loose*, *medium* and *tight* electron identification cuts for the central region of the detector with $|\eta| < 2.47$.

Type	Description	Name
loose selection		
Acceptance	$|\eta| < 2.47$	
Hadronic leakage	Ratio of E_T in the first layer of the hadronic calorimeter to E_T of the EM cluster (used over the range $|\eta| < 0.8$ and $|\eta| > 1.37$)	R_{had1}
	Ratio of E_T in the hadronic calorimeter to E_T of the EM cluster (used over the range $|\eta| > 0.8$ and $|\eta| < 1.37$)	R_{had}
Middle layer of EM calorimeter	Ratio of the energy in 3×7 cells over the energy in 7×7 cells centred at the electron cluster position	R_η
	Lateral width of the shower	$w_{\eta 2}$
medium selection (includes loose)		
Strip layer of EM calorimeter	Total shower width	w_{stot}
	Ratio of the energy difference between the largest and second largest energy deposits in the cluster over the sum of these energies	E_{ratio}
Track quality	Number of hits in the pixel detector (≥ 1)	n_{pixel}
	Number of total hits in the pixel and SCT detectors (≥ 7)	n_{Si}
	Transverse impact parameter ($|d_0| < 5$ mm)	d_0
Track–cluster matching	$\Delta\eta$ between the cluster position in the strip layer and the extrapolated track ($|\Delta\eta| < 0.01$)	$\Delta\eta$
tight selection (includes medium)		
Track–cluster matching	$\Delta\phi$ between the cluster position in the middle layer and the extrapolated track ($|\Delta\phi| < 0.02$)	$\Delta\phi$
	Ratio of the cluster energy to the track momentum	E/p
	Tighter $\Delta\eta$ requirement ($|\Delta\eta| < 0.005$)	$\Delta\eta$
Track quality	Tighter transverse impact parameter requirement ($|d_0| < 1$ mm)	d_0
TRT	Total number of hits in the TRT	n_{TRT}
	Ratio of the number of high-threshold hits to the total number of hits in the TRT	f_{HT}
Conversions	Number of hits in the B-layer (≥ 1)	n_{BL}
	Veto electron candidates matched to reconstructed photon conversions	

4.1.2 Electron identification in ATLAS

In this section are described the identification criteria used in ATLAS to distinguish electrons from fake candidates. The baseline electron identification relies on cuts using variables that provide good separation between isolated electrons and jets (faking electrons). In the central region these variables include calorimeter, tracker and combined calorimeter/tracker information. They can be applied independently and three reference sets of cuts have been defined with increasing background rejection power: *loose*, *medium* and *tight* [77]. Table 4.1 lists all variables used in the *loose*, *medium* and *tight* selections.

Shower shape variables of the EM calorimeter middle layer and hadronic leakage variables are used in the *loose* selection. Variables from the EM calorimeter strip layer, track quality requirements and track-cluster matching are added to obtain the *medium* selection. The *tight* selection adds E/p, particle identification using the TRT, and discrimination against photon conversions via a B-layer hit requirement and information about reconstructed conversion vertices [78]. The cuts are optimized in 10 bins of cluster η (defined by calorimeter geometry,

---

1. Note that the *loose* level of identification in principle does not use any track-to-cluster matching.

detector acceptances and regions of increasing material in the inner detector) and 11 bins of cluster E_T from 5 GeV to above 80 GeV.

Note that during the 2011 data taking a new menu of electron identification selection was implemented. The so-called *robust loose*, *robust medium* and *robust tight* definitions were optimized by considering their robustness for first data with new cuts on the shower shape variables and with new tracking related selections.

4.2   Efficiency and "Tag-and-Probe" Method

The results shown in this section are based on the data collected with the ATLAS detector in the 2011 at $\sqrt{s}$=7 TeV. After requiring good data-quality criteria, in particular those concerning the inner detector, the EM and hadronic calorimeters the total integrated luminosity used for the study is about $5fb^{-1}$.

The efficiency measurements are compared to expectations from the MC simulation. The $Z \rightarrow ee$ MC sample used for these studies is generated with PYTHIA [32] and processed through the full ATLAS detector simulation [79]. The different pile-up configurations during the whole 2011 data taking are taken into account in the MC simulation. The $Z \rightarrow ee$ MC sample was produced using 50 ns LHC bunch spacing, which is consistent with the bulk of the 2011 data.

A measured electron spectrum needs to be corrected for efficiencies related to the electron selection in order to derive correct number of produced physics processes. This correction factor, C, can be obtained as the product of different efficiency terms. For the case of a single electron in the final state one can write:

$$C = \epsilon_{event} \cdot \alpha_{reco} \cdot \epsilon_{ID} \cdot \epsilon_{trig} \cdot \epsilon_{isol}. \tag{4.1}$$

Here ϵ_{event} denotes the efficiency of the event preselection cuts, such as primary vertex requirements and event cleaning, the term α_{reco} accounts for the basic reconstruction efficiency to find an electromagnetic cluster and to match it loosely to a reconstructed charged particle track in the fiducial region of the detector and also for any kinematic and geometrical cuts on the reconstructed object itself, the term ϵ_{ID} denotes the efficiency of the identification cuts relative to reconstructed electron objects, the term ϵ_{trig} stands for the the trigger efficiency with respect to all reconstructed and identified electron candidates. The term ϵ_{isol} is the efficiency of any isolation requirement, if applied.

In the analysis, the MC efficiencies (Eq. 4.1) are corrected to reproduce the efficiencies measured in data. The MC-predicted values of the electron efficiency terms are corrected using *scale factors* defined as the ratios of the data to MC efficiencies which are applied multiplicatively as weight to the MC events depending on the electron E_T and η. The range of validity of such *scale factors* depends on the kinematic parameters of the electrons used in the physics analysis itself.

In this chapter the efficiency in data are measured using the tag-and-probe method. The tag-and-probe method aims to select a clean and unbiased sample of electrons, called *probe* electrons, using selection cuts, called *tag* requirements, primarily on other objects in the event. The efficiency of any selection cut can then be measured by applying it to the sample of *probe* electrons.

The following preselection are applied to obtain a clean sample of $Z \rightarrow ee$ candidates.

- Event is required to pass a set of single electron trigger with a variable E_T threshold

following the different data taking period (namely the *e2*_medium* trigger items [2]).

- Only events passing data-quality criteria, concerning in particular the LAr Calorimeter, and with at least one primary vertex with at least three tracks are considered.

- Only electrons in the central region $|\eta| < 2.47$ which are well-reconstructed and which pass calorimeter quality requirements are selected.

- At least two electrons reconstructed at the *medium* level of identification with $E_T > 20$ GeV should be present in each event.

Figure 4.1: Kinematic distributions of selected $Z \rightarrow ee$ electron probes passing the *medium* and B-layer hit requirements identification cuts for data and MC. Shown are the transverse energy E_T (top left), the pseudorapidity η (top right), the azimuthal angle ϕ (bottom left). The bottom right plot shows the invariant mass m_{ee} obtained combining all the *tag* and *probe* pairs.

After this preselection all possible combinations of the electron candidates in the event are considered to compute the *tag* and *probe* pairs. The *tag* electrons are defined as the electron candidates matching [3] the EF object passing the lowest unprescaled single electron trigger used to select the events. For the *tag* electrons is also required to have $E_T > 25$ GeV, to satisfy the *tight* electron identification cuts and to lie within $|\eta| < 2.47$ excluding the transition region

---

2. where *e2*_medium* is different for the different data period, namely *e20_medium* for period B to K1, *e22_medium* for period K2 and *e22vh_medium1* for the L and M periods (for more details see Appendix A).

3. An offline electron (electron reconstructed and identified with offline analysis program) is considered to match an EF trigger electron if the distance between them in the (η, ϕ) space is $\Delta R = \sqrt{(\Delta \eta^2 + \Delta \phi^2)} < 0.15$

between the barrel and the endcaps ($1.37 < |\eta| < 1.52$).

The number of electron candidates is then independently estimated at the *probe* level applying a invariant mass cut 80 GeV< m_{ee} < 100 GeV.

The efficiency is obtained as the fraction of *probe* candidates passing the cut of interest.
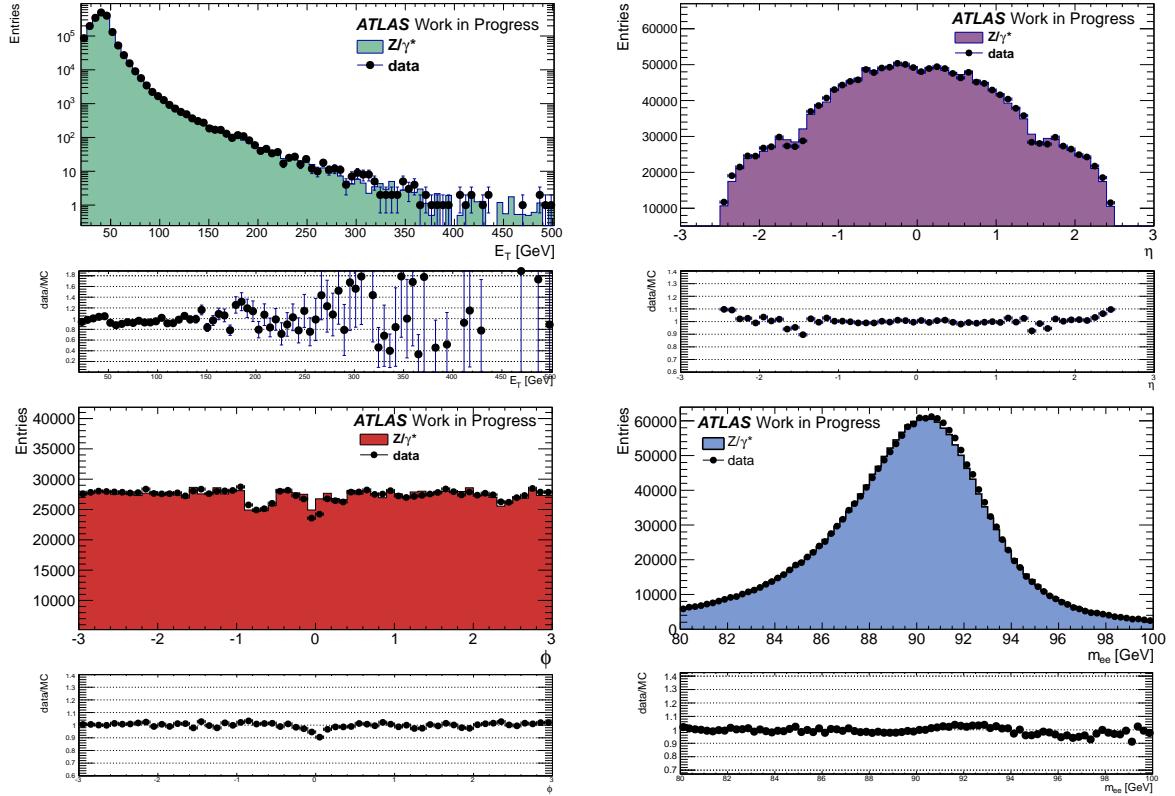
Figure 4.1 shows some kinematic distributions of the selected electron probes passing the *medium* and B-layer hit requirement identification cuts for data and MC, and the resulting $Z \to ee$ candidates invariant mass obtained combining all the *tag* and *probe* pairs.

The *medium* baseline requirement on the *probe* electron candidate increases significantly the purity of the sample. The background fraction of *tight–medium* electron pairs is below 5% in the mass window from 50 GeV to 130 GeV. The level of background in the invariant mass region between 80 and 100 GeV is of the order of 1% and this number remain very small if the selection of the probe candidates is move from *medium* to *medium* plus B-layer hit requirement as can be seen in Figures 4.2, which shows the background fraction after a fit to the data. The fit on the invariant mass distribution of the tag-and-probe pairs is done using a Breit-Wigner convoluted with a Crystal-Ball[4] distribution for the signal and a single sided decay function for the background description. The Breit-Wigner width is fixed to the measured Z width, and the experimental resolution is described by the Crystal Ball function. Therefore because the high purity of the $Z \to ee$ candidates selected no background subtraction is applied to obtain the electrons efficiency measurements at the *medium* level of the electron identification.

(a) *medium* probes   (b) *medium* plus B-layer probes
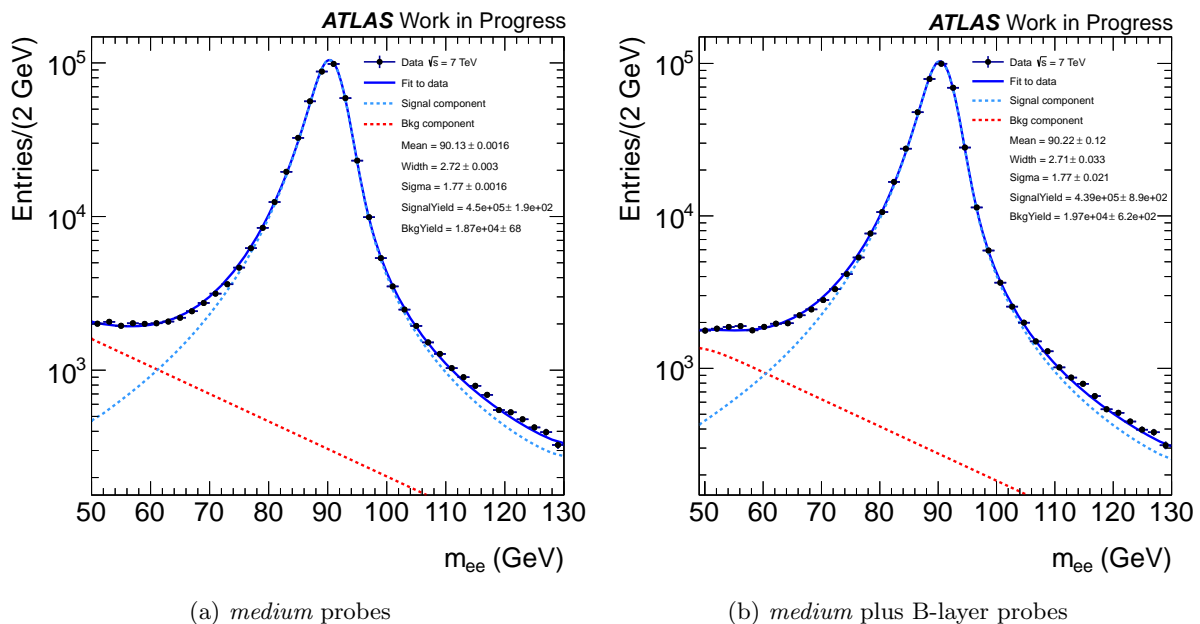
Figure 4.2: The invariant mass distribution in the data of *tag* and *probe* candidates passing the selection criteria described in Section 4.2. The *probe* electrons have to pass either the *medium* (a) or the *medium* plus B-layer hit (b) selection respectively. In the plots the invariant mass distribution is shown as well as the fit results for signal and background individually. The fit was done using a Breit-Wigner convoluted with a Crystal-Ball distribution for the signal and a single sided decay function for the background description

---

4. The Crystal Ball function consists of a Gaussian core portion and a power-law low-end tail

With the full 2011 dataset the electrons efficiency measurements are performed with the tag-and-probe method separately in bins of η and E_T of the *probe* candidates, and the resulting *scale factor* for the MC are derived. The bins in η are adapted to the detector geometry, while the E_T-binning corresponds to the optimization bins of the electron identification cuts.

4.2.1 Electron trigger efficiency

Data-driven methods can be used for the estimation of the trigger efficiency relative to an offline electron selection, which is needed in order to increase the purity of the data sample from which to start. The trigger efficiency is defined as the fraction of *probe* electrons reconstructed and identified with offline analysis program (called offline) "firing" the trigger over all the *probes* passing the offline selection criteria.

In the high-E_T dielectron analysis (details in Section 5.3), events are selected by the *2g20_loose* trigger [5]. The *medium* identification requirement is used as a baseline selection and to suppress the background from photon conversions a hit in the pixel B-layer is also required for each electron candidate.

The electron efficiency of the *2g20_loose* trigger relative to the offline selection defined above is studied with $Z \rightarrow ee$ events in data with the tag-and-probe methodology and the resulting efficiency and *scale factor* are given in the following sections.

Probe selection

As described before the tag-and-probe method consists in selecting a clean sample of $Z \rightarrow ee$ events using well identified *tag* electrons and a dielectron invariant mass cut and then measuring the efficiency of interest using the *probe* candidates. On top of the preselection described in Section 4.2, in each events, once the *tag* electrons are defined, all the other electrons which pass either the *medium* or the *medium* plus B-layer hit requirements and form with *tag* electron an invariant mass between 80 GeV and 100 GeV are regarded as *probe* electrons.

To measure the trigger efficiency, *probe* electrons in the range $E_\mathrm{T} > 20$ GeV are checked for a match to an EF object fulfilling the *2g20_loose* trigger selection. Indeed was verified that the second leg of the *2g20_loose* di-photon trigger is almost 100% efficient with respect to the trigger *tag* matching used in the analysis (for more details see at Appendix C).

The angular distance ΔR between the trigger object and offline electron candidates is required to be smaller than 0.15. This cut results in a 100% matching efficiency.

Since the selected sample has a high purity, no background subtraction is applied. A loose truth matching, in the MC sample, is then applied to reject the residual contamination from the conversions in the material and from conversions of the final state radiation photons.

Results and E_T dependence

The efficiency distributions for data and MC are compared in different bins of η and E_T of the *probe* electrons. Figure 4.3 shows the trigger efficiency for data and for MC as a function of the E_T and η of *medium* and *medium* plus B-layer *probe* electrons for the *2g20_loose* trigger. As expected, the *2g20_loose* trigger is $\sim 100\%$ efficient with respect to the offline selection, in the plateau region starting 5 GeV above the trigger threshold.

It can be seen that in general the MC simultation describe the data reasonably well. Slightly

---

5. which require at least two electromagnetic showers in the calorimeter with a transverse energy of at least 20 GeV (for more details see Chapter 2)
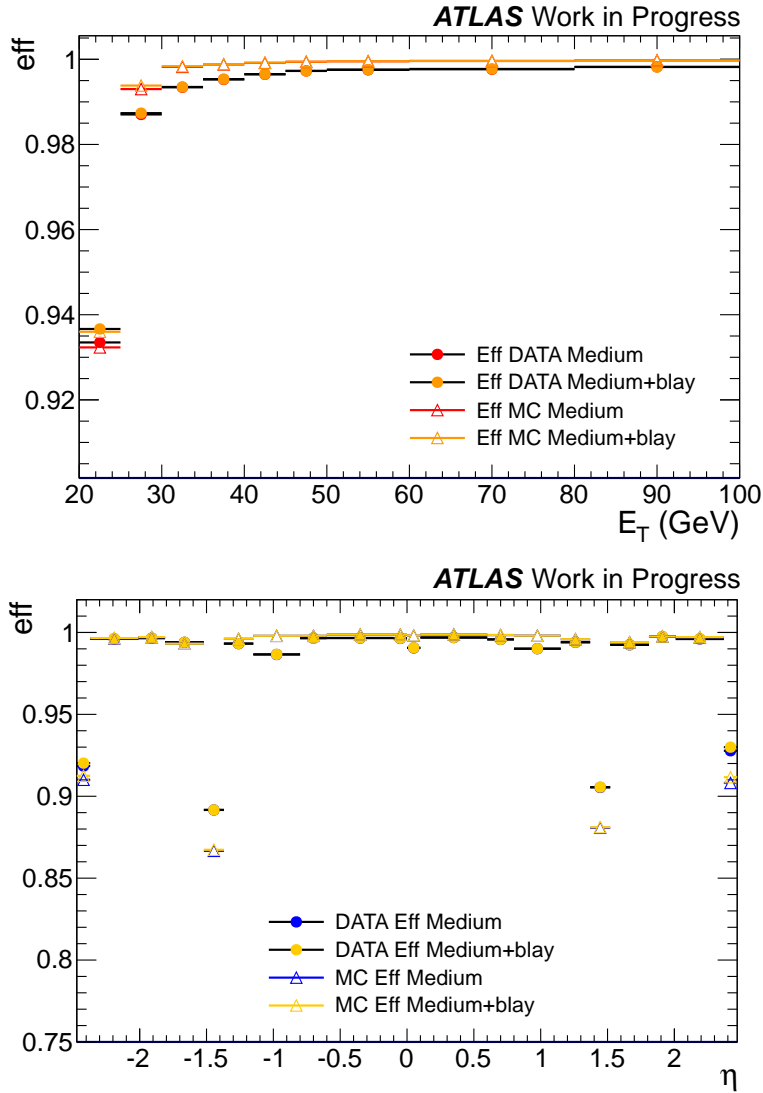
Figure 4.3: Trigger efficiency in data and in MC simulation with respect to *medium* and *medium* plus B-layer hit requirements for *2g20_loose* trigger measured as a function of (top) the electron E_T and (bottom) as a function of η for electron with $E_T > 25$ GeV. The errors evaluated in the plots take into account only the statistical uncertainties.

larger differences occur in the more complicated regions of the detector, for example the region near the barrel-endcap transition, around zero in pseudorapidity or at the end of the acceptance around $|\eta| \approx 2.5$. From this results it is also visible that the trigger efficiency for *medium* and *medium* plus B-layer *probe* electrons is almost compatible in all the E_T and η bins.

Systematic evaluation
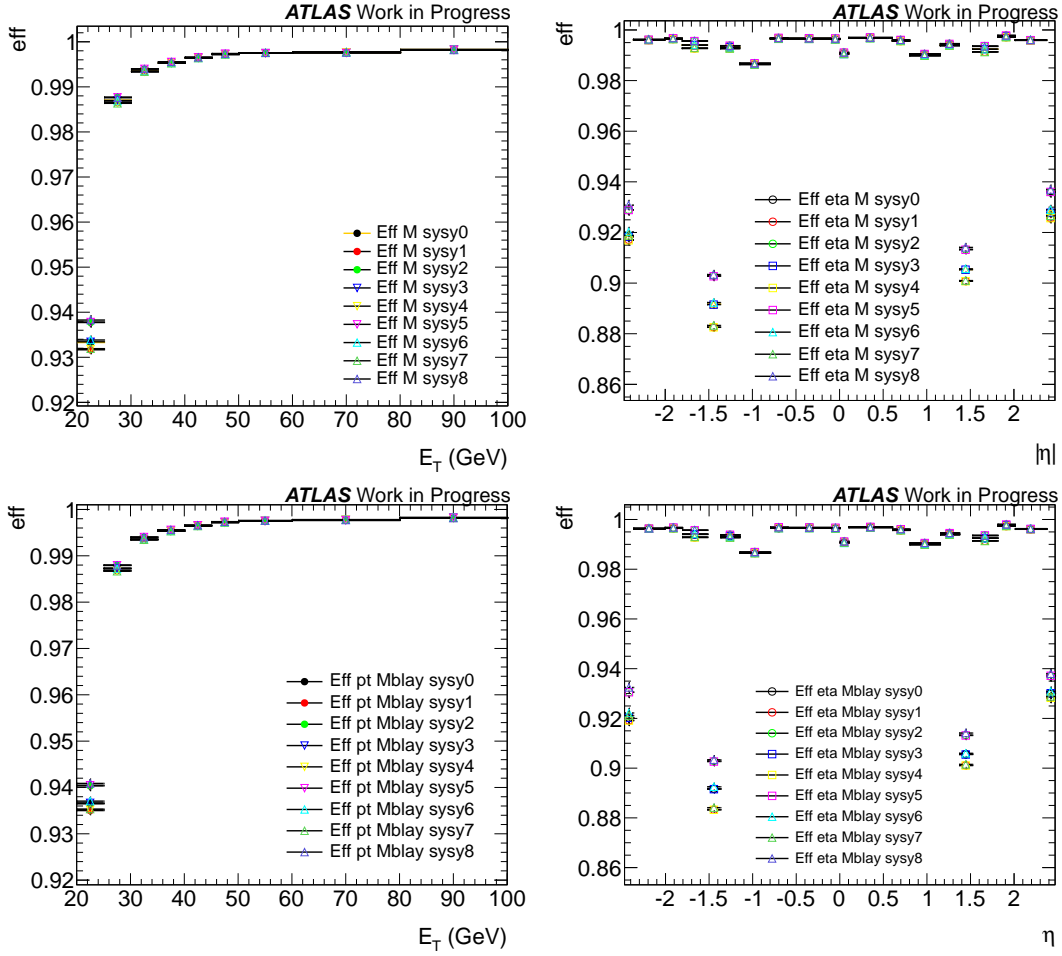
Figure 4.4: Systematic variations on the *2g20_loose* trigger efficiencies measured on data with respect to *medium* (top) and *medium* plus B-layer (bottom) *probe* electrons. Those efficiencies variations are measured as a function of the electron E_T (left) and as a function of the electron η (right). The so called sys7 correspond to the configuration with higher background and weaker *tag* cuts (see Table 4.2 for the details).

Systematic uncertainties related to the *tag* requirements, the choice of the m_{ee} window and the trigger–offline matching requirement have been studied. The effect coming from the variation of the trigger–offline matching requirement was verified to have a negligible impact. Three different variations on the *tag* identification requirement are done:

– *tight*

– robust *tight*

– *medium* plus B-layer hit requirement & Isolation.

The *tight* selection is the reference one. The robust *tight* definition corresponds to a *tight* selection where the identification cuts are tightened and optimized by considering their robustness for first data. In the last variation the *tag* is required to fulfill the *medium* plus B-layer hit requirement definition and satisfy a calorimeter isolation requirement. The details of the different m_{ee} windows choice between the *tag* and *probe* candidates are described in Table 4.2. The effect of the systematic variations on the trigger efficiency is displayed in Figure 4.4.

In each E_T and η bins the difference between the reference selection and each variation is added in quadrature for the computation of the systematic uncertainty for the two offline probes selection. On average the systematic uncertainties are found to be less than 0.5%. The highest variation corresponds to the configuration with weaker *tag* cuts and higher background and is about 1% in the transition region between the barrel and endcap EM calorimeters.

Table 4.2: Systematic variations considered for the analysis. The difference between the central values (sys 0) and each variation is added in quadrature for determining in each E_T and η bins the value of the systematic uncertainty.

Systematic variation	*tag* identification	Inv. mass window
sys 0	*tight*	80 GeV $< m_{ee} <$ 100 GeV
sys 1	*tight*	75 GeV $< m_{ee} <$ 105 GeV
sys 2	*tight*	85 GeV $< m_{ee} <$ 95 GeV
sys 3	robust *tight*	80 GeV $< m_{ee} <$ 100 GeV
sys 4	robust *tight*	75 GeV $< m_{ee} <$ 105 GeV
sys 5	robust *tight*	85 GeV $< m_{ee} <$ 95 GeV
sys 6	*medium* plus B-layer hit & Isolation	80 GeV $< m_{ee} <$ 100 GeV
sys 7	*medium* plus B-layer hit & Isolation	75 GeV $< m_{ee} <$ 105 GeV
sys 8	*medium* plus B-layer hit & Isolation	85 GeV $< m_{ee} <$ 95 GeV

The resulting trigger efficiencies for data and MC integrated in the whole pseudorapidity region are summarized in Table 4.3 together with the data/MC efficiency ratios.

Table 4.3: Efficiencies for the *2g20_loose* trigger, integrated over the full pseudorapidity range $|\eta| < 2.47$ and over electron $E_T > 25$ GeV. The measured data efficiencies are given together with the expected efficiencies from MC simulation and with their ratios. For the data measurements and for the ratios, the error corresponds to a sum in quadrature of statistic and systematic uncertainties. The systematic errors are predominant but always below 0.5%. For the MC expectations, the statistical uncertainties are negligible.

Trigger	Probe	Data [%]	MC [%]	Ratio
2g20_loose	Offline *medium*	98.81 ± 0.37	98.93	0.9988 ± 0.0037
	Offline *medium* plus B-layer	98.84 ± 0.36	98.96	0.9985 ± 0.0036

Scale factor computation

The trigger efficiency *scale factors* (SF) are defined as the ratio of the efficiency measured in data over the efficiency measured in MC for the different η and E_T bins. The resulting trigger SF values are given in Table 4.4 and in Table 4.5 and are shown in Figure 4.5.

Table 4.4: *2g20_loose* trigger efficiency scale factors as a function of different η bins with respect to *medium* and *medium* plus B-layer hit selections. For the uncertainties, statistical and systematic values are taken into account.

η	*medium*	*medium* + B-layer
-2.47,-2.37	1.00920 $\pm$0.02159	1.00849 $\pm$0.02121
-2.37,-2.01	0.99967 $\pm$0.00041	0.99970 $\pm$0.00036
-2.01,-1.81	0.99943 $\pm$0.00054	0.99938 $\pm$0.00047
-1.81,-1.52	1.00081 $\pm$0.00359	1.00088 $\pm$0.00357
-1.52,-1.37	1.02880 $\pm$0.02887	1.02808 $\pm$0.02790
-1.37,-1.15	0.99707 $\pm$0.00141	0.99708 $\pm$0.00142
-1.15,-0.8	0.98859 $\pm$0.00066	0.98865 $\pm$0.00062
-0.8,-0.6	0.99859 $\pm$0.00059	0.99855 $\pm$0.00060
-0.6,- 0.1	0.99785 $\pm$0.00032	0.99790$\pm$0.00029
-0.1,0.0	0.99768 $\pm$0.00050	0.99775 $\pm$0.00047
0.0,0.1	0.99247 $\pm$0.00108	0.99250 $\pm$0.00105
0.1,0.6	0.99812 $\pm$0.00034	0.99811 $\pm$0.00033
0.6,0.8	0.99732 $\pm$0.00065	0.99733 $\pm$0.00062
0.8,1.15	0.99204 $\pm$0.00092	0.99205 $\pm$0.00090
1.15,1.37	0.99810 $\pm$0.00104	0.99813$\pm$0.00098
1.37,1.52	1.02797 $\pm$0.01847	1.02781 $\pm$0.01793
1.52,1.81	0.99837 $\pm$0.00278	0.99837 $\pm$0.00270
1.81,2.01	0.99986 $\pm$0.00090	1.00003 $\pm$0.00087
2.01,2.37	0.99892 $\pm$0.00035	0.99898 $\pm$0.00036
2.37,2.47	1.02164 $\pm$0.01690	1.02010 $\pm$0.01467

In all MC samples each selected electron is corrected to account for data/MC efficiency differences. To factorize the η and E_T dependences with a single correction, for each η and E_T bin the MC simulation is weighted to represent the trigger efficiency in data with a 2D correction defined as:

$$f(\eta, E_T) = \text{SF}(\eta) \times \text{CF}(E_T) \tag{4.2}$$

where the SF(η) are the values of the data/MC efficiency in the different η bins and the CF(E_T) are the so-called *correction factors* computed to take into account the residual SF E_T dependence. To derived the CF(E_T) each bin of the E_T-dependent SF is scaled for the data/MC efficiency integrated over the full pseudorapidity range $|\eta| < 2.47$ and over the electron $E_T > 25$ GeV. The resulting *correction factors* computed for the *medium* and *medium* plus B-layer hit requirements are shown in Figure 4.6.

Comparing the results obtained with *tag* electron matched with *g20_loose* single-photon trigger [6] and *e2*_medium* single-electron trigger (see Appendix C for details) it was verified

---

6. Prescaled to 2Hz for most of the 2011 data-taking

Table 4.5: *2g20_loose* trigger efficiency scale factors as a function of E_T with respect to *medium* and *medium* plus B-layer hit selections. For the uncertainties, statistical and systematic values are taken into account.

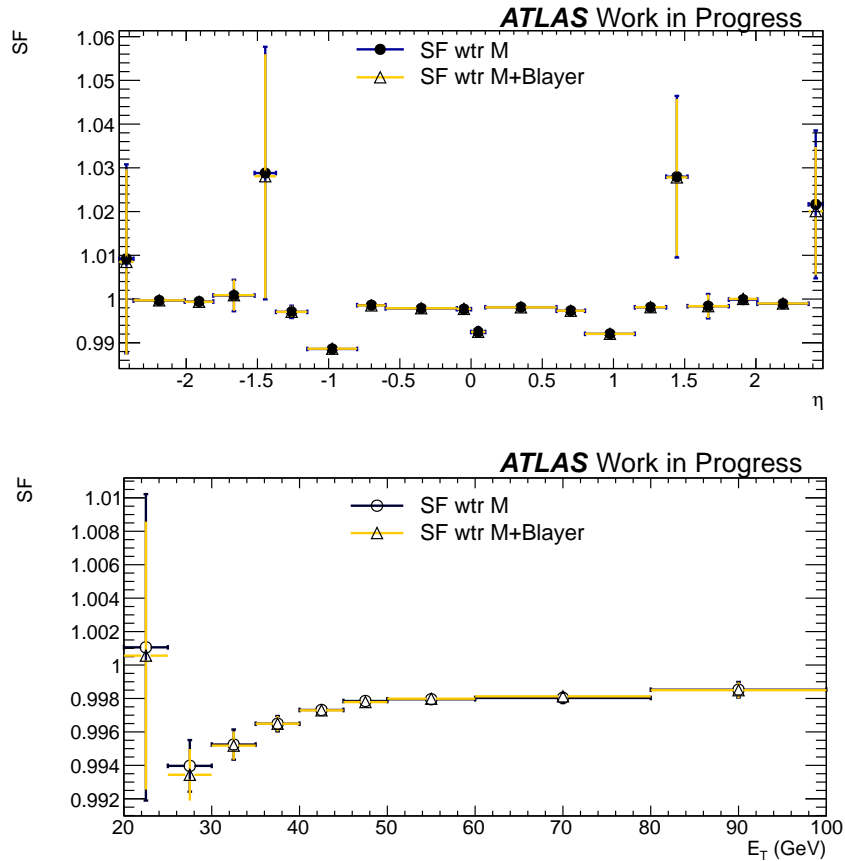| E_T [GeV]	*medium*	*medium* + B-layer
20,25	1.00106 ±0.00916	1.00056 ±0.00801
25,30	0.99397 ±0.00154	0.99343 ±0.00154
30,35	0.99524 ±0.00090	0.99518 ±0.00084
35,40	0.99649 ±0.00046	0.99649±0.00046
40,45	0.99731±0.00021	0.99729±0.00021
45,50	0.99785 ±0.00027	0.99778 ±0.00026
50,60	0.99795 ±0.00017	0.99799±0.00017
60,80	0.99803 ±0.00030	0.99813 ±0.00028
80,100	0.99852 ±0.00046	0.99849 ±0.00047

Figure 4.5: Trigger efficiency SF with respect to *medium* and *medium* plus B-layer hit requirements for *2g20_loose* trigger measured as a function of (top) the electron η and (bottom) as a function of the electron E_T. The errors evaluated in the plots take into account the statistical and systematic uncertainties.
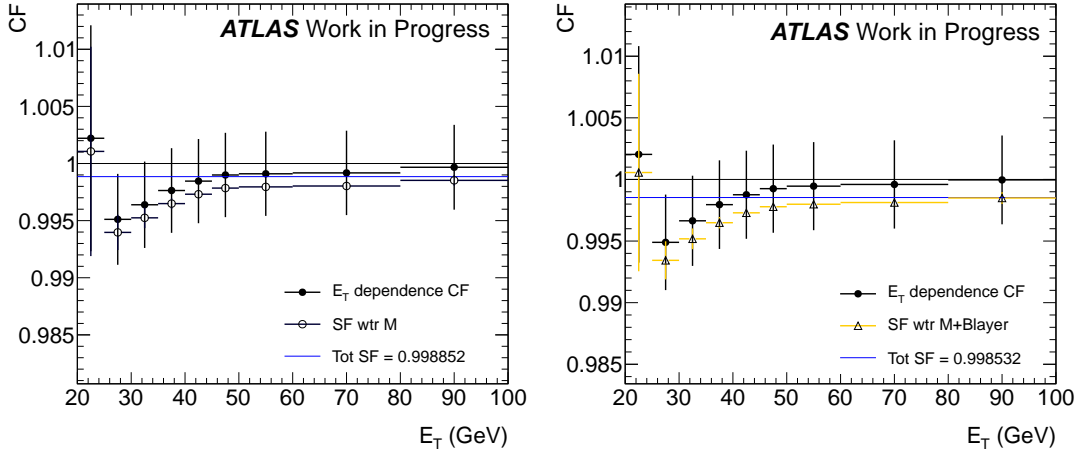
Figure 4.6: *Correction factors* (CF) of the *medium* (left) and of the *medium* plus B-layer hit requirement (right). Each bin of the E_T dependent SF is scaled for the data/MC ratio integrated over the full pseudorapidity range $|\eta| < 2.47$ and over the electron $E_T > 25$ GeV. The errors evaluated in the plots take into account the statistical and systematic uncertainties.

that the second leg of the *2g20_loose* di-photon trigger is 100% efficient with respect to the *tag* matching used in the analysis. Therefore the 2D correction defined above is applied on MC to each dielectron candidate as the product of the single electron correction. To take into account the small residual correlation between the selected electrons and the two legs of the *2g20_loose* trigger, the uncertainties on the single electron correction are added linearly. Anyway the overall average uncertainty is still less then 1%.

4.2.2 Electron reconstruction and identification efficiency

The measurement of the electron reconstruction and identification efficiency is described in Reference [76].

The electron reconstruction efficiency of *sliding-window* clusters in the EM calorimeter is studied by applying the tag-and-probe method to the $Z \rightarrow ee$ and $W \rightarrow e\nu$ decays [7]. The reconstruction efficiency defined in this way measures the combined electron track reconstruction and track–cluster matching efficiencies. Slightly higher values are observed in data with respect to the MC simulation, especially in the region $0.8 < |\eta| < 2.01$ when requirements on the numbers of silicon hits on the track are applied. The globally averaged efficiencies in the full pseudorapidity range of $|\eta| < 2.47$ for data are about 98% for the electron reconstruction, and about 94% including the track silicon hit requirements. The efficiency loss due to requirements on the numbers of silicon hits is less than 3% in the barrel and reaches almost 10% in the highest $|\eta|$ bins.

Also the identification efficiencies for *medium* electrons are measured using $Z \rightarrow ee$ and $W \rightarrow e\nu$ tag-and-probe. In order to correct the MC simulation, E_T and η dependent *scale factors* are derived by the ATLAS electron an photon performance group [80]. The values

---

7. The tag-and-probe method using the W decay, rely on testing the cuts on the *probe* electron candidate, once that a clean sample of $W \rightarrow e\nu$ events is selected applying the *tag* requirement to the high missing transverse energy expected in the events.

of the η-dependent *medium* SF are around 0.96 and the E_T-dependent one around 1.0, with uncertainties of the order of 1%.

In addition to the *medium* identification requirement to further suppress the background many physics analysis, like the Z' and W', require that the electron candidates pass the B-layer hit requirement and the calorimeter isolation cut. Calorimeter isolation is used as a discriminant variable to separate prompt electron and photon (e/γ object) from jets and from non-prompt e/γ object in many analyses. The calorimeter isolation variable, $E_T$coneXX, is defined as the sum of the transverse energy deposition around the electron direction in a cone of size $\Delta R = \sqrt{(\Delta\eta)^2 + (\Delta\phi)^2} < 0.\text{XX}$, where XX is usually 20 or 40 ($E_T$cone20 or $E_T$cone40). The transvers energy from the core of the cone in the electromagnetic calorimeter (5×7 cells around the object barycenter) is then subtracted from the sum.

An ideal isolation variable would include only energy from objects produced in the hard scatter, but in a real detector, there are other effects that contribute to the energy measured in an isolation cone. These effects include calorimeter noise, lateral leakage of the e/γ object into the isolation cone, and calorimeter energy deposits from other collisions in and before the bunch crossing of interest (i.e. pileup). Therefore the $E_T$coneXX variable is corrected for transverse shower leakage and pile-up contribution from additional pp collisions [81, 82].

In this section the tag-and-probe method is used to evaluate the efficiency of additional requirements which are applied on top of the *medium* identification, and the corresponding *scale factor*.

Probe selection and Results

For this analysis all the possible *tag* and *probe* pairs in events passing the preselection described in section 4.2 including the *medium* requirement are considered.

The efficiency of the B-layer requirement is given by the ratio between the number of *probe* candidates which pass the B-layer hit requirement and the total number of *probe* electrons counted in the Z peak region ($80 - 100$ GeV) passing all selections. In the same way the isolation efficiency is evaluated for two different calorimeter isolation cuts, as the number of *probe* electrons which pass the B-layer hit requirement and the calorimeter isolation cut:

 – $E_T$cone20 < 7 GeV or
 – $E_T$cone40 < 9 GeV.

The presence of jets faking electrons under the Z-peak in data after the *medium* selection on both *tag* and *probe* electron candidate is negligible, thus no background subtraction is applied. The biases on the isolation efficiency (with respect to *medium* electron), due to not applying background subtraction are estimated to be below 0.15% and 0.5% in barrel and end-cap respectively. In MC, the matching with generated particle is applied to find the electrons from the Z boson decay.

The identification efficiencies of the B-layer requirement and the B-layer plus either $E_T$cone20 or $E_T$cone40 isolation requirements are shown in Figure 4.7 as function of the *probe* candidates E_T and η. At high electron energy both the isolation efficiencies have a small drop due to increased energy leakage into the isolation cone. For the $E_T$cone40 < 9 GeV requirement the resulting efficiency is lower since a bigger isolation cone is chosen (see Appendix D for details). Anyhow, a good data and MC agreement is shown. The small residual difference in the efficiencies behavior between data and MC at high value of $|\eta|$ could be explain by the differences on the description of the amount of the material at the edge of the Inner Detector in MC. Moreover, due to a residual small shift between the data and the MC $E_T$coneXX distributions, a difference less than 1% between data and MC is seen in the higher E_T bins of
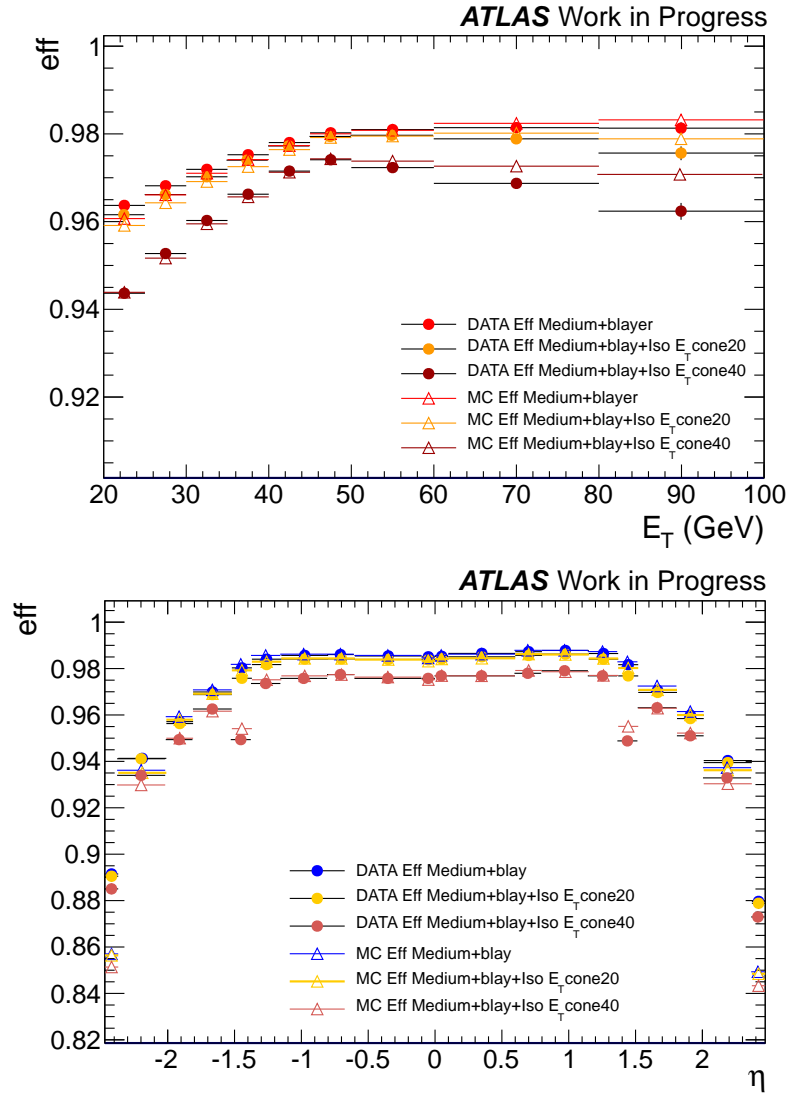
Figure 4.7: Data and MC electron identification efficiencies of the B-layer hit requirement, of the B-layer hit plus $E_T$cone20 isolation requirement, and of the B-layer hit plus $E_T$cone40 isolation requirement. Those efficiencies are measured as a function of (top) the electron E_T and (bottom) as a function of η for electron with $E_T > 25$ GeV. The errors evaluated in the plots take into account only the statistical uncertainties.

the isolation efficiencies (see Appendix D.1 for more details).

Systematic evaluation

Systematic uncertainties are evaluated by varying three mass window choices between the *tag* and *probe* candidates ($[80 - 100]$ GeV, $[75 - 105]$ GeV, $[85 - 95]$ GeV) and three different *tag* identification requirements (*tight*, robust *tight*, *medium* plus B-layer & Isolation). The effect of the systematic variations on the E_T and η identification efficiency distributions is displayed in Figure 4.8. In the same way as for the computation of the trigger efficiency systematic the details of the different variations used are presented in Table 4.2. The difference between the reference result and the result obtained by applying each variation is added in quadrature to determine the systematic value for each η and E_T bins. The largest variation is below 1%.

The resulting integrated efficiencies for data and MC in the whole η range are summarized in Table 4.6 together with the data/MC efficiency ratios.

Table 4.6: Electron Identification efficiencies for the B-layer and the B-layer plus the two isolation requirement taken into account, integrated over the range $|\eta| < 2.47$ and over electron $E_\mathrm{T} > 25$ GeV. The measured data efficiencies are given together with the expected efficiencies from MC simulation and with data to MC ratio. For the data measurements and for the ratios, the error corresponds to the sum in quadrature of the statistic and systematic uncertainties. The systematic errors are predominant but always below 1%. For the MC expectations, the statistical uncertainties are negligible.

Identification	Probe	Data [%]	MC [%]	Ratio
medium	B-layer	97.62 ± 0.23	97.54	1.0008 ± 0.0024
	B-layer & Isolation ($E_T$cone20 < 7 GeV)	97.45 ± 0.38	97.51	1.0006 ± 0.0038
	B-layer & Isolation ($E_T$cone40 < 9 GeV)	96.55 ± 0.51	96.56	0.9998 ± 0.0051

Scale factor computation

To correct the simulation for the residual small differences with respect to data, the identification efficiency SFs are calculated as the ratio of the data over the Monte Carlo efficiency in different η and E_T bins for the B-layer hit requirement and the B-layer hit plus either $E_T$cone20 or $E_T$cone40 isolation requirement. In Figure 4.9 the resulting *scale factors* are shown.
To factorize in a single correction the η and E_T dependence of the computed SFs, for each η and E_T bin a 2D correction is defined as:

$$f(\eta, E_T) = \mathrm{SF}(\eta) \times \mathrm{CF}(E_T). \tag{4.3}$$

Where the remaining small E_T dependence of the SFs is taken into account with the *correction factors*: $\mathrm{CF}(E_T)$. Each bin of the E_T-dependent SF is scaled for the data/MC ratio integrated over the pseudorapidity range $|\eta| < 2.47$ and over the electron $E_\mathrm{T} > 25$ GeV, as is shown in Figure 4.10. The values of the η dependent SF and the resulting *correction factors* as a function of E_T are displayed in Table 4.7 and Table 4.8.
The small falling trend observed in the last E_T bins of the $\mathrm{SF}(E_\mathrm{T})$ and $\mathrm{CF}(E_\mathrm{T})$ distributions was verified to be broken adding two higher E_T bins (Appendix D.2).
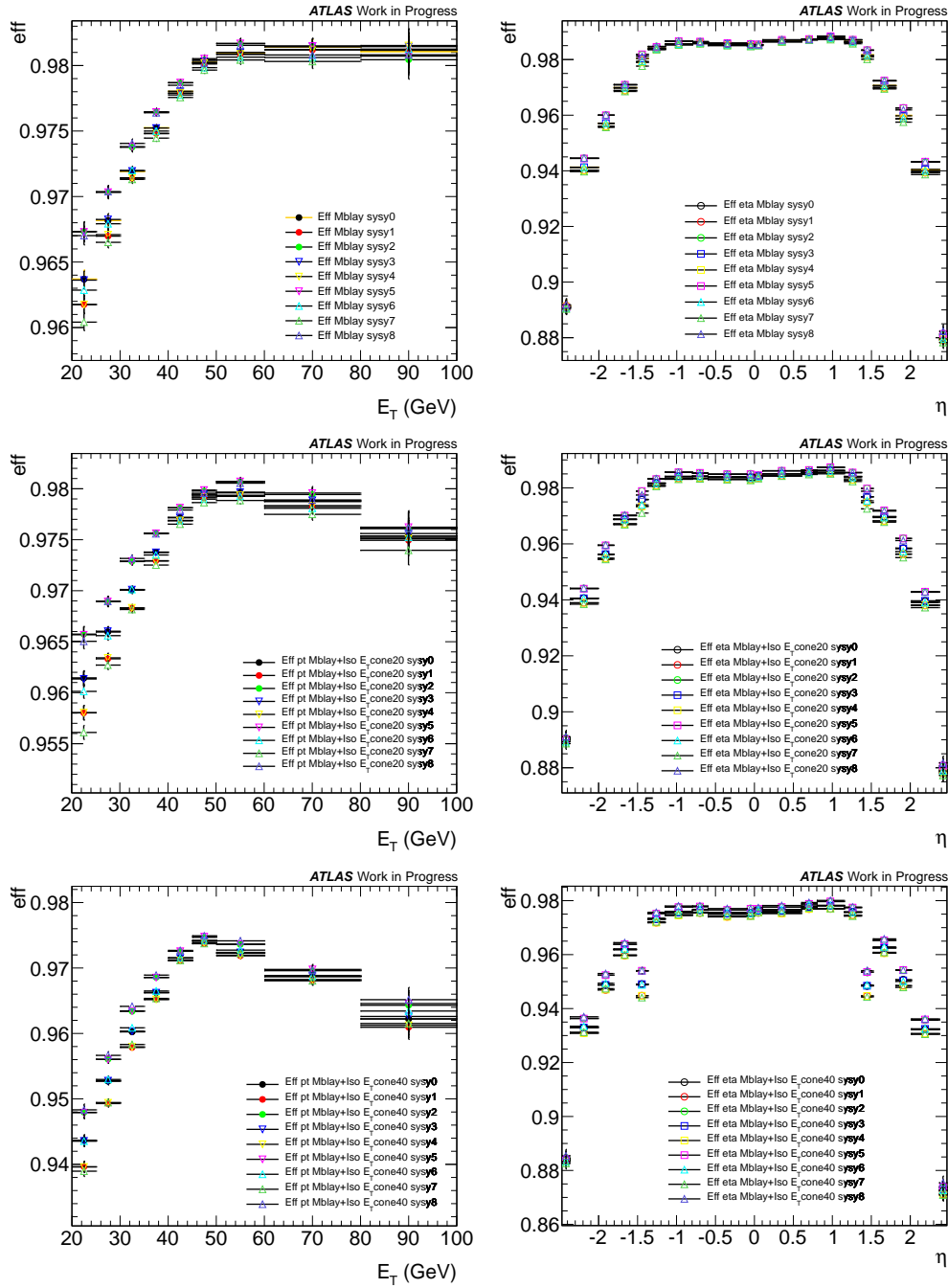
Figure 4.8: Systematic variations on the electron identification efficiencies measured in data with respect to the B-layer hit requirement (top), B-layer hit and $E_T$cone20 isolation requirement (middle), and B-layer hit and $E_T$cone40 isolation requirement (bottom). Those efficiencies variations are measured as a function of the electron E_T (left), and as a function of electron η (right). The so called sys7 correspond to the configuration with higher background and weaker *tag* cuts (see Table 4.2 for the details).
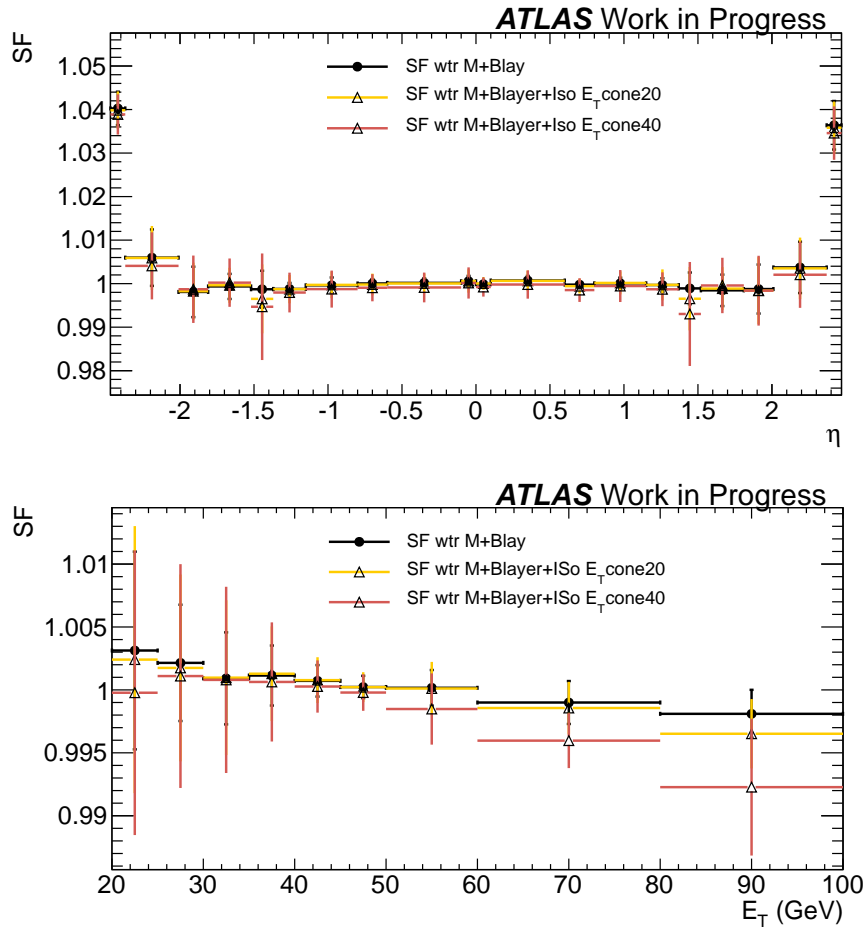
Figure 4.9: SF for the identification efficiencies for *medium* plus B-layer electrons and *medium* plus B-layer and $E_T$cone20 and $E_T$cone40 isolation requirement as a function of the electron η (top) and as a function of E_T (bottom) bins. The errors evaluated in the plots take into account the statistical and systematic uncertainties.
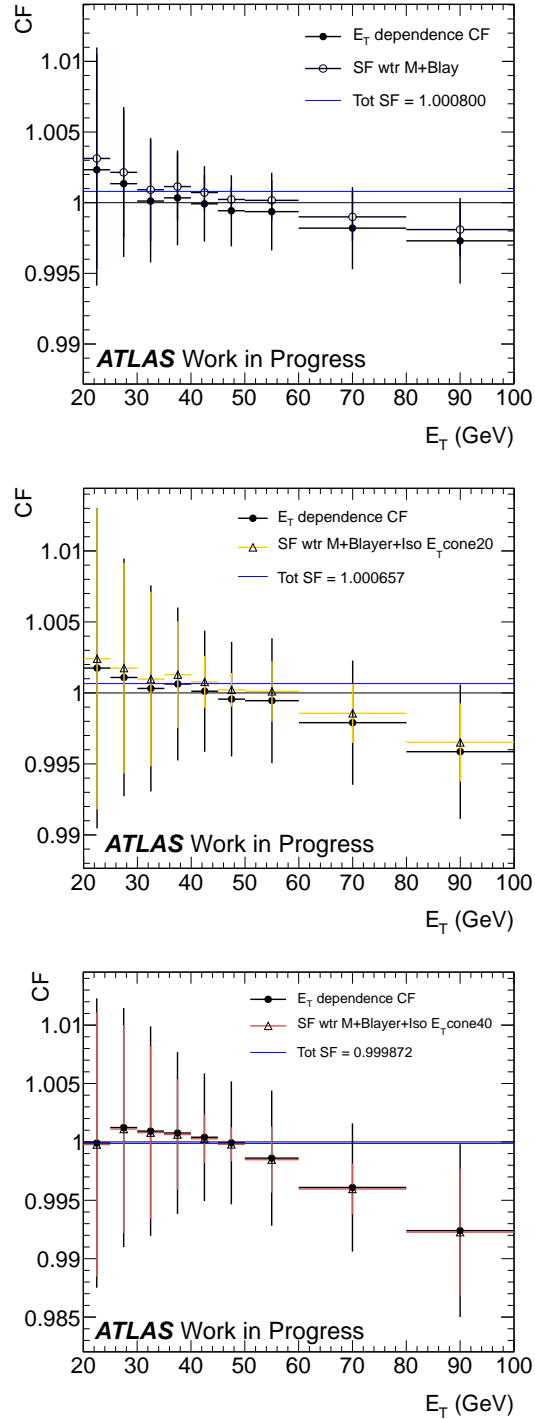
Figure 4.10: *Correction factors* (CF) of the *medium* plus B-layer (top left), B-layer plus $E_T$cone20 isolation (top right), and B-layer plus $E_T$cone40 isolation requirement (bottom plot). Each bin of the E_T dependent SF is scaled for the data/MC ratio integrated over the full pseudorapidity range $|\eta| < 2.47$ and over the electron $E_T > 25$ GeV. The errors evaluated in the plots take into account the statistical and systematic uncertainties.

In the physics analysis the MC simulation is therefore corrected for the product of the *medium* identification and reconstruction SFs and the analysis dependent additional $SF(\eta) \times CF(E_T)$ according to the different level of electron candidate selection as the *medium* plus B-layer hit or the *medium* plus B-layer hit plus isolation requirements. Also the uncertainties are combined and for each η and E_T bin. The total uncertainty is then the square root of the sum in quadrature of the total uncertainty for each component.

Table 4.7: Additional *scale factors* in η for B-layer and $E_T$cone20 and $E_T$cone40 isolation requirements (with respect to *medium* identification). The quoted uncertainties are the sum of systematic and statistical uncertainty added in quadrature.

η	B-layer only	B-layer and $E_T$cone20 isolation	B-layer and $E_T$cone40 isolation
-2.47,-2.37	1.0403 ± 0.0038	1.0398 ± 0.0043	1.0389 ± 0.0046
-2.37,-2.01	1.0060 ± 0.0065	1.0059 ± 0.0074	1.0041 ± 0.0077
-2.01,-1.81	0.9981 ± 0.0058	0.9983 ± 0.0066	0.9987 ± 0.0077
-1.81,-1.52	0.9994 ± 0.0029	0.9996 ± 0.0040	1.0002 ± 0.0055
-1.52,-1.37	0.9987 ± 0.0043	0.9965 ± 0.0079	0.9947 ± 0.0122
-1.37,-1.15	0.9988 ± 0.0014	0.9987 ± 0.0032	0.9979 ± 0.0046
-1.15,-0.8	0.9996 ± 0.0018	0.9997 ± 0.0031	0.9987 ± 0.0042
-0.8,-0.6	1.0000 ± 0.0010	0.9998 ± 0.0025	0.9990 ± 0.0031
-0.6,-0.1	1.0002 ± 0.0010	1.0000 ± 0.0023	0.9991 ± 0.0034
-0.1,0	1.0006 ± 0.0012	1.0006 ± 0.0027	1.0001 ± 0.0036
0,0.1	0.9999 ± 0.0008	1.0000 ± 0.0014	0.9992 ± 0.0022
0.1,0.6	1.0007 ± 0.0011	1.0006 ± 0.0023	0.9998 ± 0.0032
0.6,0.8	0.9998 ± 0.0006	0.9994 ± 0.0017	0.9985 ± 0.0027
0.8,1.15	1.0001 ± 0.0013	1.0002 ± 0.0026	0.9994 ± 0.0037
1.15,1.37	0.9997 ± 0.0015	0.9997 ± 0.0036	0.9987 ± 0.0039
1.37,1.52	0.9989 ± 0.0036	0.9965 ± 0.0073	0.9930 ± 0.0119
1.52,1.81	0.9985 ± 0.0036	0.9989 ± 0.0049	0.9996 ± 0.0063
1.81,2.01	0.9988 ± 0.0056	0.9984 ± 0.0077	0.9984 ± 0.0080
2.01,2.37	1.0037 ± 0.0059	1.0035 ± 0.0071	1.0020 ± 0.0076
2.37,2.47	1.0364 ± 0.0056	1.0358 ± 0.0060	1.0346 ± 0.0061

4.3   Conclusions

The Tag-and-probe method using $Z \rightarrow ee$ decays have been employed to measure the efficiency of different electron reconstruction and identification criteria as a function of η and E_T bins.
Trigger efficiencies have been measured for electrons passing at least the *medium* identification cuts and the *medium* plus B-layer hit requirement. The trigger measurements have confirmed the very high plateau efficiency of the *2g20_loose* trigger.
For the electron identification efficiency additional SF (ratios between measured efficiency in data and predicted efficiency by MC) for the *medium* plus B-layer hit requirement are provided with the precision better then 1%. Additional SF are also calculated for two different isolation

Table 4.8: E_T *correction factors* to the scale factors for B-layer and $E_T$cone20/$E_T$cone40 isolation requirements (with respect to *medium* identification). The quoted uncertainties are the sum of systematic and statistical uncertainty added in quadrature.

E_T [GeV]	B-layer only	B-layer and $E_T$cone20 isolation	B-layer and $E_T$cone40 isolation
20-25	1.0023 ± 0.0082	1.0018 ± 0.0113	0.9999 ± 0.0124
25-30	1.0014 ± 0.0052	1.0011 ± 0.0084	1.0012 ± 0.0102
30-35	1.0001 ± 0.0043	1.0003 ± 0.0073	1.0009 ± 0.0089
35-40	1.0003 ± 0.0034	1.0006 ± 0.0054	1.0008 ± 0.0069
40-45	0.9999 ± 0.0027	1.0001 ± 0.0043	1.0004 ± 0.0055
45-50	0.9994 ± 0.0025	0.9996 ± 0.0040	0.9999 ± 0.0052
50-60	0.9994 ± 0.0027	0.9995 ± 0.0044	0.9986 ± 0.0058
60-80	0.9982 ± 0.0029	0.9979 ± 0.0044	0.9961 ± 0.0055
> 80	0.9973 ± 0.0030	0.9959 ± 0.0047	0.9924 ± 0.0074

requirement $E_T$cone20 < 7 GeV and $E_T$cone40 < 9 GeV and the efficiency measurements have confirmed that there are no significant differences between data and MC in the energy range accessible with data.

Chapter 5

Search for Technihadrons in Dielectron channel

This chapter describes search for resonant deviations from the Standard Model in the high masses of the dielectron spectrum with $\sqrt{s} = 7\,\text{TeV}$ proton-proton collision data collected by the ATLAS experiment in 2011.

The search strategy is based on the ATLAS dilepton analysis described in Reference [83]. The aim of that analysis was to cover as many interpretations as possible of the high-mass dilepton invariant mass spectrum. In this work the same analysis technique is applied to the search of techni-mesons (ρ_T/ω_T, a_T, R$_1$, R$_2$) in the dilepton channel within the two different Technicolor scenarios Low-scale Technicolor (LSTC) and the Minimal Walking Technicolor (MWT), described in the first chapter in Section 1.2.4 and Section 1.2.5 respectively.

As presented in Chapter 1, the LSTC model predicts the existence of several new resonances in the dilepton final state: the nearly degenerate in mass ρ_T and ω_T and the axial technimesons a_T. A search for the technimesons ρ_T and ω_T in the dilepton final state has been performed with the first fb^{-1} of the 2011 data collected with the ATLAS experiment [36]. In that analysis the Sequential Standard Model Z'(SSM Z') search was reinterpreted in terms of the technimesons signal. This was possible because only one TC-resonance (resulting as the sum of the ρ_T and ω_T contributions) has been considered in the spectrum as the mass of a_T was set to $m(a_T) = 10.1 \times m(\rho_T)$ and its contribution was neglected in the dilepton spectrum. Although the SSM Z' resonances have a broader intrinsic width than the ρ_T and ω_T, over the considered dilepton mass range the detector resolution dominates the width of a possible signal. The consistency of the data with MC predictions of Standard Model backgrounds was checked in the dilepton invariant mass spectrum above 130 GeV. In the absence of a significant excess, 95% confidence level limit was set on the LSTC $m(\rho_T/\omega_T) - m(\pi_T)$ parameter space. The ρ_T and ω_T masses were excluded in the range 130-480 GeV and the π_T masses in the range 50-480 GeV. The ATLAS experiment has also recently published [37] a search for resonant WZ production in the first fb^{-1} of 2011 data, and LSTC ρ_T technimesons with masses from 200 GeV up to 467 GeV and 456 GeV are excluded at 95% C.L. for $m_{a_T} = 1.1 \times m_{\rho_T}$ and $m_{a_T} >> m_{\rho_T}$ respectively. The CMS experiment also perform a search within the Technicolor scenario in the diboson final state and has excluded the technicolor ρ_T with masses between 167 and 687 GeV at 95% C.L. [38].

The MWT model, as described in Section 1.2.5, predicts the presence of two technimesons called R_1 and R_2 in the measured dilepton spectrum. The widths and the masses of R_1 and

R_2 change depending on the value of the bare axial mass M_A and the coupling constant $\tilde{g}$ [1]. In this work the dilepton final state is analyzed within the MWT scenario considering different hypothesis on $\tilde{g}$ and M_A. This is the first search of this kind in lepton channel, although reinterpretation of CMS W' result to set limits in MWT exist [38].

This chapter is organized as follows: the Section 5.1 describes the dataset and Monte Carlo samples used for the background and the signal simulation, in Section 5.2 the corrections applied on the signal and Drell-Yan cross-section are presented. Section 5.3 is an overview of the event selection and Section 5.4 presents the background estimation. The systematic uncertainties evaluation is given in Section 5.5 and the statistical methods used for the new resonance search and for the limit setting are explained in Section 5.6. Finally, the results obtained for the LSTC and MWT models are given in Section 5.7.1 and 5.7.2, respectively.

5.1   Dataset and Monte Carlo

5.1.1   Dataset

The data sample used for this analysis was collected in the 2011 ATLAS data taking. The full 2011 ATLAS recorded luminosity corresponds to 5.25 fb^{-1}. Once detector quality selection is applied the integrated luminosity available for this analysis is about 4.92 fb^{-1} and 4.99 fb^{-1} in the dielectron and dimuon channels respectively.
The pile-up conditions varied all along the data taking periods since the LHC beams parameters were changed, in order to increase the machine luminosity. This result in a different number of interactions per crossing between the first half of the dataset (from March-September 2011 e.g periods B to K) and the second half (from September until November 2011 e.g periods L and M) As shown in Figure 5.1 the luminosity weighted average of the number of interactions
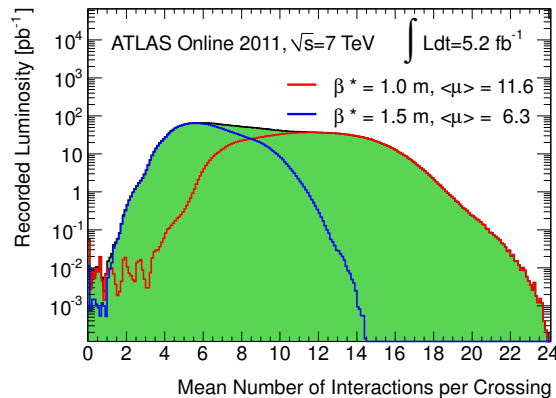
Figure 5.1: The luminosity-weighted distribution of the mean number of interactions per crossing ($< \mu >$) for 2011 data, taken with two different LHC setup

per crossing, $< \mu >$, was ~ 6.3 in the first half and ~ 11.6 in the second half of the data. The different in- and out-of-time pile-up conditions between different data taking periods were reproduced in the Monte Carlo simulation.

---

1. The ratio $g/\tilde{g}$ is phenomenologically very important because it sets the mixing among gauge bosons and technimesons.

5.1.2 Monte Carlo simulation

In this section the signal and the background simulation details are described.
In proton-proton physics, the hard scatter and particle hadronization are simulated in the Monte Carlo (MC) using a number of different software packages. The momentum distribution of constituent particles inside the proton is modeled by the parton distribution function (PDFs). These PDFs can be obtained at different orders of perturbation theory. The same order as the one of the hard-scattering calculation is often chosen.
In ATLAS, the hard scatter is handled by different event generators. The hadronization is handled by PYTHIA [32], or HERWIG [84, 85], and the interaction with the material of the detector and the detector response and reconstruction is fully simulated using GEANT [86] in the ATHENA [87] framework.

Pile-up conditions simulation

Table 5.1: Simulation pile-up conditions according to the data taking period.

Period	L_{int} [pb^{-1}]	$< \mu >$	fraction of data	fraction in MC
B-D	181.2	low	3.7%	3.3%
E-H	993.4	low	20.2%	17.8%
I-K	1229.8	low	25.0%	24.2%
L-M	2509.9	high	51.1%	54.7%

All the MC samples used for this analysis are produced using 50 ns LHC bunch spacing, which is consistent with the bulk of the 2011 data. The pile-up conditions varied in the simulation according to the real data conditions as is shown in detail in Table 5.1 where for "low" is meant $< \mu > \sim 6.3$ and for "high" $< \mu > \sim 11.6$. To account for residual differences between data and MC, the MC simulation is reweighed according the $< \mu >$ value measured in data.

Simulated background processes

Table 5.2 lists all the background MC samples used for this analysis as well as the event generator, the PDFs sets and the order of the corrections applied on the cross-section. The fake dielectron background coming from the misidentified jets and from the semileptonic decays of b and c quarks, referred as QCD multijet background, is taken from data.

In the dilepton resonance search the dominant and irreducible source of background is due to the Z/γ^* Drell-Yan process, characterized by the same final state as the signal. The SM Drell-Yan continuum spectrum accounts for the $\sim 83\%$ of the background events in the search region above 130 GeV and $\sim 99\%$ of total number of background events above 70 GeV.
Drell-Yan samples are generated with PYTHIA using MRST2007LO** PDFs. Inclusive $Z \to ee$ and $Z \to \mu\mu$ samples covering masses above 60 GeV are used to simulate the Z peak. To ensure an adequate statistics at high invariant mass additional samples are generated in dilepton invariant mass bins and used instead of the inclusive sample if the dilepton truth mass is larger

Table 5.2: Monte Carlo background datasets used for the analysis. The event generators, the level of the order of the PDFs calculation and the cross-section corrections applied are also shown.

Sample	Generator	PDF	Correction	σB [pb]
Z/γ^*	PYTHIA	LO**	NNLO QCD,EW K-Factors	989
$t\bar{t}$	MC@NLO [88]+Jimmy [89]+Herwig	NLO	scaled to NNLO cross-section	165
W + jets	Alpgen [90]+Jimmy +Herwig	LO**	scaled to NNLO cross-section	1×10^4
Diboson	Herwig	LO**	scaled to NLO cross-section	70

than 250 GeV. A $Z \to \tau\tau$ sample was also considered to show that its contribution is completely negligible.

The other SM background processes as the diboson (WW, WZ, ZZ) process, W + jets and $t\bar{t}$ with top mass set to 172.5 GeV, are evaluated with the MC simulation rescaled using the most precise available cross-section predictions.

Cross-section value for W, Z are taken from references [91] and [92]. They are performed at NLO and normalized to NNLO in the W + jets case. The theoretical uncertainties are 5% for inclusive diboson production and about 5%-8% for the inclusive W + jets production. Cross-section calculations for $t\bar{t}$ are performed at approximate-NNLO as described in reference [91]. The related uncertainty is $\sim 8\%$.

Dedicated mass dependent NNLO K-Factor are applied to the Z/γ^* cross-section calculations and this treatment is described separately in Section 5.2.

Simulated Signal processes

As described in Section 1.2.4, in the LSTC model it is assumed that techni-isospin is a good symmetry and therefore the isotriplet ρ_T and isosinglet ω_T should be approximately mass degenerate. The ω_T branching ratio to dileptons is approximately an order of magnitude larger than for the ρ_T so the dilepton signal is mostly due to the ω_T particle. It is assumed here that $m(\rho_T) = m(\omega_T)$ and therefore the signal in the dilepton mass spectrum is characterized by two visible resonances: the sum of the ρ_T and ω_T contributions [2], and the axial contribution of the technimesons a_T.

The technifermions branching fraction to a fermion pair is dependent on what other decay channels are available. The other relevant decays involve the π_T and SM weak boson pairs. In the LSTC the expectation is that $m(\rho_T/\omega_T)$ is greater than the $m(\pi_T)$. Therefore values of $m(\pi_T) > m(\rho_T/\omega_T)$ are not motivated theoretically and not considered in this search.

The phenomenology of the LSTC has been implemented in PYTHIA, using the MRST2007LO** PDF [93] [94] as a modification to the Drell-Yan propagator. Therefore PYTHIA generates the LSTC and DY processes together. This fact allows to properly account for the interference between the production of the technivector mesons and the underlying Drell-Yan (DY) process. The production cross-section times branching ratio of the ρ_T/ω_T and a_T to dileptons depends on several theoretical parameters. In this analysis to simulate the signal the PYTHIA default parameters (defined in Section 1.2.4) are used except for the following quantities:

- The charges of the up (U) and down (D) type technifermions $Q_U = Q_D + 1$ is equal to 1.

---

2. Referred as ρ_T/ω_T in the following.

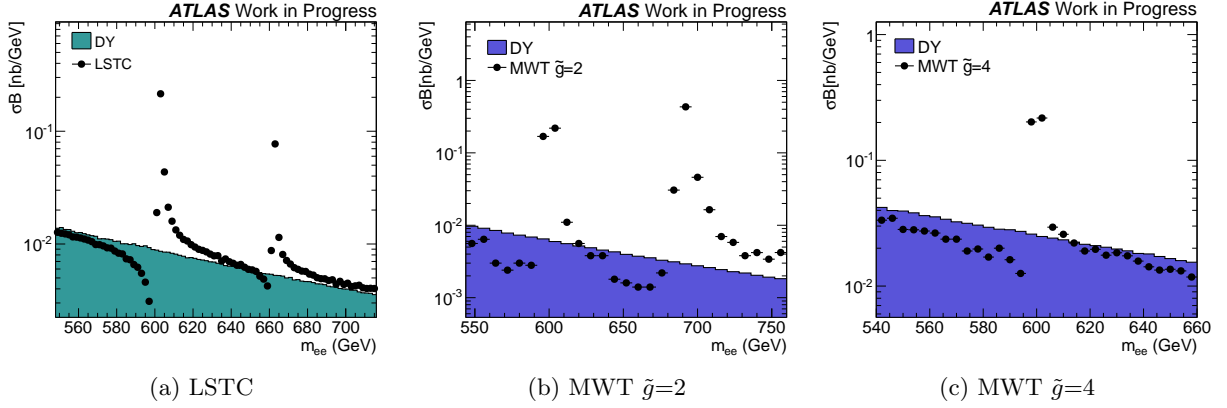(a) LSTC   (b) MWT $\tilde{g}$=2   (c) MWT $\tilde{g}$=4

Figure 5.2: Techimesons line-shape distribution at generator level. (a) The LSTC model with $m(\rho_T) = m(\omega_T) = 600$ GeV and $m(a_T) = 660$ GeV. (b) The MWT model with $\tilde{g}$=2 and $M_A = 581$ GeV, (c) The MWT model with $\tilde{g}$=4 and $M_A = 596$ GeV. In all the plots the filled histogram is the SM Drell-Yan distribution.

- The vector mass parameters M_V is equal to the axial mass parameter M_A and set as $m(\rho_T/\omega_T)$.
- The mass of the a_T is fixed to be : $m(a_T) = 1.1 \times m(\rho_T/\omega_T)$

To minimize the effect of the Drell-Yan contribution while taking into account the interference, the LSTC signal points are generated in a mass window around the peak value of the ρ_T/ω_T and a_T resonances as:

$$[(1 - 10\%) \times m(\rho_T/\omega_T) \; , \; (1 + 20\%) \times m(\rho_T/\omega_T)]$$

Only few ρ_T/ω_T mass points are fully simulated with GEANT in the ATHENA framework,

Table 5.3: List of Monte Carlo technicolor samples (LSTC model) fully simulated within the ATHENA framework. The first two columns give the mass and upper limit on the width of each resonance. The cross-section time branching fraction in dilepton is reported by the generator. Note that those cross-section take into account the LSTC contribution and the SM DY contamination within the $[-10\% \; , \; +20\%]$ interval around the resonances masses (also reported in the table).

Mass(ρ_T/ω_T) [GeV]	$\Gamma(\rho_T/\omega_T)$ [GeV]	Mass(a_T) [GeV]	$\Gamma(a_T)$ [GeV]	$m_{\ell^+\ell^-}$ generator cuts		σB [fb] generated
				Low[GeV]	High[GeV]	
400	< 1	440	< 1	360	480	117.11
600	< 1	660	< 1	540	726	24.26
800	< 1	880	< 1	720	847	7.04
1000	< 1	1100	< 1	900	1210	2.45
1200	< 1	1320	< 1	1080	1440	0.95

assuming the ρ_T/ω_T and π_T mass splitting of 100 GeV. On Table 5.3 the production cross-section times branching ratio for each sample are given as well as the most important generation

parameters.

Figure 5.2a shows the generated dielectron mass distribution for the case where $m(\rho_T) = m(\omega_T) = 600$ GeV and $m(a_T) = 660$ GeV. The interference between the technimesons and the SM DY process is visible in the spectrum as well as the natural width of the ρ_T/ω_T and a_T resonances which results to be less that 1 GeV. The final reconstructed line shape will be dominated by the detector resolution.

Table 5.4: List of Monte Carlo technicolor samples (MWT model) fully simulated within the ATHENA framework. With the $\tilde{g}=2$ hypothesis the first column gives the values of the bare axial mass parameter, M_A. The corresponding mass and width of the R_1 and R_2 resonances are given in the following columns. For each mass point the edges of the generated $m_{\ell^+\ell^-}$ interval are listed. The cross-section time the branching fraction for the MWT in dilepton with the SM DY interference is reported by the generator.

| Mass(M_A) | Mass(R_1) | $\Gamma(R_1)$ | Mass(R_2) | $\Gamma(R_2)$ | $m_{\ell^+\ell^-}$ generator cuts | | σB [fb] |
[GeV]	[GeV]	[GeV]	[GeV]	[GeV]	Low[GeV]	High[GeV]	generated
581	600	1	692	2.5	540	761	141.90
974	1000	1.3	1057	3.7	900	1162	17.23
1223	1250	2.1	1304	5.6	1125	1434	4.36
1474	1500	4.2	1569	8.5	1350	1715	1.08
1725	1750	8.4	1818	1.3	1575	2000	0.27

For MWT model only two resonances are present in the dilepton invariant mass spectrum: R_1 and R_2. Depending on the model parameters R_1 and R_2 are similar to either ρ_T or a_T. At the moment the ω_T-equivalent in the MWT implementation does not exist. As described on Section 1.2.5 the R_1 and R_2 resonances are not necessary degenerate and not necessary very narrow, depending on the M_A and $\tilde{g}$ parameters choice.

The MWT model is implemented in MadGraph4[3]. The CTEQ6l1-LO parton distribution functions are used, and PYTHIA simulate the parton showering and underlying event. Also for this model few R_1 mass points in the two benchmark coupling hypothesis $\tilde{g}=2$ and 4 are fully simulated within the ATHENA framework. For this analysis, the other model parameters are set to their default values: the Higgs boson mass is $m_H = 200$ GeV, the coupling of Higgs boson to composite spin-1 states $s = 0$ and the S-parameter set to $S = 0.3$.

In the MadGraph4 generator it is possible to switch on and off the underlying Drell-Yan process. The DY contribution in the technimesons production is taken to account within a mass windows around the peak value of the resonances:

$$[(1 - 10\%) \times m(R_1) \, , \, (1 + 10\%) \times m(R_2)]$$

Table 5.4 and 5.5, for $\tilde{g}=2$ and 4 respectively, give more details on the mass points which were fully simulated for the MWT model. For low R_1 masses (below 1 TeV) in the $\tilde{g}=4$ benchmark production the 10% mass window generator cut is applied around the R_1 alone. In fact the R_2 technimeson has a wide width and a production cross-section two order of magnitude smaller then R_1, and thus is negligible.

Figures 5.2b and 5.2c show the generated dielectron mass distribution for the case $m(R_1) = 600$

---

3. MWT model implementation in MadGraph: see http://cp3-origins.dk/research/tc-tools

Table 5.5: List of Monte Carlo technicolor samples (MWT model) fully simulated within the ATHENA framework. With $\tilde{g}=4$ hypothesis the first column gives the values of the bare axial mass parameter, M_A. The corresponding mass and width of the R_1 and R_2 resonances are given in the following columns. For each mass point the edges of the generated $m_{\ell^+\ell^-}$ interval are listed. The cross-section time the branching fraction for the MWT in dilepton with the SM DY interference is reported by the generator. Note that in *italic* are reported the values of the mass and width of the R_2 resonance, when its contribution is neglected in the spectrum.

Mass(M_A) [GeV]	Mass(R_1) [GeV]	$\Gamma(R_1)$ [GeV]	Mass(R_2) [GeV]	$\Gamma(R_2)$ [GeV]	$m_{\ell^+\ell^-}$ generator cuts Low[GeV]	High[GeV]	σB [fb] generated
397	400	0.2	*789*	*133*	360	440	118.70
596	600	0.5	*886*	*59.1*	540	660	17.39
794	800	1.2	*1007*	*24.7*	720	880	3.93
993	1000	2.8	1143	10.3	900	1258	1.57

GeV with $\tilde{g}=2$ and 4, respectively.

For both TC models those official samples are used only as a cross-check for signal templates, created from privately generated samples, which cover much better the required parameter space. More details about the use of the signal samples are described in Section 5.6.1.

5.2 Signal and Drell-Yan cross-section corrections
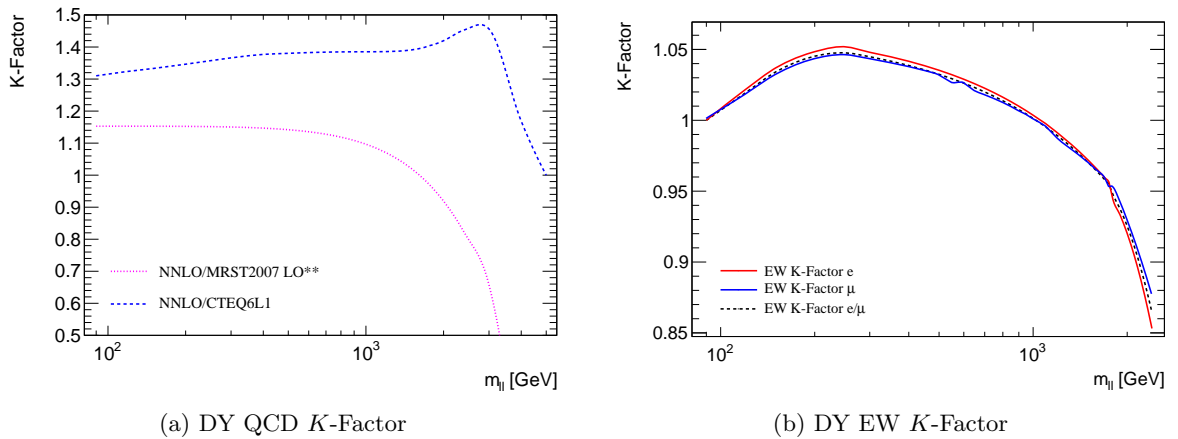

(a) DY QCD K-Factor

(b) DY EW K-Factor

Figure 5.3: Different order QCD K-Factors for Drell-Yan lepton-pair production as function of dilepton invariant mass $m_{\ell\ell}$ (a). The final electroweak mass dependent K-Factor for dielectron and dimuon final state separately and for the dielectron and dimuon case combined (b). The EW K-Factor for electron and muon case combined was considered to be the average of the two.
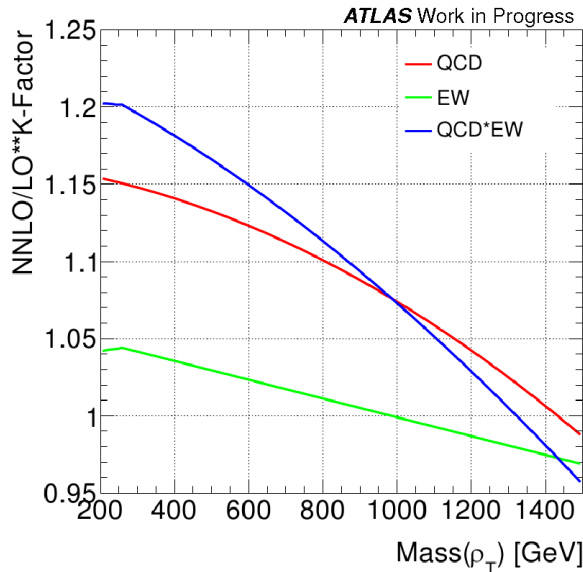
Figure 5.4: Cross section ratios for different ρ_T/ω_T mass giving the QCD, EW and full QCD times EW K-Factors.

In many cases the cross-sections and event kinematics are simulated using leading-order (LO) matrix elements generators and the corresponding PDFs. Whenever possible the results are corrected to higher-order calculation by scaling the LO cross-sections to the next-to-leading-order (NLO) or to the next-to-next-to-leading-order (NNLO) calculations. The scaling factors are called K-Factors.

In this analysis both QCD and electroweak higher-order corrections to the $Z/\gamma^* \to \ell^+\ell^-$ cross-section are applied. Since calculations combining both QCD and electroweak higher order contributions are not available, these corrections are assumed to factorize.

The production of lepton pairs with an invariant mass $m_{\ell\ell}$ via a Z/γ^* boson exchange has been calculated up to NNLO in QCD using various PDF sets and a modified version of PHOZPR [95]. The differential production cross-section ($m_{\ell\ell}^2 \frac{d\sigma_{\text{NNLO}}}{dm_{\ell\ell}^2}$) calculated at NNLO using the MSTW2008NNLO PDF set is used to compute the mass-dependent QCD K-Factor as described in reference [83]. Figure 5.3 (a) shows the mass dependent cross-section rates:

- $K_{\text{NNLO}}(m_{\ell\ell}) = \frac{d\sigma_{\text{NNLO}}}{dm_{\ell\ell}^2} / \frac{d\sigma_{\text{LO}}}{dm_{\ell\ell}^2}$: using the LO PDF sets CTEQ6L1,

- $K_{\text{NNLO}}^{**}(m_{\ell\ell}) = \frac{d\sigma_{\text{NNLO}}}{dm_{\ell\ell}^2} / \frac{d\sigma_{\text{LO}^{**}}}{dm_{\ell\ell}^2}$: using the modified LO PDF sets MRST2007LO**.

The NNLO K-Factor, $K_{\text{NNLO}}(m_{\ell\ell})$ which is based on LO predictions using the CTEQ6L1 PDF sets, increases by approximately 25% for dilepton masses between 100 GeV and 400 GeV and decreases for larger masses. $K_{\text{NNLO}}^{**}(m_{\ell\ell})$, which is based on LO predictions using the modified LO PDF set MRST2007LO**, has only a modest dependence on $m_{\ell\ell}$ over a wide range of dilepton masses but decreases rapidly for masses beyond 1 TeV.

In the analysis the Drell-Yan simulation samples have been generated using PYTHIA and the LO** PDFs, therefore the cross-section ratios K_{NNLO}^{**} define an event specific weight for DY events to obtain a normalization and a dilepton invariant mass shape which is accurate to NNLO.

Similarly, a mass-dependent electroweak correction is defined to take into account the effects of higher-order electroweak corrections beyond the real photons emission included in the

simulation. In fact for the signal and the background simulated samples used in the analysis the QED final state radiation (FSR) is accurately simulated using PHOTOS [96]. The mass dependent higher-order electroweak corrections to the $Z/\gamma^* \rightarrow \ell^+\ell^-$ cross-section, are evaluated using the HORACE event generator [97]. The EW corrections are defined as the ratio of differential cross section predictions at the exact $\mathcal{O}(\alpha)$ calculation (including virtual heavy gauge bosons loop and initial state radiation (ISR) contributions) over the prediction including only QED FSR in the parton shower approximation. Figure 5.3 (b) shows for the dielectron and dimuon final state separately and for the dielectron and dimuon case combined the final electroweak mass dependent K-Factors. Those K-Factors are derived by combining the corrections due to the virtual heavy gauge bosons loop and ISR (obtained with HORACE), and the corrections due to weak boson radiation (following Reference [98]).

The electroweak and QCD mass dependent K-Factors are applied as an event weight to the simulated $Z/\gamma^* \rightarrow \ell^+\ell^-$ samples. Because all the TC signals are generated through the Drell-Yan process, both EW and QCD K-Factors are thus applied to the simulated signal samples and on the expected cross-section (the values of the EW and QCD K-Factors separately and combined are shown in Figure 5.4 for the LSTC signal). Note that the the LSTC and the MWT model are not generated with the same PDFs set, therefore different QCD K-Factor are applied depending on the generated PDFs set.

5.3   Event Selection

In this section the event selection and the details of the analysis are given. The analysis strategy follows the event and electron selection described in reference [83].
The event selection criteria is designed to get a very clean dielectron sample. First of all a good run selection is applied allowing to remove the data where the detector conditions are not sufficiently good to be used in physics analysis. The events have also to pass the $2g20\_loose$ di-photon trigger.
To remove events which are not coming from pp collision data only events with a primary vertex with at least three associated charged particle tracks with $p_\mathrm{T} > 0.4$ GeV are considered.

5.3.1   Electron selection criteria

The selection criteria used for reconstructed electron candidates are chosen to maximize the signal efficiency keeping reasonably low the amount of background.
Only well reconstructed electron candidates (as explained in Section 4.1) in the central region of the Liquid Argon calorimeter ($|\eta| < 2.47$) and which pass calorimeter quality requirements are selected. Electrons reconstructed in the transition region $1.37 \leq |\eta| \leq 1.52$ between the barrel and the endcap calorimeters are excluded in this analysis.
To be selected each event must contain at least two electron candidates with $E_T > 25$ GeV [4] which have to fulfill the *medium* identification criteria. The cut $E_T > 25$ GeV is applied such that the electron reconstruction efficiency is not biased by the trigger selection. To suppress background from photon conversions a hit in the B-layer (first active pixel layer) is required for each electron candidate. To further suppress background from QCD jet production, an isolation requirement on the leading electron (highest E_T) is applied. The calorimeter isolation variable

---

4. The electron energy is obtained from the calorimeter measurement and its direction from the associated track.

$E_T$cone20, defined as sum of the transverse energy deposition around the leading electron direction in a cone of $\Delta R < 0.2$, is required to be below 7 GeV. The core of the electron energy deposition is excluded from the $E_T$cone20 computation and a correction to account for transverse shower leakage and for energy deposition resulting from pile-up interaction is applied as described in References [81, 82].

From MC studies was funded that at very high E_T (E_T range above 1 TeV) the calorimeter isolation variable, after the correction, still has a small E_T dependence from the energy leakage into the isolation cone. Looking at the $E_T$cone20 distribution for electrons in different E_T ranges was verified that the distribution become broader and more sensitive to the isolation requirement. Was also verified that this effect is more prominent on the sub-leading electron candidate, and part of the explanation of this phenomena comes from the bremsstrahlung activities which leaks into the isolation cone giving a lower efficiency. Therefore following those MC studies, in the analysis, to be not affected by possible signal inefficiency at high E_T the calorimeter isolation requirement is applied only on the leading electron candidate.

5.3.2   Dielectron selection criteria

The two highest$-E_T$ electron candidates with an invariant mass greater than 70 GeV passing the selection criteria described above are used to reconstruct the dielectron candidate.

No requirement is made on the opposite electric charges of the two electrons. The reason is to be insensitive to possible charge mis-identification due to bremsstrahlung or to the momentum resolution of the inner detector for very high p_T tracks. Using the high mass Drell-Yan samples, it was found that such a requirement would reduce the signal acceptance by about 4% for a 1 TeV resonance.

Table 5.6: Cut flow for the electron channel for the LSTC signal sample with $m(\rho_T/\omega_T) = 1\,\text{TeV}$ and $m(a_T) = 1.1\,\text{TeV}$, described in Table 5.3.

Selection	Relative efficiency	Absolute efficiency
Trigger and Primary Vertex	87.68 %	87.68 %
Object Quality and acceptance	89.77 %	78.70 %
medium electron requirement	90.79 %	71.47 %
B-layer requirement for both electrons	97.56 %	69.73 %
$E_T$cone20 $< 7\,\text{GeV}$ on the leading electron	98.72 %	68.84 %
$m_{ee} > 70\,\text{GeV}$	99.98 %	68.83 %

Table 5.6 shows the relative and absolute efficiencies of each stage of the event selection described above as determined from a LSTC signal with $m(\rho_T/\omega_T) = 1\,\text{TeV}$. These numbers account for the acceptance and efficiencies of the selections applied on the signal. The acceptance is defined as the number of reconstructed events after the fiducial cuts [5] divided by the number of generated events before any cut. After all the selections the total acceptance times efficiency ($\mathcal{A}\epsilon$) for the LSTC signal generated at 1 TeV is about 69%.

---

5. As fiducial cuts are considered the detector acceptance ($|\eta| < 2.47$ and $1.37 \leq |\eta| \leq 1.52$) and the E_T cut applied on the electron candidates ($E_T > 25$ GeV).

5.3.3 Electron efficiency and energy scale corrections

As describe in Section 4.2 the trigger and the identification electron efficiency are measured in data using the tag-and-probe technique.

In the energy range accessible in data (electrons with E_T up to $\sim$200 GeV) the $2g20\_loose$ trigger efficiency is found to be quite well described by the MC. As described in Section 4.2.1 the $2g20\_loose$ trigger was measured in data to be 99% efficient with respect to the event selection used for electron with high transverse energy and dielectron masses above 100 GeV. Nevertheless, scale factors to correct for the remaining data-MC discrepancy at the *medium* plus B-layer event selection stage, are derived as a function of both η and E_T. They are applied on MC as the product of each single electron value, and it is assumed that the good agreement between data and MC trigger efficiencies extends to electrons with $E_T > 200$ GeV.

Measurement of the electron reconstruction and identification efficiencies in data and MC have shown small differences in the η and E_T distributions (details in Section 4.2.2). To account for these differences weights are applied to the Monte Carlo events as the product of the data/MC ratio in each η and E_T bin for the leading (highest E_T) and and sub-leading (second highest E_T) electron. The final MC weights are, therefore, the combination of the electron reconstruction and identification SF at the *medium* level and the additional scale factors to account for the efficiencies of the B-layer and the B-layer plus isolation requirements.

With the tag-and-probe procedure only electrons with E_T up to 100-200 GeV can be probed. No hint of relevant efficiency drop with E_T is observed in data in this range. Using MC simulation was verified that the full selection efficiency is flat with E_T in all η bins up to transverse energies of about 1 TeV, far above the highest E_T observed in data (600 GeV). Above 1 TeV, a small drop in efficiency is due to the isolation selection, which has some remaining E_T dependence in spite the isolation corrections. While the combined efficiencies are well behaved, the isolation requirement on the leading electron by itself introduces an efficiency drop of about 1% for transverse energy above 1 TeV. Overall, this drop is balanced by the rising efficiency of the other requirements but was verified to have a small impact on the full selection $\mathcal{A}\epsilon$ distribution as function of the dilepton mass. Conservatively a mass-dependent systematic uncertainty is quote of about 2% due to the isolation efficiency. This value was obtained looking at the ratio of the mass-dependent $\mathcal{A}\epsilon$ distribution of the full selection with the isolation requirement to the one without the isolation requirement in the simulated DY samples up to invariant mass of 3 TeV.

At the energies relevant to this analysis, the resolution is dominated by the constant term, denoted c in the following parametrization: $\sigma(E)/E = a/\sqrt{E} \oplus b/E \oplus c$, where $\oplus$ represents addition in quadrature, and E is the energy in GeV. The latest constant term values measured in data using $Z \rightarrow ee$ events, are $(0.97 \pm 0.02)\%$ in the barrel and $(1.64 \pm 0.06)\%$ in the endcaps [99] where the error are statistical only. In this analysis the simulation is adjusted by smearing the energy to reproduce the resolution measured in data. Furthermore the data energies are also corrected to take into account the in-situ calibration measurement performed using $Z \rightarrow ee$ decays. All these corrections are derived from data at energies basically below 200 GeV. The behavior of high energy electrons is of particular importance to this analysis thus Monte Carlo-based studies verified that energy resolution are expected to improve with increasing energies (for the details see Appendix E.1).

5.4   SM Background estimate

All backgrounds are modeled using Monte Carlo simulation except the QCD multijet background which is estimated from data using a "reversed electron identification" technique [100]. The Z/γ, the diboson, the W+jets and the $t\bar{t}$ process, also denominated as non-QCD background, are obtained from MC simulation. The non-QCD backgrounds dielectron mass template is derived by adding the MC contributions according to their cross-section. Data with both electron candidates passing the *loose* identification requirement but failing one of the *medium* identification criteria are used to determine a template shape for the dielectron mass distribution of the QCD background. The difference in η between the cluster and the matched track is the fail-*medium* requirement applied on the electron candidates. Events with candidate electrons satisfying this fail-*medium* requirement are dominated by QCD processes but this feature is not unique to those processes. Therefore the same selection is ran on the non-QCD background and their contribution is subtracted to the template derived from data [6].
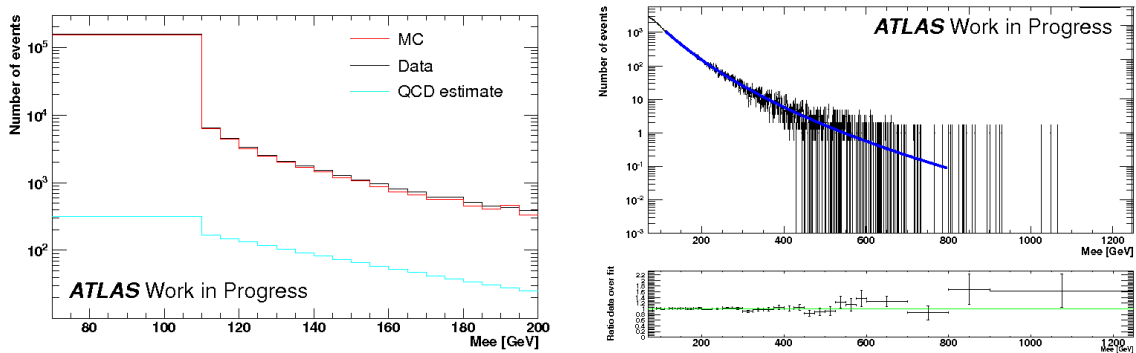

Figure 5.5: Left plot: Results of the normalization template fit performed on the data and on the QCD and non-QCD background templates. The red line represent the non-QCD backgrounds, the black one the data and the blue line the QCD template. Right plot: The QCD data template obtained with a fail-*medium* requirement corrected for the non-QCD backgrounds, fitted in the range 110 to 800 GeV with the ratio data over fit in a coarser binning.

In order to get the correct relative contributions between the QCD background sample, defined above, and the non-QCD backgrounds a template fit to the data in the mass range 70 to 200 GeV is done. This fit exploits the shape difference between the MC template shape, which is dominated by the Z peak [7], and the more flat QCD shape. The resulting relative contributions of the QCD and non-QCD backgrounds in the m_{ee} distribution are shown in Figure 5.5 (left). The template fit gives a 19% uncertainty on the QCD yield. Additionally the impact of a variation of the Drell-Yan cross-section within its uncertainty of $\pm 5\%$ was evaluated and found to be 6% on the fraction of resulting QCD events. Those two uncertainties added in quadrature reflect the normalization uncertainty.

The QCD sample obtained with this data driven estimate run out of statistic in the high invariant mass region (above 800 GeV), therefore the QCD shape is extrapolated beyond 200 GeV

---

6. The main contribution come from misidentified electrons candidates beneath the Z resonance peak

7. To be not sensitive to mis-shaping of the Z peak in the MC a single bin accounts for the whole Z peak range.

using an empirical function,

$$f(x) \;=\; p_1 x^{p_2 + p_3 \log x} \tag{5.1}$$

fitted in the 110 - 800 GeV range (Figure 5.5 (right)). The largest variation of different fit ranges is taken as systematic uncertainty of the extrapolation at high mass. The "reversed electron identification" method, described above, provides the template and the baseline QCD multijet estimate in the following.

In this analysis, in order to be unaffected by the uncertainty on the luminosity or by any other mass-independent uncertainties, the background is normalized to data beneath the Z peak in the mass range 70 to 110 GeV. For this purpose, all the background components are summed together (preserving the fraction of the QCD multijet and the non-QCD backgrounds) and then rescaled so that the sum matches the observed number of data events in the normalization region, defined as the 70 - 110 GeV mass interval. A normalization factor of 1.039 is found.

5.4.1 Data MC comparison

Figure 5.10 shows the p_{T} and rapidity distributions of the dielectron pairs. Data and MC agreement is checked with control plots for the electrons variables used in the the signal selection on this analysis.

The data/MC comparison in the η, ϕ and E_T distribution of leading and subleading electrons is shown in the control region, $m_{ee} > 70\,\mathrm{GeV}$ (in which the Z peak is included), as well as for high invariant mass candidates, $m_{ee} > 150\,\mathrm{GeV}$.

Figures 5.6 and Figures 5.7 show the η and ϕ distributions of the two electrons respectively for the whole invariant mass range and for electrons with an invariant mass above 150 GeV. To note that in the ϕ distribution the small hole in the data and MC distributions centered around -0.7 is due to a residual contribution of the defect of six LAr calorimeter FEB due to an hardware problem present in about 0.99 fb^{-1} of data. This small hole corresponds to 0.8% of the total ϕ coverage and in both data and MC this bad detector region is taken into account by applying a detector quality flag.

Figure 5.8 shows the E_T distribution of the leading (highest E_T) and sub-leading (second highest E_T) electrons after full event selection and for high invariant mass candidates ($m_{ee} > 150\,\mathrm{GeV}$). Figure 5.9 shows the isolation distribution for the leading electron after full event selection but without the isolation cut, and for the sub-leading electron after the full selection.

In Figure 5.11 the observed invariant mass distribution is compared to the SM expectation, given by the Monte Carlo simulation for all components except the QCD multijet one, which is taken from the data, as described in Section 5.4. At very high masses, the statistical significance of the MC simulation for the diboson, $W +$ jets and $t\bar{t}$ samples becomes insufficient. Therefore their invariant mass distribution is fitted to a functional form which is then used to extrapolate the $t\bar{t}$ and the $W +$ jets background above 0.8 TeV and the diboson background above 1.5 TeV. To note that for the diboson background component, the extrapolation is used above a higher value of invariant mass because different MC samples binned in dilepton invariant mass are used. This allows to have enough MC statistic up to 1.5 TeV.
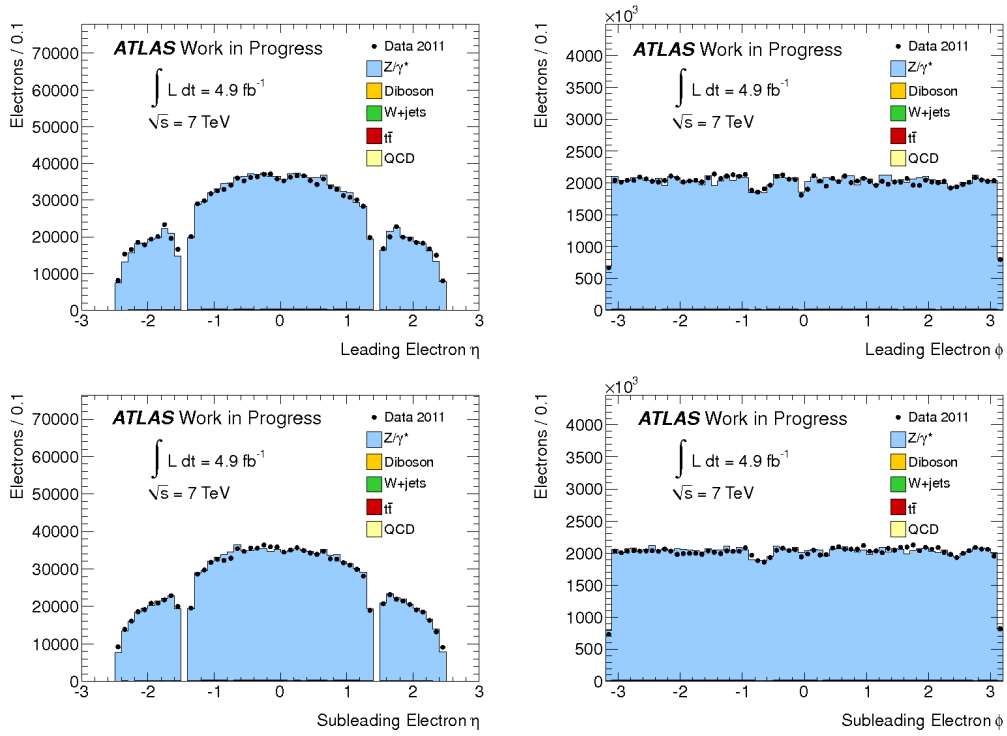
Figure 5.6: η and ϕ distributions for the leading electron and sub-leading electron after event selection.
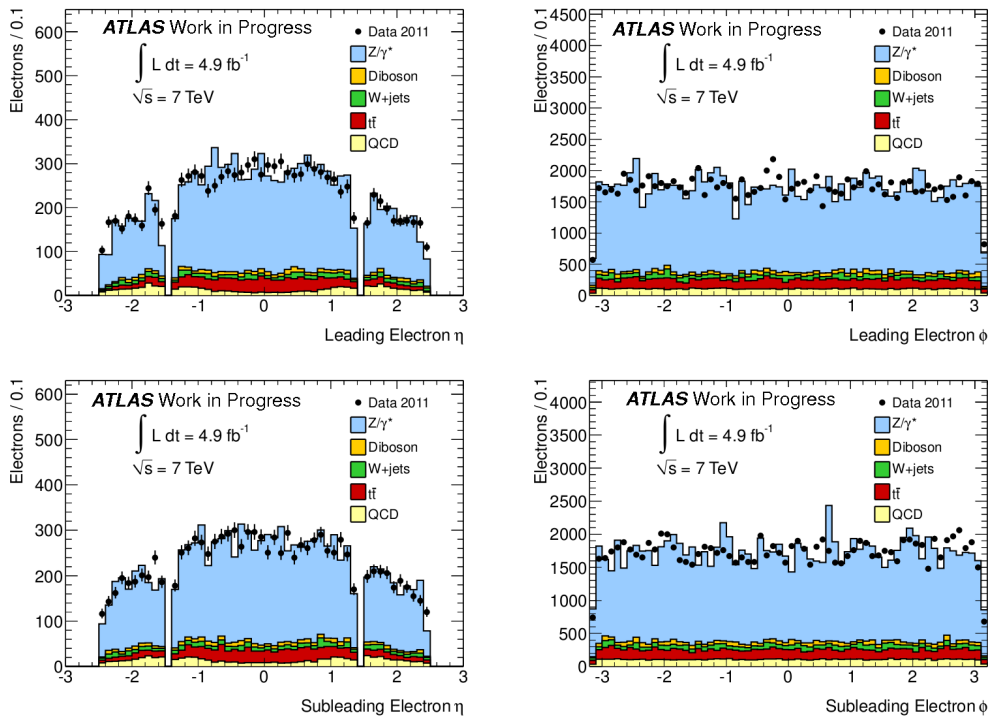

Figure 5.7: η and ϕ distributions for the leading electron and sub-leading electron after event selection and $m_{ee} > 150$ GeV.
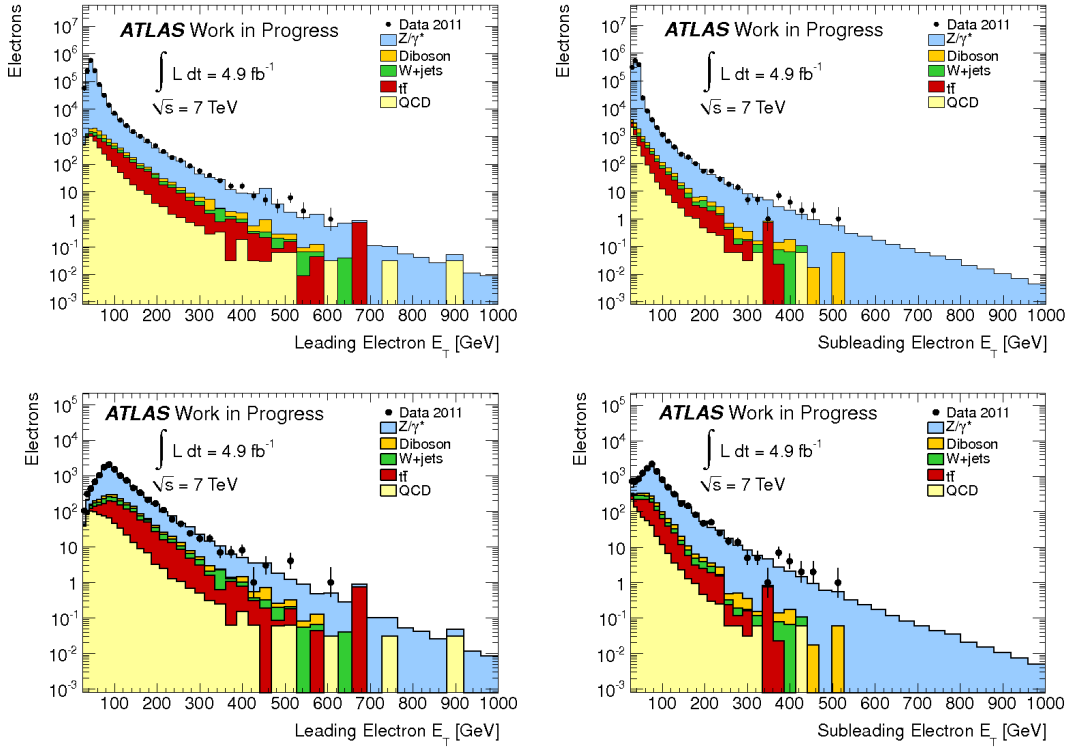
Figure 5.8: First raw: E_T distribution for the leading (left) and sub-leading (right) electron after event selection. Second raw: E_T distribution for the leading (left) and sub-leading (right) electron after event selection and $m_{ee} > 150$ GeV.
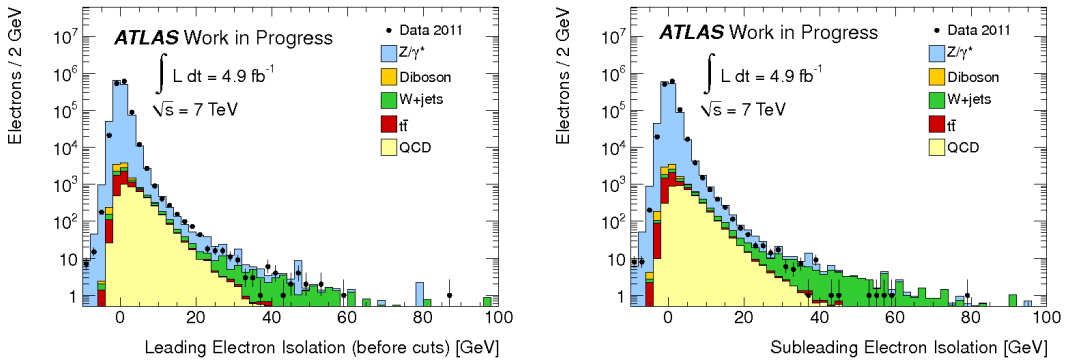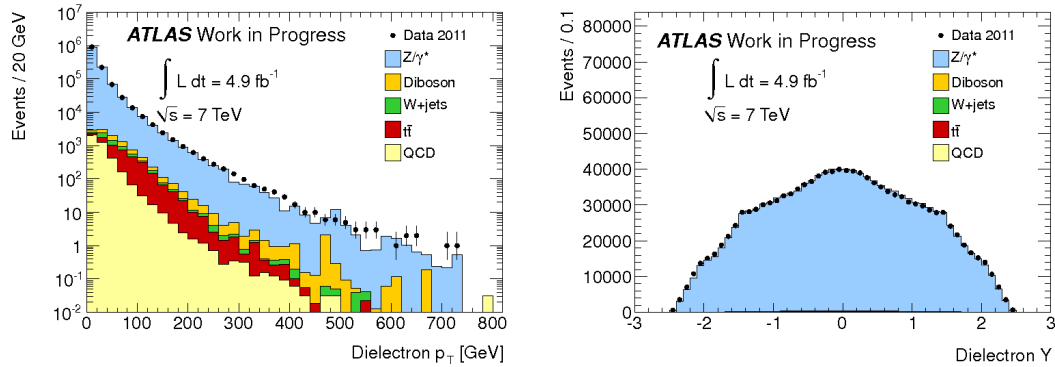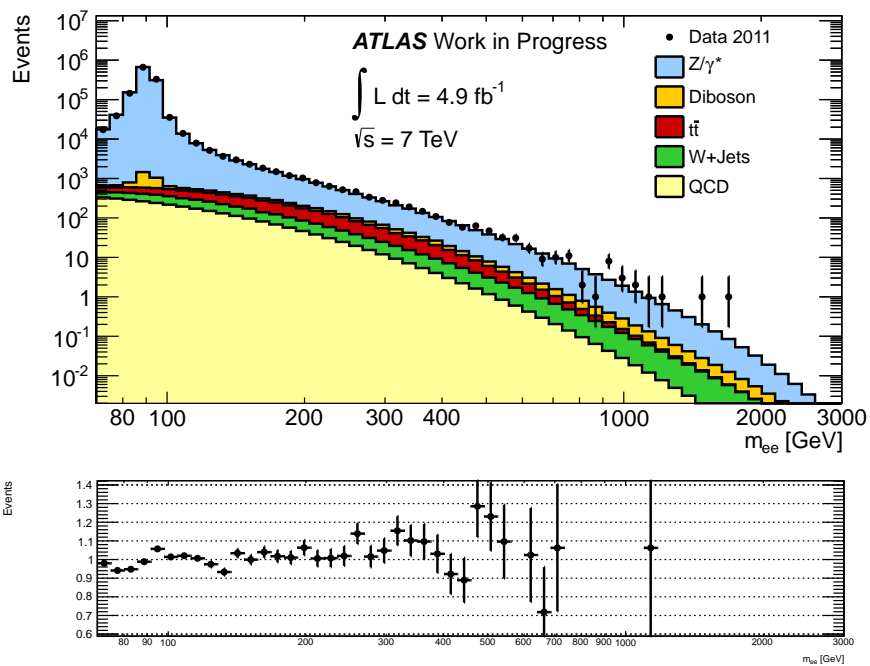

Figure 5.9: Corrected calorimeter isolation ($E_T$cone20) for the leading electron after the full event selection except the $E_T$cone20< 7 GeV selection (left) and sub-leading (right) electron after all event selection.

Figure 5.10: Dielectron p_T and rapidity after event selection.

Figure 5.11: Dielectron invariant mass (m_{ee}) distribution after event selection for the 2011 data and the SM backgrounds overlaid.

5.4.2   Dielectron m_{ee} spectrum

In the dilepton analysis describe in Reference [83] three other multijet background estimation techniques are used to cross-check the "reversed electron identification" method described in Section 5.4. The first technique is another shape-fitting procedure on the two-dimensional (leading and sub-leading) electron isolation distributions in bins of m_{ee}. The second is an independent data-driven multijet estimate based on fake rates computed from jet-enriched samples obtained from jet triggers. The third and last method is also computes fake rates, but from the electromagnetic-cluster trigger used for the signal. Since all the other data-driven techniques do not provide separate estimate for the multijet and the W + jets contributions, to compare the results from the different methods the QCD multijet estimate obtained with the reversed identification method is summed with the Monte Carlo prediction for the W + jets yield. All the multijet data driven estimates were verified to be compatible. In the dilepton analysis, the final estimate of the multijet and W + jets background component is taken as the mean of the central values of three different methods. The combination of the reverse identification and the
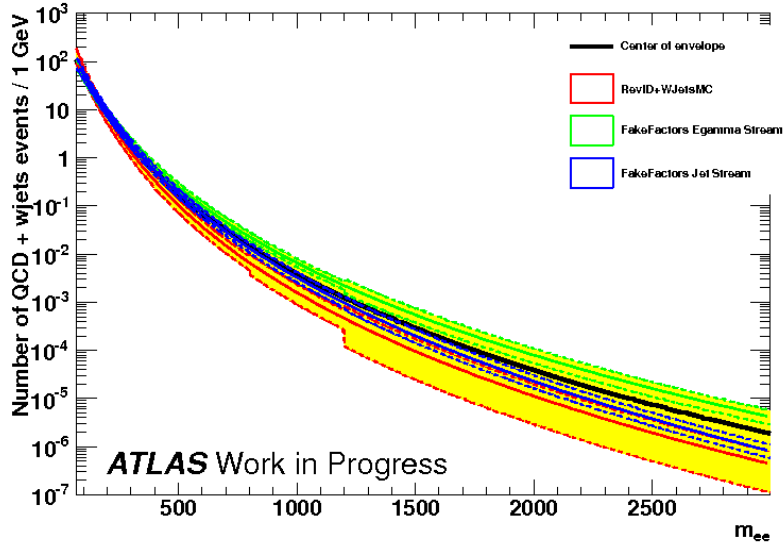

Figure 5.12: Combination of the QCD plus W + jets via the background envelope method as is done in Reference [83]. The central value of the envelope is shown in black with the yellow error band. The separate methods are shown as colored lines with their uncertainty band shown with dashed lines in the same color.

two fake rate methods is done via averaging the central values and taking as uncertainty the envelope of the largest deviation up and down of each method as is shown in Figure 5.12.
Table 5.7 shows the number of observed and expected events in bins of reconstructed m_{ee} with both statistical and systematic uncertainties for all the background components considered. Finally the invariant mass of the electron pairs distribution for the data, the expected SM background and different technicolor signals overlaid is shown for illustration in Figures 5.13. Note that in those plots the fully data-driven techniques which provides combined estimates of the multijet and W + jets contributions is shown.

(a) LSTC

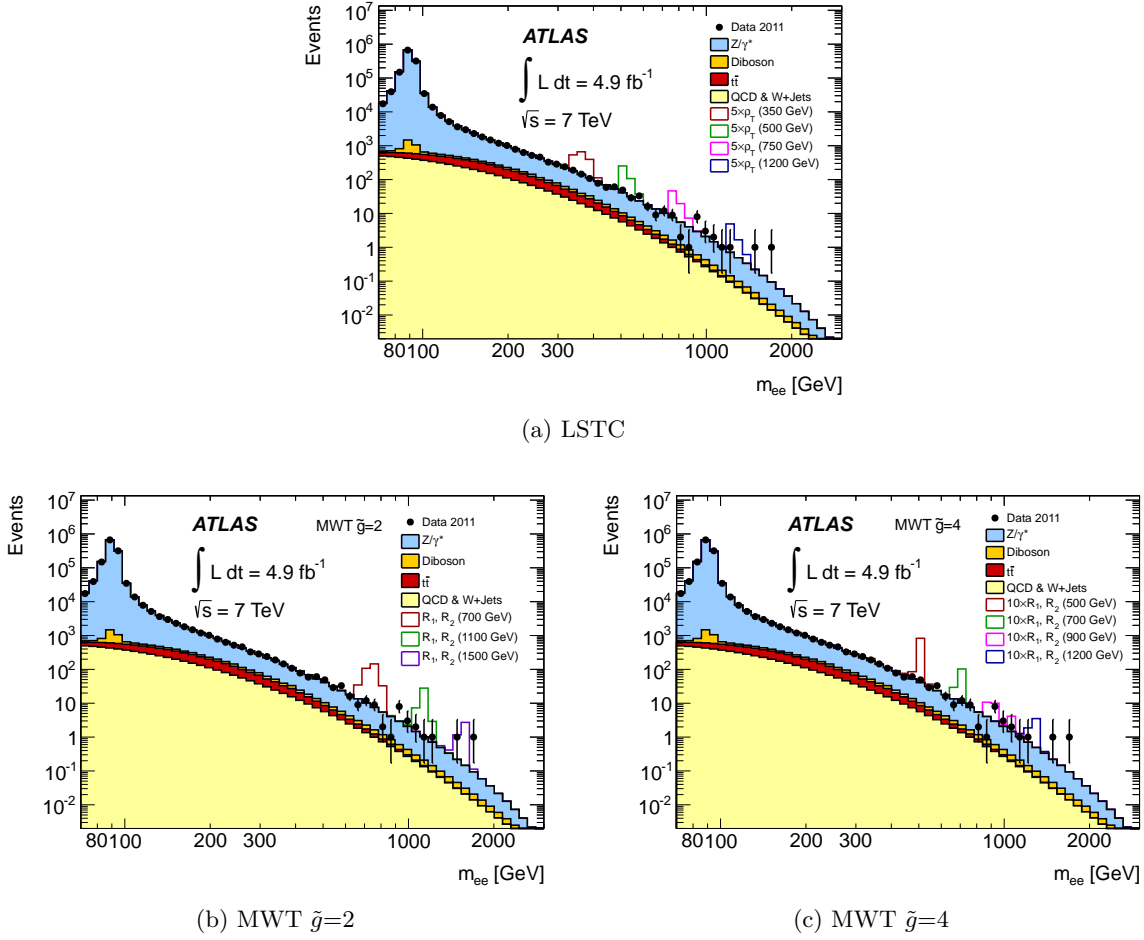(b) MWT $\tilde{g}=2$

(c) MWT $\tilde{g}=4$

Figure 5.13: Dielectron invariant mass (m_{ee}) distribution after event selection for the 2011 data and the SM backgrounds overlaid. (a): m_{ee} distribution where four different LSTC signals are overlaid. (b) and (c): m_{ee} distribution where different MWT signals are overlaid for $\tilde{g}=2$ and $\tilde{g}=4$ hypothesis respectively.

Table 5.7: Expected and observed number of events in the dielectron channel. The errors quoted include both statistical and systematic uncertainties, except the total background in the normalization region which corresponds to the squared root of the number of observed events. The systematic uncertainties are correlated across bins as is done in Reference [83].

$m_{e^+e^-}$ [GeV]	110–200	200–400	400–800	800–1200	1200–3000
Z/γ^*	26700 ± 1100	2960 ± 120	265 ± 13	12.1 ± 0.9	1.47 ± 0.18
$t\bar{t}$	1300 ± 120	410 ± 40	26.5 ± 2.8	0.41 ± 0.17	0.034 ± 0.034
Diboson	415 ± 21	146 ± 8	16.2 ± 0.9	0.88 ± 0.05	0.101 ± 0.011
QCD and W + jets	1900 ± 600	510 ± 200	50 ± 31	2.0 ± 1.8	0.26 ± 0.31
Total	30300 ± 1300	4030 ± 240	357 ± 34	15.4 ± 2.0	1.86 ± 0.35
Data	29816	4026	358	17	3

5.4.3 Dimuon selection

The muons used in this analysis have hits in either three or two (out of three) stations of the muon spectrometer [83]. Muons with hits in three stations, referred to as tight muons, comprise about 95% of the sample, and have transverse momentum (p_T) resolution at 1 TeV ranging from 10% to 25%. Muons with hits in two stations, referred to as loose muons, have slightly larger p_T resolution than the tight muons. Loose muons are accepted only in the barrel region of the muon spectrometer, excluding small geometrical regions where the detector alignment is known to be less precise. A dimuon candidate is constructed from two opposite-charge muons, each with p_T greater than 25 GeV and in a pseudorapidity range of $|\eta| < 2.4$. To suppress background from QCD multijet production, each muon must be isolated, requiring the sum of the p_T of all tracks in a cone of size ΔR smaller than 0.3 to be less than 5% of the transverse momentum of the muon. Dimuon candidates built with two tight muons are considered first. If more than one such pair is found in an event, the one with the highest scalar sum of the leptons p_T is selected. Moreover if no tight muons pair is found, pairs are built with one tight muon and one loose muon. Similarly, if more than one loose dimuon pair is found in an event, the one with the highest scalar sum of the lepton p_T is selected. For the selection criteria described above, the overall event $\mathcal{A}\epsilon$ for a LSTC signal at 1 TeV decaying into a dimuon final state is 44%. The lower acceptance compared to the electron channel is due to the stringent hit requirements in the muon spectrometer applied to assure a good transverse momentum resolution for the muon candidate.

Also in the muon channel, the dominant and irreducible background is due to the Drell-Yan process, and small contributions come from $t\bar{t}$ and diboson production. The QCD multijet background is estimated in data from a sample of non-isolated dimuon events, and the $W+$jets background is evaluated using simulated samples. In the muon channel both backgrounds are found to be negligible after the isolation selection is applied.

5.5   Systematic uncertainty

Table 5.8: Summary of systematic uncertainties on the expected numbers of events at $m_{ee} = 0.2$ TeV and at $m_{ee} = 1$ TeV. NA indicates that the uncertainty is not applicate on the samples, and "-" denotes a negligible entry (i.e. $< 3\%$). The uncertainty on the PDF includes the QCD corrections uncertainty.

Source	Dielectrons $m_{ee} = 200$ GeV		Dielectrons $m_{ee} = 1$ TeV	
	Signal	Background	Signal	Background
PDF/α_s /scale	NA	4%	NA	7%
Electroweak corrections	NA	-	NA	-
Normalization	5%	NA	5%	NA
W + jets and QCD background	NA	7%	NA	12%
Total	5%	8%	5%	14%

The systematic uncertainties in this analysis are reduced by the fact that the backgrounds are normalized to the data in the region of the Z peak. This procedure makes the analysis insensitive to all the mass-independent systematic uncertainties.

Table 5.8 summarizes the relative contribution of the main mass dependent systematic uncertainties considered in this analysis evaluated at $m_{ee} = 0.2$ TeV and at $m_{ee} = 1$ TeV. It is assumed that these uncertainties are correlated between signal and background samples, and also across all bins in the search region. The theoretical uncertainties include the effects of the PDF choice and the QCD and electroweak corrections on the dilepton cross-section. In the Table are also presented the main experimental systematic uncertainties which are mainly due to data to MC normalization, the reconstruction efficiency and the energy resolution. In addition, an uncertainty on the estimate of the QCD multijet background is treated.

All those uncertainties are evaluated as function of the dielectron mass and are discussed in detail below. Moreover, the systematic uncertainties below 3% are neglected in the statistical treatment (e.g the contributions from the reconstruction efficiency and from the energy resolution) because was verified does not affect the results.

5.5.1   Theoretical systematic uncertainties

There are various sources of theoretical systematic uncertainties. The dominant contribution to them comes from the main background (the DY). No theoretical uncertainties are applied on the signal expectation during the limit setting procedure. However, their size is illustrated by the theoretical curves on the limit plots, whose thickness represents the uncertainties.

The non-EW contributions of the theoretical uncertainties on the NNLO DY cross-section due to the choice of the PDF sets to the α_s running and to the variations of the normalization and factorization scales are shown in Figure 5.14 (left). The uncertainty on the QCD K-Factor, evaluated to be around the percent level for a 1 TeV signal, includes the effect of the variations of the renormalization and factorization scales by a factor of two of the nominal scales and the variation obtained when computing K-Factors for Z/γ^* production. The PDF and α_S uncertainties are evaluated using the MSTW2008NNLO eigenvector PDF sets and different PDF sets corresponding to variations of α_S. The α_S uncertainties are within $\sim 5\%$ up to 2 TeV. The α_S uncertainties are found to be considerably smaller than the PDF uncertainties. As one can see in Figure 5.14 (left) at high masses the largest theoretical systematic uncertainty
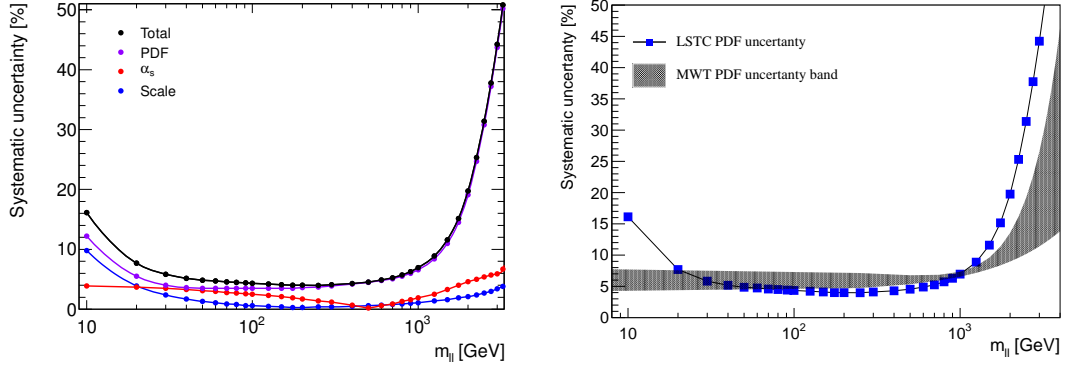
Figure 5.14: Left: PDF uncertainties on the NNLO Drell-Yan lepton-pair production cross-section as function of dilepton mass $m_{\ell^+\ell^-}$. The PDF and α_s uncertainties are evaluated using the MSTW2008 PDF error sets. Right: PDF uncertainties on the LSTC and MWT lepton-pair signal production cross-section as function of dilepton mass $m_{\ell^+\ell^-}$. The PDF uncertainty for MWT model are evaluated using the CTEQ6.6 PDF error sets, as a function of the resonance mass and for different hypothesis on the coupling $\tilde{g}$.

is associated with the variation of cross-section values due to the PDF choice.

The uncertainty on the electroweak high-other correction affecting the DY background expectation are 2.2% and 4.5% respectively at $m_{\ell^+\ell^-} = 1$ TeV and $m_{\ell^+\ell^-} = 2$ TeV. This uncertainty is computed including the effects of neglecting the running of the electromagnetic coupling and the real gauge boson emission. Moreover, the EW uncertainty takes into account the difference in the electroweak scheme defined in the PYTHIA event generation and in HORACE and potential contributions considering high-order electroweak and $\mathcal{O}(\alpha\alpha_s)$ corrections.

As mentioned before theoretical systematic uncertainties on the signal cross-section do not enter in the limits calculation and only changes the thickness of the theoretical curve on the σB limit plots. Therefore for both the TC signal systematic uncertainties related to the PDF variation were calculated similarly as is it done for the DY process. The only slightly difference is that the systematic uncertainty due to PDF variations is computed from the LO signal cross-sections and so the QCD K-Factor systematic does not apply for the signal. Different PDF sets affect the cross-section and the acceptance[8]. Each PDF has independent parameters associated with it. These parameters are known as the eigenvectors of the PDF. They can be varied to quantify the systematic uncertainties associated with the PDF. Therefore for each signal mass point the cross-section calculated with the default set is recalculated with the closest LO setand the PDF uncertainties are evaluated as the largest of the positive and negative variation calculated as:

$$\Delta\sigma^+ = \sqrt{\sum_{i=1}^{n}(max(\sigma_i^+ - \sigma_0, \sigma_i^- - \sigma_0, 0))^2} \tag{5.2}$$

$$\Delta\sigma^- = \sqrt{\sum_{i=1}^{n}(max(\sigma_0 - \sigma_i^+, \sigma_0 - \sigma_i^-, 0))^2} \tag{5.3}$$

8. The effect of the PDF choice on the acceptance is neglected

where n is the number of PDF eigenvectors, σ_i^+ is the cross-section for the higher value of the ith PDF eigenvector, σ_i^- is the cross-section for the lower value of the ith PDF eigenvector, and σ_0 is the cross-section for the central value PDF. The same PDF set used to compute the DY uncertainty can be used for the LSTC signal since the samples were produced with the same generator. While for the MWT signal as a different PDF set (CTEQ6l1) is used the theoretical uncertainty on the cross-section due to the PDF set, is recalculated using the 44 eigenvector sets CTEQ6.6. The PDF uncertainties for both the TC models are shown in Figure 5.14 (right). Also the electroweak corrections uncertainty can be applied on the theoretical curves for the TC models, because the TC resonance involves the production of SM Z/γ^* intermediate boson. An extra systematic is applied whenever the EW K-Factor for electron and muon case combined are used (see Figure 5.3b). This systematic is calculated for each mass point as the larger difference between the combined and the individual channel EW K-Factors.

5.5.2 Normalization

By normalizing the sum of the background components to the number of data events observed in the Z mass peak between 70 - 110 GeV, this analysis is insensitive to the uncertainty on the integrated luminosity and any other mass-independent systematic uncertainties. However since the TC σB limits are normalized to the predicted Z/γ^* cross-section, a flat uncertainty of 5%, to take into account the uncertainty on the Z/γ^* cross-section, is assigned to the signal expectation. In general due to this normalization the systematics are small at dilepton masses near the Z peak and grow larger at high invariant mass.

5.5.3 Efficiency and data-driven background systematic uncertainty

The systematic uncertainty on the electron reconstruction and identification efficiency at high E_T are estimated to be less then 3% even at 2 TeV. As was mentioned in Section 5.3.3 was verified that the electron isolation efficiency has a small drop for E_T above 1 TeV . With MC simulation was studied that the efficiency drop observed at high transverse momenta bring to a systematic of about 2% at 2 TeV.

The simulation was adjusted to reproduce the resolution of the energy measured by the calorimeter [101]. The resulting uncertainty has a negligible effect on the final result. In fact at large transverse energy the calorimeter resolution is dominated by a constant term which has a small uncertainty (see Appendix E.1).

The calorimeter energy calibration uncertainty is between 0.5% and 1.5% depending on transverse momentum and pseudorapidity. The non-linearity of the calorimeter response is negligible according to test beam data (valid up to $\sim 250\,\text{GeV}$) and Monte Carlo studies [102]. The uncertainty on the energy calibration has a minimal impact on the sensitivity of the search, since its main effect is a shift of a potential peak in dilepton mass spectrum without change of the line-shape.

The larger experimental systematic uncertainty comes from the estimate of the multijet and $W + $jets background components. The multijet and $W + $jets backgrounds are a minor component on the total number of the background events, therefore the large systematic uncertainty associated it is translate into a systematic uncertainty on the total background of 7% at 200 GeV and 12% at 1 TeV. Those numbers are obtained by taking the ratio of the total background, when the multijet and $W + $jets backgrounds are increased by 1σ and the total nominal background, and obviously does not affect the signal expectation.

5.6 Statistical Method

5.6.1 Weighting procedure and Signal Template

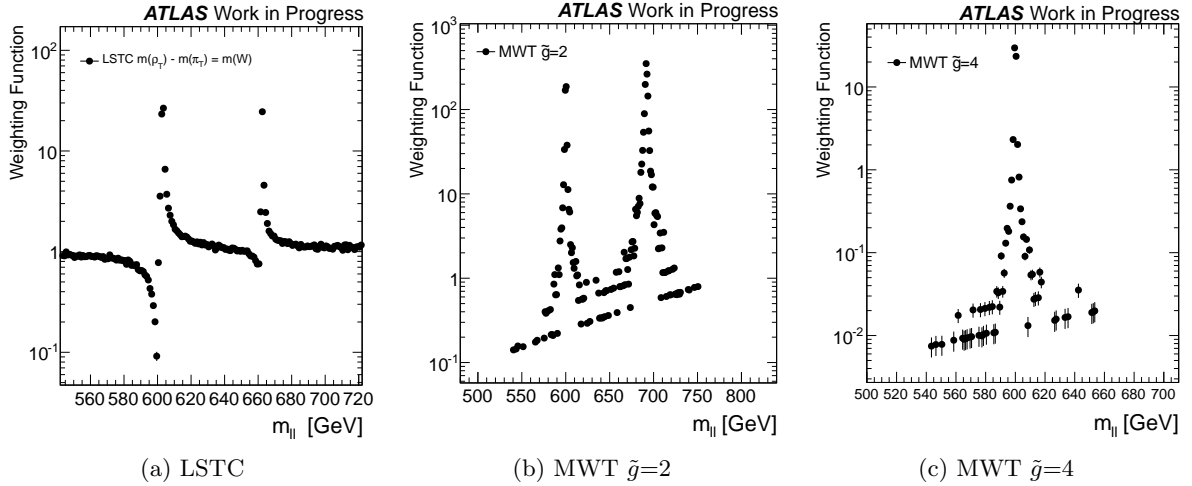

Figure 5.15: For a mass point at = 600 GeV: weighting function used to reshape the dilepton mass distribution in the officially produced Drell-Yan sample to that of a LSTC or MWT samples. (a) The LSTC case where $m(\rho_T) = m(\omega_T) = 600$ GeV and $m(a_T) = 660$ GeV. (b) The MWT scenario for $\tilde{g}$=2 case $m(R_1) = 600$ and $m(R_2) = 692$, and (c) The MWT scenario for $\tilde{g}$=4 case where $m(R_1) = 600$. Note that in the MWT case the two resonances are generated without the Drell-Yan component.

Signal templates as a function of the dilepton invariant mass provide the expected line-shape of the searched dilepton resonances.

A weighting procedure is introduced to construct as many signal templates as needed. Due to the fact that the technimeson production is resonating through the Drell-Yan process it is possible to produce signal templates by applying suitable weights to the DY MC samples.

For each TC signal mass points a high statistic [9] sample is generated, as well as for the binned DY samples, where 1 million events are generated for each of the invariant mass bins. The weighting functions are then determined, by dividing the generated mass distribution of the technimesons by the generated mass distribution of the underlying DY process. The statistics of the generated samples is defined such that the statistical uncertainty on the number of entries per 1 GeV bin of the weighting function is negligible.

The so-obtained weighting functions (Wf), shown in Figure 5.15 for a 600 GeV pole mass, are used to reshape the dilepton mass distribution (at the truth level) in the officially produced Drell-Yan samples to that of a LSTC or MWT model for each pole mass of interest.

In the LSTC case in order to be consistent with the TC interpretation of the ATLAS WZ search [37], all the private signal samples are generated with $m(\rho_T/\omega_T) - m(\pi_T) = m(W)$ mass splitting. In the MWT case as MadGraph event generator uses a different PDF set then the one used for the DY modeling (obtained with PYTHIA), to be consistent in the weighting procedure all the MWT points are generated without the DY component. Figure 5.16 shows,
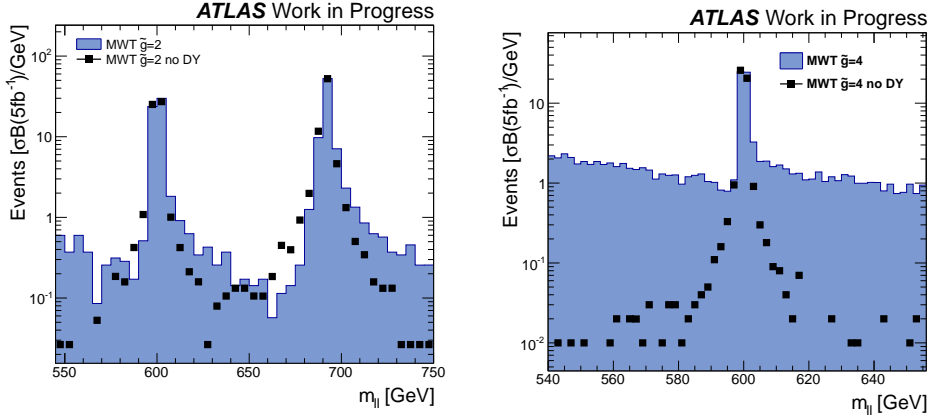
---

9. 500k events.

Figure 5.16: On the left plot: The dilepton invariant mass distribution in the MWT scenario for $\tilde{g}=2$ case, where $m(R_1) = 600$ and $m(R_2) = 692$, the fill histogram is the MWT process with the Drell-Yan component and the points represent the case in which the resonance is generated without the Drell-Yan component. Note that in the latter case only the interference between the two resonance is present.

On the right plot: the dilepton invariant mass distribution in the MWT scenario for $\tilde{g}=4$ case, where $m(R_1) = 600$, the fill histogram is the MWT process with the Drell-Yan component and the points represent the case in which the resonance is generated without the Drell-Yan component. Note that the two distributions are normalized to the same cross-section.

for the two MWT benchmark scenario ($\tilde{g}=2$ and $\tilde{g}=4$), the $m(R_1) = 600$ mass point where the SM DY component is included or not included at the generator level.

The final signal templates for both models used in this analysis are created from the reconstructed dilepton mass distribution of the Drell-Yan samples suitably weighted as described above. The remaining SM DY continuum component is subtracted as follows:

- $DY(1 - Wf)$ for the LSTC model where the Wf contains the residual DY continuum;

- $DY \times Wf$ for the MWT model where the Wf has only R_1/R_2 contributions.

Note that was also been verified that the angular distribution of the SM DY and the TC process is the same, thus no further scaling on other distributions are needed (for more details see Appendix F.1).

5.6.2   Discovery statistics

Figure 5.13 and Tables 5.7 show in each bin of invariant mass a good agreement between data and the SM prediction. To test the consistency of the observed data with the Standard Model prediction several statistics methods are used.

A p-value test is used to evaluate the significance of potential excess of the TC candidate events by testing the inconsistency with the SM background expectation and by confirming the consistency of data with signal + background hypothesis.

In the absence of an evidence of the TC signal the Bayesian approach [103] is used to set 95% confidence level (C.L.) limits on the cross-section and resonance mass.
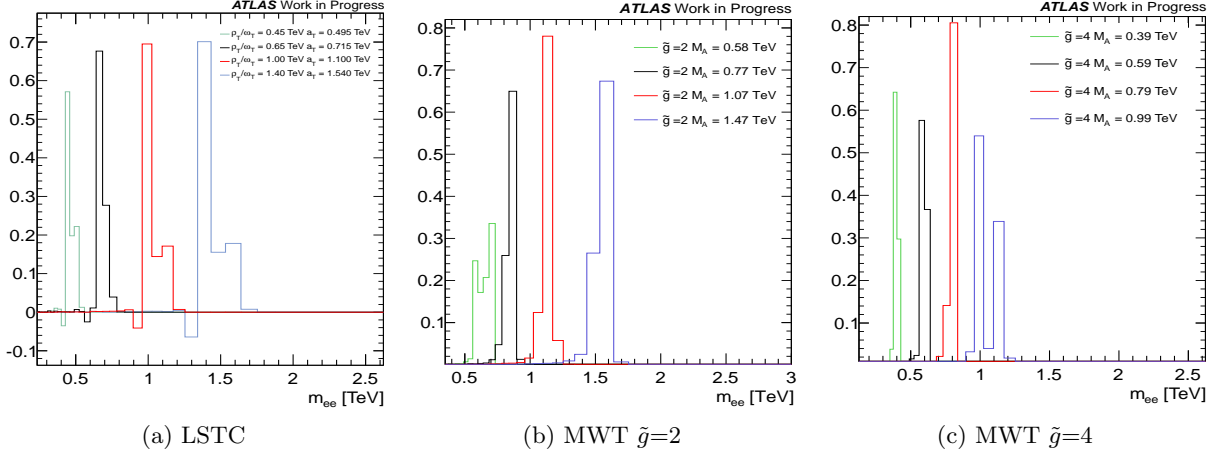
Template shape fitting

Figure 5.17: Technimesons line shape distribution at reconstruction level in the electron channel. (a) The LSTC case where each signal templates are simulated according with the theoretical cross-section. (b) and (c) In the MWT scenario for $\tilde{g}=2$ and for $\tilde{g}=4$ cases, signal template for four different M_A hypothesis. Note that in the MWT case the signal templates are normalized to unity.

A template shape fitting technique is used to search for a TC signal of unknown mass and unknown rate in the ATLAS dilepton data. The template shape fitting is essentially a counting experiment in many bins of the m_{ll} distribution. The resulting likelihood function is the product of the single bin counting experiment likelihood function.

As it is described above, the signal templates are created from the reconstructed dilepton mass distribution in the Drell-Yan sample suitably reshaped with the corresponding weighting function. Figure 5.17 shows some examples of signal template in the electron channel used for the LSTC model (a) and for the two benchmark scenario in the MWT with $\tilde{g}=2$ and $\tilde{g}=4$, (b) and (c) respectively. To note that in the signal templates for the LSTC model (Figure 5.17a) only the positive interference with the Drell-Yan process is taken into account because the negative contribution is set to zero in the statistical framework. However the contribution of the negative interference is less then 5% with respect to the peak contribution therefore neglecting it do not change the discrimination potential of the model. In the MWT model any interference with the DY continuum is taken in to account. The background template is built as the sum of the DY continuum and all the other SM background expectation normalized to the data at the Z peak, as is described in Section 5.4.

The invariant mass search region start from $m_{\ell^+\ell^-}$ above 130 GeV, and in this region the templates provide the expected yield of events (μ) in each $m_{\ell^+\ell^-}$ bin: $\mu = n_X(\lambda, \bar{\nu}) + n_{DY}(\bar{\nu}) + n_{obg}(\bar{\nu})$ when neglecting interference, and $\mu = n_{X+DY}(\lambda, \bar{\nu}) + n_{obg}(\bar{\nu})$ when including interference, where λ represents the model parameters, $\bar{\nu}$ the set of nuisance parameters and n_X, n_{DY}, n_{obg} are respectively the number of TC resonance, Drell-Yan and other backgrounds events.

The significance of a potential signal on the data

The significance of a potential TC signal is summarized by a p-value: the probability of observing an outcome at least as signal-like as the one observed in data, assuming that a signal is absent. The common convention is that a p-value less than 1.35×10^{-3} constitutes evidence for a signal and a p-value less than 2.87×10^{-7} constitutes a discovery. These values corresponds to one-sided integrals of the tails of a unit Gaussian distribution beyond $+3\sigma$ and $+5\sigma$, respectively. Experimental outcomes are ranked on a one-dimensional scale using a test statistic that is used to calculate the p-value. A natural choice for the test statistics is based on the Neyman-Pearson lemma which states that when performing a hypothesis test between two hypotheses, in this case one assuming the presence of signal and background (S+B) and the other that assumes only SM background (B), the profile log-likelihood-ratio (LLR) :

$$LLR = -2 \ln \frac{L(S+B)}{L(B)} \tag{5.4}$$

is the best test to reject (B) in favor of (S+B). The expected distribution of LLR assuming the background only (B) hypothesis is computed numerically performing pseudo-experiments varying all sources of systematic uncertainty. The p-value is then:

$$p = p(LLR \leq LLR_{obs} | SM \ only) \tag{5.5}$$

Since the mass and the rate of a hypothetical technimeson is unknown *a-priori*, a likelihood fit for the best-fit signal cross-section (σ_{TC}) and the best-fit mass of TC (M_{TC}) present in data is performed. Figure 5.18 (left) shows the absolute value of the profile LLR test statistic as
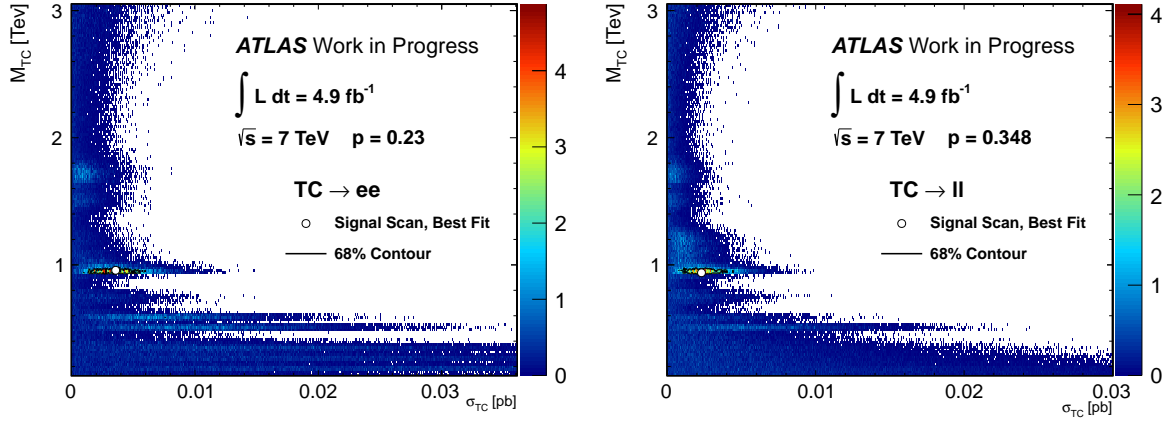

Figure 5.18: The absolute value of the profile LLR test as a function of σ_{TC} and M_{TC} for the likelihood fit (left) to ATLAS data in the dielectron channel; (right) to ATLAS data for the combination of the dielectron and dimuon channel.

a function of σ_{TC} and M_{TC} for the likelood fit using the Markov Chain Monte Carlo [103] marginalization to ATLAS data in the electron channel, while on the right side of Figure 5.18 are shown the same for the combination of electrons and muons channels. The 'hot' regions (absolute value of the numerical results of the profile LLR) support the (S+B) hypothesis for particular values of σ_{TC} and M_{TC} and correspond to localized excesses in the dilepton spectrum.

Mass-dependent systematic uncertainties (summarize in Table 5.8 for the electron channel) are incorporated as nuisance parameters in the likelihood function; no theoretical uncertainties are applied on the signal expectation when setting limits. The systematic uncertainties are correlated across all bins in the search region of $m_{\ell\ell} > 130$ GeV, and correlations between signal and background are taken into account. From this statistical test, in the dielectron spectra the most significant deviation between the SM expectation and the data is observed for invariant mass around 900 GeV with a corresponding p-value of 23%. The same test is done for the dimuon sample and the most significant deviation is found for invariant mass around 1.1 TeV with a p-value of 63%. For the combination of both the channels the most significant deviation between the SM expectation and the data has a p-value of 35% and is found for invariant mass around 900 GeV.

Local significance

Figure 5.19 display the local significance of the difference between the observed data and SM expectation in each mass bin as described in Reference [104]. The statistical significance
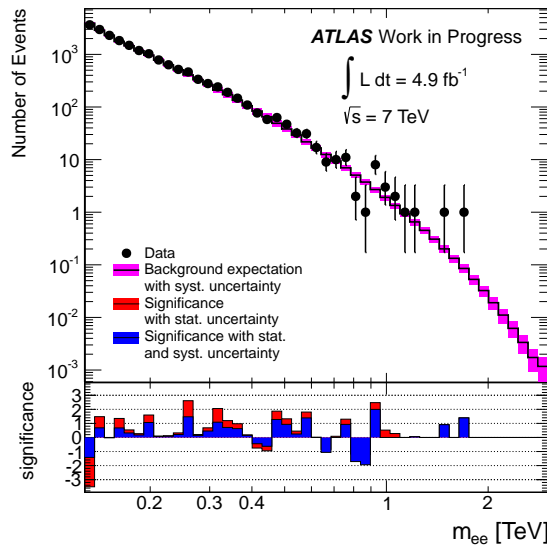

Figure 5.19: Differences between data and expectation in the electron channel. The mass range goes from 130 GeV to 3 TeV.

of a deviation of bin contents from the expectation, gives at the same time an intuitive picture of the relevant deficits and excesses on a certain distribution. This is achieved by computing the exact p-value and, when its value is smaller that 50% probability, by mapping it into the z-value which gives the deviation in units of Gaussian standard deviations. The sign of z-values is always positive for excesses and negative for deficits. The local significance is defined here as the difference between data and expectation based on the significance of the difference in each bin. Considering both the statistical and systematic uncertainty the largest positive local significance founded in the dielectron spectrum is less then 2σ and the largest negative local significance is about -2σ.

The differences between the observed data and SM expectation in each bin of the dimuon invariant mass were also evaluated. In the muon channel the largest positive local significance was found to be about 1σ and the largest negative local significance was about 2σ.

In conclusion: the dilepton invariant mass spectrum in data is consistent with the Standard Model expectation. In the absence of an evidence of a TC signal, an upper limit on σB of a TC resonance is determined at the 95% C.L. using a Bayesian approach [103], in exactly the same manner as in the ATLAS dilepton analysis described in Reference [83].

5.6.3   Limit setting

To determine limits on the TC models, the invariant mass distribution in data is compared to the background templates and to different amounts of signal at various technimesons masses (and coupling values for the MWT case).
A likelihood function is defined as the product of the Poisson probabilities over all mass bins in the search region, where the Poisson probability in each bin is evaluated for the observed number of data events given the expectation from the template. The total acceptance for signal as a function of mass is propagated into the expectation. For each X pole mass, a uniform prior in the X production cross-section is used.
The expected number of events in bin k (N_j) is represented by the Poisson mean μ_k, which is a sum of TC signal and total background. The binned likelihood function is shown in Equation 5.6 with n_k being the number of data events in each bin.

$$L(data|N_j, \theta_i) = \prod_{k=1}^{N_{bin}} \frac{\mu_k^{n_k} e^{-\mu_k}}{n_k!} \prod_{i=1}^{N_{sys}} G(\theta_i, 0, 1) \quad , \text{where} \quad \mu_k = \sum_i \sum_j N_j T_{jk}(1 + \theta_i \epsilon_{jik}) \quad (5.6)$$

Signal and total background correspond to template numbers $j = 1$ and $j = 2$ respectively. $G(\theta_i, 0, 1)$ is a unit width Gaussian prior for nuisance parameters θ_i (with $i = 1, \cdots, N_{sys}$) that control bin-by-bin systematic variations (ϵ_{jik}) of the (unit area) template shapes T_{jk} in the likelihood function.
Employing Bayesian statistics the reduced likelihood, which is only a function of the parameter of interest (N_X) is obtained by means of marginalization technique using Markov Chain Monte Carlo as implemented in the Bayesian Analysis Toolkit [103].

$$L'(data|N_X) = \int L(N_j, \theta_1, ..., \theta_N) d\theta_1, ..., d\theta_N \quad (5.7)$$

The limit on N_X is converted into a limit on cross-section times branching ratio $\sigma B(X \to \ell^+\ell^-)$ by scaling with the observed number of Z boson events (N_Z) and the known value of $\sigma B(Z \to \ell^+\ell^-)$:

$$\sigma B(X) = \sigma B(Z) \frac{N_X \, \mathcal{A}\epsilon(Z)}{N_Z \, \mathcal{A}\epsilon(X)}, \quad (5.8)$$

where
  – $\sigma B(Z) = 0.989$ nb is the inclusive Z cross-section at NNLO for $m_{\ell^+\ell^-} > 60$ GeV [92];
  – $\mathcal{A}\epsilon(Z)$, calculated with the inclusive Z MC sample, is the efficiency of requiring $m_{\ell^+\ell^-} > 0.13$ TeV times the average selection efficiency for events with $m_{\ell^+\ell^-} > 60$ GeV:
$\mathcal{A}\epsilon(Z) = 0.0032 = N^{MC}(\text{selected events, } m_{\ell^+\ell^-} > 130\,\text{GeV})/N^{MC}(\text{all events, } m_{\ell^+\ell^-} > 60\,\text{GeV});$
  – $N_Z = 15159.5$ is the number of Z events above 0.13 TeV;
  – $\mathcal{A}\epsilon(X)$ is the acceptance times efficiency for a given X pole mass.
With this formula the luminosity normalization is replaced by a normalization to the data, using the number of Z events and acceptance above 0.13 TeV in order to cancel the mass-independent systematic uncertainties (i.e. $L = \frac{N_Z}{\sigma B(Z) \, \mathcal{A}\epsilon(Z)}$). A residual source of systematic uncertainty in
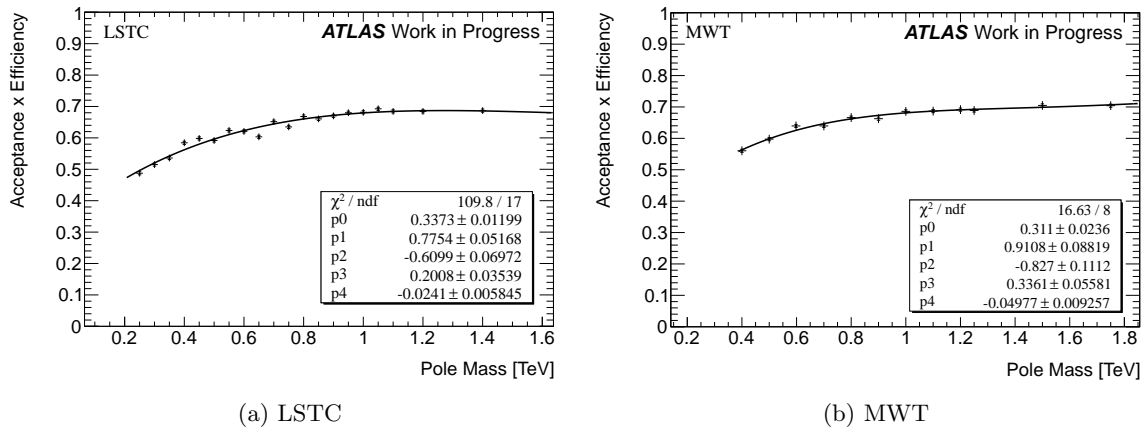
(a) LSTC   (b) MWT

Figure 5.20: Electron channel: total acceptance times efficiency as a function of the pole mass for the technicolor models: LSTC (left), MWT (right).

this approach is the theoretical uncertainty on the Z boson production cross section ($\sigma B(Z)$) which is taken to be 5% and it is applied on the signal expectation as explained in Section 5.5.2.

For each new resonance X, $\mathcal{A}\epsilon(X)$ is obtained from a weighted average of $\mathcal{A}\epsilon$ versus $m_{\ell^+\ell^-} >$ 130 GeV over the full signal line-shape. In Figures 5.20, in the electron channel for the LSTC and the MWT model respectively, is shown the result of a polynomial fit performed on the $\mathcal{A}\epsilon$, to obtain the analytical parametrization used in the limit setting procedure. The product $\mathcal{A}\epsilon$ is different for the two TC models due to the different resonant line-shapes.
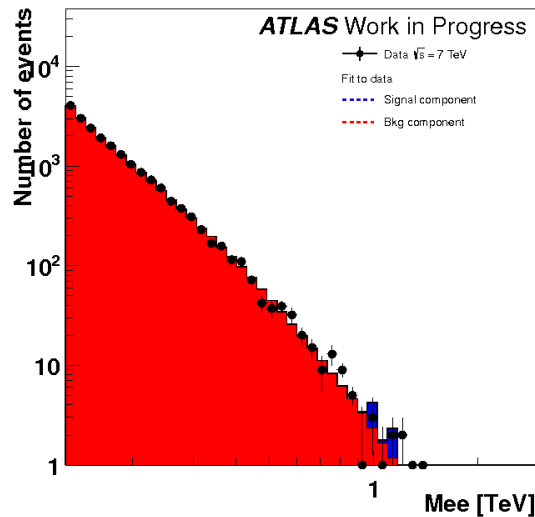

Figure 5.21: Background template in red, the pseudo-experiments are the back point and the best fit for a Techimesons line shape is show in blue.

For each TC signal hypothesis the expected exclusion limits are determined using simulated pseudo-experiments containing only Standard Model processes by evaluating the 95% C.L. upper limits for each pseudo-experiment for each fixed value of M_X. Figure 5.21 shows an example of the comparison between the background template, the pseudo-experiments and best-fit on a signal template.

The median of the distribution of the pseudo-experiment upper limits is chosen to represent the expected limit for each fixed value of M_X. The ensemble of limits is also used to find the 68% and 95% envelope of the expected limits as a function of M_X. Finally, lower limits on M_X are obtained by comparing the expected σB with the upper limits on σB as a function of M_X.

5.7 Results

As the predicted resonances can decay in both dielectron and dimuon final state the two orthogonal decay channels provide a mostly independent measurement of the limit. To calculate the combined limit, assuming the flavor universality $BR(X \to ee) = BR(X \to \mu\mu)$, the joint likelihood is simply the product of Poisson probabilities of each individual bin in each channel, accounting for the correlation among the systematic uncertainties across channel as well as across processes.

The results reported in the following section are computed for the dielectron channel and for the combination of the dielectron and dimuon channels. In Appendix G are reported the limit results for both the LSTC and the MWT models obtained for the muon channel alone.

5.7.1 LSTC Limit

Table 5.9: e^+e^-, $\mu^+\mu^-$ and combined 95% C.L. mass limits on ρ_T/ω_T (LSTC model).

	Observed limit mass [TeV]	Expected limit mass [TeV]
$\rho_T/\omega_T \to e^+e^-$	0.84	0.84
$\rho_T/\omega_T \to \mu^+\mu^-$	0.70	0.71
$\rho_T/\omega_T \to \ell^+\ell^-$	0.85	0.89

Given the absence of a technicolor signal, limits are set on the $m(\rho_T/\omega_T)$ in the context of Low-scale technicolor model discussed in Chapter 1.2.4. The upper limit on the number of signal events is converted in a limit on the cross-section times the branching ration as a function of $m(\rho_T/\omega_T)$. This limit is set on a LSTC model with templates built assuming the $m(\rho_T/\omega_T) - m(\pi_T) = m(W)$ mass splitting, consistent with the TC interpretation in the ATLAS WZ search [37]. For each pole mass considered the signal templates have always both a_T and ρ_T/ω_T resonances, and the negative interference between the underlying SM DY and the TC resonances is neglected. The intrinsic width of the two resonances present in the spectrum, ρ_T/ω_T and a_T, is very small, less that 1 GeV, so that the observed signal line shape is due to detector resolution alone, details on the Appendix F.2.

Figure 5.22 shows the 95% C.L. exclusion limit on σB for the electron channel and for the combination of the electron and muon channels. All dielectron, dimuon and combined σB limits are used to set mass limits at the 95% C.L. displayed in Table 5.9.
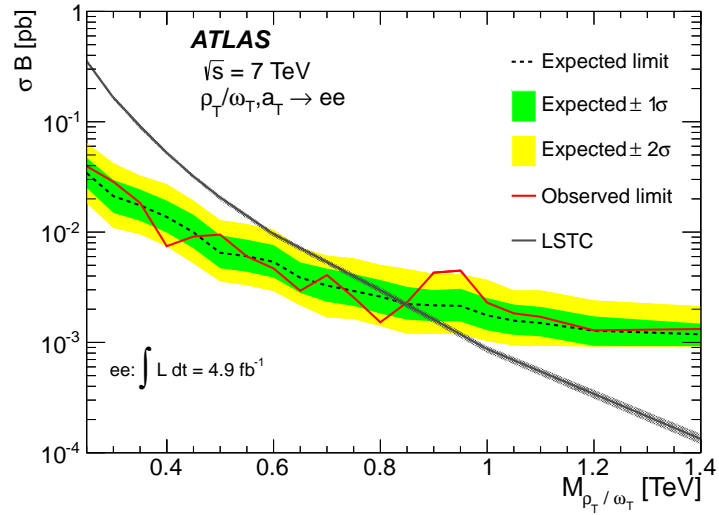
(a) electron channel
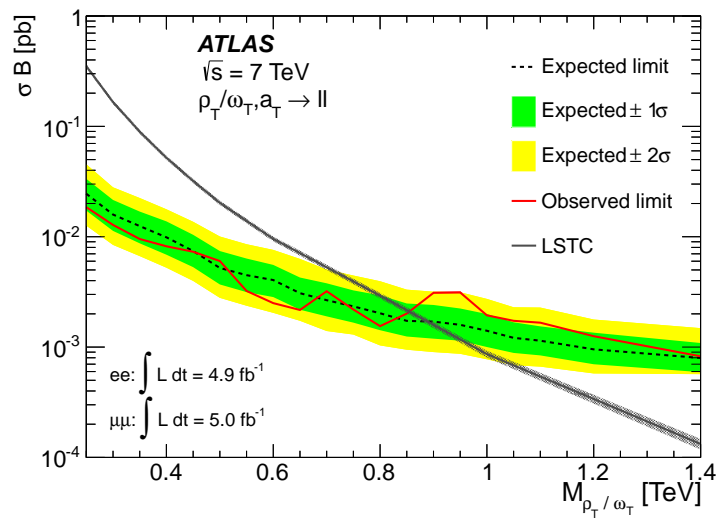
(b) electron and muon combined

Figure 5.22: Expected and observed 95% C.L. limits on σB for ρ_T/ω_T, a_T production for the electron channel (a) and for the combination of electron and muon channels (b). In the plot the thickness of the theoretical curve represents the systematic uncertainties on the signal cross-section.

The σB limits are then translated into a exclusion region in the $m(\rho_T/\omega_T) : m(\pi_T)$ plane. In the LSTC the expectation is that $m(\rho_T/\omega_T)$ is greater than the $m(\pi_T)$ but since there is no way to know a priori what is the mass splitting between the ρ_T/ω_T and the π_T the scan is performed for values of $m(\pi_T)$:

$$\frac{1}{3} \times m(\rho_T/\omega_T) \leqslant m(\pi_T) \leqslant m(\rho_T/\omega_T). \tag{5.9}$$

The $1/3 \times m(\rho_T/\omega_T)$ threshold is choose as lower bound because the $\rho_T \to \pi_T \pi_T$ decay channel are kinematically impossible and, even more strongly, the $\omega_T \to 3 \times \pi_T$ and $a_T \to 3 \times \pi_T$ channels [105]. Note that the $m(\pi_T) \geq 1/2 \times m(\rho_T)$ threshold is not used because in the dilepton channel the ρ_T accounts for only 10% of the signal produced.
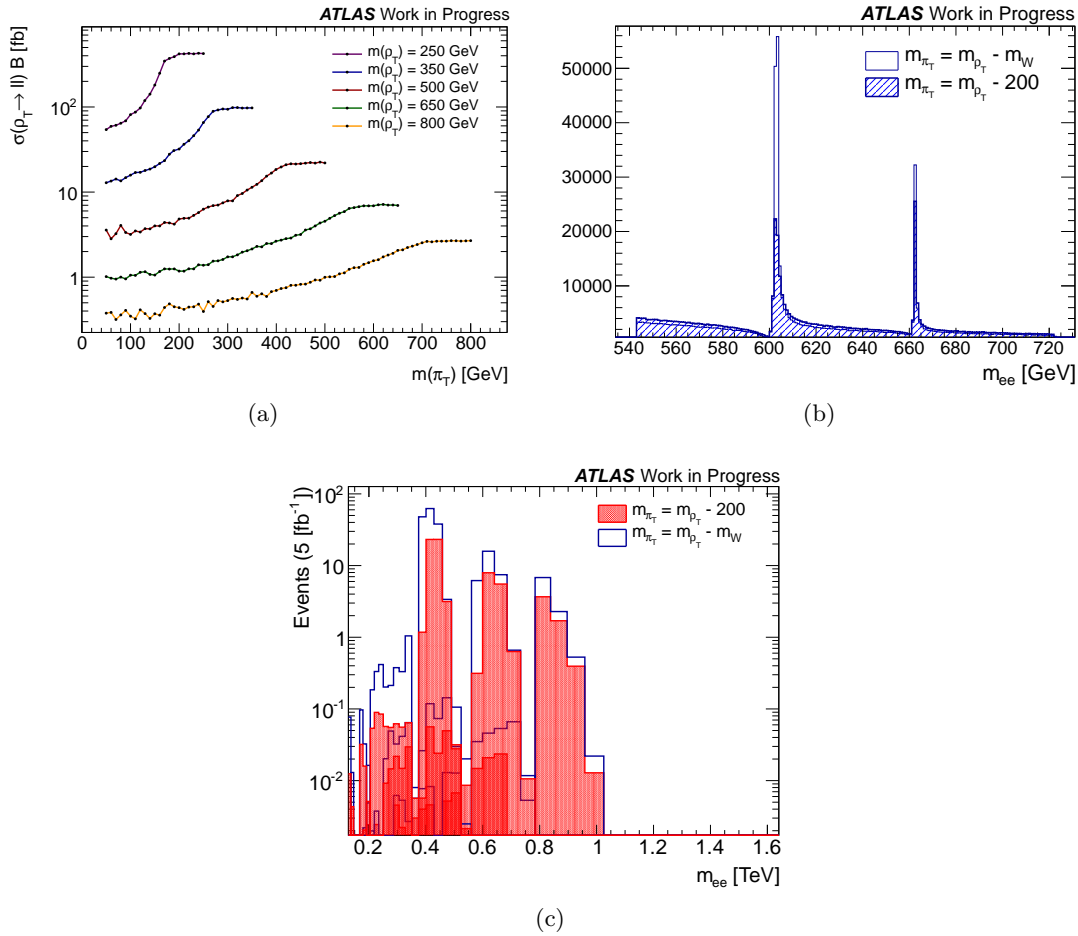

(a)

(b)

(c)

Figure 5.23: (a) The ρ_T/ω_T dilepton cross-section times the branching fraction as a function of m_{π_T}. (b) At generator level, line shape for $m_{\rho_T/\omega_T} = 600$ GeV generated with two different mass splitting hypothesis: $m(\rho_T/\omega_T) - m(\pi_T) = m(W)$ for the filled histogram and $m(\rho_T/\omega_T) - m(\pi_T) = 200$ GeV for the empty histogram. (c) LSTC signal templates for $m_{\rho_T/\omega_T} = 400, 600, 800$ GeV generated with $m(\rho_T/\omega_T) - m(\pi_T) = m(W)$ for the black histograms and $m(\rho_T/\omega_T) - m(\pi_T) = 200$ GeV for the red histograms. Note that the templates are normalized to the predicted cross-section.

In the Low-scale Technicolor model changing the m_{π_T} has an impact on the cross-section of the
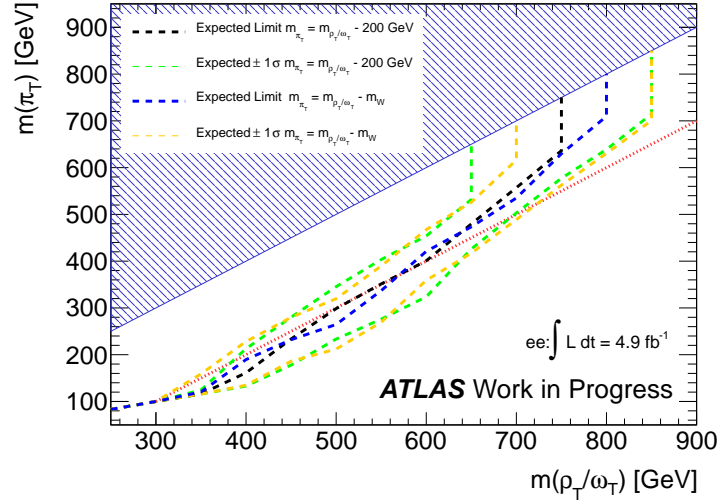
Figure 5.24: For the dielectron channel only, expected exclusion region in the parameter space $m(\rho_T/\omega_T)$ vs $m(\pi_T)$, obtained with $m(\rho_T/\omega_T) - m(\pi_T) = m(W)$ for the blue dashed line and $m(\rho_T/\omega_T) - m(\pi_T) = 200$ GeV for the black dashed line. For both hypothesis the $\pm 1\sigma$ bands are also displayed. The dark red dashed line shows the $m(\pi_T) = m(\rho_T/\omega_T) - 200$ GeV.

dileptonic decays of the ρ_T/ω_T. The mass splitting between the ρ_T/ω_T and the π_T determines if decay modes (such as $\rho_T/\omega_T \to W\pi_T$ or multi-π_T) are kinematically allowed. Figure 5.23 (a) shows the resulting dependence of the $\rho_T/\omega_T \to l^+l^-$ cross-section on the π_T mass choice. Changing the ρ_T/ω_T and π_T mass difference has also an effect on the a_T contribution to the signal spectrum. Figure 5.23 (b) shows the generated line shape for a technirho with $m_{\rho_T/\omega_T} = 600$ GeV for two different mass splitting hypothesis $m(\rho_T/\omega_T) - m(\pi_T) = m(W)$ (filled histogram) and $m(\rho_T/\omega_T) - m(\pi_T) = 200$ GeV (empty histogram). Increasing the mass splitting decreases the total σ_{ρ_T/ω_T} cross-section but increases the a_T contribution. For signal templates build with $m(\rho_T/\omega_T) - m(\pi_T) = 200$ GeV the a_T contribution to the total integral increases from 28% to 32% and the signal fraction of the a_T with respect to the ρ_T/ω_T peak increases from 36% to 44% with respect to the default case. However the technimesons mass splitting and the following increase of the a_T contribution in the spectrum has a small effect on the signal fiducial acceptance (less then 2%).

This behavior at generator level slightly modifies the signal templates: Figure 5.23 (c) shows for three different mass points, $m_{\rho_T/\omega_T} = 400, 600, 800$ GeV, the signal templates generated with the two different mass splitting hypothesis: $m(\rho_T/\omega_T) - m(\pi_T) = m(W)$ and $m(\rho_T/\omega_T) - m(\pi_T) = 200$ GeV. For low masses a small difference in the template line-shape is visible. However, as is shown in Figure 5.24, it has a minimal impact on the expected limits within the systematic uncertainty on the predicted cross-section. Furthermore, the $m(\rho_T/\omega_T) - m(\pi_T) = m(W)$ hypothesis was chosen as the more conservative one.

To translate the σB limits into exclusion regions in the $m(\rho_T/\omega_T) : m(\pi_T)$ plane at each value of $m(\rho_T/\omega_T)$ the intersection of the 95% C.L. exclusion cross-section measurement with the theoretically predicted σ_{TC} is done. This intersection, along with the constraint defined in Equation 5.9, defines an exclusion region in the $m(\rho_T/\omega_T) : m(\pi_T)$ parameters space. Figure 5.25 shows the predicted $TC \to l^+l^-$ cross-section as function as the π_T mass as well as the 95% C.L. exclusion cross-section measurement, for three different mass points chosen on
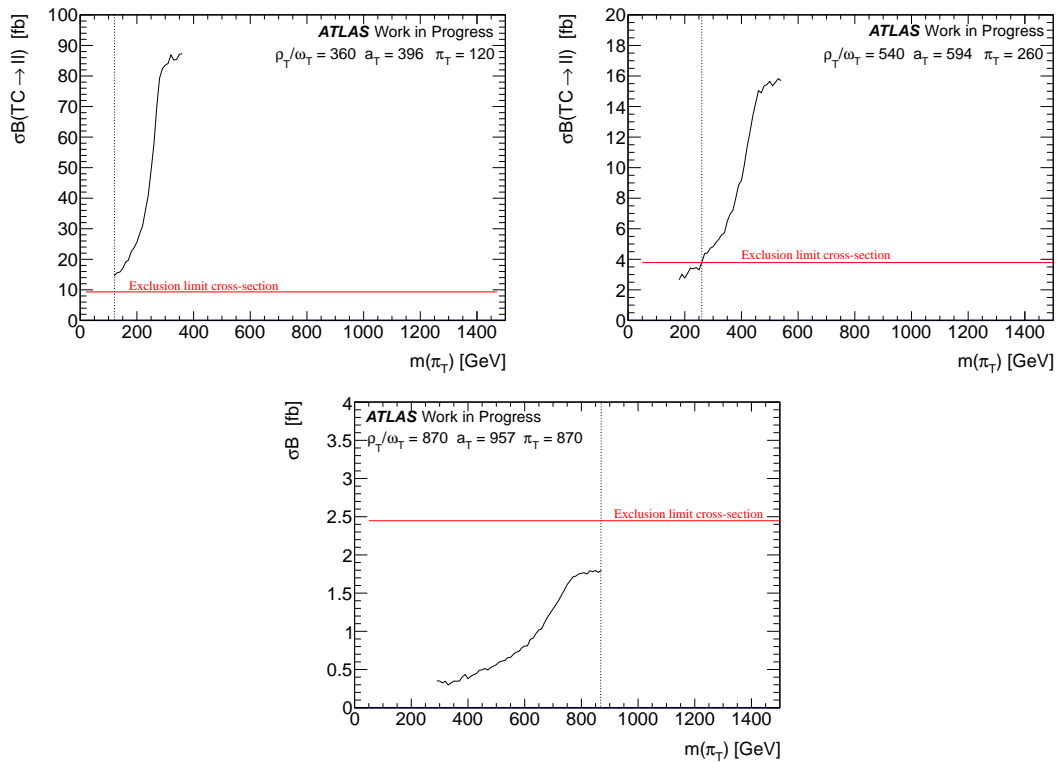
Figure 5.25: The predicted $\rho_T/\omega_T \to l^+l^-$ cross-section as function as the π_T mass for three different points in the $m(\rho_T/\omega_T) : m(\pi_T)$ plane. For each value of $m(\rho_T/\omega_T)$ the $m(\pi_T)$ corresponding to the intersection of the 95% C.L. exclusion cross-section measurement (the red line) with the theoretically predicted σ_T is displayed.
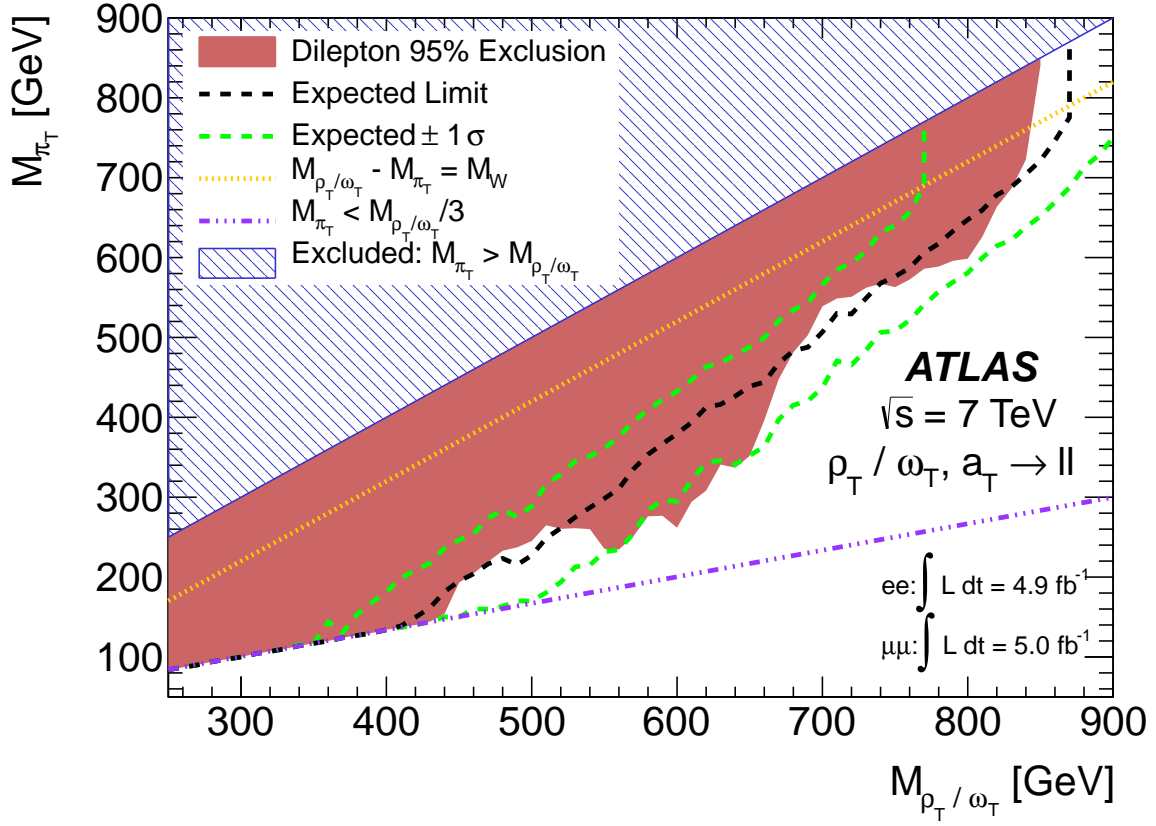
Figure 5.26: The 95% C.L. exclusion region as a function of the ρ_T/ω_T and π_T masses is shown in red, assuming $m(a_T) = 1.1 \times m(\rho_T/\omega_T)$. The yellow dotted line corresponds to $m(\rho_T/\omega_T) - m(\pi_T) = m(W)$. The black dashed line shows the expected limit, with the green dashed lines showing the $\pm 1\sigma$ bands. The blue hashed region in which $m(\pi_T) > m(\rho_T/\omega_T)$ is excluded by theory. This search is insensitive in the region below the violet dotted line $(m(\pi_T) < m(\rho_T/\omega_T)/3)$ due to vanishing branching ratio of ρ_T and ω_T to dileptons, as is explain in the text.

the edge of the exclusion contour in the $m(\rho_T/\omega_T) : m(\pi_T)$ plane.

The contour region is calculated within 10 GeV $m(\rho_T/\omega_T)$ spacing to provide good coverage of the phase-space and reduce the extrapolation needed between the nearly points. Figure 5.26 shows the resulting exclusion region for the combination of the electron and the muon channels. Masses of ρ_T/ω_T are excluded between $250 - 840$ GeV for $m(\pi_T)$ between $50 - 840$ GeV.

5.7.2 MWT Limit

Given the absence of a technicolor signal, limits are also set on the M_A in the context of Minimal Walking technicolor discussed in Chapter 1.2.5. The upper limit on the number of signal events is converted into a limit on the cross-section times branching fraction as describe in Section 5.6.

In order to build the signal templates, $m(R_1)$ is scanned in steps of 100 GeV for each value of $\tilde{g}$. Once defined a value for M_A and $\tilde{g}$ $m(R_1)$, $m(R_2)$ are uniquely defined, and a signal template is produced accordingly (for the two benchmark $\tilde{g}$ values template examples are done in Figure 5.17b and 5.17c).

To scan the M_A - $\tilde{g}$ plane for the five $\tilde{g}$ values considered ($\tilde{g} = 2, 3, 4, 5, 6$) new templates are built for each different M_A assumption.

Note that for the $\tilde{g}=5$ hypothesis the same templates as in the $\tilde{g}=4$ case are used. In fact for both hypothesis at low values of M_A the presence of R_2 is negligible. As already mentioned in Section 1.2.5, in the region of parameter space where R_1 is mostly an axial-like vector (for a mass less than or about one TeV) and R_2 mostly a vector state, the following qualitative dependence of the couplings of the heavy technimesons with the SM fields as function of the electroweak gauge coupling g and the heavy technimesons self-interaction coupling $\tilde{g}$ is observed:

$$g_{R_{1,2}\rightarrow ff} \sim \frac{g}{\tilde{g}}; \qquad g_{R_2\rightarrow WW} \sim \tilde{g}; \qquad g_{R_1\rightarrow HZ} \sim \tilde{g}.$$

For this reason, for high values of the coupling $\tilde{g}$, the R_2 diboson branching fraction is higher than the corresponding dilepton one. This has an impact on the R_2 dilepton cross-section which is $o(10^2)$ lower than the R_1 one, and on the R_2 width which is very broad for masses lower then 1 TeV. That is why the R_2 contribution is neglected in the dilepton spectrum for low M_A and high $\tilde{g}$ values.

Therefore, the only difference between the $\tilde{g}=4$ and $\tilde{g}=5$ cases is verified to be in the R_1 line-shape. The intrinsic R_1 width, which in the $\tilde{g}=4$ case is ~ 0.5 GeV, is about 40% higher in the $\tilde{g}=5$ case. These differences at generator level are completely negligible at the template level because the observed signal width is due to detector resolution alone (see Figure 5.17c).

Figure 5.27 shows the 95% C.L. exclusion limits on σB for the electron channel and for the combinations of the electron and muon channel, together with the theoretical cross-section times branching ratio, for the two benchmark values of the $\tilde{g}$ coupling. Figure 5.28 shows the 95% C.L. exclusion limits on σB for $R_{1,2}$ production, together with the theoretical curve, for the combinations of the electron and muon channel for the coupling value $\tilde{g}=3$, $\tilde{g}=5$ and $\tilde{g}=6$.

In the same way than in the LSTC case the combine limits on $\sigma B(R_{1,2} \rightarrow \ell^+\ell^-)$ are used to constraint the $(M_A - \tilde{g})$ parameter plane in the MWT scenario. In fact, from the upper limits on the R_1 mass, obtained assuming $\tilde{g} = 2, 3, 4, 5, 6$, is possible to limit the corresponding values for the parameter M_A. The resulting 95% C.L. exclusion area in $M_A - \tilde{g}$ parameter space is presented in Figure 5.29 and the corresponding numbers are given in Table 5.10. With this results higher bounds in the $(M_A, \tilde{g})$ plane of the MWT parameter space are set with respect to the previous Tevatron results [50] and the indirect limit described in detail in [49]. To note that this result is obtained with $m_H = 200$ GeV and $s = 0$, however it was verified there that the edge of the excluded area varies only very weakly as a function of s and m_H.
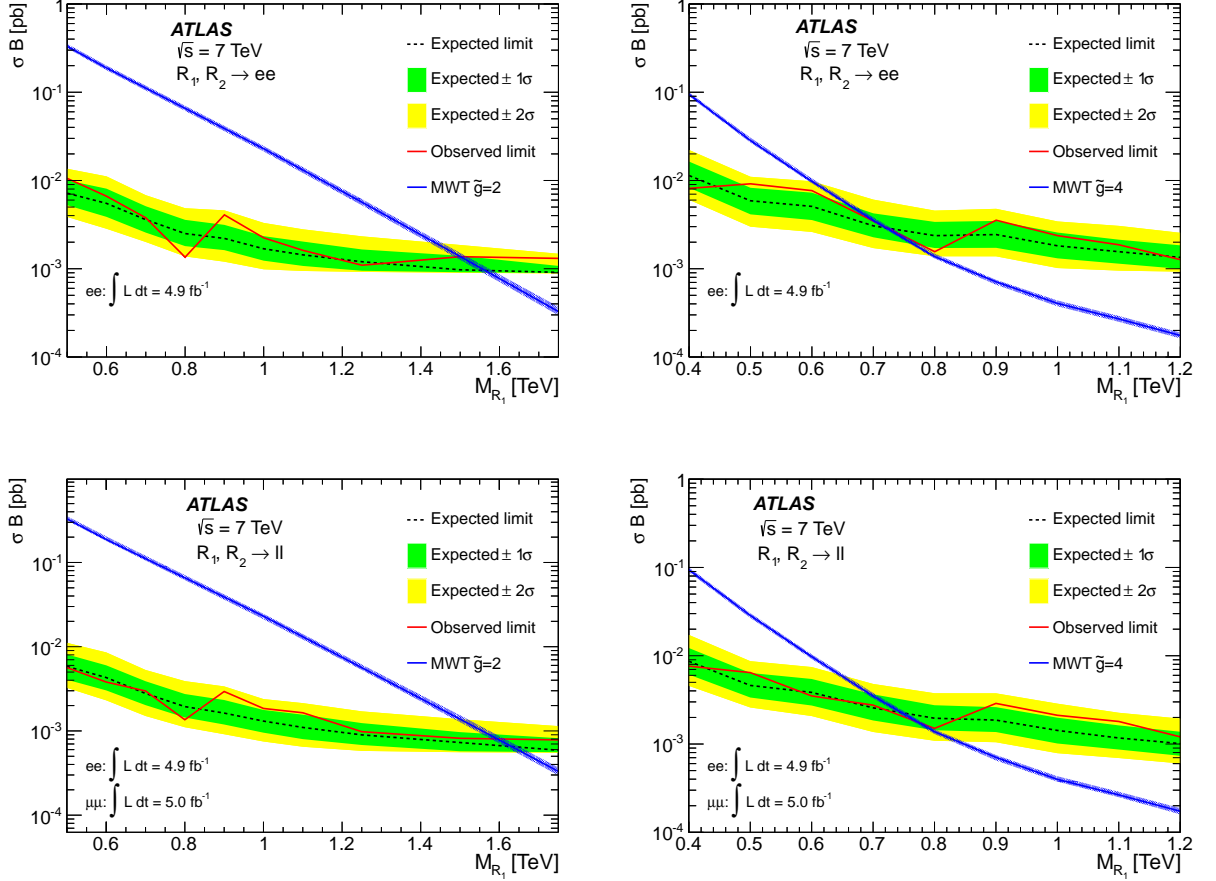
Figure 5.27: Expected and observed 95% C.L. limits on σB for $R_{1,2}$ production as a function of $m(R_1)$ for the electron channel (top) and for the combination of the dielectron and the dimuon decay channels (bottom). On the left side MWT limits for the benchmark coupling point $\tilde{g}=$ 2 and on the right side for $\tilde{g}= 4$. In the plots the thickness of the theoretical curve represents the systematic uncertainties on the signal cross-section.

Table 5.10: Combined mass limits at 95% C.L. on the M_A parameter with varying coupling.

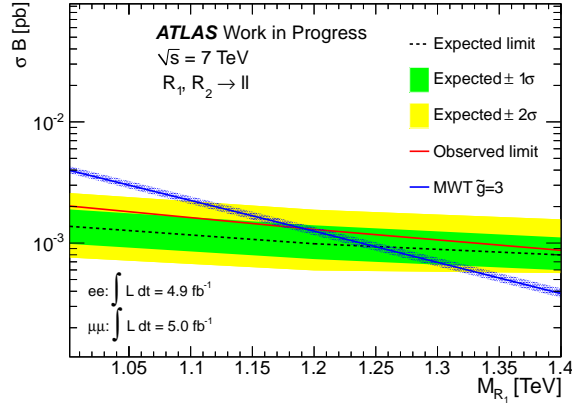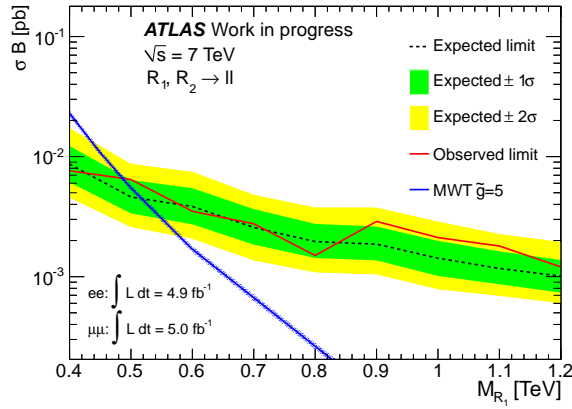| $\tilde{g}$	6	5	4	3	2
Observed limit [GeV]	359.4	485.1	767.6	1175.2	1565.7
Expected limit [GeV]	351.8	515.9	741.9	1233.5	1604.6

(a) $\tilde{g} = 3$

(b) $\tilde{g} = 5$
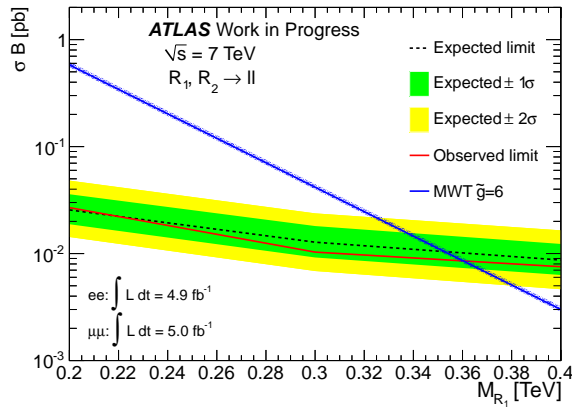
(c) $\tilde{g} = 6$

Figure 5.28: Expected and observed 95% C.L. combined limits on σB for $R_{1,2}$ production as a function of $m(R_1)$ for the combination of the dielectron and the dimuon decay channels. The different limit plots corresponds to different value of the coupling $\tilde{g}$. In the plots the thickness of the theoretical curve represents the systematic uncertainties on the signal cross-section.
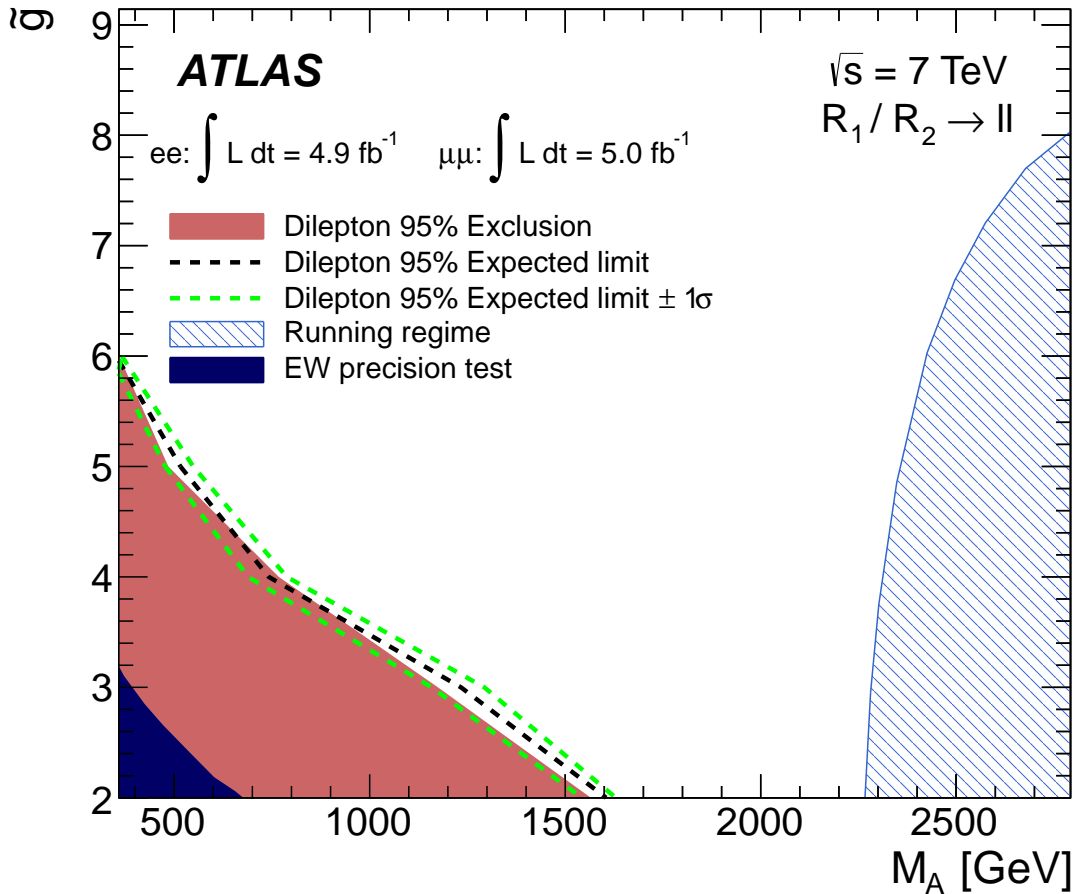
Figure 5.29: Bounds in the $(M_A, \tilde{g})$ plane of the MWT parameter space: (i) The 95% C.L. measurement of the electroweak precision parameters W and Y excludes the area in the left bottom corner. (ii) Imposing the modified Weinberg Sum Rules excludes the uniformly shaded area in the right corner (Running Regime). (iii) The shaded red area (dashed black line) shows the observed (expected) exclusion at 95% C.L. in dilepton channel, with $m_H = 200$ GeV and $s = 0$.

5.8   Conclusions

To conclude, a search for technimesons in the high masses of the dilepton spectrum with $\sqrt{s} = 7$ TeV proton-proton collision data has been presented. The search methodology and the final results are included in the ATLAS searches for heavy dilepton resonances reported in Reference [106]. The observed invariant mass spectrum is consistent with the SM expectation. No evidence for a TC signal is observed in 4.91 fb^{-1} (4.98 fb^{-1}) of data for the *ee* ($\mu\mu$) channel. Limits are set on the cross-section times branching fraction of technimesons in the LSTC and MWT scenarios. Also exclusion region on the parameter phase space in 2D are evaluated.

In the Low-scale Technicolor model the $m_{\pi_T} : m_{\rho_T/\omega_T}$ parameter space is limited at 95% CL for $m(\rho_T/\omega_T)$ between $250 - 840$ GeV and for $m(\pi_T)$ between $50 - 840$ GeV. The hypothesis of signal at $m(\rho_T) = 290$ GeV and $m(\pi_T) = 160$ GeV as suggested in Reference [42] was excluded. These limit results are more stringent than the Tevatron and previous LHC limits, and for the first time in the LHC era, direct limit are set on technimesons within the Minimal waking Technicolor model. In the MWT model the $M_A : \tilde{g}$ parameter space is excluded at 95% CL for M_A between 360 GeV and 1500 GeV for a $\tilde{g}$ values corresponding to 6 and 2, respectively. To note that some checks were performed to verify how changing the mass of the H particle (m_H), within the MWT model, from 200 GeV to 125 GeV changes the current results. It was verified that changing the m_H almost does not change the width of the R_1 and R_2 resonances. And the impact on the predicted production cross-section is less than 1% for the $\tilde{g}$=2 hypothesis in the whole R_1 mass range scanned $[500 - 1750]$. In the $\tilde{g}$=4 case the impact on the cross-section is $\sim 5\% - 10\%$ for low R_1 masses $[400 - 800]$ but again around 1% for high R_1 masses $[1000 - 1200]$ where both the R_1 and R_2 contribution are taken into account. It is then possible to conclude that changing the m_H value does not change the current limit on the MWT model since all those cross-section variations are within the theoretical uncertainty evaluate for the PDF set choice.

Conclusion

The Large Hadron Collider offers the possibility to answer to the open questions and to probe the Standard Model at new kinematic regions unreachable before. The ATLAS experiment is one of the main experiments at the LHC and it has been built with very high performance detectors in order to sustain the huge collision rate and to collect and precisely reconstruct the interesting events for physics analysis. In the 2011 the ATLAS experiment has collected about 5 fb^{-1} of proton-proton collisions at $\sqrt{s} = 7$ TeV. This data-sample allowed to perform the commissioning of the detector, to study the physics object reconstruction performances and finally to search for new physics phenomena.

A study on the LAr timing alignment was performed with the 2011 collision data. After the latest timing adjustment the global timing alignment of the whole LAr calorimeter is better than one ns for all the LAr partitions, and the EMB time resolution below a ns level is reached.

The Tag-and-probe method using $Z \rightarrow ee$ decays have been employed to measure electron reconstruction and trigger efficiencies from data. Trigger efficiencies have been measured for electrons passing at least the *medium* identification cuts and the *medium* plus B-layer hit requirement. The trigger measurements have confirmed the very high plateau efficiency of the *2g20_loose* trigger. For the electron identification efficiency additional SF (ratios between measured efficiency in data and predicted efficiency by MC) for the *medium* plus B-layer hit requirement are provided with the precision better then 1%. Additional SF are also calculated for two different isolation requirement $E_T$cone20 < 7 GeV and $E_T$cone40 < 9 GeV and the efficiency measurements have confirmed that there are no significant differences between data and MC in the energy range accessible with data.

Finally, a search for resonant deviations from the Standard Model in the high masses of the dielectron spectrum with $\sqrt{s} = 7$ TeV proton-proton collision data has been presented. The observed invariant mass spectrum is consistent with the SM expectation. No evidence for a TC signal is observed in 4.91 fb^{-1} (4.98 fb^{-1}) of data for the ee ($\mu\mu$) channel. Limits are set on the cross-section times the branching fraction of technimesons in two different Technicolor scenarios Low-scale Technicolor (LSTC) and the Minimal Walking Technicolor (MWT). Exclusion regions in the parameters phase space were also evaluated. In the Low-scale Technicolor model the $m_{\pi_{TC}} : m_{\rho_{TC}/\omega_{TC}}$ parameters space is excluded at 95% CL for $m(\rho_{TC}/\omega_{TC})$ between $250 - 840$ GeV and for $m(\pi_{TC})$ between $50 - 840$ GeV. These limit results are more stringent than the Tevatron and previous LHC limits. Moreover the hypothesis of signal at $m(\rho_T) = 290$ GeV and $m(\pi_T) = 160$ GeV as suggested in Reference [42] to explain the excess of data in the di-jet mass spectra in the $W + jj$ final state by the CDF experiment is excluded with this result at 95% of CL.

For the first time in the LHC era direct limits are also set on technimesons within the Minimal

waking Technicolor model. In the MWT model the $M_A : \tilde{g}$ parameter space is excluded at 95% CL for M_A between 360 GeV and 1500 GeV for the coupling $\tilde{g}$ corresponding to 6 and 2, respectively.

To note that some checks were performed to verify how changing the mass of the H particle (m_H), within the MWT model, from 200 GeV to 125 GeV changes the current results. It was verified that changing the m_H almost does not change the width of the R_1 and R_2 resonances. And the impact on the predicted production cross-section is less than 1% for the $\tilde{g}$=2 hypothesis in the whole R_1 mass range scanned $[500 - 1750]$. In the $\tilde{g}$=4 case the impact on the cross-section is $\sim 5\% - 10\%$ for low R_1 masses $[400 - 800]$ but again around 1% for high R_1 masses $[1000 - 1200]$ where both the R_1 and R_2 contribution are taken into account. It is then possible to conclude that changing the value of the m_H parameter does not change the current limit on the MWT model since all those cross-section variations are within the theoretical uncertainty evaluate in the analysis for the PDF set choice.

Appendix A

The ATLAS electron and photon Triggers

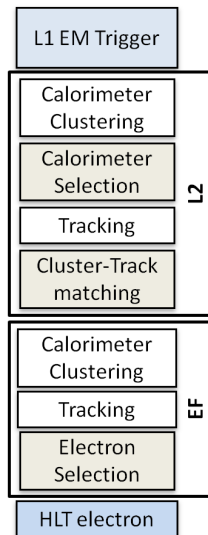Figure A.1 shows a schema of the electron trigger chain.

Figure A.1: The electron trigger chain.

At L1 electron and photon clusters are triggered using a hardware based information from the EM and hadronic calorimeter system in the form of so-called *Trigger Towers* (TT) [59] a projective region of the calorimeter over which signals are summed to provide input to L1. The TTs have a size of approximately $\Delta\eta \times \Delta\phi = 0.1 \times 0.1$ in the central part of the calorimeter, $|\eta| < 2.5$, and are larger and less regular in the more forward region. In those regions the cells are summed over the full depth of either the EM or hadronic calorimeter. The L1 selection for EM-clusters is based on a sliding window algorithm which looks for local maxima in a 4×4 group of TT. The trigger object is considered to contain an electron or photon candidate if the central 2×2 *core*-region consisting on both EM and hadronic towers is a local E_T maximum and if contains one pair of neighboring TT with a combined energy that passes the threshold [59]. Figure A.2 shows a schematic view of the calorimetric L1 algorithm.

At L2, the e/γ calorimeter algorithms build clusters within the RoI ($\Delta\eta \times \Delta\phi = 0.4 \times 0.4$)
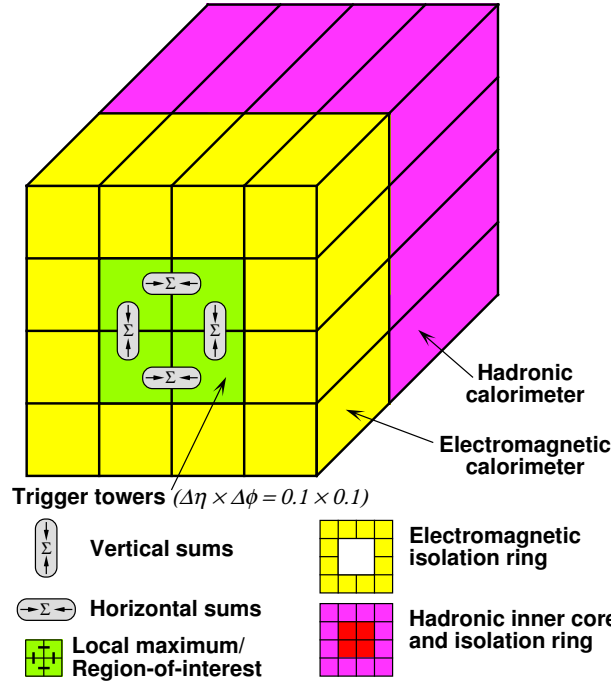
Figure A.2: A scheme of the L1 algorithm to find EM RoIs [58].

defined by the L1. Due to the tight time constraints, the L2 algorithm uses only the the second layer of the EM calorimeter to find a cell with the largest deposited transverse energy in the L1 RoI. This cell is called the pre-seed. The final cluster position is obtained by calculating the energy weighted average cell positions on a 3×7 grid centred on the pre-seed. In order to accumulate the energy, two cluster sizes are used, following the same policy used by the offline electron reconstruction: 3×7 ($\Delta\eta \times \Delta\phi = 0.075 \times 0.175$) cells grid when the cluster is the barrel ($|\eta| < 1.4$) and 5×5 ($\Delta\eta \times \Delta\phi = 0.125 \times 0.125$) when the cluster is in the end-cap ($1.4 < |\eta| < 2.47$). Several corrections which are completely based on the offline reconstruction are used at L2 in order to improve the resolution of the cluster position and energy among other quantities. If all the criteria for calorimeter based electrons are fulfilled, a search for tracks is performed in the region in front of the cluster. The electron trigger candidates are identified by the presence of a matching reconstructed track.

At the EF, offline-like algorithms are used for the reconstruction of electron and photon candidates (see chapter 4 for details). After retrieving the cell information from a region slightly larger than the RoI, the EF uses the offline sliding window algorithm [76] to build the cluster and apply all the offline based corrections.

During the 7 TeV proton-proton collision data taking period, the trigger menu continuously evolved in order to fully benefit from the increasing LHC luminosity. Initially, the trigger relied on the L1 decision only while the HLT decisions were recorded but not used to reject events. As the luminosity increased, the HLT began actively rejecting events with higher and higher E_T thresholds and more stringent selections. A detailed description of the trigger configuration and selection criteria applied in 2010/2011 data taking can be found in Refs. [107, 108].

Table A.1 shows the rates of the main single electron, di-electron and photon triggers, widely used in ATLAS physics analyses, and how they evolved in the 2011 pp collision run. When referring to the electron and photon chain the L1 seed has "EM" as a prefix, so L1_EM14 refers

Trigger Signature	L1 Seed	Luminosity Range of Validity ($cm^{-2}s^{-1}$)	L1 Rate (Hz)	L2 Rate (Hz)	EF Rate (Hz)
Single electron triggers					
e20_medium	EM14	up to 2×10^{33}	7300	273	50
e22_medium	EM16	$2 - 2.3 \times 10^{33}$	5700	273	45
e22vh_medium1	EM16VH	from 2.3×10^{33}	3600	150	22
Double electron triggers					
2e10_medium	2EM5	up to 0.7×10^{33}	13600	83	1.6
2e12_medium	2EM7	$0.7 - 1.5 \times 10^{33}$	5900	36	0.9
2e12T_medium	2EM10	$1.5 - 2.3 \times 10^{33}$	2100	36	0.9
2e12Tvh_medium	2EM10VH	from 2.3×10^{33}	800	36	0.9
Single and double photon triggers					
g60_loose	EM30	up to 0.7×10^{33}	760	17	8
g80_loose	EM30	from 0.7×10^{33}	760	9	3.4
2g20_loose	2EM14 (2EM12)	all year 2011	780 (1450)	5	2.5

Table A.1: Lowest threshold, unprescaled, electron and photon triggers, with their L1 seeds and their corresponding rates for physics data taken in 2011 in a given 'Luminosity Range of Validity' (i.e. luminosity range when they were used as primary triggers for physics analysis), at peak luminosity normalized to L=$1.0 \times 10^{33} cm^{-2}s^{-1}$.

to the electron and photon L1 trigger item with a 14 GeV threshold.

The terminology used for the trigger signature column is the following:

- *2g20_loose*, for example, stands for two photon objects with $E_T > 20$ GeV at EF and *loose* identification requirements;
- *e20_medium* is a single electron trigger with a threshold of 20 GeV and *medium* identification criteria.

The rates of single electron triggers were controlled by changing the thresholds or applying different sets of selection cuts to keep constant the total e/γ trigger rate as the LHC instantaneous luminosity increased. For example in the 2011 data taking, the HLT selection had to be tightened to reduce the strain on the L2 computational resources and keep the EF output rate at about 400 Hz on average per LHC fill. To do that, the L2 identification selections of *medium* and *tight* electron triggers were tightened to become increasingly close to the EF requirements. Furthermore, the EF threshold was slightly raised from 20 GeV to 22 GeV on the single electron trigger in August 2011 (when the luminosity exceeded $2 \times 10^{33} cm^{-2}s^{-1}$); subsequently in September (for luminosities $\geq 3 \times 10^{33} cm^{-2}s^{-1}$) the electron identification requirements were also tightened so as to avoid raising the threshold, i.e. from *medium* to *medium1*. The *medium1* requirements include tighter cuts on shower shapes and additional requirements on the track. The online *medium1* identification has been defined to trigger on electrons satisfying the offline robust *medium* identification (see Chapter 4 and Section 4.1.2 for more details). When the instantaneous luminosity delivered by LHC exceeded $2.5 \times 10^{33} cm^{-2}s^{-1}$ a hadronic leakage requirement and a variable threshold setting following the coarse L1 calorimeter cluster granularity were incorporated to some L1 triggers. Therefore the two letters *vh* were added to the HLT triggers seeded by L1 thresholds with η-dependent thresholds and the hadronic leakage requirement, e.g. *e22vh_medium1*. Photon trigger selection remained stable and loose throughout 2011, however the threshold of the unprescaled single photon trigger was raised from 60 GeV to 80 GeV at a luminosity of $1 \times 10^{33} cm^{-2}s^{-1}$.

Appendix B

Energy scan at the FEB level
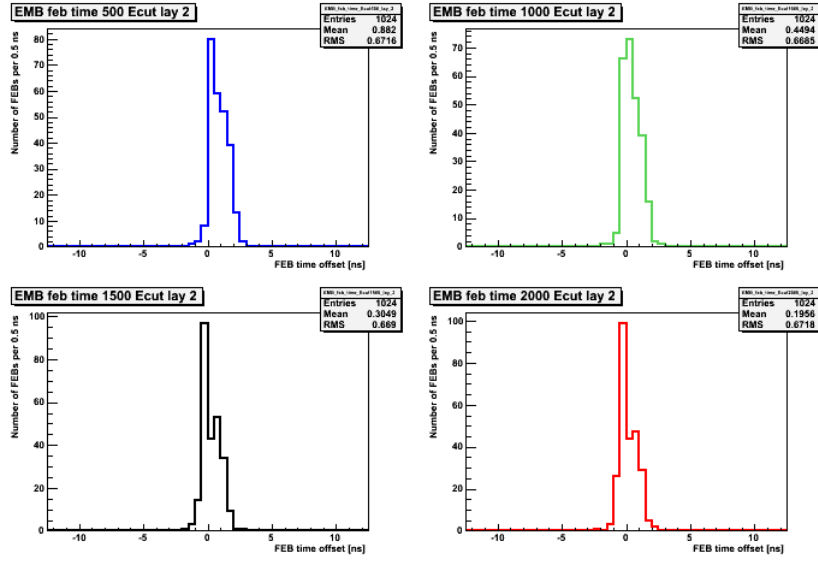
(a) EM Barrel

Figure B.1: The $< time >_{FEB}$ for the EM Barrel Layer 2 computed using four different energy cut: $500, 1000, 1500, 2000$ MeV.

To reduce the bias of the energy versus time tail on the $< time >_{ch}$ and $< time >_{FEB}$ measurement, only the time computed for channels with a energy above a certain threshold are selected.

Two effect should be taken in to account to choose the better energy threshold. In fact on one hand the timing resolution, and thus the time measurement, improves with energy, but on the other hand it should considered that the single channel occupancy decrease with energy and to get a consistent $< time >_{ch}$ a relevant statistic is needed.

To find the optimal value for the energy cut to apply, a energy scan at the level of $< time >_{FEB}$ is performed for each layer of each LAr sub-detector. In Figure B.1 is shown the $< time >_{FEB}$ for the FEBs in the EMB Layer 2 computed using four different energy cut 500, 1000, 1500, 2000 MeV. The different in the shape and in the mean value of those distributions is due to the fact that the $< time >_{ch}$ is affected by the worst time resolution of the channels with a low energy. Figures B.1 and B.2 show the mean of the $< time >_{FEB}$ for the different layer for

125

all the LAr partitions for each energy cut scanned.

The energy threshold used in the 2011 timing analysis are chosen from the distributions in
Figure B.2 (for each subsystem) as the lower values for which the mean of the FEBs time offset
stay constant while the single channel time distribution maintains reasonable statistics.

(a) EM Barrel

(b) EMEC Outer

(c) EMEC Inner

(d) HEC

(e) FCal

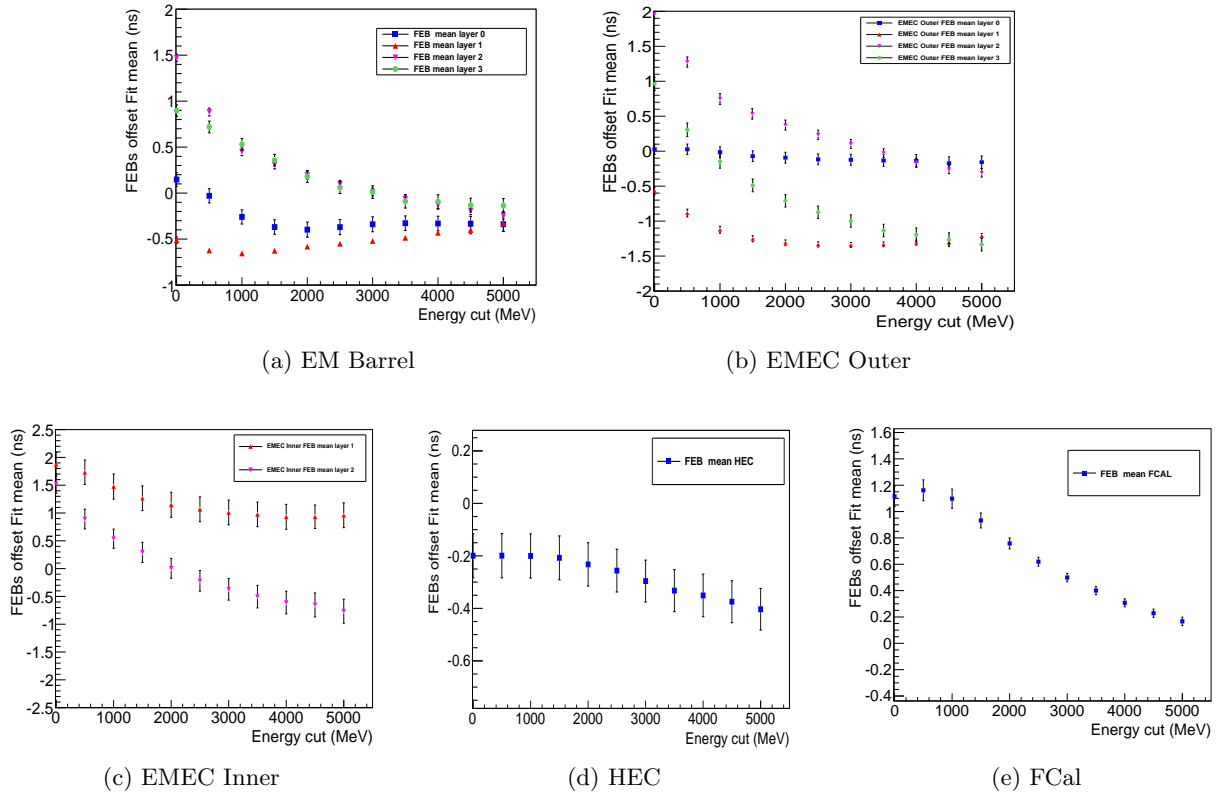Figure B.2: The mean of the FEB average time, $< time >_{FEB}$, for all the FEBs in the different
layer for the EMB (a) and EMEC (b,c) and for all the FEB in the HEC (d) and FCal (e) calorimeters
computed for each energy cut scanned. The errors on the plot correspond to the RMS of the FEB
average time distribution over the square root of the total number of entries.

Appendix C

Trigger matching comparison in the *tag* selection

As described in Chapter 4 in Section 4.2.1, the electron trigger efficiency is calculated with a data-driven method called tag-and-probe using $Z \rightarrow e^+e^-$ events selected in the full 2011 data set. Data-driven methods can be used for the estimation of the trigger efficiency relative to an offline electron selection.

The goal of this study is to investigate in detail the efficiency of the *2g20_loose* double-photon trigger relative to the offline selection described in Section 5.3, and calculate the trigger *scale factor* (data over MC efficiency) to correct any discrepancies between data and MC simulation.

The tag-and-probe method ideally consists of selecting a clean sample of $Z \rightarrow e^+e^-$ events using one electron (*tag*) to identify the event as a $Z \rightarrow e^+e^-$ one and then measuring the efficiency of interest using the second electron (*probe*). The purity of the sample is inferred from the dielectron invariant mass distribution cut.

In this section the idea is to verify the effects of the *2g20_loose* trigger efficiency, by selecting *tag* electron matched with either *g20_loose*[1] single-photon trigger or with *e2*_medium*[2] single-electron trigger. An offline electron is considered to match an online (EF Trigger object) electron if the distance between them in the (η, ϕ) space is $\Delta R = \sqrt{(\Delta\eta^2 + \Delta\phi^2)} < 0.15$.

Following the preselection described in Section 4.2 the following steps are performed for two different *tag* match hypothesis, for about half of the full 2011 data-set (period B-K2):

1. *g20_loose* matched *tag*:
   - Select events that pass the *g20_loose* single photon trigger and the standard preselection;
   - Require one *tight* electron to be matched to one *g20_loose* object at L1 and at EF level. This electron is considered to be a *tag* electron;
   - All the other electrons which pass the *medium* and the B-layer offline selection criteria are regarded as *probe* electrons;

2. *e2*_medium* matched *tag*:
   - Select events that pass the *e2*_medium* single electron trigger and the standard preselection;

---

1. Prescaled to 2Hz for almost the whole 2011 data taking

2. This trigger items was kept in the main trigger menu only for data periods from B to K, corresponding to about $\sim 2.5fb^{-1}$ of data. *e2*_medium* is different for the different data periods, namely *e2*_medium* for period B to K1 and *e22_medium* for period K2.

– Require one *tight* electron to be matched to one *e2*_medium* object at L1 and at EF level. This electron is considered to be a *tag* electron;

– All the other electrons which pass the *medium* and the B-layer offline selection criteria are regarded as *probe* electrons;

The trigger efficiency in both the *tag* match configuration, is computed as the ratio between the number of *probe* electrons matching the *2g20_loose* trigger object and the total number of offline *probe* electrons in bins of η and E_T.
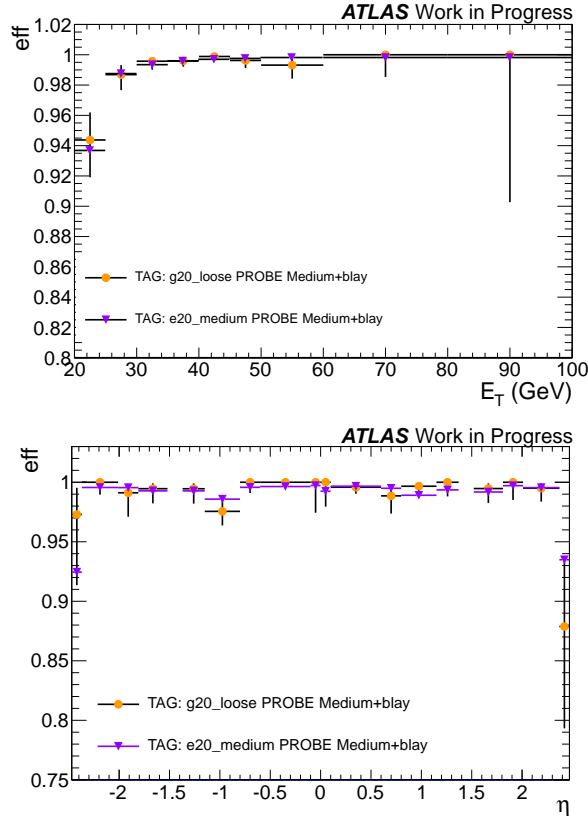

Figure C.1: For the *tag* electron matched with the *g20_loose* or the *e2*_medium* trigger items. Data efficiencies comparison with respect to offline *medium* plus B-layer *probe* electrons for *2g20_loose* trigger measured as a function of the offline electron E_T, and the offline electron η with $|\eta| < 2.47$ and $E_T > 25$ GeV, for both case the transition region between the barrel and endcap EM calorimeters are excluded. Note that about $\sim 50\%$ of the 2011 data are used, corresponding to $\sim 2.7 fb^{-1}$.

Figure C.1 shows the comparison of the *2g20_loose* di-photons trigger efficiency for offline *medium* plus B-layer electrons obtained with the two different *tag* electron matched choices. Within the statistical uncertainty no different are seen on the *2g20_loose* di-photons trigger efficiency. Statistics is limited for the sample selected with the *g20_loose* items because this trigger was prescale to 2Hz for almost the whole 2011 data taking which leads to $\sim 10\%$ uncertainty in some bins.

In Table C.2 and Table C.1 for each E_T and η bins the *2g20_loose* trigger efficiency for data with respect to *medium* plus B-layer selections is compared between the different *tag* selection.

From this study one can see that a *tag* electron matched to an EF object fulfilling the

e2*_medium trigger selection is almost 100% efficient with respect to the *g20_loose* matching and that the two methods give compatible results.

Table C.1: For the *tag* electron matched with the *g20_loose* or the *e2*_medium* trigger items: for data *2g20_loose* trigger efficiency as a function of E_T respect *medium* plus B-layer electrons selections. The uncertainties displayed are only statistical.

p_T [GeV]	*g20_loose* tag *medium* + B-layer	*e2*_medium* tag *medium* + B-layer
20,25	0.944 ±0.043	0.936 ±0.002
25,30	0.986 ±0.019	0.987 ±0.001
30,35	0.997 ±0.007	0.993 ±0.001
35,40	0.998 ±0.005	0.996 ±0.001
40,45	0.998 ±0.004	0.997 ±0.001
45,50	0.997 ±0.007	0.997 ±0.001
50,60	0.989 ±0.013	0.998 ±0.002
60,80	0.998 ±0.022	0.998 ±0.001
80,100	0.998 ±0.185	0.998 ±0.002

Table C.2: For the *tag* electron matched with the *g20_loose* or the *e2*_medium* trigger items: for data *2g20_loose* trigger efficiency as a function of η respect *medium* plus B-layer electrons selections. The uncertainties displayed are only statistical.

η	*g20_loose* tag *medium* + B-layer	*e2*_medium* tag *medium* + B-layer
-2.47,-2.37	1.000 ±0.089	0.924 ±0.004
-2.37,-2.01	1.000 ±0.015	0.995 ±0.001
-2.01,-1.81	1.000 ±0.024	0.995 ±0.001
-1.81,-1.52	0.991 ±0.021	0.993 ±0.001
-1.37,-1.15	0.992 ±0.019	0.993 ±0.001
-1.15,-0.8	0.977 ±0.016	0.986 ±0.001
-0.8,-0.6	1.000 ±0.014	0.996 ±0.001
-0.6,- 0.1	1.000 ±0.038	0.996 ±0.001
-0.1,0.0	1.000 ±0.038	0.997 ±0.001
0.0,0.1	1.000 ±0.030	0.992 ±0.001
0.1,0.6	0.997 ±0.008	0.997 ±0.001
0.6,0.8	0.982 ±0.029	0.995 ±0.001
0.8,1.15	0.995 ±0.012	0.989 ±0.001
1.37,1.52	1.000 ±0.017	0.993 ±0.001
1.52,1.81	0.991 ±0.019	0.992 ±0.001
1.81,2.01	1.000 ±0.023	0.997 ±0.001
2.01,2.37	0.992 ±0.018	0.995 ±0.001
2.37,2.47	0.916 ±0.100	0.935 ±0.004

Appendix D

Electron Identification efficiency

D.1 Electron Isolation variables

As described in Chapter 4 in Section 4.2.2, efficiency measurements for the B-layer hit requirement and for two different isolation cuts ($E_T$cone20 < 7 GeV and $E_T$cone40 < 9 GeV), are evaluated using the tag-and-probe method with $Z \rightarrow e^+e^-$ events selected in the full 2011 data set.

From those tag-and-probe results a small hint of efficiency drop is observed for the isolation efficiencies as function as the E_T of the *probe* electrons. Figure D.1 shows the sum of the transverse energy deposition around the *probe* electrons direction in the isolation cone with radius 20 ($E_T$cone20) and with radius 40 ($E_T$cone40) for data and for $Z \rightarrow ee$ MC simulation. The residual small shift between the data and the MC distributions is due to the corrections for the transverse shower leakage and the pile-up contribution on the $E_T$coneXX variable which are tuned on data and apply to both distribution.
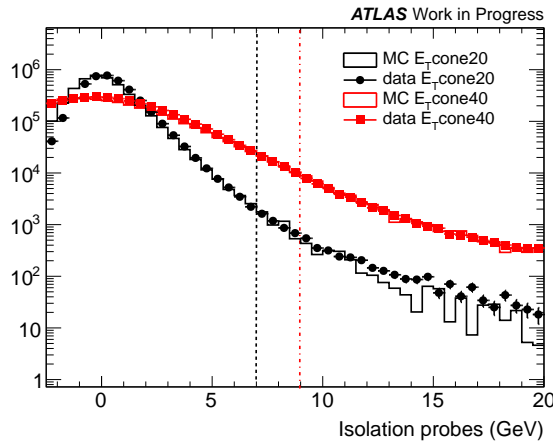
Figure D.1: The Calorimeter isolation variable, $E_T$coneXX, for two different cone size (20 and 40) for *probes* electron in data and in MC. In the plot are displayed as well two horizontal lines which corresponds to the cuts applied on those variables: in black $E_T$cone20 < 7 GeV and in red $E_T$cone40 < 9 GeV.

Even though the calorimeter isolation variables are in principle corrected for the E_T dependence of the energy leakage in the cone, it is verified that both the $E_T$cone20 and the $E_T$cone40 distributions still have a small dependence from the E_T of the electrons. Figure D.2 shows

the $E_T$cone20 (a) and the $E_T$cone40 (b) distributions for different E_T *probe* bins. A shift on
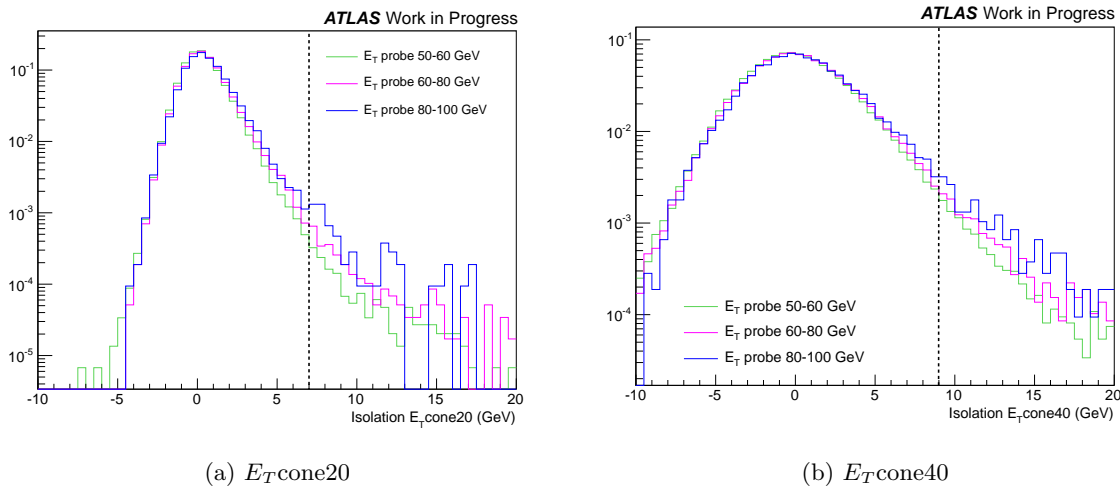

(a) $E_T$cone20

(b) $E_T$cone40

Figure D.2: $E_T$coneXX distribution on data for different *probe* electrons E_T bins.

the $E_T$coneXX distributions is shown as function of the E_T of the *probe* electron, which cause at the percent level a decrease in the efficiencies as function of the electrons E_T. This effect is higher for the $E_T$cone40 case since a bigger isolation cone is chosen and the distribution is broader.

D.2 Electrons Identification efficiency for higher E_T bins

With the tag-and-probe procedure only electrons with E_T up to 100-200 GeV can be probed. The data/MC corrections computed with the tag-and-probe procedure are assume valid also for electrons with $E_T > 200\,\text{GeV}$. The electron identification SFs computed in Section 4.2.2 evaluated as function of the η and E_T of the *probe* candidates, are very close to one. Nevertheless a small trend in the highest E_T bins on the SF(E_T) in Figure 4.9 is present. To verify if this small trend is a feature due to the statistic of the samples or it is a real feature of the MC simulation the electrons identification efficiency for the B-layer hit requirement and for the two different isolation cuts are calculated for higher E_T bins in data and in MC simulation.

The last two bins of the identification efficiencies shown in Figure D.3, e.g $100 - 150$ GeV and $150 - 250$ GeV break the falling trend for the SFs that was seen in the lower E_T bins as is visible in Figures D.4 and in Table D.1. The last three E_T bins have a larger errors, which is still $\sim 1\%$ in the last one. The uncertainties on the SF(E_T) are dominated by the systematic uncertainties evaluated from the data efficiencies as explained in Section 4.2.2.

Based on this check is possible to conclude that the obtained SFs, computed for the B-layer hit requirement and the B-layer hit and $E_T$coneXX isolation requirement, are almost one also for high E_T electrons within an error of 1%, and no significant trend with respect to the E_T of the electrons is observed in data in this range.
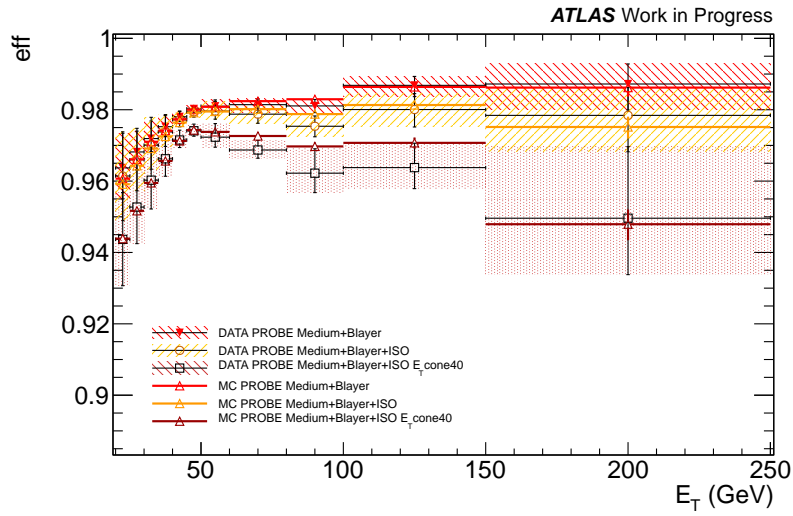
Figure D.3: Data and MC electron identification efficiencies of the B-layer hit requirement, of the B-layer hit plus $E_T$cone20 isolation requirement, and of the B-layer hit plus $E_T$cone40 isolation requirement. For the data points the errors evaluated in the plot take into account both the statistical and the systematic uncertainties.

Figure D.4: SF for the identification efficiencies for *medium* plus B-layer electrons and *medium* plus B-layer and $E_T$cone20 and $E_T$cone40 isolation requirement as a function of the electron E_T bins. The errors evaluated in the plots take into account the statistical and systematic uncertainties.

Table D.1: E_T *scale factors* of the *medium* plus B-layer, B-layer plus $E_T$cone20 isolation, and B-layer plus $E_T$cone40 isolation requirement. The quoted uncertainties are the sum of systematic and statistical uncertainty added in quadrature.

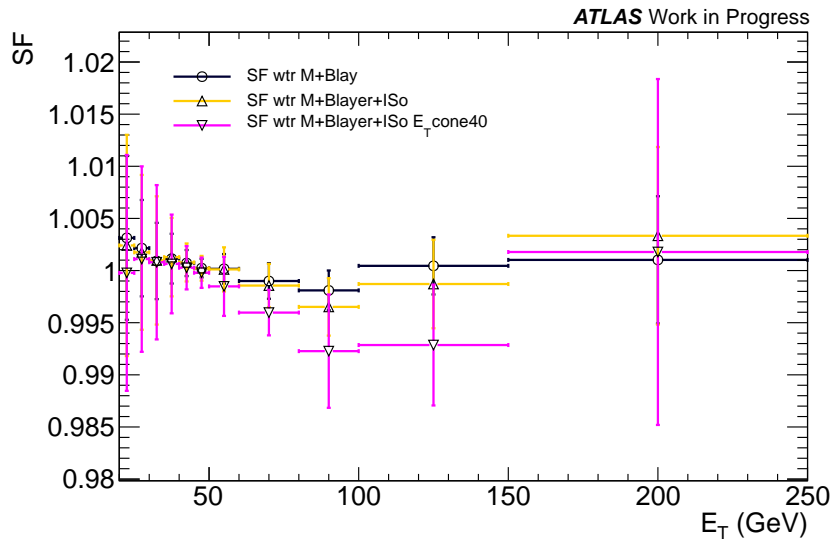| E_T [GeV]	B-layer only	B-layer and $E_T$cone20 isolation	B-layer and $E_T$cone40 isolation
20-25	1.0031 ± 0.0078	1.0024 ± 0.0106	0.9998 ± 0.0113
25-30	1.0021 ± 0.0046	1.0017 ± 0.0074	1.0011 ± 0.0089
30-35	1.0009 ± 0.0036	1.0010 ± 0.0061	1.0008 ± 0.0074
35-40	1.0011 ± 0.0024	1.0013 ± 0.0038	1.0006 ± 0.0047
40-45	1.0007 ± 0.0012	1.0008 ± 0.0018	1.0003 ± 0.0021
45-50	1.0002 ± 0.0009	1.0002 ± 0.0012	0.9998 ± 0.0014
50-60	1.0002 ± 0.0014	1.0001 ± 0.0021	0.9985 ± 0.0028
60-80	0.9990 ± 0.0017	0.9986 ± 0.0021	0.9960 ± 0.0022
80-100	0.9981 ± 0.0019	0.9965 ± 0.0027	0.9923 ± 0.0054
100-150	1.0004 ± 0.0027	0.9987 ± 0.0042	0.9928 ± 0.0058
150-250	1.0010 ± 0.0061	1.0033 ± 0.0085	1.0018 ± 0.0166

Appendix E

Performance of the very high E_T electron

E.1 Electron energy Resolution

At the energies relevant to this analysis, the resolution is dominated by the constant term, denoted c in the following parametrization: $\sigma(E)/E = a/\sqrt{E} \oplus b/E \oplus c$, where $\oplus$ represents addition in quadrature, and E is the energy in GeV. The latest constant term values measured in data using $J/\psi \rightarrow e^+e^-$ (mostly measurment of the sampling term contribution of the resolution and indirect measurement at low E_T for the constant term) and and $Z \rightarrow ee$ (high E_T) events, are $(0.97 \pm 0.02)\%$ in the barrel and $(1.64 \pm 0.06)\%$ in the endcaps [99] where the error are statistical only. The simulation is adjusted by smearing the energy to reproduce the resolution measured in data. In the end, the uncertainty on the resolution has a negligible effect. Furthermore the data energies are also corrected to take in to account the in-situ calibration measurement performed using $Z \rightarrow ee$ decays. All these corrections are derived from data at energies basically below 200 GeV. As the behavior of high energy electrons is of particular importance to the dielectron analysis described in Chapter 5, three Monte Carlo-based studies are done to investigate the expected behavior of the electron energy bias, energy resolution and the mass resolution of the reconstructed invariant mass.

The relative residual of the energy difference between a truth electron and a reconstructed electron is given by:

$$\frac{\sigma_e}{E_{truth}} = \frac{E_{truth} - E_{reco}}{E_{truth}} \tag{E.1}$$

where E_{truth} is the electron energy on generator level before QED final state radiation and E_{reco} the electron energy after QED final state radiation and the full detector simulation and digitization, i.e. the energy in the calorimeter cluster. The distribution of $\frac{\sigma_e}{E_{truth}}$ describes the energy loss of electrons through final state radiation processes and the reconstruction process. This distribution can be characterized by two variables: the energy bias derived from the mean of the distribution, describing the average shift in energy, and the energy resolution derived from the width of the distribution. The comparison between truth and reconstructed electrons is done after a number of cuts on the reconstructed electron, derived from the full event selection (described in Section 5.3) and adjusted to allow the study of single electrons:

- $\eta_{cluster}$ within the detector acceptance range ($|\eta| \leq 2.47$ and not within the crack region $1.37 \leq |\eta| \leq 1.52$)
- electron *medium* identification

– B-layer hit, if expected

– $\Delta R \leq 0.1$ between truth and reconstructed electron

The last cut is implemented to ensure that the truth and reconstructed electrons are the same electron. The distribution in Equation E.1 is then fitted iteratively with a Gaussian distribution in the range $(-2.5\sigma, +2.5\sigma)$ as a function of the true electron energy. In order to study the variations across the different calorimeter sections, the $\frac{\sigma_e}{E_{truth}}$ distribution is considered in four reagions with boundaries at $|\eta| \leq 0.8$, $0.8 \leq |\eta| \leq 1.37$, $1.52 \leq |\eta| \leq 1.81$ and $1.81 \leq |\eta| \leq 2.47$, where the missing region corresponds to the crack between the barrel and the endcap region.
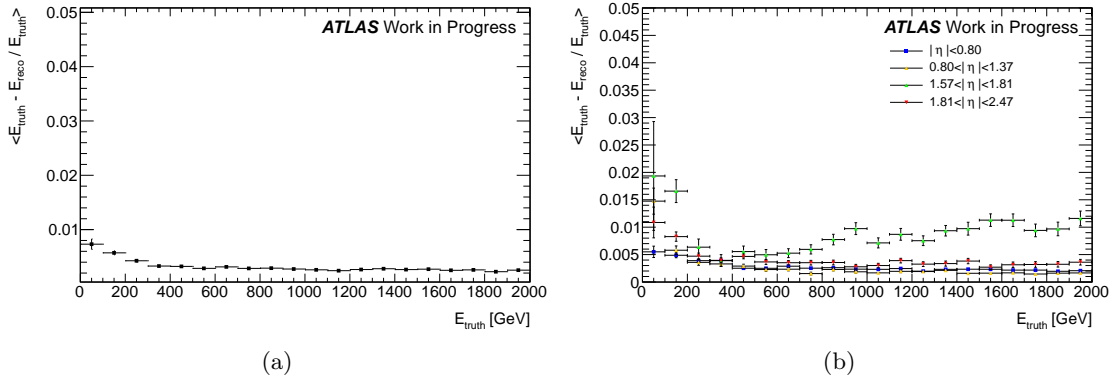

Figure E.1: Energy bias as a function of E_{truth}. (a) energy bias over full η range; (b) energy bias in η bins. The points in the plots correspond to the mean value of the $\frac{\sigma_e}{E_{truth}}$ distribution obtained with a gaussian fit.
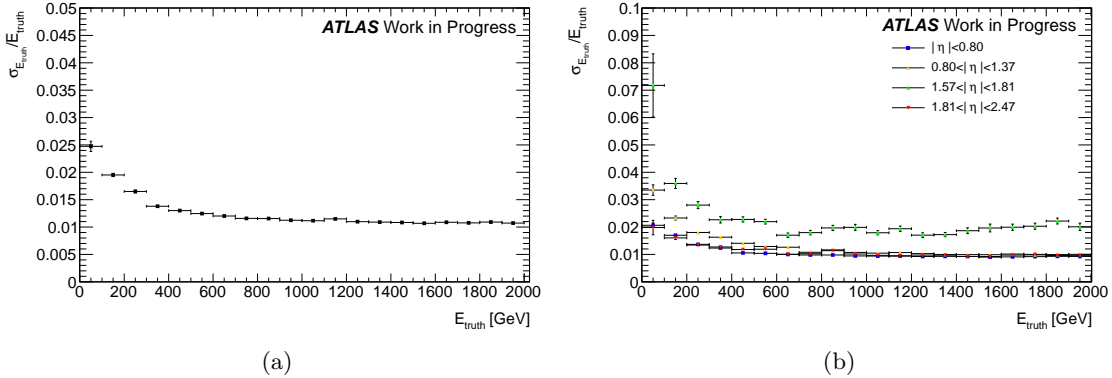
Figure E.2: Energy resolution as a function of E_{truth}. (a) energy resolution over full η-range; (b) energy resolution in η bins. The points in the plots correspond to the width of the $\frac{\sigma_e}{E_{truth}}$ distribution obtained with a gaussian fit.

The result, as shown in Figure E.1, is that the overall energy bias remains nearly constant for higher masses. Within the barrel ($|\eta| \leq 1.37$) and for upper end of the η-range of the endcap ($1.81 \leq |\eta| \leq 2.47$) the same behavior is observed, though the energy bias is increased for the endcap region. The endcap region immediately after the crack region ($1.52 \leq |\eta| \leq 1.81$), shows a rise in energy bias for higher energies, but the overall effect remains small. A further investigation into the $1.52 \leq |\eta| \leq 1.81$ region has shown that the residual distribution in that

region develops a broader tail, leading to the increased energy bias. This is understood to be an effect of the increased material after the crack region, leading to higher energy losses.

Figure E.2 shows the result of the single electron resolution determination. The variation across the different η bins is similar to the variation in the energy bias. The resolution remains constant for higher energies within the barrel ($|\eta| \leq 1.37$) and the high η part of the endcap ($1.81 \leq |\eta| \leq 2.47$) and is overall worse in region after the crack ($1.52 \leq |\eta| \leq 1.81$). As seen for the energy bias, the impact of the region after the crack on the overall resolution is small. The source of the worsened resolution, similar to the increase in the energy bias, is the broad tail in the $\frac{\sigma_e}{E_{truth}}$ distribution.
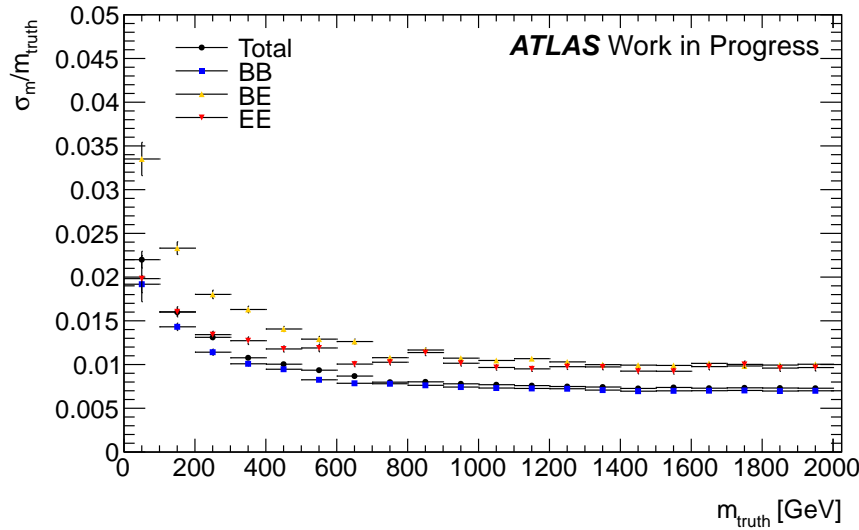

Figure E.3: Mass resolution as function of M_{truth}, showing overall mass resolution and the three possible different event configurations.

The invariant mass of a candidate event electron pair is calculated from the electron energy and momentum, where the momentum direction is derived from track measurements. Therefore, the mass resolution can differ from the energy resolution. To determine whether the behavior varies from the energy resolution, the mass resolution is determined in a procedure parallel to the determination of the energy resolution, but requiring the full event selection together with $\Delta R \leq 0.1$ between the truth and reconstructed electrons. The invariant mass of the generated electron pair was compared to the invariant mass calculated from the reconstructed electrons. The relative residual of the mass difference between truth and reconstruction is then defined as

$$\frac{\sigma_M}{M_{truth}} = \frac{M_{truth} - M_{reco}}{M_{truth}} \tag{E.2}$$

where M_{truth} is the invariant mass of the electron pair on generator level and M_{reco} the invariant mass as calculated from the reconstructed electrons. The $\frac{\sigma_M}{M_{truth}}$ distribution is then fitted iteratively with a Gaussian distribution in the range $(-2.5\sigma, +2.5\sigma)$, deriving the resolution from the width of the fit.

The mass resolution study is done for the whole η-range and for the three possible event configurations separately: both electrons in the barrel (BB), both in the endcap (EE), one in the barrel and one in the endcap (BE). The result, as shown in Figure E.3, is that the overall mass resolution remains constant at higher energies, as well as for barrel-barrel events. If one

or both electrons are in the endcap, the resolution is worsened, but the effect on the overall resolution is again small.

These MC studies shown that both energy resolution and bias are expected to improve with increasing energies. For electrons up to 0.5-1 TeV the mass resolution is verified to be $\sim 7.5 - 15$ GeV, which could allow to disentangle the two resonances structure for the TC signal in the m_{ee} spectrum (see Appendix F.2).

Appendix F

Technicolor Signal templates

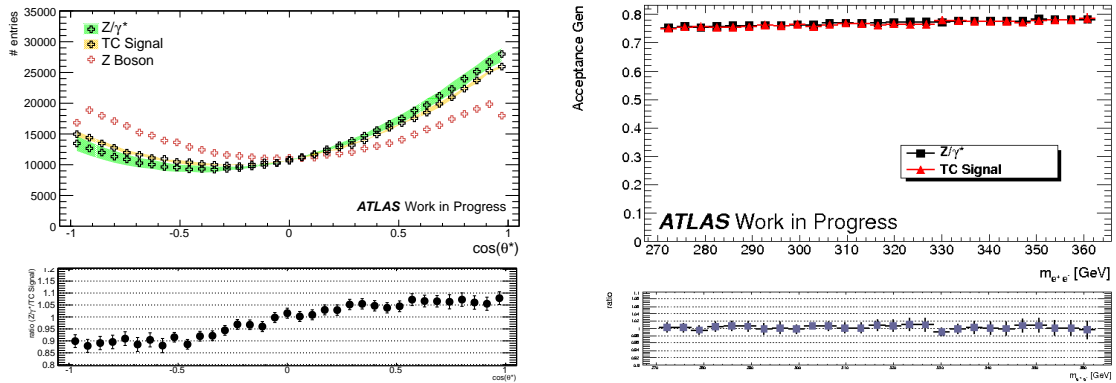## F.1 Angular distribution of TC signal

Figure F.1: On the left plot $\cos(\theta^*)$ distribution at generator level for the Z bosons, the Z/γ^*, and TC signal process, the colored bands define the variation of the $\cos(\theta^*)$ distribution for different m_{ee} values. On the right plot at generator level the total acceptance as a function of the $m(e^+e^-)$ for the Drell-Yan process and for a TC signal at 300 GeV. Note that Z/γ^* process is generated in the same mass range as the TC signal as described is section 5.1.2.

In the Z/γ^* process the presence of both vector and axial-vector couplings of the quarks and leptons to the gauge intermediate boson gives rise to an asymmetry in the polar emission angle θ of the electron in the rest frame of the e^+e^- pair. At the Z-pole the asymmetry is dominated by the couplings of the Z boson and arises from the interference of the vector and axial components of its coupling. At large invariant mass the asymmetry is dominated by Z/γ^* interference and is almost constant independent of invariant mass.

The sign of $\cos\theta$ is not directly measurable, since the original quark direction is unknown in proton-proton collisions (it can originate with equal probability from either proton). To minimize the effect of the unknown transverse momenta of the incoming quarks the electron polar angle is measured in the Collins-Soper reference frame [109]. This reference frame reduces the uncertainty in electron polar angle due to the finite transverse momentum of the incoming quarks. The particle four-vectors are transformed to the e^+e^- rest frame and the polar angle θ^* is defined as the angle between the incoming quark and the outgoing lepton in the dilepton rest frame.

$$\cos(\theta^*) = \frac{2}{m(e^+e^-)\sqrt{m^2(e^+e^-) + p_T^2(e^+e^-)}} \left[p^+(e^-)p^-(e^+ - p^+(e^+)p^-(e^-) \right] \qquad \text{(F.1)}$$

where $p\pm = \frac{1}{\sqrt{2}}(E\pm p_z)$, E is the energy and p_z is the longitudinal component of the momentum.

In all the TC signals considered, the presence of both the vector and axial-vector couplings of the quarks and leptons to an intermediate particle leads to the same forward-backward asymmetry. Figure F.1 shows, on the left, the $\cos(\theta^*)$ distributions for events with the m_{ee} close to the Z mass, for DY events and for TC events. The resulting angular distribution for the DY and the TC processes are very close since in both case there is the presence of the vector and axial-vector components of the coupling. The overall 10% difference in higher and lower value of $\cos(\theta^*)$, is verified to not affect the acceptance at generator level for the two process as is shown in the right of Figure F.1.

F.2   Linear templates

The linear templates for some signal mass points in the two different technicolor scenario are shown in Figures F.2 normalized to an unit area. In those plots the dielectron invariant mass (m_{ee}) distribution after event selection is displayed in linear scale to better see the line shape of the two resonances present in the spectrum within the detector resolution.

The log binning used to display the $m_{\ell^+\ell^-}$ discriminating variable in the statistical methods used in this analysis is quite rough: each mass bin spans 6-8 times the mass resolution. For instance, around 600 GeV, there is one bin from 598 to 640, and the next one is 640-684, so in the end the 2 peaks are in neighboring bins and look like just one, although the detector would be able to separate them (at least in the electron channel). Therefore for some mass points due to the log-binning it is not possible to distinguish the double peak structure in the TC spectrum. The linear plot in Figure F.2 shows not only the line shape for the different mass points within the detector resolution, but also the different structure for the different model taken into account.
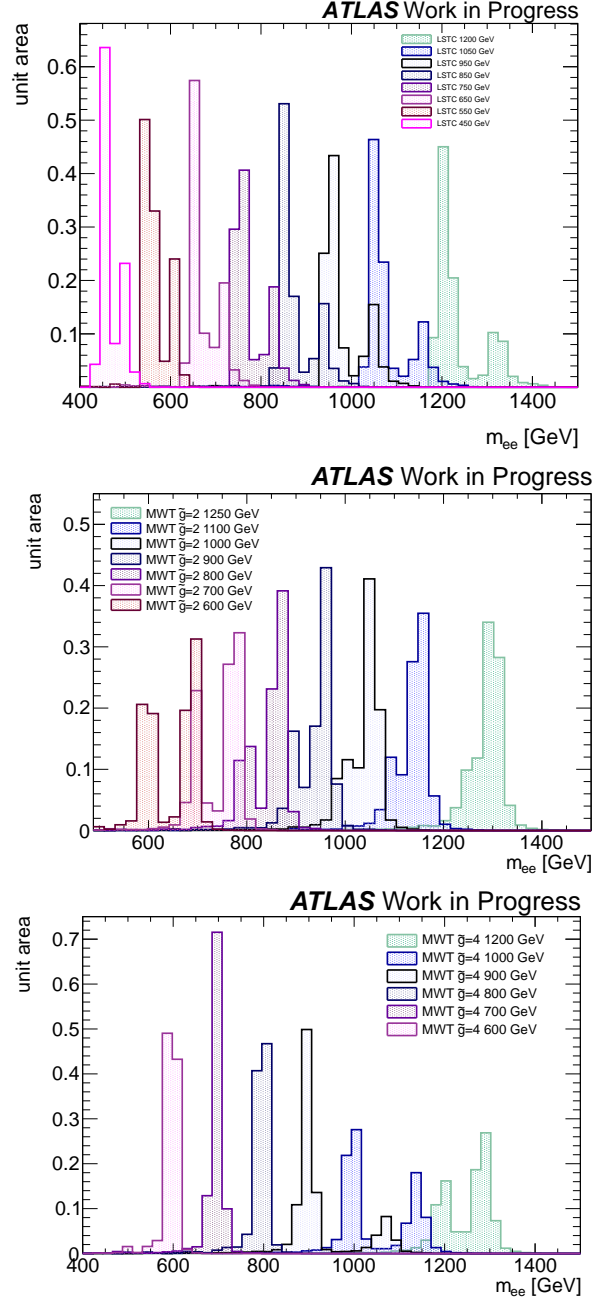
Figure F.2: Dielectron invariant mass (m_{ee}) distribution after event selection for a few TC pole masses, for the LSTC and the MWT for $\tilde{g}=2$ and $\tilde{g}=4$. In those plots the dielectron invariant mass (m_{ee}) distribution after event selection is shown in linear scale to better see the line shape of the two resonances present in the spectrum.

Appendix G

Limit results in the muon channel

In the absence of a signal, upper limits on the number of events produced by the decay of a new resonance are determined at the 95% CL. The limit on the number of signal events is converted into a limit on the ratio of cross-section times branching fraction $\sigma B(X \to \ell^+\ell^-)/\sigma B(Z \to \ell^+\ell^-)$ by dividing by the observed number of Z boson events and the ratio of corresponding acceptances. This ratio of σB is then converted into a limit on $\sigma B(X \to \ell^+\ell^-)$ by multiplying it by the theoretical value of $\sigma B(Z \to \ell^+\ell^-)$. To set the limit the Bayesian approach [103] is used. A flat prior on the signal cross-section times branching fraction (σB) is chosen. The most likely number of signal events, and the corresponding confidence intervals, are determined from a likelihood function defined as the product of the Poisson probabilities over all mass bins in the search region, using the appropriate signal templates. The systematic uncertainties are incorporated via Gaussian-distributed nuisance parameters which are integrated out.

The dimuon resonances searched for in this analysis are narrow compared to the detector resolution. Following the selection criteria described in Section 5.4.3 signal templates in the muon channel are defined including the acceptance times efficiency of the signal, at a given pole mass M_X, over the full search region. Also in the muon channel the product $\mathcal{A}\epsilon$ is different for the two TC models due to the different line-shapes. The expected exclusion limits are determined using simulated pseudoexperiments with Standard Model processes only by evaluating the 95% CL upper limits for each pseudoexperiment for each fixed value of the resonance pole mass M_X. The median of the distribution of limits is chosen to represent the expected limit. The ensemble of limits is also used to find the 68% and 95% envelopes of the expected limits as a function of M_X. The results reported in Sections 5.7.1 and 5.7.2 are the combination of the dielectron and dimuon channels. In this section the LSTC and the MWT limit on $\sigma B(X \to \mu^+\mu^-)$ are shown at the 95% CL.

The muon signal templates for the LSTC model are built assuming a $m(\rho_T) - m(\pi_T) = m(W)$ mass splitting, neglecting the contribution of the negative interference with the SM DY process. Because the intrinsic width of the ρ_T, ω_T and a_T resonances is less that 1 GeV, the observed line shape in the dimuon case is due to detector resolution alone and the ρ_T/ω_T and a_T resonances cannot be resolved. For the MWT case, in order to build the signal templates in the same way as for the electron channel the $m(\mathrm{R}_1)$ is scanned in steps of 100 GeV for different values of the coupling $\tilde{g}$. Once defined a value for $m(\mathrm{R}_1)$, $m(\mathrm{R}_2)$ and M_A are uniquely defined and a signal template is produced accordingly. Figure G.1 shows the 95% C.L. observed and expected exclusion limits on $\sigma B(\rho_T \to \mu^+\mu^-)$, together with the theoretical cross-section times branching ratio for the two TC models considered.
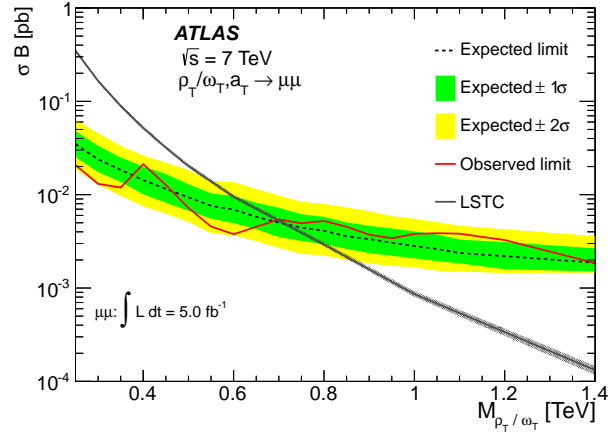
(a) LSTC
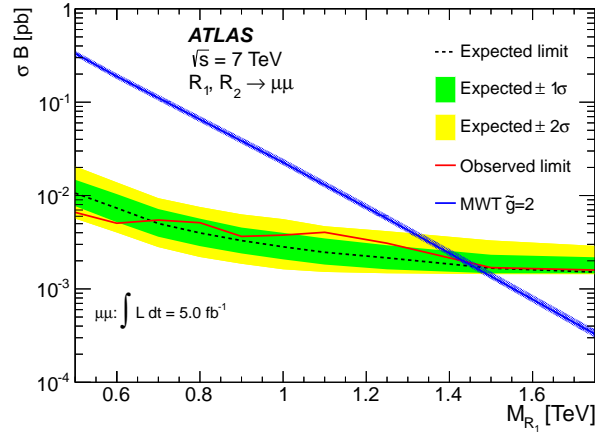
(b) MWT $\tilde{g}= 2$
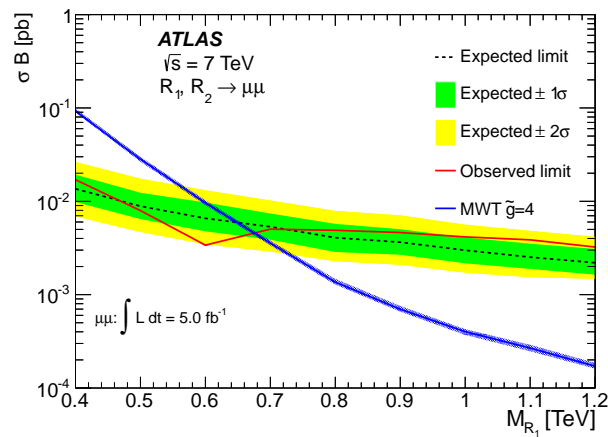
(c) MWT $\tilde{g}= 4$

Figure G.1: (a) Expected and observed 95% C.L. limits on σB and expected σB for ρ_T/ω_T production in muon decay channel. (b),(c) Expected and observed 95% C.L. limits on σB as a function of $m(\mathrm{R}_1)$ and expected σB for $\mathrm{R}_{1,2}$ production in the dimuon decay channels.

Résumé

L'un des efforts scientifiques les plus difficiles, de ces dernières années, a été la découverte et la compréhension des composants de la nature. Le Modèle Standard (MS) de la physique des particules résume aujourd'hui les particules élémentaires et leurs interactions. Cependant, le mécanisme qui rompt la symétrie électrofaible dans le MS n'a pas été vérifiée expérimentalement. Ce mécanisme du MS, qui donne une masse aux particules élémentaires massives, implique l'existence d'une particule scalaire, le boson de Higgs. La recherche du boson de Higgs, est l'un des points forts du programme de physique dans le Grand Collisionneur de Hadrons (LHC).

Cet été les expériences ATLAS et CMS ont rapporté un excès d'événements à 5σ dans l'ensemble de données obtenues en 2011 et 2012 avec une énergie dans le centre de masse de $\sqrt{s} = 7\,\mathrm{TeV}$ et $\sqrt{s} = 8\,\mathrm{TeV}$. Les désintégrations en paires de vecteurs bosons dont la charge électrique totale est nulle a permis d'identifier la nouvelle particule comme un boson neutre. L'observation dans le canal diphoton rejette l'hypothèse du spin-1. Bien que ces résultats sont compatibles avec l'hypothèse que cette particule soit le boson de Higgs prédit par le MS, davantage de données sont nécessaires pour évaluer sa nature en détail.

Cette thèse décrit le travail que j'ai réalisé durant mes trois années de thèse de doctorat sur l'expérience ATLAS. Dans chaque chapitre sont présentés les différentes activités que j'ai effectuées, à partir de la mise en marche des performances du détecteur, les études sur la performance de la reconstruction et enfin la réalisation d'une recherche de nouveaux phénomènes physiques.

Dans le premier chapitre de cette thèse, une introduction au MS est présentée. Elle résume le succès du MS et explique la génération des masses *via* le mécanisme du Higgs. Les lacunes du MS sont également présentées avec des modèles alternatifs (appelé TechniCouleur (TC)). Dans les théories de TC, les champs scalaires qui assurent la brisure de symétrie électrofaible sont des états liés produits par une nouvelle dynamique forte à une nouvelle échelle. Dans cette théorie le secteur de Higgs du MS devient une description efficace d'une théorie plus fondamentale.

Dans la première partie du deuxième chapitre de cette thèse, l'accélérateur LHC et les paramètres opérationnels pour la prise de données 2010/2011 sont présentés. L'expérience AT-LAS est l'une des deux expériences polyvalentes situées autour de l'anneau du LHC. Il a été conçu pour la recherche du boson de Higgs et pour la recherche des nouveaux phénomènes physiques. Dans la seconde partie, le detecteur ATLAS est présentée, en se concentrant plus en détail sur les performances des sous-systèmes utilisés dans cette thèse.

Dans le troisième chapitre, le calorimètre à argon liquide (LAr) est décrit en détail. Une très bonne connaissance de ce calorimètre est nécessaire, pour permettre de mesurer l'énergie des électrons, photons et jets et de l'énergie transverse manquante. Pour assurer la reconstruction optimale de l'énergie des particules, mais également synchroniser le système de lecture du détecteur avec les croisements du LHC, tous les canaux du calorimètre doivent être alignés en temps. Un alignement précis de touts ces canaux est important pour parvenir à une bonne

résolution temporelle qui est necessaire pour les différentes analyses de physique. Le troisième chapitre de cette thèse décrit aussi l'analyse de la synchronisation en temps effectuée avec les données des collisions recueillies en 2011.

Le quatrième chapitre décrit les mesures d'efficacité de la reconstruction et de l'identification d'électrons. Les événements $Z \to ee$ venant des 5 fb^{-1} de données recueillies en 2011 avec une énergie dans le centre de masse de $\sqrt{s} = 7$ TeV sont utilisés. La détermination précise des performances d'électrons est en effet indispensable pour toute recherche de phénomènes de nouvelle physique avec des électrons dans l'état final.

Enfin, le dernier chapitre présente une recherche de nouvelle physique dans l'état final diélectron. Le spectre dilepton est une sonde indépendante du modèle de nouvelle physique. Tout les excès par rapport au MS peuvent être interprétés comme la preuve d'une nouvelle physique. De nombreux modèles prédisent des résonances à haute masse tels que les modèles TC où un signal composite est mis en évidence par un excès d'événements dans le spectre de masse dilepton au-dessus dû processus de Drell-Yan qui constitue le bruit de fonds principal. Cette composante du bruit de fond diminue fortement à haute masse invariante dilepton et il est modélisée en utilisant l'extrapolation à partir de la partie basse de la masse des spectres.

Le Modèle Standard

Le Modèle Standard permet d'expliquer toutes les interactions sensibles à l'échelle des particules : l'interaction électromagnétique, l'interaction forte et l'interaction faible. Par contre, il ne permet pas d'expliquer l'interaction gravitationnelle.
Le Modèle Standard est une théorie des champs quantiques. Toutes les particules y sont représentées par des champs. Les particules vecteurs des interactions possèdent un spin entier et sont appelées bosons de jauges. Les quarks et les leptons sont des particules élémentaires sensibles à ces interactions ; elles sont dotées d'un spin demi entier et sont appelées fermions.
Le Modèle Standard est une théorie invariante sous le groupe de jauge $SU(3)_C \times SU(2)_L \times U(1)_Y$, produit des groupes de symétries associées à l'interaction forte et les interactions électromagnétique et faible, qui sont décrites par la théorie électrofaible. La théorie électrofaible, est basée sur l'invariance de jauge du groupe $SU(2)_L \times U(1)_Y$. Dans ce modèle, pour conserver cette invariance de jauge, toutes les particules physiques sont sans masse, car l'introduction d'un terme de masse briserait l'invariance du Lagrangien sous la symétrie locale $SU(2)_L \times U(1)_Y$.
Le Modèle Standard pose donc un problème dans sa version initiale. La génération des masses est assurée par un mécanisme de brisure spontanée de symétrie. C'est à dire que le système est invariant sous les transformations de jauge locales associées aux groupes $SU(2)_L \times U(1)_Y$, mais que l'état fondamental du système, donc le vide, ne respecte pas une telle invariance. Ça s'appelle le mécanisme de Higgs. Même si le mécanisme de Higgs permet de donner une masse à l'ensemble des particules connues, le Modèle Standard reste insatisfaisant à plusieurs égards. Il ne permet en effet pas de répondre à plusieurs questions, telle que le nombre de générations de quarks et des leptons. Par exemple le problème de hiérarchie, est caractérisé par une dépendance théorique des masses prédites de certaines particules aux échelles d'unification des interactions, qui est bien plus élevé que celles observé expérimentalement. Ou encore le fait que si l'on extrapole les constantes de couplages des interactions forte et électrofaible vers les hautes énergies, celles ci ne convergent pas, interdisant de fait au Modèle Standard d'être un candidat à une théorie de grande unification. Enfin si l'on considère que le Modèle Standard est englobé dans une théorie plus fondamentale, le problème de la naturalité de la masse du boson de Higgs apparait.

La TechniCouleur

Un modèle alternatif au mécanisme de Higgs a été introduit au début des années 1970 pour explique la brisure spontanée de la symétrie électrofaible. Ce modèle appelé TechniCouleur (TC), en référence à la QCD, part du Modèle Standard actuel où le secteur de Higgs devient une description efficace d'un théorie plus fondamentale. Cette théorie est invariante sous le groupe de jauge $SU(3)_C \times SU(2)_L \times U(1)_Y$. Par opposition avec le modèle de Higgs standard, la TechniCouleur fournit un mécanisme de rupture dynamique de la symétrie électrofaible. L'idée de base de la TechniCouleur est de construire un modèle analogue à la dynamique de la théorie QCD, qui pourrait être utilisée pour expliquer la masse des bosons $W^{\pm}$ et Z^0. En QCD, les quarks ressentent l'interaction forte et l'interaction faible. L'interaction forte couple les quarks dans un condensat qui brise la symétrie électrofaible. La QCD, permet donc de donner une masse aux bosons $W^{\pm}$ et Z^0, bien que celle ci soit mille six cent fois plus faible que ce qui a été observé expérimentalement, mais qui possède le bon ratio des masses des bosons de jauge.

La TechniCouleur introduit donc une nouvelle interaction similaire à la QCD, qui permet de briser de manière dynamique la symétrie électrofaible. Cette théorie est invariante sous un groupe de jauge $SU(N_{TC})_{TC}$, et introduit l'existence de nouveaux fermions : les techni-quarks. En TechniCouleur, la constante de couplage est α_{TC}. Elle devient forte aux alentours d'une centaine de GeV, ce qui a pour effet de briser spontanément l'équivalent de la symétrie chirale pour les techni-quarks, faisant apparaître des bosons de Goldstone, dont trois deviennent les composantes longitudinales de $W^{\pm}$ et Z^0. Et de manière équivalente à la QCD, il fait apparaître les masses de ces deux bosons. Les masses des fermions et des techni-pions sont assurées par un mécanisme de brisure spontanée de symétrie appelé Extended TechniColor, où TechniCouleur étendue. L'avantage de la TechniCouleur est qu'elle dispose de la liberté asymptotique de la QCD, ce qui permet de résoudre les problèmes de naturalité et de hiérarchie évoqués précédemment. Le problème est, de manière générale, que les modèles issus de la TechniCouleur vont à l'encontre des tests de précisions réalisés sur le Modèle Standard. Pour passer les tests de précisions électrofaibles, les modèles du TechniCouleur plus récents, introduisent la constante de couplage dite rampante (*"walking"*), à la différence de la QCD, où on considère que la constante de couplage monte très rapidement (*"running"*).
Les deux modèles étudiés ici sont appelés : "Low Scale Technicolor", où TechniCouleur à basse échelle (LSTC) et "Minimal Walking Technicolor" où TechniCouleur a marche minimale (MWT). Dans ceux types de modèles les particules recherchées sont des états liés de techni-quarks. Plus exactement ce sont des technimésons vecteurs, formés par le doublet de techni-quarks les plus légers. Ces particules sont : ρ_T, ω_T et a_T dans le LSTC et R_1 et R_2 dans le MWT. Ces technimésons sont attendus dans une gamme de masse de la centaine de GeV à quelques TeV. Dans la simulation les masses des particules sont des paramètres libres, les largeurs de désintégrations attendues pour chaque résonances sont étroites, de l'ordre de $\lesssim 1$ GeV pour le LSTC et avec un largeur variable en fonction de la valeur de couplage pour le MWT. En effet, le modèle LSTC impose que les masses des techni-pions soient à des valeurs comparables à celle des différents mésons. Ceci interdit cinématiquement les canaux de désintégration équivalent QCD type $\rho \rightarrow \pi\pi$. Pour le modèle MWT, les paramètres du modèle R_1 et R_2 sont semblable à ρ_T ou a_T. Les deux résonances ne sont pas nécessairement dégénérées ni très étroites, et leur caractéristiques dépendent du choix des paramètres M_A et $\tilde{g}$.

Les désintégrations des techni-mésons sont donc uniquement dues à l'interaction faible. Au LHC, on espère pouvoir découvrir l'ensemble de ces particules, dans des modes de désintégrations comprenant deux leptons, oú deux bosons de jauges électrofaibles : (γ, $W^{\pm}$ ou Z^0).

Le LHC et l'expérience ATLAS

Le Grand collisionneur de hadrons (LHC) est un anneau supraconducteur avec deux faisceaux de proton et collisionneur, installé dans un tunnel 26.7 km. L'une des missions principales de cette machine est de faire collisionner des protons à des énergies encore jamais atteintes afin de rechercher de nouvelles particules ou de processus de physique au-delà des prédictions du Modèle Standard. Comme ils sont censés être des phénomènes rares, avec des sections efficaces des production de l'ordre d'une centaine de picobarn ou inférieur, l'exigence principale de la machine est de fournir un grand nombre du collisions. Les trois premières années de fonctionnement du LHC ont été effectuée à la moitié de l'énergie nominale, $\sqrt{s} = 7$ TeV en 2010 et 2011, et $\sqrt{s} = 8$ TeV en 2012.

Les résultats présentés dans cette thèse ont été obtenus avec les données recueillies par le détecteur ATLAS en 2011. ATLAS est l'une des deux expériences généralistes présentes autour du LHC. Elle est composée de plusieurs sous-détecteus. Au plus proche du faisceau se trouve le détecteur à trace. Il permet d'assurer la détection des particules chargées, de mesurer leurs impulsions et de reconstruire les vertex. Il est décomposé en un tonneau et deux bouchons, chacun contenant un détecteur à pixels, un détecteur à transition de radiation et un détecteur au silicium. Le trajectographe est immergé dans un champ magnétique solénoïdal de 2 T qui dévie les particules chargées pour mesurer leurs impulsions. Autour du trajectographe se situent les calorimètres électromagnétiques puis hadroniques. Le calorimètre électromagnétique sert à identifier les photons et les électrons, tandis que le calorimètre hadronique sert à l'identification des hadrons. Les deux calorimètres sont constitués de deux demis tonneaux, de deux bouchons et, très proche du faisceau, de deux petits calorimètres permettant de mesurer les particules émises vers l'avant. L'ensemble du calorimètre électromagnétique et les bouchons du hadronique utilisent de l'Argon liquide comme milieu ionisant. Ils seront présentés plus en détails dans la prochaine partie. Le calorimètre hadronique du tonneau est quant à lui constitué d'une alternance de tuiles scintillantes et d'acier. L'ensemble du détecteur ATLAS a été construit à l'intérieur de six aimants toroïdaux. Ces derniers, fournissent un champ magnétique variable, compris entre 1 et 7.5 T, dans un très grand volume. Il permet de mesurer les impulsions des muons, jusqu'à environ 1 TeV. Le système de détection à muons est constitué de quatre boucliers à muons répartis de part et d'autre du détecteur, et de deux plans parallèles de détecteurs entourant l'intégralité du tonneau. Enfin l'expérience ATLAS possède un système de déclenchement décomposé en trois niveaux permettant de réduire le taux d'interaction de 40 MHz et de sélectionner seulement ≈ 300 Hz d'événements intéressants.
Cette décomposition du détecteur permet d'avoir une grande couverture dans le plan transverse : (η, ϕ). Il devrait permettre d'obtenir une très grande précision, pour identifier et mesurer les caractéristiques des particules créées dans les collisions.

Les calorimètres à argon liquide

Les calorimètres à argon liquide sont des calorimètres à échantillonnage. Ils regroupent l'intégralité des calorimètres électromagnétiques, les deux bouchons du calorimètres hadroniques et les deux calorimètres avant. Les calorimètres électromagnétique sont constitués d'un ensemble de plaques de plomb pliées en accordéon. Ces plaques servent de milieux absorbeurs, et baignent dans de l'argon liquide, comme milieu ionisant. Dans les bouchons du calorimètre hadronique le plomb est remplacé par du cuivre. Enfin les calorimètres avant sont constitués d'un ensemble de trois couches : la première servant à l'étude des particules électromagnétiques,

avec un milieu absorbeur en cuivre, et les deux autres servant aux particules hadroniques, avec des milieux absorbeurs en tungstène.

Le calorimètre électromagnétique est segmenté en trois compartiments, de granularités différentes. Le premier compartiment possède une granularité très fine en η, servant essentiellement à la réjection γ/π^0. Les particules électromagnétiques déposent la majorité de leur énergie dans le second compartiment. Le troisième et dernier compartiment sert à différencier les particules hadroniques des particules électromagnétiques.

Les calorimètres à argon liquide sont constitués en tout de 182468 cellules. Les cellules sont connectées par groupe de 128 à des cartes électroniques de lecture avant (FEB). Ces cartes électroniques ont pour rôle de faire la sommation de l'énergie recueillie dans les cellules, et de mettre en forme ce signal. Le signal échantillonné est ensuite envoyé à l'électronique de lecture, où l'énergie, le temps d'arrivée de signal et un facteur de qualité sont calculés. En periode de prise de données, pour chaque événement, chaque cellule du calorimètre à argon liquide est échantillonnée toutes les 25 ns. Un mécanisme d'amplification avec trois gains permet d'éviter que l'électronique ne sature pas en changeant le gain à certaines valeurs d'énergie. Ce changement de gain, avec un ADC à 14 bits, permet de reconstruire l'énergie d'une cellule, de quelques MeV à environ un TeV, tout en gardant une bonne résolution. Pour reconstruire une valeur d'énergie correcte pour chaque canal, il est essentiel que les temps de chaque canaux soient alignés.

Pendant ma thèse j'ai travaillé sur l'alignement temporel du calorimètre argon liquide. Le temps de tous les canaux du calorimètre doit être aligné non seulement pour synchroniser le système de lecture de détecteur avec l'horloge du LHC, mais aussi pour assurer la reconstruction optimale de l'énergie. Un alignement du temps du calorimètre à Argon liquide d'ATLAS est aussi essentiel pour obtenir une bonne résolution temporelle qui est une propriété importante pour plusieurs analyse de physique.

Depuis le début de la prise des données dans ATLAS, plusieurs études ont été réalisées pour obtenir le meilleur alignement en temps entre les signaux des canaux LAr. Il existe deux sources principales de desalignement en temps : les variations de synchronisation du FEB par rapport aux autres FEB et le défaut d'alignement de chaque canal connecté au même FEB. Durant ma thèse, j'ai effectué une analyse temporelle en utilisant les données de collisions recueillies en 2011 par le détecteur ATLAS. Après les derniers ajustements en temps obtenus à partir de la variation de temps entre le FEB et le mis-alignement entre le canaux, l'alignement en temps dans l'ensemble des cellules des calorimètres argon liquide est meilleur que 0.5 ns. Ce résultat a un impact direct sur la reconstruction des objets physique qui est fait pendant chaque prise de données.

Mesures de l'efficacité d'électrons

La détermination précise des performances du détecteur ATLAS pour les électrons est essentielle pour toute recherche de nouvelle physique avec ces particules dans l'état final. Électrons d'une gamme d'énergie jusqu'à plusieurs TeV, ils sont censés être produits dans les différentes processus de physique produit dans les collisions pp au LHC. Dans les recherches de nouvelle physique, une excellente capacité d'identification d'électrons, avec une grande efficacité et un taux élevé de rejet des jets, est requise sur une large gamme d'énergie pour surmonter le faible rapport signal sur bruit de fond. Dans la région centrale, définie comme la région avec $|\eta| < 2,47$, les performances sont assurées par l'aide d'une puissante combinaison de technologies de détection différents : des détecteurs au silicium avec un traqueur à rayonnement

de transition, et un système de calorimètre électromagnétique répartis longitudinalement en couches avec une segmentation latérale très fine.

Au cours de ma thèse, j'ai travaillé sur les mesures d'efficacités du système de déclenchement, de reconstruction et d'identification d'électrons, en utilisant des événements $Z \rightarrow ee$ recueillies en 2011 avec une énergie dans le centre de masse de $\sqrt{s} = 7$ TeV.
La méthode tag-and-probe était utilisée. Elle vise à sélectionner un lot pour d'électrons (*probe* électrons) avec des coupures lâchés à partir d'évents diélectrons ou l'autre électron passe des coupures strictes et de masse invariante proche du Z. Le rendement d'une coupure de sélection peut alors être mesurée sur l'échantillon de *probe* électrons.
Les mesures d'efficacité d'électrons sont effectuées avec la méthode tag-and-probe séparément dans des bin η et E_T des candidats *probe*, et les corrections pour le MC sont aussi dérivés. En premier lieu, cette méthode basées su les données a été utilisées pour l'estimation de l'efficacité de déclenchement. L'efficacité de déclenchement est définie comme la fraction de *probe* électrons reconstruits qui ils ont déclenché le système sur tous les *probe* passant les critères de sélection. La coupure d'identification appelée *medium* est utilisée comme base de référence de sélection et pour supprimer la contamination du bruit de fond qui vient de la conversion des photons, la trace doit contenir au moins un point venant du B-layer. L'efficacité de la sélection hors-ligne d'électrons par rapport au système de déclenchement appelé *2g20_loose* a été calculé aussi.
Après quoi, l'efficacité d'identification des *medium* électrons est mesurée en utilisant le méthode tag-and-probe. Durant ma thèse, j'ai travaillé aussi sur les mesures d'efficacité d'identification des électrons *medium* avec des conditions supplémentaires requises comme un point venant du B-layer et l'isolation. L'isolation calorimétrique est utilisée dans de nombreuses analyses, comme variable discriminante pour séparer électrons et photons, de jets et d'objets électromagnétiques non-prompt. La méthode de tag-and-probe a été utilisée pour évaluer l'efficacité d'autres critères qui ont été utilisées par nombreuses analyses avec des électrons a haut énergie transverse dans l'état final.

Recherche de TechniCouleur dans le canal dielectron

Les deux modèles TechniCouleur déjà décrits prédisent l'existence de nouvelle particules se désintégrant en deux leptons. Dans la dernière partie de ma thèse la recherche de telles particules est présentée dans l'état final diélectron. Cette recherche a été conduite en utilisant $\mathcal{L} = 5$ fb^{-1} de données de collision pp à une énergie dans le centre de masse de $\sqrt{s} = 7$ TeV.
L'état final diélectron est caractérisé par la présence de deux électrons de haute énergie. Avant de conduire une recherche de nouvelle physique, il convient d'obtenir en premier lieu une bonne description des différents processus physiques qui contribuent à cet état final dans le modèle standard. Une partie des processus peuvent être étudié à l'aide de générateur Monte Carlo et de la simulation du détecteur, mais certains bruits de fonds nécessitent un étude détaillée sur les données. Les bruits de fonds considérés dans cette étude tels que la production simple ou en paire de quarks top, dibosons et $W +$ jets sont évalués en utilisant la simulation et sont normalisés par rapport à leurs section efficace de production. Le bruit de fond irréductible dans cette analyse est le Drell-Yan (DY). La forme de la distributions en masse invariante est obtenue à partir de la simulation ; la modélisation est calculée à partir des sections efficaces évalués à l'ordre supérieur. La contribution du bruit de fond résiduel, QCD multi-jet est complètement calculé à partir des données. La forme du bruit de fond multi-jet est estimée en inversant des critères d'identifications. Pour l'évaluation des normalisations de tous les bruits de fonds, les MC et le multi-jet sont normalisés aux données dans la zone du contrôle définie par le pic du

Z.

Dans les modèles TechniCouleur, les résonances sont censées se désintégrer dans l'état final dilepton, avec une largeur de désintégration étroite. Si de telles particules existent la masse invariante dilepton devrait donc être une variable discriminante, puisqu'on attend un pic au dessus d'un continuum venant du bruit de fond du DY.

Enfin la distribution de masse invariante du fond MS et les modèles de signaux différents sont comparés avec les données en utilisant la méthode statistique bayésienne.

La recherche a été conduite sur les données, mais aucune déviation significative des prédictions du Modèle Standard n'a été observée dans la distribution de masse dilepton pour des particules TechniCouleur comprises dans un intervalle de masses $[130, 2000]$ GeV. En plus pour le modèle LSTC, l'hypothèse d'un signal avec $m(\rho_T) = 290$ GeV comme suggérée dans la Ref [42] a été testée, mais aucune déviation significative par rapport au Modèle Standard n'a été observée. Cette analyse à néanmoins permis de mettre une limite sur la production des particules TechniCouleur dans deux modèles et les régions d'exclusion dans différentes espaces des phases ont également été évaluées.

Conclusion

Le grand collisionneur de hadrons offre la possibilité de répondre aux questions ouvertes et de sonder le modèle standard dans de nouvelles régions cinématiques inaccessibles auparavant. L'expérience ATLAS est l'une des principales expériences du LHC. Elle a été construite avec des détecteurs de très hautes performances afin de maintenir le taux de collision raisonnable et pour recueillir et reconstruire les événements intéressants pour l'analyse de physique. En 2011 l'expérience ATLAS a recueilli environ 5 fb^{-1} de collisions proton-proton à $\sqrt{s} = 7$ TeV. Cet échantillon de données a permis d'effectuer la mise en service du détecteur, d'étudier les performances de reconstruction physique des objets et, enfin, de rechercher des nouveaux phénomènes physiques.

Une étude sur l'alignement temporel des calorimètres à argon liquide a été réalisée avec les données 2011. Après le réglage des dernières synchronisations temporelles, l'alignement obtenu de l'ensemble calorimètre LAr est meilleur que $0, 5$ ns pour tous l'ensemble du détecteur, et une résolution temporelle en dessous de la ns a été atteinte.

La méthode tag-and-probe utilisant les désintégrations $Z \rightarrow ee$ a été employée pour mesurer l'efficacité de reconstruction et d'identification d'électrons. Les différences entre les efficacités mesurées dans les données et MC sont calculés et indiquent valeur inférieure à 1%. Aussi l'efficacité de déclenchement a été mesurée pour les électrons passant au moins la *medium* coupure et le *medium* plus B-layer hit. Les mesures de déclenchement ont confirmé l'efficacité très élevée pour le déclenchement di-photon.

Enfin, une recherche des résonances dans le spectre diélectron à grande masse, avec les données des 2011 a été présentée. La recherche a été conduite avec 4,91 fb^{-1} (4,98 fb^{-1}) de données pour le canal *ee* ($\mu\mu$). Aucune déviation significative par rapport aux prédictions du Modèle Standard n'a été observée dans le spectre de masse invariante.

Cette analyse a néanmoins permis de mettre des limites sur les rapports de branchement de technimésons dans deux scénarios de TechniCouleur : la TechniCouleur à faible échelle (LSTC) et TechniCouleur a marche minimale (MWT). Les régions d'exclusion dans l'espace des phases

paramètres ont également été évaluées.

Dans le modèle LSTC l'espace des paramètres $m(\pi_{TC}) : m(\rho_{TC}/\omega_{TC})$ est exclue à 95% CL pour $m(\rho_{TC}/\omega_{TC})$ entre $250-840$ GeV et pour $m(\pi_{TC})$ entre $50-840$ GeV. Ces résultats sont plus strictes que les limites précédentes obtenues par Tevatron et LHC. En plus, le hypothèse de signal à $m(\rho_T) = 290$ GeV et $m(\pi_{TC}) = 160$ GeV comme suggérée dans la référence [42] par l'expérience CDF est exclue avec résultat à 95% de CL.

Pour la première fois dans l'ère du LHC des limites directes sont également calculées sur la production du technimésons dans le modèle MWT. Dans ce modelé l'espace des paramètres $M_A :$ $\tilde{g}$ est exclu à 95% CL pour M_A entre 360 GeV et 1500 GeV avec le couplage $\tilde{g}$ correspondant à 6 et 2, respectivement.

Bibliography

[1] A. Salam. *in Elementary Particle Theory, p. 367.* Almqvist and Wiksell, Stockholm, 1968.

[2] G. Altarelli. *in Elementary Particles (Landolt-Boernstein, New Series / Elementary Particles, Nuclei and Atoms).* Springer, Berlin, 2008.

[3] H. Fritzsch, M. Gell-Mann and H. Leutwyler. *Phys. Lett.*, B 47:365, 1973.

[4] S. Weinberg. *Phys. Rev. Lett.*, 31:494, 1973.

[5] S.L. Glashow. *Nucl. Phys.*, 22:579, 1961.

[6] K. Nakamura et al. Review of particle physics. *J. Phys.*, G37:075021, 2010.

[7] N. Cabibbo. Unitary symmetry and leptonic decays. *Physical Review Letters*, 10(12):531–533, 1963.

[8] M. Kobayashi and T. Maskawa. CP-violation in the renormalizable theory of weak interaction. 1973.

[9] M. E. Peskin and D. V. Schroeder. *An introduction to quantum field theory.* Westview Press, 1995.

[10] F. Englert and R. Brout. Broken symmetry and the mass of gauge vector mesons. *Physical Review Letters*, 13(9):321–323, 1964.

[11] P. W. Higgs. Broken symmetries and the masses of gauge bosons. *Physical Review Letters*, 13(16):508–509, 1964.

[12] G. S. Guralnik, C. R. Hagen, and T. W. B. Kibble. Global conservation laws and massless particles. *Phys. Rev. Lett.*, 13(20):585–587, Nov 1964.

[13] Y. Fukuda and All. Measurements of the solar neutrino flux from super-kamiokande's first 300 days. *Phys. Rev. Lett.*, 81(6):1158–1162, Aug 1998.

[14] F. Zwicky. On the Masses of Nebulae and of Clusters of Nebulae. *APJ*, 86:217–+, October 1937.

[15] F. Zwicky. Die Rotverschiebung von extragalaktischen Nebeln. *Helvetica Physica Acta*, 6:110–127, 1933.

[16] Chris Quigg and Robert Shrock. Gedanken Worlds without Higgs: QCD-Induced Electroweak Symmetry Breaking. *Phys.Rev.*, D79:096002, 2009.

[17] Y. Nambu and G. Jona-Lasinio. Dynamical model of elementary particles based on an analogy with superconductivity. i. *Phys. Rev.*, 122:345–358, Apr 1961.

[18] Y. Nambu and G. Jona-Lasinio. Dynamical model of elementary particles based on an analogy with superconductivity. ii. *Phys. Rev.*, 124:246–254, Oct 1961.

[19] J. Bardeen, L. N. Cooper, and J. R. Schrieffer. Theory of superconductivity. *Phys. Rev.*, 108:1175–1204, Dec 1957.

[20] J. Goldstone. Field theories with *⟨e⁺e⁻Superconductor≫* solutions. *Il Nuovo Cimento (1955-1965)*, 19(1):154–164, 1961.

[21] Steven Weinberg. Implications of Dynamical Symmetry Breaking: An Addendum. *Phys.Rev.*, D19:1277–1280, 1979. (For original paper see Phys.Rev.D13:974-996,1976).

[22] Leonard Susskind. Dynamics of Spontaneous Symmetry Breaking in the Weinberg-Salam Theory. *Phys.Rev.*, D20:2619–2625, 1979.

[23] J.R. Andersen, O. Antipin, G. Azuelos, L. Del Debbio, E. Del Nobile, et al. Discovering Technicolor. *Eur.Phys.J.Plus*, 126:81, 2011.

[24] Michael E. Peskin and Tatsu Takeuchi. A New constraint on a strongly interacting Higgs sector. *Phys.Rev.Lett.*, 65:964–967, 1990.

[25] Michael E. Peskin and Tatsu Takeuchi. Estimation of oblique electroweak corrections. *Phys.Rev.*, D46:381–409, 1992.

[26] Christopher T. Hill and Elizabeth H. Simmons. Strong dynamics and electroweak symmetry breaking. *Phys.Rept.*, 381:235–402, 2003.

[27] Kenneth Lane. Two lectures on technicolor. 2002.

[28] Kenneth D. Lane. Technicolor and precision tests of the electroweak interactions. 1994.

[29] Gustaaf H. Brooijmans et al. New Physics at the LHC: A Les Houches Report. Physics at Tev Colliders 2007 – New Physics Working Group. 2008.

[30] G. Brooijmans et al. New Physics at the LHC. A Les Houches Report: Physics at TeV Colliders 2009 - New Physics Working Group. 2010.

[31] Kenneth Lane and Stephen Mrenna. The Collider phenomenology of technihadrons in the technicolor straw man model. *Phys. Rev.*, D67:115011, 2003.

[32] T. Sjöstrand, S. Mrenna, and P. Skands. PYTHIA 6.4 physics and manual. *JHEP*, 05:026, 2006.

[33] Louis Helary, Nicolas Berger, and Isabelle Wingerter-Seez. *Recherche de techni-couleur avec l'expérience ATLAS. Développement d'outils et étude des performances du calorimètre à argon liquide.. oai:cds.cern.ch:1426605.* PhD thesis, Grenoble U., Annecy-le-vieux, 2011. Presented 09 Dec 2011.

[34] Jeremy R Love and J Butler. *A Search for Technicolor at The Large Hadron Collider. oai:cds.cern.ch:1443455.* PhD thesis, Boston U., Dec 2011. Presented 14 Nov 2011.

[35] Karishma Sekhon, Jeremy Love, Alex Long, and John Butler. Production Cross-Sections for Technicolor Vector Mesons at the LHC. *ATLAS Note*, ATL-COM-PHYS-2011-760, 2011.

[36] ATLAS Collaboration. Search for technihadrons in pp collisions at $\sqrt{s} = 7$ tev with the atlas detector. ATLAS-CONF-2011-125, Sept 2011.

[37] ATLAS Collaboration. Search for resonant WZ production in the $WZ \to \ell\nu\ell'\ell'$ channel in sqrt(s) = 7 TeV pp collisions with the ATLAS detector. 2012.

[38] CMS Collaboration. Search for exotic particles decaying to WZ in pp collisions at sqrt(s)=7 TeV. 2012.

[39] A Abulencia et al. Search for new high mass particles decaying to lepton pairs in $p\bar{p}$ collisions at $\sqrt{s} = 1.96$ TeV. *Phys. Rev. Lett.*, 95:252001, 2005.

[40] T. Aaltonen et al. Invariant Mass Distribution of Jet Pairs Produced in Association with a W boson in $p\bar{p}$ Collisions at $\sqrt{s} = 1.96$ TeV. *Phys.Rev.Lett.*, 106:171801, 2011.

[41] Viviana Cavaliere. Measurement of ww + wz production cross section and study of the dijet mass spectrum in the lnu + jets final state at CDF. 2010. Ph.D. thesis (advisor: Maria Agnese Ciocci).

[42] Estia J. Eichten, Kenneth Lane, and Adam Martin. Technicolor Explanation for the CDF W_{jj} Excess. *Phys.Rev.Lett.*, 106:251803, 2011.

[43] Victor Mukhamedovich Abazov et al. Bounds on an anomalous dijet resonance in W+jets production in ppbar collisions at sqrts =1.96 TeV. *Phys.Rev.Lett.*, 107:011804, 2011.

[44] C ATLAS, P Catastini, M Franklin, J Guimaraes da Costa, J Huth, F Nuti, C Roda, F Ruehr, A Solodkov, P Wells, and G Zevi Della Porta. Invariant mass distribution of jet pairs produced in association with a leptonically decaying w in the atlas experiment with 0.93 fb^{-1}. Technical Report ATLAS-COM-CONF-2011-114, CERN, Geneva, July 2011.

[45] T. Aaltonen et al. Search for Technicolor Particles Produced in Association with a W Boson at CDF. *Phys. Rev. Lett.*, 104:111802, 2010.

[46] Thomas Appelquist and Francesco Sannino. The Physical spectrum of conformal SU(N) gauge theories. *Phys.Rev.*, D59:067702, 1999.

[47] Johan Alwall et al. MadGraph/MadEvent v4: The New Web Generation. *JHEP*, 09:028, 2007.

[48] CalcHEP web site: http://theory.sinp.msu.ru/pukhov/calchep.

[49] Jeppe R. Andersen, Tuomas Hapola, and Francesco Sannino. W' and Z' limits for Minimal Walking Technicolor. 2011.

[50] Alexander Belyaev, Roshan Foadi, Mads T. Frandsen, Matti Jarvinen, Fracesco Sannino, et al. Technicolor Walks at the LHC. *Phys.Rev.*, D79:035006, 2009.

[51] http://public.web.cern.ch/public/en/research/AccelComplex-en.html.

[52] http://press.web.cern.ch/press/PressReleases/Releases2008/PR10.08E.html.

[53] (ed.) Evans, Lyndon and (ed.) Bryant, Philip. LHC Machine. *JINST*, 3:S08001, 2008.

[54] https://twiki.cern.ch/twiki/bin/view/AtlasPublic.

[55] (ed.) Carli, Christian. LHC performance. Proceedings, Workshop, Chamonix, France, January 24-28, 2011. 2011.

[56] https://twiki.cern.ch/twiki/bin/view/AtlasPublic/ApprovedPlotsATLASDetector.

[57] (ed.) Carli, Christian. LHC performance. Proceedings, Workshop, Chamonix, France, January 25-29, 2010. 2010.

[58] The ATLAS Collaboration. The ATLAS experiment at the CERN large hadron collider. *Journal of Instrumentation*, 2008.

[59] The ATLAS Collaboration. Expected Performance of the ATLAS Experiment: Detector, Trigger and Physics,(CERN, Geneva, 2008). Technical report, CERN-OPEN-2008-020.

[60] Alignment of the ATLAS Inner Detector Tracking System with 2010 LHC proton-proton collisions at $sqrts = 7$ TeV. Technical Report ATLAS-CONF-2011-012, CERN, Geneva, Mar 2011.

[61] The ATLAS Collaboration. Calorimeter Performance Technical Design Report. Technical report, CERN/LHCC/96-40, 1996.

[62] M. L. Andrieux et al. Construction and test of the first two sectors of the ATLAS liquid argon presampler. *Nuclear Instruments and Methods in Physics Research A*, 479(2):316–333, 2002.

[63] M Aharouche et al. Response uniformity of the ATLAS Liquid Argon electromagnetic calorimeter. *Nucl. Inst. and Meth. A*, 582:429–455, 2007.

[64] The ATLAS Collaboration. Supersymmetry signatures with high-pt photons or long-lived heavy particles. *ATLAS Note*, ATL-PHYS-PUB-2009-069, 2009.

[65] ATLAS Collaboration. Search for Massive Long-lived Highly Ionising Particles with the ATLAS Detector at the LHC. *submitted to Phys.Rev.Lett.*

[66] T. Guillemin, G. Perrot, L. Iconomidou-Fayard, G. Unal, H. Wilkens. Time alignment of the ATLAS liquid argon calorimeters. *ATLAS Note*, ATLAS-COM-LARG-2009-001, 2009.

[67] Alexander Penson and Kathrin Leonhardt. Timing Alignment of the entire ATLAS Liquid Argon Calorimeter with cosmic rays. *ATLAS Note*, ATLAS-COM-LARG-2009-048, 2009.

[68] Ludovica Aperio Bella. ATLAS LAr Timing alignment with collision data. *ATLAS Note*, ATLAS-COM-LARG-2012-017, 2012.

[69] J. Colas et al. Electronics calibration board for the ATLAS liquid argon calorimeters. *Nucl. Instr. and Meth.*, A593,A556, 2008.

[70] C. Cerna, J. Colas, et. al. Cabling of the ATLAS Liquid Argon Calorimeters. *CERN EDMS document*, ATL-A-EN-0001, December 2004.

[71] D. Breton, et al. HAMAC, a rad-hard high dynamic range analog memory for ATLAS calorimetry. *Electronics for LHC Experiments*, pages 203–207, in Cracow 2000.

[72] J. Christiansen, A. Marchioro, P. Moreira and T. Toifl. A Timing, Trigger and Control Receiver ASIC for LHC Detectors. *TTCrx Reference Manual*, 2005.

[73] E.G. Stern W.E. Cleland. Signal processing considerations for liquid ionization calorimeters in a high rate environment. *Nucl. Instr. and Meth.*, A338:467–497, 1994.

[74] L. Courneyea , D. Dannheim, M. Delmastro, S. Elles, M. Gouighri, L. Iconomidou-Fayard, I. Koletsou, W. Lampl, Z. Liang, L. March, P. Strizenec, F. Tarrade, R. Ueno, M. Vincter, Z. Weng, H. Zhang. Computation and validation of the electronic calibration constants for the ATLAS Liquid Argon Calorimeters. *ATLAS Note*, ATL-COM-LARG-2010-008, 2010.

[75] M Aharrouche, et al. Time resolution of the ATLAS barrel Liquid Argon electromagnetic calorimeter. *Nuclear Instruments and Methods in Physics Research*, NIM A 597:178–188, 2008.

[76] ATLAS Collaboration. Electron performance measurements with the ATLAS detector using the 2010 LHC proton-proton collision data. *Eur.Phys.J.*, C72:1909, 2012.

[77] ATLAS Collaboration. Expected electron performance in the ATLAS experiment. ATL-PHYS-PUB-2011-006.

[78] The ATLAS Collaboration. Expected photon performance in the ATLAS experiment. ATL-PHYS-PUB-2011-007.

[79] S. Agostinelli et al. GEANT4: A simulation toolkit. *Nucl. Instrum. Meth.*, A506:250, 2003.

[80] See: https://twiki.cern.ch/twiki/bin/viewauth/AtlasProtected/EfficiencyMeasurements.

[81] ATLAS Collaboration. Measurement of the inclusive isolated prompt photon cross section in pp collisions at $\sqrt{s} = 7$ TeV with the atlas detector. *Phys. Rev. D*, 83:052005, Mar 2011.

[82] Matteo Cacciari, Gavin P. Salam, and Gregory Soyez. The Catchment Area of Jets. *JHEP*, 0804:005, 2008.

[83] Exotics dilepton group. Search for high-mass dilepton resonances in $5fb^{-1}$ of pp collisions at $\sqrt{s} = 7$ TeV. ATLAS-COM-CONF-2012-016.

[84] G. Corcella et al. HERWIG6: an event generator for hadron emission reactions with interfering gluons (including supersymmetric processes). *JHEP*, 01:010, 2001.

[85] G. Corcella, I.G. Knowles, G. Marchesini, S. Moretti, K. Odagiri, P. Richardson, M.H. Seymour, and B.R. Webber. HERWIG 6.5 Release Note. *arXiv:hep-ph/0210213*.

[86] John Allison et al. *Geant4 developments and applications. IEEE Trans. Nucl. Sci.*, 53:270, 2006.

[87] ATLAS Collaboration. *Eur. Phys. J.*, C70:823–874, 2010.

[88] S. Frixione and B.R. Webber. Matching NLO QCD computations and parton shower simulations. *JHEP*, 0206:029, 2002.

[89] J. M. Butterworth, Jeffrey R. Forshaw, and M. H. Seymour. Multiparton interactions in photoproduction at HERA. *Z. Phys.*, C72:637–646, 1996.

[90] Michelangelo L. Mangano, Mauro Moretti, Fulvio Piccinini, Roberto Pittau, and Antonio D. Polosa. ALPGEN, a generator for hard multiparton processes in hadronic collisions. *JHEP*, 07:001, 2003.

[91] R. Blair et al. ATLAS Standard Model Cross Section recommendations for 7 TeV LHC 2 running. https://svnweb.cern.ch/trac/atlasgrp/export/50132/Physics/StandardModel-/xsectf/note/xsectf.pdf, 2010.

[92] J. M. Butterworth et al. Single and Diboson Production Cross Sections in pp collisions at $\sqrt{s} = 7$ TeV. *ATL-COM-PHYS-2010-695*, 2010.

[93] A. Sherstnev and R. S. Thorne. Parton Distributions for LO Generators. *Eur. Phys. J.*, C55:553–575, 2008.

[94] A. Sherstnev and R.S. Thorne. Different PDF approximations useful for LO Monte Carlo generators. page 149, 2008.

[95] R. Hamberg, W. L. van Neerven, and T. Matsuura. A Complete calculation of the order α_s^2 correction to the Drell-Yan K factor. *Nucl. Phys.*, B359:343–405, 1991. Program code available at `http://www.lorentz.leidenuniv.nl/neerven/DECEASED`.

[96] P. Golonka and Z. Wąs. PHOTOS Monte Carlo: a precision tool for QED corrections in Z and W decays. *Eur. Phys. J. C*, 45:97–107, 2006.

[97] C. M. Carloni Calame, G. Montagna, O. Nicrosini, and A. Vicini. Precision electroweak calculation of the production of a high transverse-momentum lepton pair at hadron colliders. *JHEP*, 10:109, 2007.

[98] U. Baur. Weak Boson Emission in Hadron Collider Processes. *Phys. Rev.*, D75:013005, 2007.

[99] E Gamma group. Energy Scale Resolution Recommendations. https://twiki.cern.ch/-twiki/bin/view/AtlasProtected/EnergyScaleResolutionRecommendations.

[100] ATLAS Collaboration. Search for dilepton resonances in pp collisions at $\sqrt{s} = 7$ TeV with the ATLAS detector. *Phys. Rev. Lett.*, 107:272002, 2011.

[101] E Gamma group. Energy Scale and Resolution recommendations. https://twiki.cern.ch/twiki/bin/view/AtlasProtected/EnergyScaleResolutionRecommendations.

[102] M Aharrouche et al. Energy linearity and resolution of the ATLAS electromagnetic barrel calorimeter in an electron test-beam. *Nucl. Instrum. Meth.*, A568:601–623, 2006.

[103] A. Caldwell, D. Kollar, and K. Kröninger. BAT - The Bayesian Analysis Toolkit. *Computer Physics Communications*, 180:2197, 2009.

[104] G. Choudalakis and D. Casadei. Plotting the differences between data and expectation. *The European Physical Journal Plus*, 127:1–11, 2012. 10.1140/epjp/i2012-12025-y.

[105] Kenneth D. Lane and Estia Eichten. Two Scale Technicolor. *Phys. Lett.*, B222:274, 1989.

[106] ATLAS Collaboration. Search for high-mass dilepton resonances in $5 fb^{-1}$ of pp collisions at $\sqrt{s} = 7$ TeV with the ATLAS detector. CERN-PH-EP-2012-19.

[107] The ATLAS Collaboration. Performance of the atlas trigger system in 2010. *Eur. Phys. J.*, C, 2012.

[108] Performance of the Electron and Photon Trigger in pp Collisions at $\sqrt{s} = 7$ TeV with the ATLAS Detector at the LHC. (ATLAS-CONF-2011-114), 2011.

[109] J.C. Collins and D.E. Soper. *Phys. Rev.*, D16:2219, 1977.

Acknowledgment

The last three years of activities in the ATLAS Lapp group and in the ATLAS Collaboration were really intensive and constructive. I had the possibility to experience different aspects of the high energy physics and to learn from very different people.

First I would like to thank all the members of my jury. Je voudrais tout d'abords remercier Marc Besancon d'avoir accepté d'être un de rapporteurs de ma thèse et de l'avoir lu avec attention et intérêt et de m'avoir donné des commentaires intéressantes et très utiles. Je tiens ensuite à remercier Guillaume Unal d'avoir accepté d'être rapporteur de ma thèse, de l'avoir lu et de m'avoir donné beaucoup de conseils pour l'améliorer, mais surtout je voudrais le remercier car j'ai eu la chance de travailler avec lui sur l'alignement temporel du calorimètre a Argon liquide d'ATLAS et grâce à lui j'ai appris beaucoup de choses. Of course, a big thanks goes to Leandro Nisati who agreed to read the manuscript and to be part of the jury despite his onerous commitments. I would like to thank him, not only for having participated to my thesis defense, but also for the very constructive exchanges we had. Enfin je vais remercier chaleureusement Jean-Pierre Lees d'avoir lu le manuscrit et d'avoir accepté d'être le président de mon jury. With this small paragraph, I would like to express my gratitude to my thesis advisors. I would like to thanks Tetiana Berger-Hryn'ova, for the stimulating discussions we had and all the suggestions for the work presented in this thesis. I am very glad to her help during the writing of this thesis and during the preparation of the infinite number of presentation that I made during this experience. I would also like to thanks Lucia Di Ciaccio, for her precious suggestions, and for the revision work of this thesis. I am very grateful for her contagious enthusiasm for the research and for giving me the opportunity to join and work in a so exciting experiment.

Pour m'avoir donné l'occasion de faire un thèse je voudrais remercier Yannis Karyotakis et Jean-Pierre Lees, que m'ont accueilli au Laboratoire d'Annecy-le-Vieux de Physique des Particules pendant ces trois ans. Merci aussi aux personnels administratif du laboratoire, Chantal, Marie Claude et Brigitte pour leur disponibilités et pour tout leur aide.
Then, I would like to acknowledge all the LAPP ATLAS group because I had the opportunity to learn a lot of useful things from each of them. Their help and feedbacks, coming from deep experiences, were a real precious gift to my scientific experience.

The ATLAS Collaboration was an amazing group where to move the first steps in high energy physics. In particular, I had the opportunity to work mostly in two ATLAS working groups: the LAr group and the Exotic dilepton group. Therefore I would like to thank all the persons who worked in those groups and helped me with really good advices and discussions. I would also like to deeply thanks Kenneth Lane and Mads Frandsen for having helped me to really understand the technicolor theories and for the numberous discussions we had which made possible a big part of the work in my thesis.

Maintenant je ne peux manquer de remercier les ainsi dits "jeunes du labo", présents et passés, qui ont rempli mes trois années a Annecy. Prima di tutto Livia che é stata una guida per me, e un incredibile e perfetta shopping-friend, con il suo amore per Annecy spesso contrapposto al mio... Then Dimitra who made more or less everything with me in this 3 years, with up and down moments becomes one of my best friends here. Maud que je trouve génial, très jeun et très très français. Mayuko who helps me always with a big and kind smile. Élisabeth qui a fait ses biscuites pour mon pot, and Oanh who has cooked the best nem that I never eat! Après un gros merci aux différentes personnes avec lesquelles j'ai partagé mon bureau ici au LAPP: Olivier et Houry. Je vais ensuite remercier tout les nombreux (autres) jeunes du laboratoire avec lesquelles j'ai plus or moins partage les activités de cette belle ville d'Annecy. Merci donc à: Timur, Florent, Sean, Guillaume Chalons, Guillaume Drieu, Daniel, Mathieu, Laura, Olivier, Caroline, Ambroise, Gwenaële, Loïc, Benedicte, Iro, Armand, Michael et Marie, et bien sure Thimothé, Florian, Vincenzo et aussi Guilhem, Lisa, Laurent et Jonathan.

Dopodiché qualche riga ai miei MBF, perché senza di loro non ce l'avrei mai fatta... Grazie a Daddino, Sara e Marco per essere stati la mia *famiglia* per i 5 mesi piu' super-mariosi della mia vita. Grazie a Manu per essere la migliore amica fiorentina che ho. Grazie ad Andrea per aver accolto il mio Raggetto di sole. Grazie a Roberto per le spalle su cui piangere e a Piccolo-Lord per essere un piccolo-lord. Due parole anche agli annessi e connessi dei MBF, grazie a Francesca di avermi fatto conoscere Trucebaldazzi, a Shervin e Grazia per gli inviti a cena, a Ennio per non avermi raccolta quella sera a Ginevra, a Cocchi e Anna per essere cosi carini tra di loro e con gli altri, e per finire a Valerio C. per essersi fatto chiamare sanguisuga.

Ora non posso fare a meno di ringraziare la mia cittá: Roma, e tutto quello che ció rappresenta per me: tutto il mio mondo, tutti i miei amici, tutte quelle persone che sono lí e che ogni volta che torno riescono a farmi sentire come se non fossi mai partita.
E poi la mia famiglia. La mia unica e straordinaria famiglia, che mi ha permesso di essere qui senza (quasi) sentire la loro mancanza...... E Flamy perché nonostante tutto riusciamo ancora a leggerci nel pensiero.

Comunque, forse, l'ultima parola va a Luigi, che incredibilemente e senza volerlo é diventato parte della mia vita qui....

Grazie

Résumé : La campagne du LHC dans les premières années de prise de données a été un succès. La prise de données 2011 a permis d'enregistrer plus de 5 fb^{-1} de données à $\sqrt{s} = 7$ TeV avec l'expérience ATLAS. Dans le travail présenté dans cette thèse l'ensemble de données 2011 est utilisé pour les différentes études. Cette thèse est organisée en cinq chapitres. Dans le premier chapitre est présenté une introduction théorique au modèle standard (MS) et son extension éventuelle la Technicouleur (TC). Le deuxième chapitre donne un aperçu du LHC et du détecteur ATLAS. Dans le troisième chapitre l'analyse temporelle des canaux de lecture du calorimètre à argon liquide est rapportée. Un alignement temporel de l'ensemble du calorimètre permet la synchronisation du système de lecture du détecteur avec l'horloge du LHC et est également utilisé dans des analyses de physique telles que celles pour la recherche de particules à longue durée de vie. Dans le cadre de recherches de nouvelle physique une excellente capacité identification des électrons avec un rendement élevé est nécessaire sur une gamme d'énergie étendue. Le quatrième chapitre de cette thèse présente les mesures d'efficacité du trigger (systeme de déclenchement) et d'identification des électrons en utilisant les événements $Z \rightarrow ee$. Enfin le dernier chapitre décrit la recherche de résonances à grandes masses dans le canal diélectron, ceci dans les cadre de deux scénarios différents, la Technicouleur "Low-scale" et la Technicouleur "Minimal Walking". L'importance de l'excès potentiel des événements TC par rapport aux prédictions du MS est évaluée dans la distribution de masse invariante dilepton. En l'absence d'écart significatif par rapport aux prédictions du MS des limites avec un niveau de confiance de 95% sont fixées sur la section transversale et sur la masse de résonance.

Mots-clés : LHC, ATLAS, calorimètre à argon liquide, alignement temporel, efficacité des électrons, technicouleur, dilepton, haute masse.

Abstract : The LHC campaign in the first years of data taking was successful. The 2011 run has allowed to record more than 5 fb^{-1} of data at $\sqrt{s} = 7$ TeV with the ATLAS experiment. In the work presented in this this thesis the whole 2011 data set is used to performed different studies. This thesis is organized in five chapters. In the first chapter is presented a theoretical introduction to the Standard Model (SM) and to one of its possible extension the TechniColor (TC). The second chapter gives an overview of the LHC complex and of the ATLAS detector components. In the third chapter the timing analysis on all the readout channels of the Liquid Argon Calorimeter is reported. A precise timing alignment over the whole calorimeter is used to synchronize the detector readout system with the LHC bunch crossing and has also application in some physics analysis such as those looking for long lived particles. In the searches for new phenomena an excellent electron identification capability, with high efficiency and high jet rejection rate, is required over a broad energy range. The fourth chapter of this thesis presents the measurements of the trigger and the identification electron efficiency using $Z \rightarrow ee$ events. Finally the last chapter describes a search for resonant deviations from the Standard Model in the high masses of the dielectron spectrum within two different Technicolor scenarios the Low-scale Technicolor and the Minimal Walking Technicolor. The significance of potential excess of the TC candidate events over the SM background expectation is evaluated in the dilepton invariant mass distribution. In the absence of any significant signal 95% confidence level limits are set on the cross section and on the resonance mass.

Key-words : LHC, ATLAS, LAr calorimeter, timing alignment, electron efficiency, technicolor, dilepton, high mass.